

SIMULATIONS OF DETONATION QUENCHING AND RE-INITIATION USING A GLOBAL FOUR-STEP COMBUSTION MODEL

by

MOHNISH PESWANI

Submitted in partial fulfillment of the requirements for the degree of
Doctor of Philosophy

Department of Mechanical and Aerospace Engineering

CASE WESTERN RESERVE UNIVERSITY

May, 2023

**CASE WESTERN RESERVE UNIVERSITY
SCHOOL OF GRADUATE STUDIES**

We hereby approve the thesis/dissertation of

Mohnish Peswani

candidate for the degree of **Doctor of Philosophy**¹.

Committee Chair

Dr. Brian Maxwell

Committee Member

Dr. Bryan Schmidt

Committee Member

Dr. Steve Hostler

Committee Member

Dr. Shane Parker

Date of Defense

February 22, 2023

¹We also certify that written approval has been obtained for any proprietary material contained therein.

DEDICATION

Dedicated to my family:

Taylor, Lorraine, Ghanshyam, & Nihal

TABLE OF CONTENTS

Dedication	iii
List of Tables	vii
List of Figures	viii
Acknowledgements	xvii
Nomenclature	xix
Abstract	xxiii
Chapter I: Introduction	1
1.1 Motivation	1
1.2 The Detonation Cellular Structure	3
1.3 Detonation diffraction	5
1.4 Numerical modeling of detonation re-initiation and the need for better chemistry descriptions	7
1.5 Overview	9
1.6 Thesis Objective	11
Chapter II: Literature Review	12
2.1 Flame Acceleration (FA) and Deflagration to Detonation Transition (DDT) Background and History	12
2.2 Shock–Flame Interaction	17
2.3 Detonation Diffraction	18
2.3.1 The role of cellular instabilities on the detonation diffraction problem	22
2.4 Detonation Interaction With Perforated Plates and Obstacles	24
2.5 Numerical Investigations of FA and DDT	30
2.5.1 Summary of detonation quenching and re-initiation investigations using global reaction mechanisms (GRMs)	35
2.5.2 State of the art combustion models	40

2.6 Numerical Modeling Approach in the Current Study	43
Chapter III: Proposed Methodology	45
3.1 Governing Equations	45
3.2 The four-species, four-step combustion model	48
Chapter IV: Combustion Properties of a Simple and Efficient Four-Step Model	53
4.1 Preliminary Results for Stoichiometric, Lean, and Diluted Mixtures .	53
4.1.1 Stoichiometric Undiluted Reactive Mixtures	54
4.1.2 Dilution by Inert Species	58
4.1.3 Fuel Lean Mixtures	60
4.2 Important Combustion Properties	63
4.2.1 Explosion Limits	63
4.2.2 Global Activation Energy (E_a) And Heat Release (Q)	66
4.2.3 Chapman-Jouguet (CJ) Detonation Velocity	68
4.2.4 Induction to Reaction Time Ratio (t_i/t_e)	70
4.2.5 Detonation Stability and the χ Parameter	71
4.2.6 Expansion Ratio (σ) and the Zel'dovich Number (β)	74
4.3 Error Analysis	77
4.4 Model Limitations	79
4.5 Conclusion	81
Chapter V: Detonation Wave Diffraction in Stoichiometric C_2H_4/O_2 Mixtures	83
5.1 Domain, initial and boundary conditions	83
5.2 Results	85
5.2.1 Regimes observed following diffraction	85
5.2.2 Critical quenching (CQ)	93
5.2.3 Critical re-initiation (CR)	95
5.2.4 Critical transmission (CT)	97
5.2.5 Effects of grid resolution	99
5.3 Discussion	102

5.3.1	Transverse detonation re-initiation distance and wall reflection length	102
5.3.2	Origin and role of transverse detonations during re-initiation	106
5.3.3	Triple point and transverse detonation speeds	116
5.3.4	The overdriven second triple point	120
5.4	Conclusion	123
Chapter VI: Detonation Wave Interaction With a Single Half-Cylinder Obstacle		125
6.1	Numerical Implementation	127
6.2	Origin and Role of Transverse Detonations During Re-initiation	129
6.3	Conclusion	140
Chapter VII: Conclusions and Recommendations for Future Work		143
7.1	Conclusions	143
7.2	Recommendations	145
Appendix A: Important Four-Step Model Equations		147
Appendix B: Four-Step Model Parameters for the different mixtures considered in Section 4		149
B.1	Stoichiometric acetylene-oxygen mixture	149
B.1.1	Stoichiometric methane-oxygen mixture	150
B.1.2	Stoichiometric propane-oxygen mixture	151
B.1.3	Stoichiometric ethylene-oxygen mixture	153
B.1.4	Lean acetylene-oxygen mixture ($\phi = 0.714$)	154
B.1.5	Lean acetylene-oxygen mixture ($\phi = 0.5$)	155
B.1.6	Lean acetylene-oxygen mixture ($\phi = 0.33$)	156
Bibliography		158

LIST OF TABLES

<i>Number</i>	<i>Page</i>
1.1 List of recent major accidents in the United States. Damages reported in millions of dollars.	2
5.1 Regimes observed at different initial pressures at the finest resolution of 20 μm resolution.	92
6.1 Regimes observed by Floring [52] at different initial pressures at the finest resolution of 78 μm resolution.	128

LIST OF FIGURES

<i>Number</i>	<i>Page</i>
1.1 Sketch showing the triple point collision process. Various waves indicated are incident shocks (I), Mach shocks (M), and transverse shocks (T). (R) shows the reaction zone [136].	4
1.2 Soot-foils showing (A) a regular detonation structure in $2\text{H}_2 + \text{O}_2 + 17\text{Ar}$ with $p_0 = 20$ kPa and (B) an irregular detonation structure in $\text{C}_3\text{H}_8 + 5\text{O}_2$ with $p_0 = 20$ kPa [7].	5
1.3 Regimes of detonation diffraction for the critical diameter problem [195].	6
1.4 Transverse detonations and multiple re-initiation mechanisms observed during critical re-initiation in the study by Xu et al. [242]. . .	8
2.1 Sequence of shadow photographs showing the tulip flame and boundary layers ahead of the accelerated flame propagating from left to right. Mixture is stoichiometric hydrogen–oxygen at initial pressure 60 kPa [94].	13
2.2 Stroboscopic schlieren photographs [226] showing the explosion within an explosion in an equimolar hydrogen–oxygen mixture with $p_0 = 22\text{mm Hg}$	14
2.3 Shock–flame interaction [219], a) initial shock–flame interaction and reflected shock with $M_s = 1.7$, b) resulting <i>strange-wave</i> observed for $M_s = 1.7$, and c) resulting detonation with $M_s = 1.9$	19
2.4 Soot-plate record from study by Khasainov et al. [88] showing detonation diffraction in stoichiometric acetylene–oxygen mixtures with (A) $p_0 = 0.035$ bar and $\alpha = 15^\circ$, and (B) $p_0 = 0.07$ bar and $\alpha = 45^\circ$.	22

2.5	Re-initiation event and detailed view of transverse detonation from the study by Pintgen and Shepherd [174] following diffraction of a detonation wave initiated in an irregular $\text{H}_2 - \text{N}_2\text{O}$ mixture with $p_0 = 45$ kPa.	25
2.6	Open-shutter photograph of detonation quenching and re-initiation experiments by Radulescu and Maxwell.	29
2.7	Detonation re-initiation by a transverse detonation observed by Bhattacharjee [15] following detonation interaction with a single obstacle in a stoichiometric methane–oxygen mixture with $p_0 = 12.3$ kPa. . .	30
2.8	Borghi diagram of characteristic turbulent combustion regimes [31]. .	32
2.9	Two-dimensional transition from a shock–flame complex to detonation in using the CLEM-LES [134].	34
2.10	Numerical density field results from Bhattacharjee et al. for $\text{CH}_4 + 2\text{O}_2$ and $p_0 = 10$ kPa using a 1-step model showing the critical ignition regime.	36
2.11	Numerical soot foils from the study by Shi et al. [204] showing detonation re-initiation following diffraction using a one-step model for (A) a planar detonation with no cells, and (B) a cellular detonation wave.	37
2.12	Numerical soot foils from the study by Xu et al. [242] showing (A) detonation failure following diffraction and (B) detonation re-initiation by a transverse detonation with an obstacle perturbation using a two-step chemistry model.	39
2.13	Numerical results from Lau-Chapdelaine [98] for $\text{CH}_4 + \text{O}_2$ and $p_0 = 11.9$ kPa using a two-step chemistry model showing detonation quenching and re-initiation. The transverse detonation disappears shortly after Frame (c).	39

2.14	Numerical results from Mével et al. using a 9 species, 17 reaction model [146] for $2\text{H}_2 + \text{O}_2 + 2\text{Ar}$ and $p_0 = 13.8$ kPa for detonation diffraction [147].	42
3.1	Constant volume reaction for a stoichiometric $\text{C}_2\text{H}_2 - \text{O}_2$ with $T_0 = 2500$ K and $p_0 = 1$ atm, showing the different zones where all of the fits are performed for calibrating the four-step model with data from detailed chemistry [34].	49
4.1	Constant volume ignition time predictions of the four-step model (points) compared to the detailed chemistry mechanisms (lines) of (A) Konnov [34] for the stoichiometric acetylene–oxygen mixture, (B) GRI-3.0 [208] for the stoichiometric methane–oxygen mixture, (C) USC for the stoichiometric propane–oxygen mixture [232], and (D) USC [232] for the stoichiometric ethylene–oxygen mixture. . . .	54
4.2	Constant volume ignition temperature profiles of the four-step model (points) compared to the detailed chemistry mechanisms (lines) for stoichiometric (A) acetylene–oxygen, (B) methane–oxygen, (C) propane–oxygen, and (D) ethylene–oxygen mixtures with $T_0 = 1500, 2000,$ and 2500 K and $\rho = 1.0$ kg/m ³	56
4.3	Temperature profiles for ZND detonation using the four-step model (points) and detailed chemistry mechanisms (lines) for stoichiometric (A) acetylene–oxygen, (B) methane–oxygen, (C) propane–oxygen, and (D) ethylene–oxygen mixtures with $T_0 = 300$ K.	57
4.4	Temperature profiles behind a Mach 6.35 (2262.6 m/s) shock in stoichiometric methane–oxygen at $T_0 = 300$ K and $p_0 = 5.5$ kPa computed using conventional one- and two-step perfect gas models [98], a one-step model with temperature-dependent heat capacities, the four-step model [173], and the detailed GRI-3.0 mechanism [208]. . .	59

- 4.5 Constant volume ignition time predictions and ZND detonation temperature profiles with $T_0 = 300$ K using the four-step model (points) and detailed chemistry mechanisms (lines) for (A) dilute stoichiometric acetylene-oxygen [$2\text{C}_2\text{H}_2 + 5\text{O}_2 + 7\text{Ar}$] and (B) dilute stoichiometric methane-oxygen [$\text{CH}_4 + 2\text{O}_2 + 2\text{N}_2$] mixtures. 60
- 4.6 Constant volume ignition time predictions and ZND detonation temperature profiles with $T_0 = 300$ K using the four-step model (points) and detailed Konnov mechanism [34] (lines) for two lean acetylene-oxygen mixtures (A) $\phi = 0.5$ and (B) $\phi = 0.33$ 61
- 4.7 Constant volume ignition delay (τ) for acetylene-oxygen mixtures as a function of equivalence ratio (ϕ) using the four-step model (points) and the detailed Konnov mechanism [34] (lines). 62
- 4.8 Explosion limit predictions for stoichiometric acetylene-oxygen, methane-oxygen, propane-oxygen, and ethylene-oxygen using the four-step model (points) and detailed chemistry mechanisms (lines) along with experimental data points for methane [117] and propane [155] (black points). 64
- 4.9 Non-dimensional activation energy (E_a) for stoichiometric hydrocarbon-oxygen mixtures, all at an initial density of $\rho = 1.0$ kg/m³ using the four-step model (points) and detailed chemistry mechanisms (lines). 67
- 4.10 Dimensionless heat release (Q/RT) predictions for stoichiometric (A) acetylene oxygen and (B) methane oxygen mixtures using the four-step model (points) and detailed chemistry mechanisms (lines). 67
- 4.11 CJ detonation speed and temperature predictions using the four-step model (points) and detailed chemistry mechanisms (lines) for stoichiometric (A) acetylene-oxygen, (B) methane-oxygen, (C) propane-oxygen, and (D) ethylene-oxygen mixtures with varying initial pressures and $T_0 = 300$ K. 69

4.12	CJ detonation speed and temperature predictions using the four-step model (points) and detailed chemistry mechanisms (lines) for the lean acetylene mixtures (top) and dilute hydrocarbon mixtures (bottom).	70
4.13	Ignition time to reaction time ratio (t_i/t_e) predictions using the four-step model (points) and detailed chemistry mechanisms (lines) for stoichiometric acetylene–oxygen (top) and methane–oxygen mixtures (bottom).	72
4.14	Dimensionless χ parameter predictions using the four-step model (points) and detailed chemistry mechanisms (lines) for the four different hydrocarbon mixtures (top) and dilute acetylene-oxygen mixtures (bottom).	73
4.15	Expansion ratio (σ) predictions using the four-step model (points) and detailed chemistry mechanisms (lines) for the stoichiometric (A) acetylene–oxygen and (B) methane–oxygen mixtures for varying initial pressures.	75
4.16	Zel’dovich number (β) predictions using the four-step model (points) and detailed chemistry mechanisms (lines) for the four different stoichiometric hydrocarbon mixtures with (A) $P_0 = 1$ atm and (B) $P_0 = 10$ atm.	76
4.17	Error function (E) results for the four-step model for ignition time predictions (τ), non-dimensional activation energy (E_a), non-dimensional heat release (Q), CJ speed, induction time to reaction time ratio (t_i/t_e), detonation χ parameter, expansion ratio (σ), and Zel’dovich number (β) for the four different stoichiometric hydrocarbon mixtures under consideration.	79
5.1	Numerical set-up, with a zero-gradient condition on the right boundary, and symmetric elsewhere.	84

5.2	Numerical soot foils for the different regimes observed, all at $20\ \mu\text{m}$ resolution. (a) the sub-critical regime, (b) critical quenching, (c) critical re-initiation.	87
5.3	A continuation of the results shown in Fig. 5.2 showing the numerical soot foils for the (d) critical transmission and (e) super-critical regime outcomes observed.	88
5.4	Speed of the wave front (U_s) as a function of z -distance for each outcome observed. (a) the sub-critical regime, (b) critical quenching, (c) critical re-initiation, (d) critical transmission, and (e) super-critical regime. Measurements are taken at the tube axis with $r = 0.0\ \text{m}$	90
5.5	Density field evolution showing the failure of the detonation wave for critical quenching (CQ) with $p_0 = 13.5\ \text{kPa}$ (frames a-d). Experimental schlieren images for $p_0 = 15\ \text{kPa}$ with $U/U_{\text{CJ}} = 1.027$ (frames e and f) [195].	94
5.6	Density field evolution showing the failure and subsequent re-initiation of the detonation wave for critical re-initiation (CR) with $p_0 = 13.8\ \text{kPa}$ (a-d). Re-initiation observed in the experiment by Schultz for $p_0 = 20\ \text{kPa}$ with a velocity deficit of 2% reported prior to diffraction (e).	96
5.7	Density field evolution showing the critical transmission (CT) outcome with $p_0 = 14.5\ \text{kPa}$ (a-d). CT observed in the experiment by Schultz for $p_0 = 20\ \text{kPa}$ with an overdriven detonation (1% overdrive) reported prior to diffraction (e-f).	98
5.8	(a)The different outcomes observed at each minimum grid resolution and initial quiescent pressure (p_0). (b) D/λ for the different outcomes observed at each minimum grid resolution.	99

5.9	Density gradient evolution for the CR outcome as seen at a minimum grid resolution of $78 \mu\text{m}$ for $p_0 = 8 \text{ kPa}$ (a-c), $39 \mu\text{m}$ for $p_0 = 10.75 \text{ kPa}$ (d-f), and $20 \mu\text{m}$ for $p_0 = 13.8 \text{ kPa}$ (g-i).	100
5.10	Ratio of transverse detonation initiation length to detonation cell size (l_t/λ) as a function of initial pressure (p_0). Dashed lines represent limits established in previous experiments by Xu et al. [242] and Nagura et al. [153].	104
5.11	Ratio of transverse detonation reflection length to detonation cell size (l_w/λ) as a function of initial pressure (p_0). Dashed lines represent limits established in previous experiments by Nagura et al [153].	105
5.12	Density gradient evolution for $p_0 = 13.8 \text{ kPa}$ showing the mechanism by which the transverse detonation is triggered. Frames a-d show the localized explosion and onset of the transverse detonations.	107
5.13	Continuation of Fig. 5.12. Frames e-h then show the failure of the first transverse detonation and sustained propagation of the second transverse detonation.	108
5.14	Density gradient evolution showing the establishment of the second transverse detonation (a-c) and subsequent detonation re-initiation in the channel (d and e) for $p_0 = 13.8 \text{ kPa}$	110
5.15	Details of the density gradient, temperature, and ignition delay times for CR observed with $p_0 = 13.8 \text{ kPa}$	111
5.16	Continuation of Fig.5.15.	112
5.17	Pressure and ignition delay time profiles measured along $r = 0.072 \text{ m}$ for $p_0 = 13.8 \text{ kPa}$. Distances are given in the frame of reference of the Mach shock.	113
5.18	Density gradient evolution showing the establishment of the second transverse detonation (a-e) and subsequent detonation re-initiation in the channel (f and g) for $p_0 = 13.9 \text{ kPa}$	115

5.19	Comparison of numerical (frames a and c) and experimental [242] (frames b and d) soot foils showing the different pathways to detonation re-initiation for the CR outcome.	117
5.20	Triple point speed (U_{TP}) normalized to the CJ speed of the quiescent mixture as a function of time for (a) the first transverse detonation and (b) the second transverse detonation.	118
5.21	Transverse detonation speed (U_{TD}) normalized to the CJ speed of the shocked unburned mixture as a function of time for (a) the first transverse detonation and (b) the second transverse detonation.	120
5.22	Speed of the wave front (U_s) as a function of z -distance for the Mach detonation measured along the top boundary at $r = 0.072\text{m}$ for (a) CR for $p_0 = 13.8\text{ kPa}$ and (b) CR for $p_0 = 13.9\text{ kPa}$	121
5.23	Density gradient composites showing the propagating transverse detonation waves for $p_0 = 13.8\text{ kPa}$ along with the sample spaces where the shocked gas mixture velocity is extracted from (A and B). Frames (C) and (D) show the magnitude and the direction of the triple point speed (U_{TP}), transverse detonation speed (U_{TD}), and resultant velocity of the shocked mixture for the sample space (\tilde{U}) for the first and second transverse detonations respectively.	122
6.1	Different simulated density fields observed by Floring [52] and compared to experimental schlieren images, reproduced from Bhattacharjee [15]. (a) detonation quenching, (b) critical ignition without detonation, (c) critical detonation re-initiation, and (d) critical detonation re-initiation without transverse detonation.	126
6.2	Numerical set-up used by Floring [52], with zero gradient boundary condition on the right, and symmetric elsewhere.	127
6.3	Density gradient evolution at the moment of detonation re-initiation for an initial pressure of $p_0 = 9.5\text{ kPa}$ and a resolution of $78\ \mu\text{m}$	129

6.4	Details of temperature, pressure, and ignition delay times for detonation re-initiation of $p_0 = 9.5$ kPa and a resolution of $78 \mu\text{m}$	132
6.5	Temperature, pressure, and ignition delay time profiles measured along along $y = 0.064$ m (the dashed line indicated in Fig. 6.4a) for $p_0 = 9.5$ kPa. Distances are given in the frame of reference of the Mach shock.	133
6.6	Density gradient evolution at the moment of detonation re-initiation for an initial pressure of $p_0 = 10.25$ kPa and a resolution of $78 \mu\text{m}$	134
6.7	Details of temperature, pressure, and ignition delay times for detonation re-initiation of $p_0 = 10.25$ kPa and a resolution of $78 \mu\text{m}$	135
6.8	Density gradient evolution at the moment of detonation re-initiation for an initial pressure of $p_0 = 13$ kPa and a resolution of $78 \mu\text{m}$	137
6.9	Details of temperature, pressure, and ignition delay times for detonation re-initiation of $p_0 = 13$ kPa and a resolution of $78 \mu\text{m}$	138
6.10	Temperature, pressure, and ignition delay time profiles measured along $y = 0.002$ m (the dashed line indicated in Fig. 6.9b) for $p_0 = 13$ kPa. Distances are given in the frame of reference of the Mach shock.	141

ACKNOWLEDGEMENTS

The author would like to personally thank his advisor, Dr. Brian Maxwell, for his guidance, mentorship, and support throughout the project. Further acknowledgment goes to committee members Dr. Bryan Schmidt, Dr. Steve Hostler, and Dr. Shane Parker for their valuable input and constructive criticism. Contributions from fellow graduate students Grace Floring, Joshua Smith, and Curran Schmidt from the Computational Fluid Dynamics and Supersonic Combustion Research Laboratory (CFDSC) at Case Western Reserve University (CWRU) were also crucial for completing this work. Special thanks also go to Dr. Y. Zhu and Dr. J. Yang for their guidance and recommendations for developing the combustion model utilized in the study. The author would also like to thank his previous academic advisors, Dr. Alexis Abramson and Dr. Steve Hostler, for their mentorship during the initial stages of his tenure as a graduate student. Significant computational resources were required to complete this work provided by the Core Facility for Advanced Research Computing at CWRU and the Ohio Supercomputer Center (OSC).

This work would also not be possible without constant support from family and friends. Most of all, the author would like to thank his parents, Lorraine and Ghanshyam Peswani, his partner Taylor Combs, and brother Nihal Peswani for their unconditional love, invaluable guidance, and unwavering support. Finally, special thanks also go to fellow graduate students Akhil Kandhari, Kenneth Moses, Fletcher Young, Ronald Leibach, Ru-Ching Chen, and Zachary Abraham for their lifelong friendship and valuable discussions.

NOMENCLATURE

Acronyms

AMR	Adaptive Mesh Refinement
CJ	Chapman-Jouguet
CLEM	Compressible Linear Eddy Model
CPU	Central Processing Unit
DDT	Deflagration to Detonation Transition
DNS	Direct Numerical Simulation
ERM	Elementary Reaction Mechanism
GRM	Global Reaction Mechanism
LES	Large Eddy Simulation
LKM	Localized subgrid Kinetic energy Model
NS	Navier Stokes
PDE	Pulse Detonation Engine
RANS	Reynolds-Averaged Navier Stokes
RDE	Rotating Detonation Engine
RM	Richtmyer-Meshkov
VN	von Neumann
ZND	Zel'Dovich-Neumann-Doring

Greek Symbols

α	Heat diffusivity
$\bar{\Delta}$	Filter length scale
β	Zel'Dovich number
χ	Detonation chi parameter
$\dot{\omega}$	Reaction rate
ε	Dissipation rate per unit mass
η	Kolmogorov scale
γ	Ratio of specific heats
μ	Dynamic viscosity
ν	Kinematic viscosity
ϕ	Equivalence ratio
ρ	Density
σ	Expansion ratio
τ	Stress, Ignition time

Roman Symbols

\dot{P}	Subgrid kinetic energy production rate
C	Model constants ($C_v, C_\varepsilon, C_\kappa$)
c	Speed of sound
c_p	Specific heat capacity at constant pressure
c_v	Specific heat capacity at constant volume

D	Mass diffusivity
E	Total energy
E_a	Activation energy
h	Specific enthalpy
I	Identity matrix
k	Thermal Conductivity
k^{sgs}	Subgrid kinetic energy
K_a	Karlovitz number
Le	Lewis number
M	Mach number
p	Pressure
Pr	Prandtl number
q	Heat flux vector
r, z	Cylindrical coordinate
R	Specific gas constant
Re	Reynolds number
Sc	Schmidt number
T	Temperature
u	Velocity
u_d	Molecular diffusion velocity

V	Volume
W	Molecular weight
Y	Mass fraction

Superscripts

\cdot	Rate form
\sim	Favre averaged quantity
$-$	Spatially averaged quantity
T	Transpose

Subscripts

b	Burned state
i	Species index
O	Quiescent reference state
t	Turbulent quantity
u	Unburned state

Simulations of Detonation Quenching and Re-initiation Using a global Four-Step Combustion Model

Abstract

by

MOHNISH PESWANI

In the current study, the quenching and subsequent re-initiation of detonations in irregular premixed hydrocarbon mixtures are investigated using high-resolution numerical simulations. Since appropriate combustion modeling is crucial when simulating the reactive detonation phenomenon, a four-step combustion model is adopted here. First, an investigation of the four-step model is carried out for different reactive mixtures to highlight the model's applicability for detonation applications. In comparison with detailed chemistry mechanisms, the model demonstrates an ability to accurately predict the complete ignition process over a wide range of initial conditions. With the ignition structures and key combustion parameters correctly predicted, it is concluded that the four-step model is an effective and economical tool for studying complex explosion phenomena in situations where pre-combustion temperature and density are constantly changing.

In the second half of the study, the four-step combustion model is coupled to an adaptive mesh refinement (AMR)-enabled compressible flow solver to simulate the re-initiation of quenched detonation waves propagating near the critical limit. Two experiments for detonation diffraction and detonation interaction with a single half-cylinder obstacle were successfully simulated. In both cases, the re-initiation of the attenuated detonation was invariably a result of transverse detonation waves. While past attempts using simple chemistry models have failed to capture transverse detonations, for these scenarios, our simulations have demonstrated that the four-

step combustion model is able to capture this feature. Thus, it is concluded that to correctly model detonation re-initiation in characteristically unstable mixtures, an applied combustion model should contain at least an adequate description to permit the correct ignition and state variable response when changes in temperature and pressure occur. The re-initiation mechanisms for both cases, along with the propagation of the transverse detonation, are then analyzed in great detail.

Chapter 1

INTRODUCTION

1.1 Motivation

Flame acceleration (FA) and deflagration to detonation transition (DDT) have been significant research topics since the first evidence of detonations became available in 1883, primarily to understand and mitigate explosions in coal mines [131]. Despite many decades worth of research, predicting a slow-moving flame's transition to an explosion or detonation remains challenging. While some limited, primary necessary conditions have been established for both FA and DDT [31], the exact sufficient conditions leading to the initiation of a detonation wave have not. This is particularly significant from an accident prevention standpoint since detonations, which are supersonic combustion waves with large over-pressures (≈ 20 to 30 times increase at their peak), possess massive destructive potential. To this day, unintended explosions are a source of billions of dollars spent worldwide in damages, posing a significant threat to human lives. Table 1.1 provides a brief summary of recent significant accidents in the United States and the estimated cost of damages (in millions of dollars). Thus there exists a need to determine the underlying physics of how flames accelerate in compressed fluids and the mechanisms by which these fast flames can transition to a detonation wave that is sustained.

While it is possible for an accident scenario to develop into a detonation through the direct initiation of a detonation wave through deposition of sufficient energy (via a powerful spark or shock initiation) [102], the most likely route is through flame acceleration (FA) in confined areas. In fact, FA, through a series of obstacles, was identified as the primary mechanism that triggered a strong explosion event at the Buncefield oil storage depot in England following the accidental release of hydro-

Table 1.1: List of recent major accidents in the United States. Damages reported in millions of dollars.

Incident	Date	Location	Damages
· West Pharmaceutical Services explosion	09/23/2001	Kinston, NC	155
· Texas City Refinery explosion	03/23/2005	Texas City, TX	1,500
· Falk Corporation explosion	12/06/2006	Milwaukee, WI	40
· Upper Big Branch Mine disaster	04/05/2010	Raleigh, NC	220
· Deepwater Horizon oil spill and explosion	04/20/2010	Gulf of Mexico	65,000
· Consolidated Edison explosion	10/29/2012	New York City, NY	425
· West Fertilizer Company explosion	04/17/2013	West, TX	240
· Williams Olefins Plant explosion	06/13/2013	Geismar, LA	29
· East Harlem gas explosion	03/12/2014	New York City, NY	153
· Husky Energy Refinery Explosion	04/26/2018	Superior, WI	750
· Merrimack Valley gas explosions	09/13/2018	Merrimack Valley, MA	500
· PC Group Explosion	11/27/2019	Port Neches, TX	750
· Androscoggin Mill Explosion	04/15/2020	Jay, ME	351

carbon vapors [22, 72]. Unfortunately, the FA mode is also the least understood path through which detonation initiation is possible. FA is the process of a laminar flame becoming turbulent through instabilities and interactions and eventually accelerating to become a choked flame (i.e., a Chapman-Jouguet deflagration) whose velocity is sonic relative to its products [188, 191, 192]. In this state, the reactive mixture is susceptible to detonation. This has been identified as a necessary but insufficient condition for DDT.[31] The role of transverse waves has also been investigated regarding their relation to DDT, and it has been shown that they must be maintained to drive a critical deflagration that could lead to a detonation [254]. The final stages of DDT are of particular importance to isolate and investigate, as these moments encompass the critical combustion regime changes from a choked flame to a self-sustained supersonic combustion phenomenon where a shock wave be-

comes coupled to and supported by a thin reaction zone. The mechanisms involved in the final stages of DDT can be studied by deliberately creating a critical shock–flame complex that is susceptible to re-initiation. They include experiments for detonation interaction with obstacles [15] or by forcing a quasi-planar detonation propagating in a tube or channel to undergo a sudden area expansion (detonation diffraction) [195]. In both sets of experiments, following the detonation wave interaction with an obstacle or detonation diffraction, the strength of the shock wave weakens, leading to the formation of a metastable shock–flame complex.

1.2 The Detonation Cellular Structure

Before further discussing the FA and DDT phenomena, it is crucial first to understand the cellular dynamics of propagating detonation waves. From optical visualizations [237] and by using the “soot-foil” technique [7], to date, it is well known that multi-dimensional detonations exhibit a characteristic “cellular” structure on their fronts as they propagate in a reactive medium. The cellular structure is a manifestation of the instability of the detonation front and is associated with wave interactions whose directions are predominantly transverse to the direction of the flow. Figure 1.1 shows a 2–D sketch of an unstable detonation front with the main features highlighted. As the detonation wave propagates forward, transverse waves that propagate perpendicularly to the overall direction of the leading shock wave periodically collide, accompanied by a region of high temperature and pressure. As a result, the leading shock wave is first accelerated and then decays as the gas expands till the next transverse collision. This oscillation along the front is referred to as a “cell cycle”. The triple point is a key feature of detonation waves and exists at the junction of the principal shock waves: the Mach shock and incident shock, which are associated with the leading wave front, and the transverse wave. As the propagating unstable detonation front undergoes continuous cell cycles, the cellular structure of detonations observed in experimental soot foils is a history of the triple

point tracks. Moreover, the width of cells appearing on a soot foil is referred to as the detonation cell size (λ) and is used as a global length scale in detonation studies since different mixtures exhibit different characteristic values of λ .

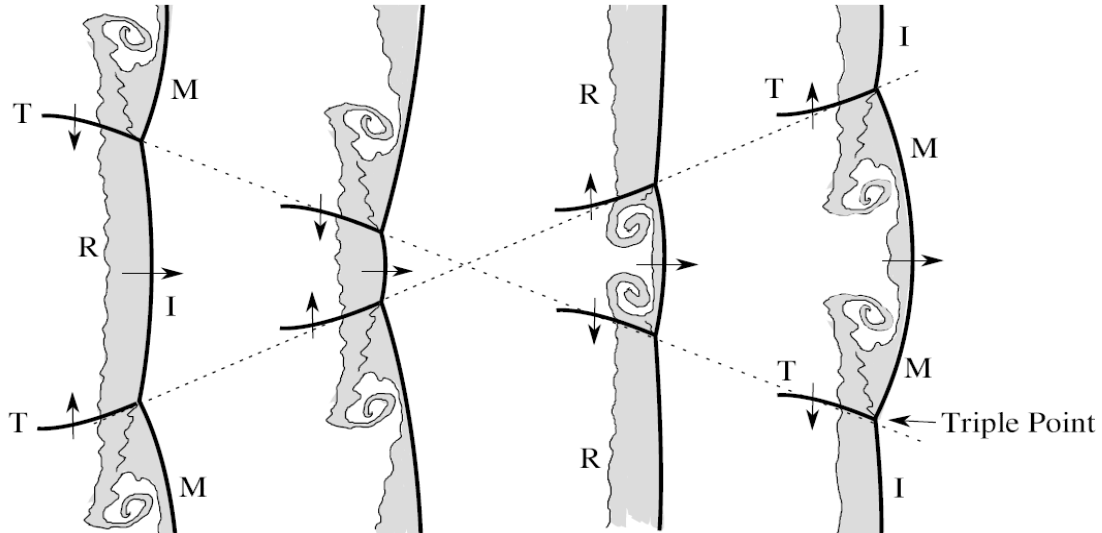


Figure 1.1: Sketch showing the triple point collision process. Various waves indicated are incident shocks (I), Mach shocks (M), and transverse shocks (T). (R) shows the reaction zone [136].

Apart from the detonation cell size, the regularity of the cellular structure has been traditionally used to characterize detonations observed in different reactive mixtures. Based on the cellular structure, detonations are characterized as regular (sometimes referred to as stable) if they have a single dominant cell size or irregular (sometimes referred to as unstable) if they have a broad spectrum of cell sizes. An example of this is shown in Fig.1.2. In general, regular detonations are associated with fuel mixtures having low activation energies. Typical examples are hydrogen–oxygen mixtures or fuel–oxygen mixtures diluted with argon. Irregular detonations are associated with stoichiometric hydrocarbon–oxygen mixtures and exhibit stochastic-looking cellular structures. The cell sizes vary significantly for these mixtures and do not exhibit consistent and repeating cell sizes. While most experimental and numerical detonation studies have concentrated on regular mix-

tures that do not exhibit large cellular instabilities, irregular detonations, such as in hydrocarbons, are more important for detonation applications to practical problems of explosion hazard analysis.

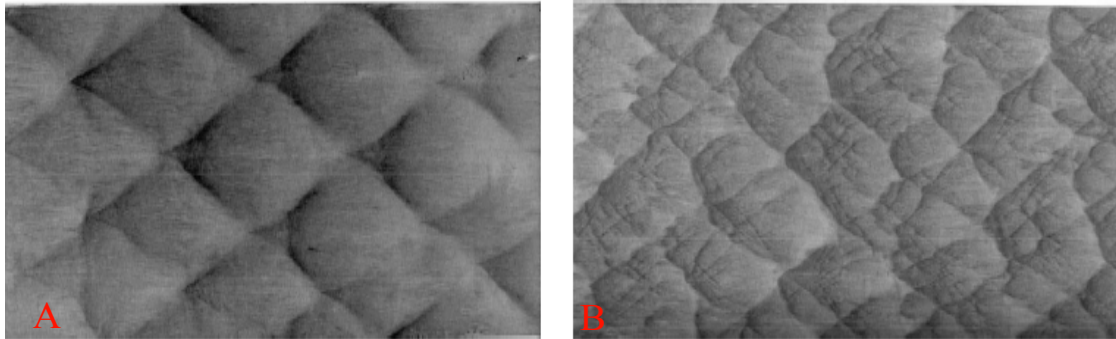


Figure 1.2: Soot-foils showing (A) a regular detonation structure in $2\text{H}_2 + \text{O}_2 + 17\text{Ar}$ with $p_0 = 20$ kPa and (B) an irregular detonation structure in $\text{C}_3\text{H}_8 + 5\text{O}_2$ with $p_0 = 20$ kPa [7].

1.3 Detonation diffraction

Detonation diffraction is a fundamental problem for characterizing detonation propagation and has practical applications in developing next-generation rotating detonation engines (RDEs) and pulse detonation engines (PDEs) where the detonation is initiated in a tube before expanding into the annular chamber [148, 168, 190]. As a detonation propagates from a confined channel to an unconfined space, it undergoes diffraction through a change in geometry from a quasi-planar wave to a cylindrical or spherical wave [248]. In general, depending on the reactive mixture composition, thermodynamic conditions, speed of the wave, and experimental geometry, following the sudden area expansion, the detonation wave can either be extinguished (sub-critical regime), re-initiated (critical regime), or successfully propagate (super-critical regime). The three different scenarios are shown in Fig. 1.3. The re-initiation of detonation wave is particularly important to understand for the development and validation of numerical strategies to simulate and predict the

final stages of deflagration to detonation transition (DDT), as critical shock flame complex regimes may be established close to the choked Chapman-Jouguet (CJ) deflagration velocity.

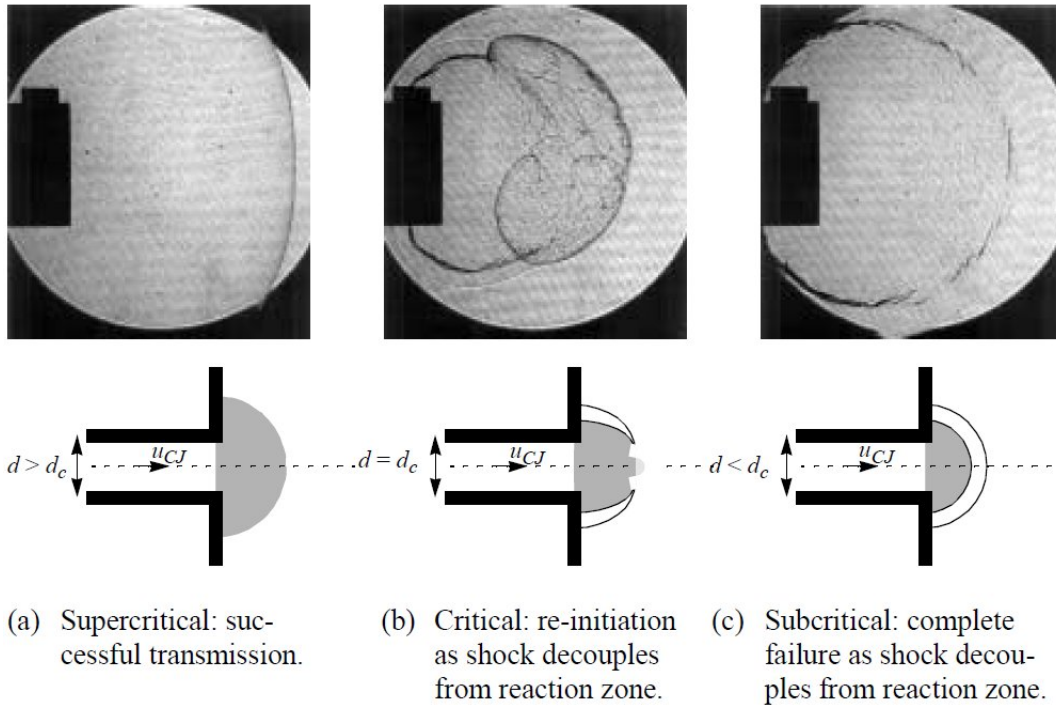


Figure 1.3: Regimes of detonation diffraction for the critical diameter problem [195].

A universal feature of detonation re-initiation following diffraction is the presence of transverse detonation waves, which play a key role in the re-initiation process. An example of this is shown in Fig. 1.4 from the experimental study by Xu et al. [242] where the transverse detonations are present as bright bands separating the zones of typically observed cellular structure from zones without any visible cellular structure. The bright bands observed in the figure result from increased chemical reactivity and have been observed in several detonation diffraction experiments where re-initiation was observed [88, 154, 233, 242]. These transverse detonation waves have since been identified as corresponding to the path of triple points where multidimensional shock wave structures meet [174]. While previous exper-

iments have been useful in learning about the onset of re-initiation by transverse detonations, they have limitations, particularly with data collection methods. Most experiments to date have acquired only pressure diagnostics and limited temporal schlieren imaging, the latter of which was largely limited by the very small time scales involved. As a result, the results from previous experiments are largely qualitative in nature, and despite several decades of experimental detonation diffraction studies, predictive models for the problem are still in development. This is particularly true for detonations initiated in premixed hydrocarbon mixtures which exhibit irregular detonation structures [7], and the enhanced cellular instabilities and transverse waves heavily influence the re-initiation process. This is highlighted in several recent studies where markedly different pathways to re-initiation and multiple transverse detonations were observed following diffraction, which are poorly understood [88, 233, 242].

1.4 Numerical modeling of detonation re-initiation and the need for better chemistry descriptions

Numerical studies have been conducted to investigate the re-initiation of a quenched detonation wave by a transverse detonation. Unfortunately, past numerical studies that simulated detonation re-initiation [14, 88, 117, 204, 242] have revealed drawbacks to the state-of-the-art strategies used. A common approach to detonation modeling is to solve Euler's equations of motion for a calorically perfect gas and to include a one-step Arrhenius reaction model, where reactants are converted to products in a single global reaction step [2, 5, 15, 55, 66, 69, 78, 87, 88, 181, 204, 240]. This strategy, however, is known to be insufficient for capturing important features observed during re-initiation. For example, Shi et al. [204], in a recent study, attempted to simulate detonation diffraction using a one-step model but failed to capture the re-initiation by the transverse detonation. A similar outcome was observed by Bhattacharjee et al. [14], and Radulescu and Maxwell [181] where a one-step

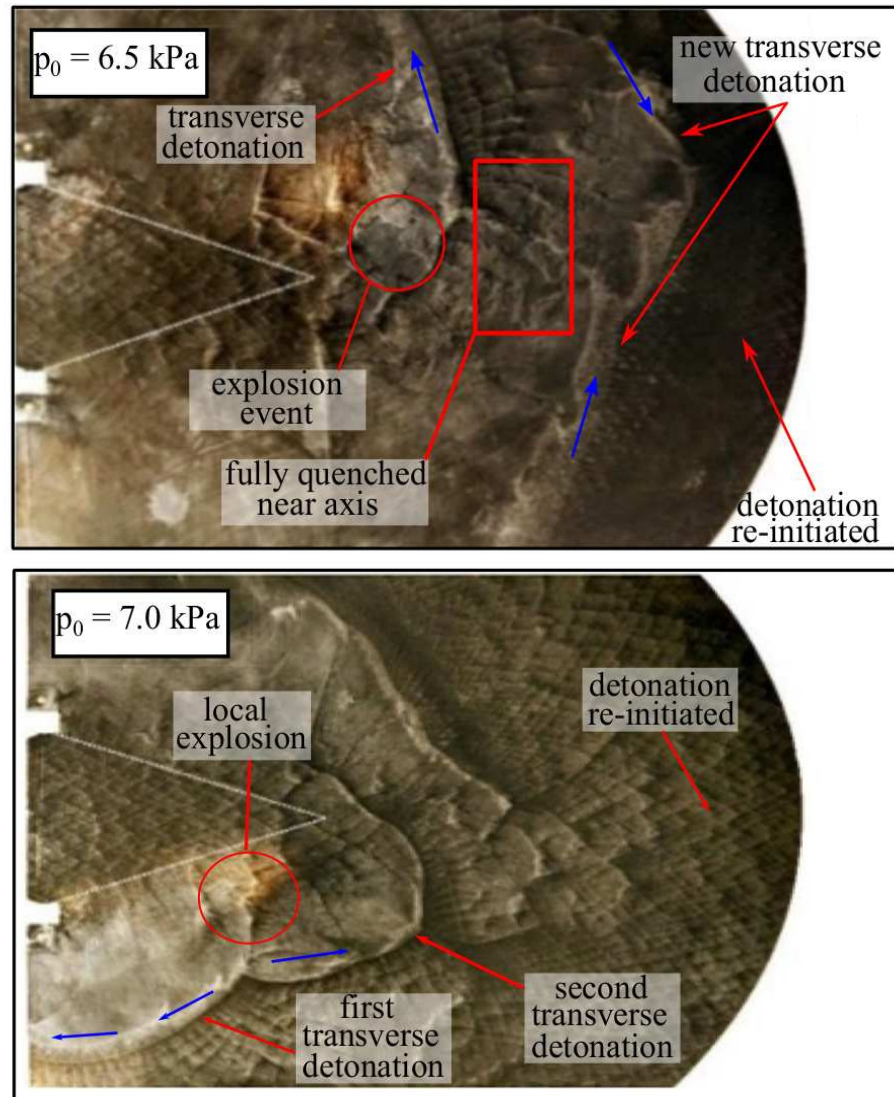


Figure 1.4: Transverse detonations and multiple re-initiation mechanisms observed during critical re-initiation in the study by Xu et al. [242].

model failed to capture the transverse detonation for detonation re-initiation behind a single obstacle. They attributed this to the inability of the one-step model to predict short power pulses in the one-dimensional reaction zone compared to that expected from detailed chemistry. More recently, Maxwell et al. [134] investigated the effect turbulent mixing and shock compression have on the final stages of DDT during flame acceleration by providing turbulent combustion closure, but also through the application of a one-step reaction model. In the study, turbulence

closure provided a means to predict detonation re-initiation for specific conditions. However, transverse detonation waves were again not captured.

Other strategies to model detonation propagation have used more detailed chemistry mechanisms [36, 53, 147, 228]. Results from these studies not only resemble experimental flow fields much more closely, but the transverse detonation wave was also successfully observed during re-initiation of the detonation wave. This insinuates that a better description of the chemistry is necessary to capture the transverse detonations during re-initiation, which is a critical objective in the current study. It is worth noting here that detailed chemistry with thermally perfect gas behavior (i.e., ideal gas with temperature-dependent heat capacities) is only feasible for hydrogen mixtures when investigating detonation diffraction. It is well known that the application of much larger and more complex detailed chemistry mechanisms for hydrocarbon mixtures at sufficiently high resolution is prohibitively expensive to adopt for full-scale numerical studies involving detonations. Unlike detailed hydrogen mechanisms, hydrocarbon mechanisms contain several dozen species and hundreds of reactions [6, 231], if not more. There is clearly a need for a modeling strategy that is more accurate than a one-step model but also practical to apply in terms of computational expense for modeling industrially relevant explosion scenarios involving hydrocarbon fuels.

1.5 Overview

This work aims to numerically investigate the quenching and re-initiation of detonation waves to understand better the mechanisms by which a transverse detonation is triggered in the final stages of DDT. To achieve this goal, the current study consists of two main components. Since the lack of chemical accuracy is currently believed to be the primary reason for poor qualitative agreement with experiments in previous numerical studies, an in-depth review of commonly adopted chemistry models is first conducted along with a detailed literature review in Sec-

tion 2. Since detailed chemistry mechanisms for hydrocarbon mixtures are not amenable for high-resolution numerical studies involving detonations, the applicability of a four-species, four-step global combustion mechanism developed by Zhu et al. [253] for stoichiometric acetylene–oxygen combustion is explored in the current study. Section 4 is then dedicated to developing the combustion model further to include several different premixed hydrocarbon mixtures and extensively validating the model as an efficient and accurate choice for simulating critical detonation scenarios in irregular hydrocarbon mixtures.

Following the implementation of the combustion model into an in-house computational fluid dynamics (CFD) solver, the different outcomes following detonation diffraction are studied in Section 5 using high-resolution numerical simulations. A key feature that the study aims to capture numerically is the re-initiation of the detonation in the critical regime by the transverse detonation wave. Not only do these transverse waves appear in the critical regime following detonation diffraction, but they also appear and play a crucial role in near-critical failure limit scenarios of detonation propagation, including critical quenching and re-initiation of a detonation following the interaction with an obstacle [14], spinning detonation propagation [229], and marginal planar detonation propagation [212]. The particular scenarios modeled in the current thesis are based on the experiments conducted by Schultz [195] for detonation diffraction in premixed ethylene–oxygen mixtures. Additionally, as part of validating the four-step model parameters developed by the author, the re-initiation of a quenched detonation based on the experiments by Bhattacharjee [14] was previously investigated by our research group [52]. While good qualitative agreement with experiments was observed and the transverse detonation observed during re-initiation was successfully captured, the mechanisms by which the transverse detonation was initiated were not adequately investigated. The author expands on these results in the current study to include specific details in Section 6. Finally, the important conclusions from the study, along with recommendations for

future work, are summarized in Section 7.

1.6 Thesis Objective

The overarching objective of the current work is to numerically simulate and validate to past experiments, the re-initiation of detonation waves in premixed hydrocarbon mixtures by transverse detonations, and highlight the importance of adopting an economical but accurate chemistry model. To achieve this goal, the specific fundamental objectives of the proposed work are as follows:

- Develop and improve the four-species, four-step model by Zhu et al. [253] to include different premixed hydrocarbon mixtures.
- Extensively validate the four-step model's ability to predict important combustion properties for different reactive hydrocarbon mixtures to a high level of accuracy for ignition processes over a wide range of initial temperatures and densities. This is crucial for studying complex explosion phenomena in situations where pre-combustion temperature and density are constantly changing, such as detonation re-initiation and the final stages of DDT.
- Couple the four-step model to a compressible flow solver to investigate detonation re-initiation following detonation diffraction as observed by Schultz [195] and detonation interaction with a single obstacle as observed by Bhattacharjee et al. [15].
- To investigate, in detail, the role that shock collisions, burnout of pockets of unburned gas, and local hot-spots have on the re-initiation of the quenched detonation wave and the formation of transverse detonation.
- To investigate in depth the propagation and characteristics of the transverse detonation waves and the role that these waves have on the re-initiation of a self-sustained detonation.

Chapter 2

LITERATURE REVIEW

2.1 Flame Acceleration (FA) and Deflagration to Detonation Transition (DDT) Background and History

The exact process by which a flame transitions to a detonation has been a major research topic since the 1880s when the first evidence of detonations became available [11, 131]. In the earliest experimental studies, detonation initiation resulted from flame acceleration in smooth tubes, with the flame run-up distance required to form a detonation considered a mixture property. While these experiments crucially developed the CJ theory for detonation waves, very little was known about the flame acceleration process, with the concept of turbulent combustion still in its infancy. In 1935, Bone et al. [17] studied FA in smooth tubes and established that shock waves play a key role in the transition to detonation, with observed combustion events in the shocked gas. Salamandra et al. [193] was the first to document each stage of the flame acceleration process in smooth tubes leading up to the detonation transition. A series of photographs clarified the sequence of events through which the initial laminar flame becomes choked and susceptible to detonations. Following the initial laminar propagation, the flame starts to become wrinkled due to Darrieus-Landau instabilities associated with the expansion of product gases leading to the formation of a cellular flame. This, coupled with the natural instabilities of the flame surface, increase the flame surface area, burning rate, and overall velocity. Interaction of the turbulent flame with turbulent boundary layers formed along the tube wall due to the forward motion of the gas gives rise to the well-known *tulip flame* [32] visible in Fig. 2.1. The system is then eventually susceptible to detonation due to an exponential increase in the burning rate, which causes a bulk acceleration of the flame,

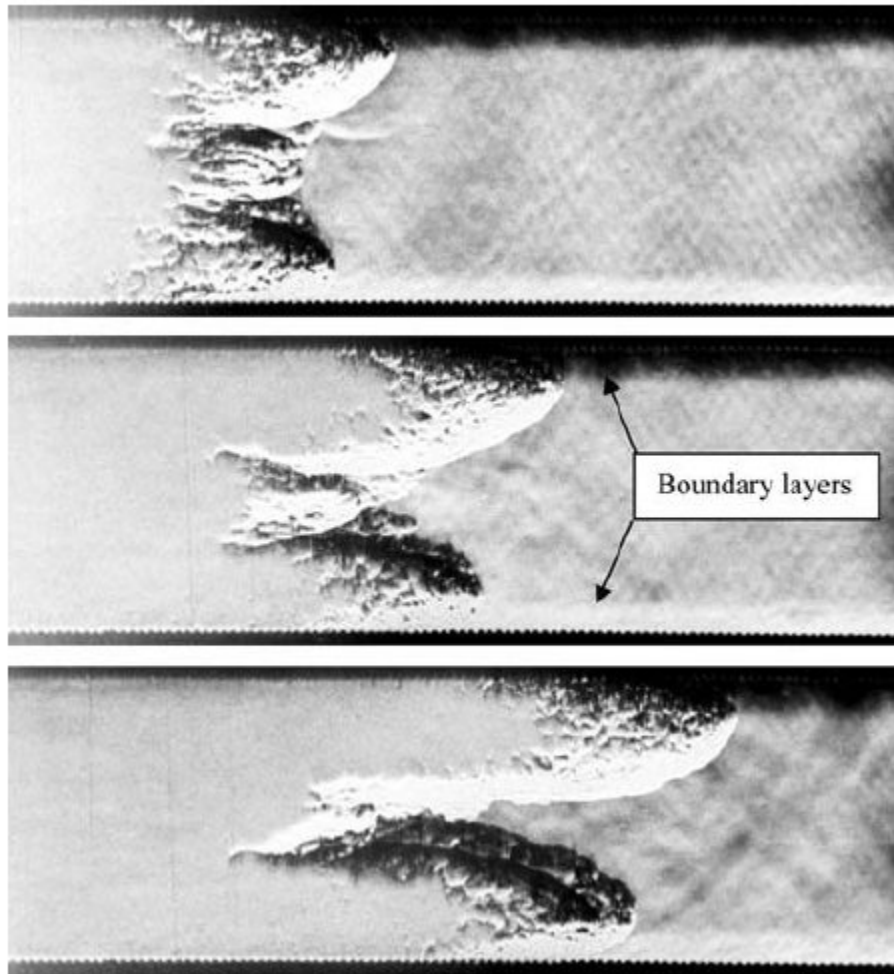


Figure 2.1: Sequence of shadow photographs showing the tulip flame and boundary layers ahead of the accelerated flame propagating from left to right. Mixture is stoichiometric hydrogen–oxygen at initial pressure 60 kPa [94].

forming a shock wave, or series of shock waves, in the unburned mixture upstream from the flame.

Following the introduction of stroboscopic flash schlieren imaging techniques [193, 209], the publications by Urtiew and Oppenheim [162, 226] represent a milestone in the study of DDT phenomenon. Oppenheim coined the term “explosion in the explosion” when his experimental results clearly show the initiation of a detonation from a local explosion within the shock flame complex. In fact, these studies concluded that different modes of DDT exist, depending on the initial shock wave

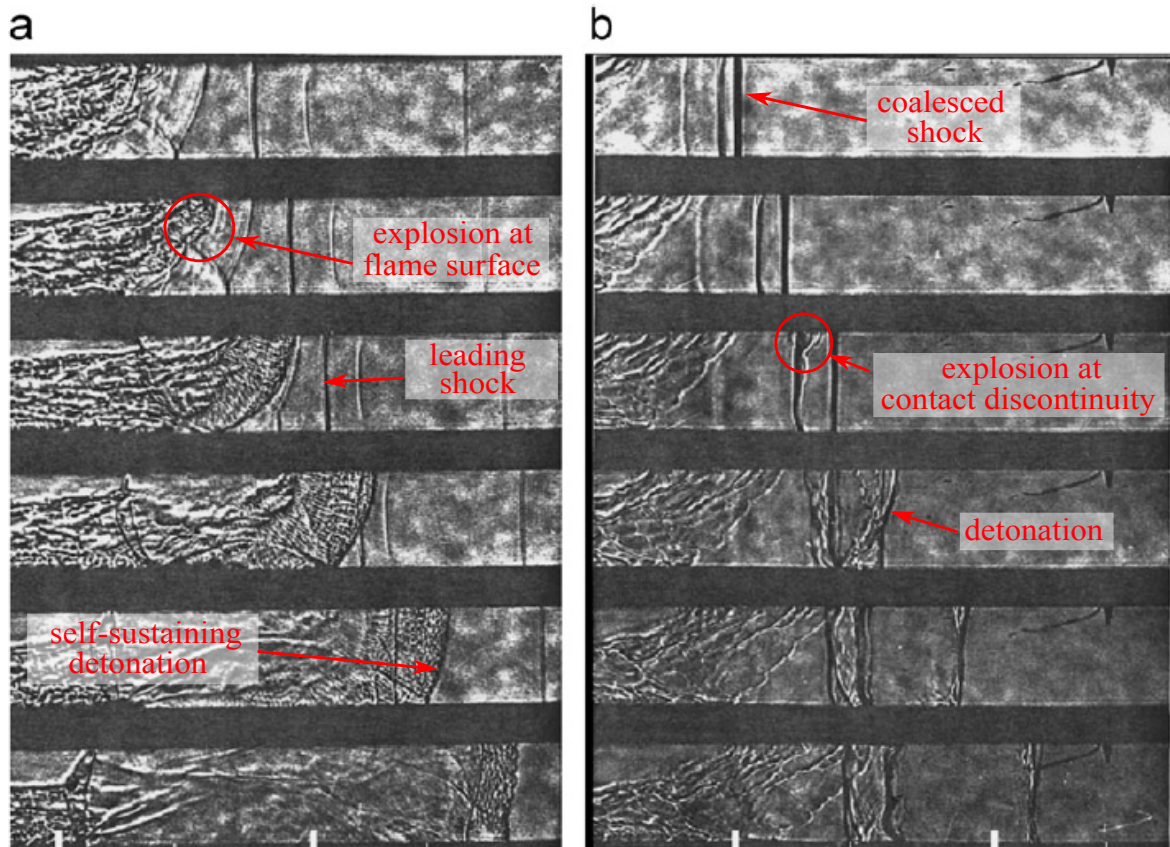


Figure 2.2: Stroboscopic schlieren photographs [226] showing the explosion within an explosion in an equimolar hydrogen–oxygen mixture with $p_0 = 22\text{mm Hg}$.

development with the explosion occurring either at the flame front or the shock front. Figures 2.2a and 2.2b show the detonation initiation occurring at the flame front in an environment of higher pressure and temperature produced by the passage of a curved shock wave and detonation initiation formed as a result of two shock waves coalescing, respectively. These results represent a significant breakthrough since the general consensus was that DDT was initiated when the deflagration merges with the leading shock wave to form a detonation.

Alternate approaches to studying FA and DDT are based on early experimental evidence that obstacles in the flow field generate turbulence and significantly accelerate a propagating flame. Chapman and Wheeler [27] were the first to study the flame acceleration process by placing obstacles in a smooth wall tube to promote

the acceleration of the flame. In the presence of the obstacles, an approximately 400% increase in the maximum flame velocity was achieved, but no detonation initiation was observed. The experiments conducted by Shchelkin [199, 200] further highlight the importance of flame interaction with the boundary layers in promoting the FA process. Through these experiments and others [209], it was also concluded that the surface roughness of the tubes has a strong influence on the FA process. In the 1980s, the effect of obstacles on flame acceleration leading to DDT received significant attention in connection with industrial explosion safety [104, 106, 151]. In these experiments, the use of obstacles to generate turbulence in the flow field was found to have an accelerating effect on flame propagation, and in some cases, transition to detonation. These results would suggest that turbulence plays an important role in DDT. In fact, such obstacles were found necessary to maintain flame acceleration, with the effects of fuel type, mixture composition, tube diameter, and blockage ratio on the flame velocity also investigated. The studies also arrived at the conclusion that the flame must accelerate to a sufficiently high speed prior to the onset of detonation, i.e., at least of the order of the speed of sound in the post-combustion mixture. It was also concluded that the transverse size of the channel or tube is not the only defining criteria for the onset of detonation, with both the obstacle configuration (blockage ratio) and spacing influencing the critical criteria for DDT. Li et al. [110] recently studied the FA and DDT process in a channel with continuous triangular obstacles and found that the equivalence ratio of the reactive mixture significantly influences DDT by affecting the deflagration speed and shock strength.

Following detailed reviews of the characteristics of DDT by Lee and Moen [106] and Shepherd and Lee [202], the DDT phenomenon is usually divided into two separate phases (1) *the creation of the conditions necessary for the onset of detonations* by the processes of flame acceleration, vorticity production, formation of jets, and mixing of products and reactants, (2) *the actual onset of the detonation*.

To date, it has been established that a necessary, but not necessarily sufficient, condition for DDT is the establishment of a choked flame [31]. A choked flame is a deflagration traveling at the speed of sound relative to its burned products. During the flame acceleration up to a choked flame, the flame generates pressure waves that coalesce and form an incident shock wave upstream. This choked shock-flame complex is also referred to as a Chapman-Jouguet (CJ) deflagration [191]. Once the critical shock-flame complex is established, it can transition into a detonation, where a close coupling between the shock and reaction zone occurs. Work has been done to create correlative relations to predict the flame acceleration run-up distance to a choked flame. Kuznetsov [94] found through experiments with stoichiometric hydrogen-oxygen in sufficiently long tubes that initial pressure was approximately inversely proportional to the run-up distance to detonation onset. Dorofeev [42] provided a more detailed theoretical model to predict the run-up distance required for a flame to reach a choked state. However, this model was only $\pm 25\%$ accurate compared to experimental data and did not predict the distance to DDT. Although the onset of detonation can occur through various pathways for different experimental configurations, there is evidence that the transition may be controlled by a single underlying mechanism. It was suggested by Zel'dovich et al. [250], and later by Lee et al. [105] and Yoshikawa [243] that induction time gradients associated with temperature and concentration nonuniformities can lead to detonation initiation. The proposed mechanism suggests that induction time gradients result in the formation of a spontaneous flame which produces a compression wave through a spatial time sequence of energy release. The compression wave can then gradually amplify into a strong shock wave that can auto-ignite the mixture and produce DDT. This process is commonly referred to as the “*Shock Wave Amplification by Coherent Energy Release*” (SWACER) mechanism and is currently believed to be ultimately responsible for a wide range of detonation initiation observations [106, 202]. For DDT in tubes, studies by Peraldi et al. [170], and Guirao et al. [65]

have shown that the minimum tube diameter, D , for the onset of detonation to occur should be greater than the detonation cell size (λ). However, more recently, a more conservative limiting tube diameter has been defined as $D > \lambda/\pi$ using the hydraulic diameter (πD) instead of the tube diameter [116]. The $D > \lambda/\pi$ criteria has been shown to agree very well with the study by Kogarko and Zeldovich [93], who initially proposed that the onset of the single-head spin detonation represents an approximate criterion for the onset of a detonation.

Overall, the mechanisms for flame acceleration leading to a choked flame have been studied extensively and are, for the most part, well understood. The final stages of DDT, i.e. the onset of detonation from the critical shock-flame complex, are not as well understood and are still a topic of active investigation. Ciccarelli (2008) [31] summarized from what had been seen experimentally that the onset of detonations could be categorized into two types: shock reflection/shock focusing or instabilities and mixing processes. The latter can include flame interactions, explosions of unburned gas pockets, and fluctuations in the properties of the flow. The source of these events, the sequence in which they occur, and what conditions lead to which type of detonation initiation are all still being studied. To gain insight into the exact dynamics in the final stages of DDT, several experimental studies have since attempted to study the phenomenon by deliberately creating a choked turbulent shock-flame complex that permits better control and diagnostic measurement compared to examining the complete FA process. These approaches include the experiments involving shock–flame interactions [132, 194, 219], detonation diffraction [195, 242], and detonation interaction with perforated plates [26, 159, 254], blockages [122, 216, 218], and obstacles [181].

2.2 Shock–Flame Interaction

The shock–flame experiments leading to the formation of a turbulent flame are based on the work by Markstein [132]. These experiments include shock inter-

actions with a single flame kernel [219] shown in Fig. 2.3 or multiple flame kernels [194]. The experiments showed that the first major effect of a curved flame and a shock interaction is a large funnel of unburned material that extends into the burnt region. This funnel forms as a result of Richtmyer–Meshkov (RM) [144, 189] and baroclinic instabilities, which develop as a shock impulsively accelerates the perturbed flame surface. The RM interaction distorts the flame surface and provides an important mechanism for turbulence generation, drastically accelerating the development of a turbulent flame that may eventually transition to detonation. Whether or not DDT occurred in the system also depended on the Mach number of the incident shock, with the detonation finally initiating in the region between the flame brush and shock wave or inside the brush itself. A key finding from the experiments by Thomas et al. [219] is the increased combustion rates due to the reflected shock are capable of sustaining a highly unsteady turbulent combustion wave that travels at about $\approx 60\%$ of the theoretical CJ velocity. This strongly-coupled shock wave and reaction zone were termed a *strange-wave* by Thomas [219], with the energy release in the regime dominated by turbulent mixing rather than compression ignition alone. The *strange-wave* also shares many similarities with the *fast-flame* phenomenon observed in porous medium experiments [14, 127, 128, 130, 181, 187, 192, 207]. The remaining studies for detonation interaction with plates, obstacles, blockages, and detonation diffraction are all based on the idea of quenching a detonation wave and investigating its re-initiation to study the final stages of DDT.

2.3 Detonation Diffraction

Since the early discovery of detonation diffraction failure by Lafitte [96] and the experimental work by Zel'dovich [248] that established the existence of a critical diameter below which detonation failure was observed following an abrupt area change, analyzing the conditions separating the detonation quenching and propagation limits for the detonation diffraction problem has attracted much interest. For

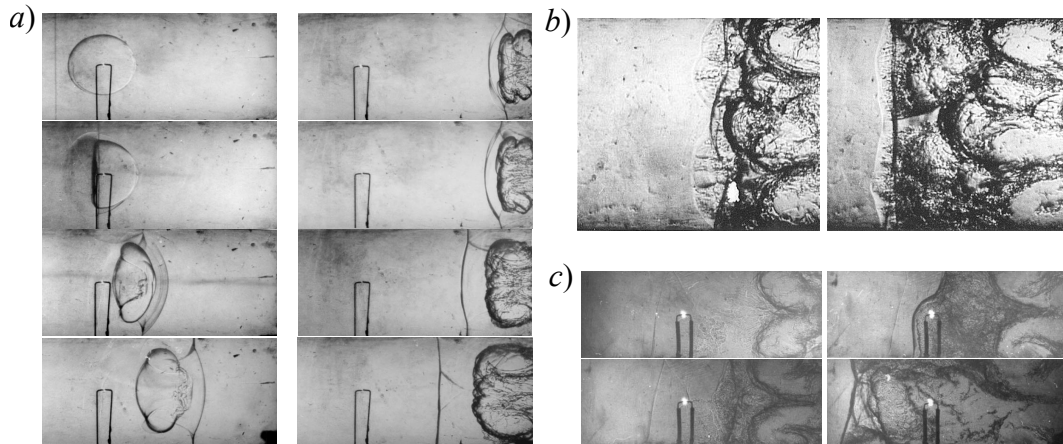


Figure 2.3: Shock–flame interaction [219], a) initial shock–flame interaction and reflected shock with $M_s = 1.7$, b) resulting *strange–wave* observed for $M_s = 1.7$, and c) resulting detonation with $M_s = 1.9$.

five different reactive mixtures, Zel’dovich expressed a critical tube diameter (D_c) below which detonation failure was observed after diffraction from a circular tube as $D_c = 500\Delta_I - 700\Delta_I$, where Δ_I is the length of the detonation induction zone. Following the discovery of the characteristic detonation cell size (λ), this criterion has been re-expressed in several early studies as $D_c = 13\lambda$ [47, 91]. Although several different studies have reported values of D_c ranging from $13\lambda - 24\lambda$ [149, 225], which is partially due to the highly subjective nature of detonation cell size measurements, the $D_c = 13\lambda$ is widely accepted as the best estimate for detonation diffraction in hydrocarbon mixtures. Liu et al. [118] showed that if a rectangular geometry is applied instead, the critical channel height H_c varies from 10 to an asymptotic value of 3 when the aspect ratio H/W of the openings varies from 1 to 7 (H is the height of the channel, while W is the depth). Jones et al. [73] reported a critical channel height of $H_c \approx 3 - 7\lambda$ for high aspect ratio rectangular channels, while Deiterding [36] observed a critical channel height of approximately $H_c = 10\lambda$ in square channels. Both these results agree with the experimental results of Benedick et al. [10] for detonation diffraction in premixed hydrogen–air and ethylene–air mixtures. Although the aforementioned empirical correlations can be quite ade-

quate for most gaseous hydrocarbon explosive mixtures, it is shown to be invalid for mixtures with regular cell patterns such as mixtures with heavy argon dilution [37, 143, 150, 203, 251]. Moen et al. [150] and Desbordes et al. [37] showed that dilution from 50% to 80% by helium, argon, or krypton changes D_c from 13λ to 26λ for detonation diffraction out of tubes and suggested that the increase in D_c is due to the reduced activation energy of a mixture on dilution. Zhang et al. [251] recently found that the classical $D_c = 13\lambda$ relationship holds for 0-30% argon diluted acetylene–oxygen mixtures while increasing the amount of argon dilution causes D_c to increase proportionally to a value of 25λ with 70% argon. Meredith et al. [143] found that for detonation diffraction in channels for acetylene–oxygen mixtures, H_c increased from 3λ to 12λ when the mixture was heavily diluted by argon. This difference suggests that the critical tube diameter or channel height depends on the tube size and the mixture’s thermodynamic state and stability, with different failure mechanisms existing for stable and unstable mixtures.

Many studies have also shown that a significant improvement of detonation transmission (i.e., a decrease in D_c) from a tube can be achieved by: (1) shock reflection and focalization achieved by introducing an obstacle in the exit section [89, 150, 152, 177] and (2) reduction of lateral expansion by a cone or a limited increase of the diameter of the tube [18, 64, 88, 92, 220, 221]. Moen et al. [150] studied the decrease in D_c for a wide range of blockage ratios (BR) and concluded that $BR \approx 0.5$ allows for the maximum enhancement of transmission by an order of 1.8-2.0. Priault [177] studied the influence of the obstacle shape on the transmission for $BR = 0.5$ and found that the different obstacle shapes have a weak influence on the transmission improvement with $D_c = 5.7 - 7\lambda$ for the different obstacles considered. Another way to favor the detonation transmission is to diffract the detonation wave in a divergent channel or through a cross-sectional step based on the experiments by Kogarko [92]. The divergent channels have been studied for rectangular channels [220, 221] and for cylindrical tubes [18, 64, 88]. In gen-

eral, for large divergence angles ($\alpha = 45 - 180^\circ$), the $D_c = 13\lambda$ criteria still holds. However, for small divergence angles ($\alpha < 45^\circ$), D_c decreases linearly from 13λ to 1λ (for $\alpha = 0^\circ$). Since re-initiation of the detonation wave is always possible in the critical limit following detonation diffraction, an important parameter influencing the re-initiation is the expansion ratio of the set-up. Here, the expansion ratio (D/d) refers to the ratio of the larger channel diameter into which the detonation diffracts to the tube diameter. Sorin et al. [210] found that for $D/d < 2.5$, the reflection of the diffracted shock at the wall contributes to the re-initiation, with the super detonation triggered directly near the wall. In contrast, the wall reflection does not contribute to the re-initiation process for transmission to free space, with the super detonation being triggered near the tube axis instead. The influence of the expansion ratio on the re-initiation process was also studied by Pantow et al [169]. It was reported that the decoupled shock waves did not, by themselves, cause the re-initiation of the detonation at the wall. Rather, Mach reflection generating transverse waves were responsible for the re-initiation. Ohyagi et al. [160] studied a detonation behind a backward-facing step and noted that the re-initiation point at the wall moved away from the step at lower pressures. For detonation diffraction into diverging channels or tubes, rather than the expansion ratio, the divergence angle has been found to be a controlling parameter for detonation re-initiation. Khasainov et al. [88] found that if α was greater than 40° , the re-initiation observed is similar to expansion into a semi-infinite space with the transverse detonation triggered near the tube axis. In contrast, for smaller expansion cones ($\alpha < 40^\circ$), the cone wall favors the detonation transition with the transverse detonation originating directly at the wall as shown in Fig. 2.4. Similar conclusions were also drawn in previous studies [18, 64] although the critical tube angle observed was slightly larger with $\alpha \sim 55-60^\circ$.

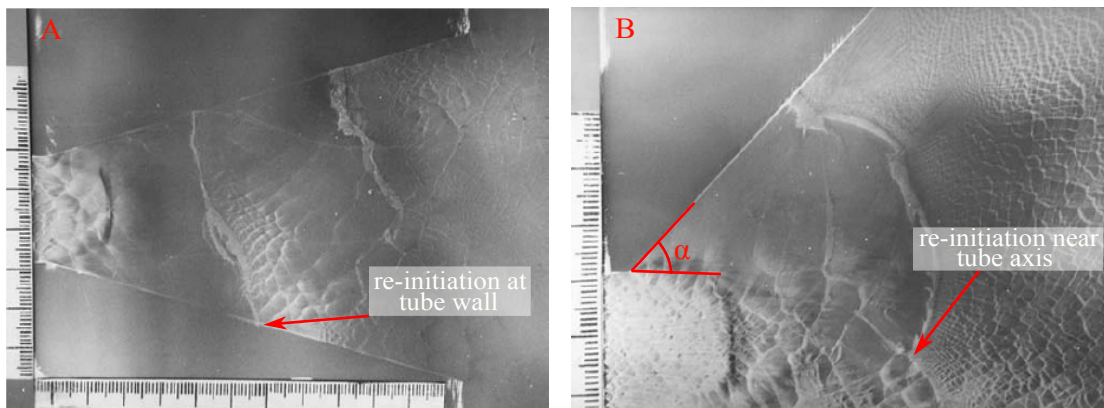


Figure 2.4: Soot-plate record from study by Khasainov et al. [88] showing detonation diffraction in stoichiometric acetylene–oxygen mixtures with (A) $p_0 = 0.035$ bar and $\alpha = 15^\circ$, and (B) $p_0 = 0.07$ bar and $\alpha = 45^\circ$.

2.3.1 The role of cellular instabilities on the detonation diffraction problem

It has long been suggested that the detonation stability or cell structure plays an important role in the outcome of a detonation undergoing a sudden area expansion into open space. Shultz [195] studied the different regimes following detonation diffraction (sub-critical, critical, and super-critical) for several different reactive mixtures and noted that the transition between the different regimes was observed at lower pressure for stoichiometric hydrocarbon mixtures compared to hydrocarbon mixtures diluted with argon. The influence of cellular regularity on the outcome of the critical diameter problem is also confirmed by the vast variation in D_c for mixtures that exhibit regular and irregular cell structures. Using sophisticated planar laser-induced fluorescence (PLIF) and chemiluminescence imaging, Pintgen and Shepherd [174, 175] focused on visualization of the detailed structure of the diffracted detonation wave and reaction zone in highly regular $\text{H}_2 - \text{O}_2 - \text{Ar}$ and irregular $\text{H}_2 - \text{N}_2\text{O}$ mixtures. It was found that the reaction front velocity along the center axis decays significantly faster in irregular mixtures with a higher global activation energy. As a result, the critical condition was linked to the mixture activation energy that controls the degree of coupling between the reaction front and the lead

diverging shock. This agrees with a past study by Arienti et al. [5] and is based on the model by Eckett et al. [45], which shows that the decoupling of the shock and reaction zone will take place when the time scale characterizing the lead shock decay is comparable to the critical shock decay time computed from idealized reaction zone models. Although these studies provide an estimation of the critical condition, experimental visualization of the critical re-initiation clearly suggests that cellular instabilities and transverse waves are important factors [242]. Lee [100] proposed two failure mechanisms for stable and unstable mixtures. For stable mixtures, Lee attributed the detonation wave's failure to the attenuated detonation's excessive curvature following diffraction. This 'excessive curvature' argument was recently verified by Li et al. [109] where it was observed that the critical tube diameter (D_c) differed by a factor of 2 for spherical and cylindrical detonations. For hydrocarbons with irregular detonation cell sizes, the role of cellular instabilities and transverse waves have been shown to influence the critical tube diameter [242]. As a result, Lee conjectured that for unstable mixtures, detonation failure is a result of the suppression of transverse waves by the corner expansion. The experiments conducted by Mehrjoo et al. [140, 141] and Nagura et al. [153, 154] confirm this hypothesis by demonstrating that successful transmission invariably originates from localized explosion centers in the failure wave, where sufficient instabilities are maintained and eventually amplified to sustain the detonation propagation. Two series of experiments were conducted by Mehrjoo. One by generating artificially small instabilities using small obstacles and the other by damping transverse instabilities using porous media. In both sets of experiments, generation or suppression of flow instabilities led to a significant change in the critical condition for detonation transmission of unstable mixtures while no noticeable effect was observed in the stable mixtures. These experiments demonstrate that the mechanism responsible for detonation failure in irregular undiluted mixtures is linked to the suppression of instabilities. Mehrjoo et al. [140] further suggested that transverse triple point col-

lisions along the detonation front are, in fact, crucial for sustaining the detonation wave after diffraction and that re-initiation is typically accompanied by the triggering of a transverse detonation wave. Similarly, Nagura et al. [153, 154] studied detonation diffraction in irregular $C_2H_4 - O_2$ and regular $C_2H_2 - O_2 - Ar$ mixtures. In the irregular mixture, a clear re-initiation event was observed, and the cell structure was recovered by a transverse detonation wave while in the regular mixture, no such re-initiation event was observed. As a result, it was concluded that transverse instabilities and triple point collisions are the primary mechanisms influencing the outcome of the detonation diffraction in irregular mixtures. The results observed by Xu et al. [242] further elucidate the role of cellular instabilities on the critical diameter problem. For detonation diffraction in irregular stoichiometric $C_2H_2 - O_2$ mixtures, in the critical regime, sufficient cellular instabilities in the shock-flame complex lead to the formation of an explosion bubble which re-initiated the detonation. Figure 2.5 shows the onset of the explosion bubble and the propagating transverse detonation following diffraction in an irregular $H_2 - N_2O$ mixture [174]. Sun et al. [213] recently investigated detonation diffraction for quasi-detonations propagating in tubes and found that in the presence of significant velocity deficits, the $D_c = 13\lambda$ criteria is invalid. Instead, D_c was found to be approximately 8λ . The lower critical value again indicates the importance of cellular instabilities, which provides a favorable effect on detonation transmission by inducing stronger local hot spots.

2.4 Detonation Interaction With Perforated Plates and Obstacles

The use of a perforated plate has been found to be an effective experimental configuration to produce the gasdynamic conditions critical for the onset of a detonation. When a detonation is reflected from a perforated plate, the combustion products are transmitted downstream through the holes at approximately the sound speed, forming a quasi-steady metastable reaction front. After a certain period, the onset

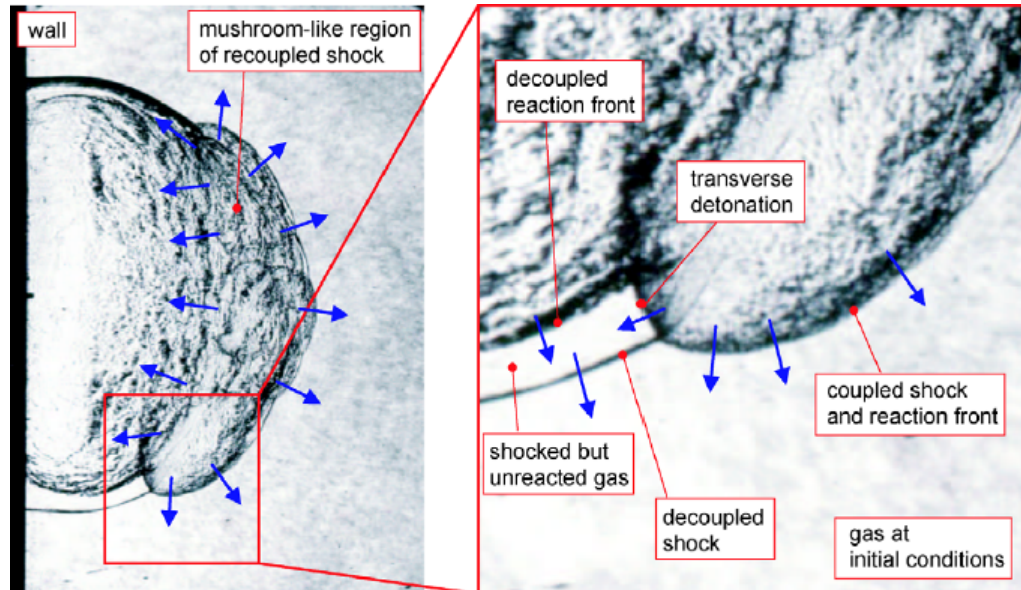


Figure 2.5: Re-initiation event and detailed view of transverse detonation from the study by Pintgen and Shepherd [174] following diffraction of a detonation wave initiated in an irregular $\text{H}_2 - \text{N}_2\text{O}$ mixture with $p_0 = 45$ kPa.

of detonation occurs from the metastable reaction front. For example, the studies by Chao [26], and Obara et al. [159] used perforated plates and rectangular plates with slits, both with openings smaller than the detonation cell size λ to quench the detonation prior to re-initiation. Chao [26] concluded that the turbulent deflagration must travel at the CJ deflagration speed for the onset of a detonation in a smooth tube. Radulescu et al. [185] formulated a closed-form self-similar model to predict these high-speed deflagrations. Once the critical turbulent flame was established, the generation of transverse pressure waves coupled to the chemical energy release was observed. It was also found that the turbulent length scale required for DDT should be roughly on the order of the cell size. Obara et al. [159] found that re-initiation occurred due to the diffracted shock wave interacting with the walls. It was concluded that if the slit width is less than the detonation cell size, the presence of the wall is necessary for the detonation to re-initiate with the detonation re-initiated along the Mach stem, accompanied by transverse waves. This is con-

trary to the cases where the slit width is larger than the cell size. In this case, the detonation is immediately re-initiated following the collision of the two diffracted waves. Zhu et al. [254] used the same experimental setup as Chao et al. [25] and concluded that the onset of detonation following its interaction with the perforated plate is preceded by a critical high-speed turbulent deflagration that propagates at a relatively constant velocity that corresponds to $0.5U_{CJ}$, where U_{CJ} is the detonation CJ velocity. This critical deflagration speed of $0.5U_{CJ}$ agrees with several other studies where high-speed deflagration waves were observed [46, 103, 180, 217]. Grondin and Lee [62] studied the onset of a detonation wave downstream of a perforated plate in highly regular $C_2H_2 - O_2 - Ar$ and irregular $C_3H_8 - O_2$ mixtures. The major difference between the two mixtures is that the metastable reaction front can be maintained for relatively long distances for the propane—oxygen mixture. It was also observed that the onset of detonation in the propane—oxygen mixture was caused by a strong local explosion within the turbulent reaction zone. In two separate studies, Rakotoarison et al. [187, 188] studied the interaction of a shock—flame complex generated by reflecting a detonation from a perforated plate with a single obstacle. For interaction with a single cylindrical obstacle [187], it was found that the shock wave reflections from the obstacle enhanced the burning velocity of the turbulent flame by the Richtmyer-Meshkov instability. This gave rise to burning velocities approaching the sound speed in the unburned gas just ahead of the flame, which led to the formation and amplification of shocks, eventually igniting a detonation. To see if the features for the onset of detonation were consistent across interactions with obstacles of different shapes, the second study involved shock—flame complex interactions with square, flat plate, C-shaped, and H-shaped obstacles. Although the choice of obstacle had an influence on the critical initial pressure necessary to observe the onset of detonation, the transition mechanism remained unchanged.

Similar to detonation diffraction, where the incident detonation wave is weak-

ened and quenches following the abrupt area expansion, a detonation will quench behind an obstacle because as the shock diffracts and expands, its strength weakens. As a result, the ignition delay behind the shock increases, and the detonation ultimately decouples, leading to the formation of a CJ-deflagration that is susceptible to re-initiation. Makris [129] experimented with a detonation encountering a porous medium with spheres of the same diameter. By varying the pore size (space between the spheres), it was found that the relationship between the critical tube diameter and pore size determined the detonation behavior. When the detonation propagated, the governing mechanism was periodic detonation failure followed by re-initiation due to shock wave interactions at the Mach stem and turbulent mixing. Experiments looking at a detonation hitting a singular obstacle, such as detonation diffraction around a single cylinder, provide similar findings. In a study by Kamel in 1993 [80], a detonation hit a full cylinder, tested with different sizes, to reveal a correlation between the cylinder diameter to cell size ratio and the distance of re-initiation behind the cylinder. The re-initiation itself was again observed to be caused by the collisions of reflected transverse waves. Slungaard et al. [207] studied detonation propagation through various granular filters and found that the detonation wave approached a constant velocity in the granular filter if not extinguished. If re-initiation occurred, it was due to hot spot ignition by single or multiple shock reflections. Radulescu and Maxwell [181] investigated the re-initiation of detonation waves in equimolar acetylene–oxygen mixtures downstream of a porous medium, which comprised of a two-dimensional array of staggered cylinders. They reported that high-speed deflagrations require autoignition spots via shock reflections to drive strong pressure wave activity. Bright bands were observed in open-shutter photographs shown in Fig. 2.6. These bands were due to increased chemical luminosity and have since been identified as transverse detonations propagating into the shocked yet unreacted gas [15]. Maley et al. [130] investigated detonation interaction with cylindrical obstacles and found that the propagation mechanism of

the choked flames is via punctuated hotspot ignitions followed by turbulent mixing. Moreover, it was concluded that irregular mixtures exhibit a higher propensity for hotspot generation and, as a result, transition to detonation. Saif et al. [191] studied a detonation encountering a column of cylinders to create fast flames. This study confirmed through experimentation that the CJ-deflagration was a necessary limit to reach for DDT in a wide range of reactive mixtures, including methane-oxygen, ethane, ethylene, acetylene, and propane. Saif had the additional goal of finding a universal correlation based on the thermo-chemical properties of the mixture to predict the critical length of CJ deflagrations into detonations. The data showed that this length is inversely proportional to the χ parameter introduced by Radulescu in 2013 [178], which is dependent on the non-dimensional activation energy, ignition delay, and reaction time. A high χ parameter has been shown to indicate a high likelihood for the formation of hot spots, and the data from Saif strongly supported that with increasing χ , the length to detonation decreases, indicating that a mixture with the tendency to form hotspots transitions to a detonation in less time. Kellenberger and Ciccarelli [84] studied the propagation mechanism of a detonation wave in an obstructed channel. Two unique propagation modes, one symmetrical and one asymmetrical, about the channel line were observed due to local detonation initiation by shock reflections. The asymmetrical initiation was found to be due to the head-on collision of a transverse detonation with the channel wall. In a separate study, three-dimensional effects on the re-initiation process were investigated by considering a wider channel [85]. Detonation propagation in a round tube equipped with repeating orifice plates was investigated by Rainsford et al. [186]. The propagation involved repeated detonation failure and re-initiation along the tube for two different blockage ratio (BR). The main difference in the results from the two sets of experiments was that the re-initiation of the detonation was observed at the tube wall for a lower BR and at the obstacle face for a high BR.

A universal feature that has been identified for re-initiation in the critical regime

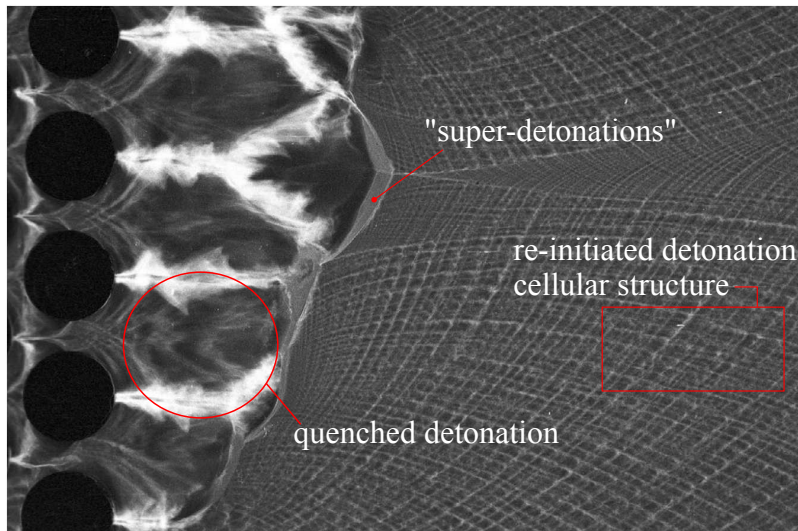


Figure 2.6: Open-shutter photograph of detonation quenching and re-initiation experiments by Radulescu and Maxwell [181].

for the detonation diffraction problem, as well as following detonation interaction with obstacles or blockages, is the appearance of a transverse wave that sweeps through the unreacted, compressed gas trapped in the reaction zone separated from the shock front. Bhattacharjee [15] sought to make clear the key mechanisms of re-initiation through experimentation. In the experiments, a detonation propagating at CJ velocity moved down a rectangular channel, where it then encountered an obstacle. The outcome showed repeatable results of detonation quenching and subsequent re-initiation using a stoichiometric methane-oxygen mixture. According to Bhattacharjee [15](shown in Fig. 2.7), the sequence of events for detonation re-initiation includes detonation quenching behind the obstacle, the shock-flame complex reflecting to form a Mach reflection, re-ignition behind the Mach stem, and a newly formed re-initiated detonation wave. This is characterized by the Mach and transverse waves becoming self-supported detonation waves, observable by their cellular structure. It is also important to note that a pocket of unburned gas was present behind the shock front and trailing the transverse wave, and it was concluded that the rapid ignition of that tongue of unburned gas near the transverse

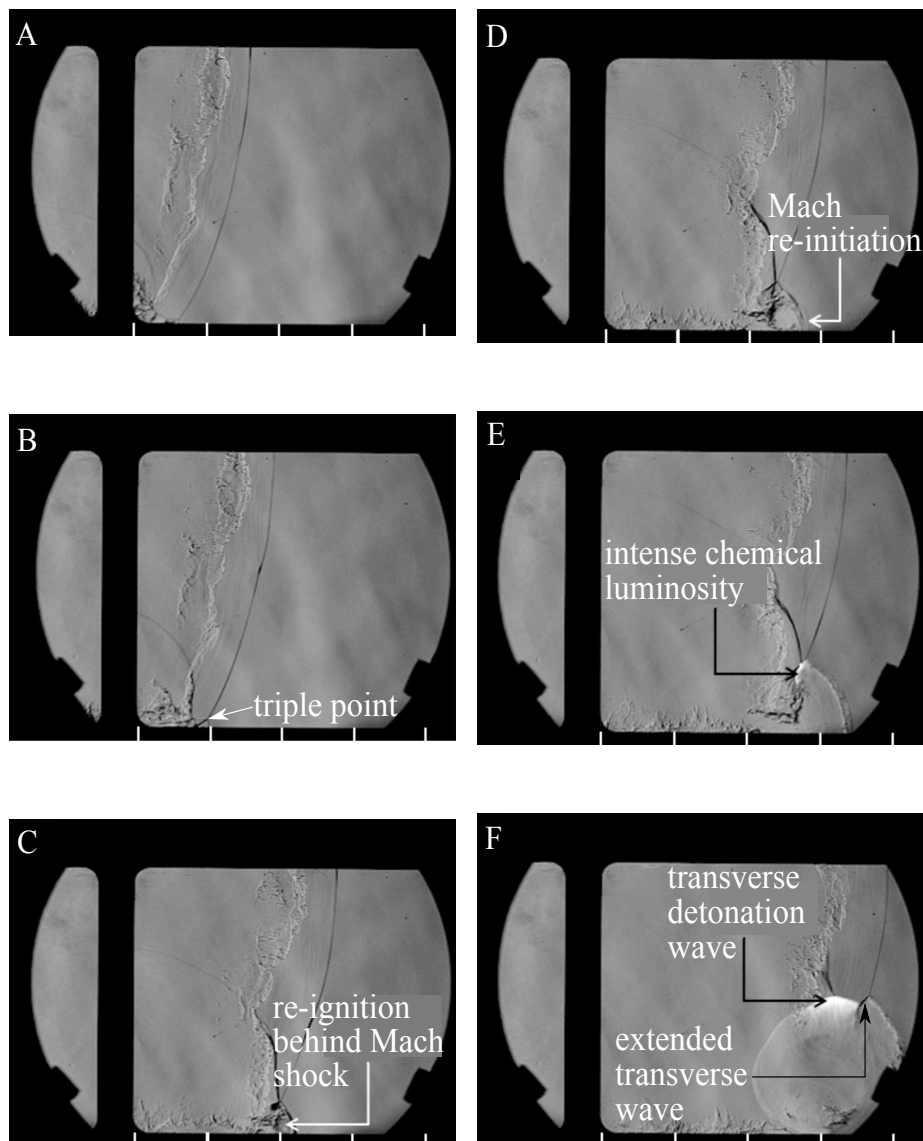


Figure 2.7: Detonation re-initiation by a transverse detonation observed by Bhattacharjee [15] following detonation interaction with a single obstacle in a stoichiometric methane–oxygen mixture with $p_0 = 12.3$ kPa.

wave is what led to re-initiation.

2.5 Numerical Investigations of FA and DDT

To help develop a predictive model for FA and DDT, numerical simulations have been conducted to better understand the phenomena. A common approach thus

far has been to simulate the FA and DDT processes from first principles using Direct Numerical Simulation (DNS). These include DNS studies for FA and DDT in smooth tubes with and without obstacles [1, 2, 8, 24, 44, 54, 57, 66, 69, 78, 90, 114, 115, 125, 164, 167, 240], and for the shock–flame problem [38, 39, 56, 165]. Despite significant advances in computational power and resources, full-scale DNS of the complete FA and DDT problem remains prohibitively expensive. In general, DNS of flame acceleration is problematic for industrial relevance, owing to the large range of scales that must be resolved. In most cases, only millimeter scale tubes have been fully resolved, while larger scale simulations have remained under-resolved [55, 86, 87, 239]. Nevertheless, results from these simulations have been instrumental in detailing the different stages through which flames accelerate while speculating on how the transition to detonation occurs. Starting with the pioneering study by Khokhlov et al. [90], the DNS studies outlined also represent the most successful effort so far to isolate the SWACER mechanism [102]. These results have been summarized and reviewed by Oran and Gamezo [165]. An alternate approach to DNS is to apply Reynolds Averaging to the Navier-Stokes equations (RANS) and simulate only the large-scale fluid motion while modeling the small-scale contributions. Thus far, the RANS methodology has been successfully applied to model relatively steady and fully developed supersonic combustion problems where large fluctuations in flow properties are not expected in very short time scales. Since this approach only provides mean values of the flow field properties averaged over large time steps, RANS is considered unsuitable for studying FA and DDT. In general, the trade-off between preciseness and computational expense remains a dilemma, with a need to apply adequate models to properly capture the unresolved scales.

A compromise, and realizable alternative, to both DNS and Reynolds Averaged Navier Stokes (RANS), is to model the turbulent scales in a Large Eddy Simulation (LES) formulation. In this approach, the exact Navier Stokes equations are solved down to the inertial scales of the problem [176], such that the energy-carrying ed-

dies are resolved. Models are then applied to describe only the small-scale turbulent mixing and combustion. These models apply Kolmogorov scaling laws to describe the self-similar nature of the energy cascade associated with vortical motion in order to account for the small-scale fluctuations with higher accuracy than RANS. To this end, LES has proven to be useful at accounting for small-scale turbulent effects on combustion rates of compressed gases, allowing for more affordable and scale-relevant simulations compared to DNS. Although LES allows for sufficient closure on viscosity and mixing rates due to turbulence, there are several proposed modeling strategies for providing closure for the reaction rates in simulations based on the different possible turbulent combustion regimes.

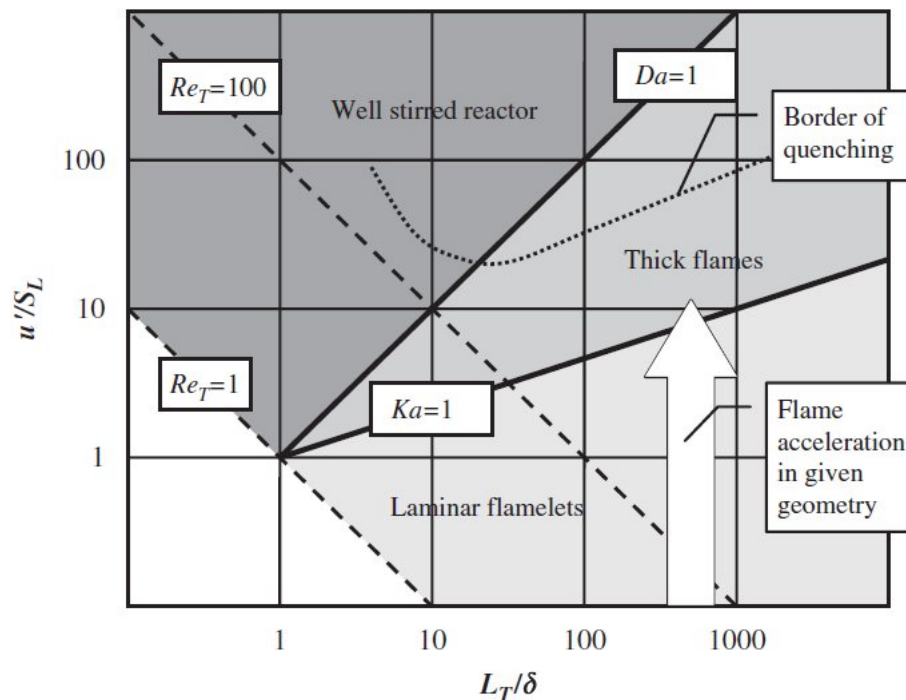


Figure 2.8: Borghi diagram of characteristic turbulent combustion regimes [31].

Turbulent premixed combustion regimes have traditionally been categorized by the characteristic Damkholer number (Da), which is the inverse of the rate at which burning occurs over the flame structure, and Karlovitz number (Ka), which relates the chemical time scales to the Kolmogorov scale. Specifically, three major tur-

bulent combustion regimes for premixed combustion have been identified, namely, (1) The well-stirred reactor or broken reaction zones, (2) The thin reaction zone or thick flame regime, and (3) The flamelet regime, as shown in Fig. 2.8. The well-stirred method is the easiest to implement numerically, where it is assumed that the combustion is locally limited by the chemistry alone. That is, the turbulent mixing scales are much quicker than the chemical reaction time scales, with each computational cell then treated as a constant volume reactor with uniform reactant concentration and temperature at each time step. Unfortunately, LES attempts at modeling detonation waves using the well-stirred reactor assumption have had difficulty resolving the correct reaction rates [126] and, in some cases, predicting a much faster than expected burning rate [61]. On the other hand, flamelet methods represent the opposite end of the regime spectrum, where chemical reaction time scales are much quicker than the rate at which turbulent energy is dissipated. However, like the well-stirred assumption, the flamelet methods are unsuitable for the full-scale DDT problem. While the initial flame acceleration process has been successfully modeled using the flamelet assumption in the past [71], achieving the correct reaction rates has proven to be difficult in the DDT limit where thin reaction zones are expected [28, 63, 71, 236, 238, 252]. In fact, Ciccarelli [31] points out that during the flame acceleration process, the characteristic combustion regime evolves from laminar flamelets towards the thin reaction zones shown in Fig. 2.8. In general, the flamelet and well-stirred reactor assumptions break down when the mixing rates are comparable to the chemistry rates, which has been recently argued to be the case for the final stage of fast flame acceleration and DDT [137]. One way to address this deficiency is by applying the *compressible linear eddy model for large eddy simulation* (CLEM-LES) specifically designed to handle compressible and reactive flows with varying degrees of both turbulence and reaction time scales [136]. As a result, CLEM-LES is capable of simulating any combustion regime, including the thin reaction zone regime. Using the CLEM-LES, Maxwell

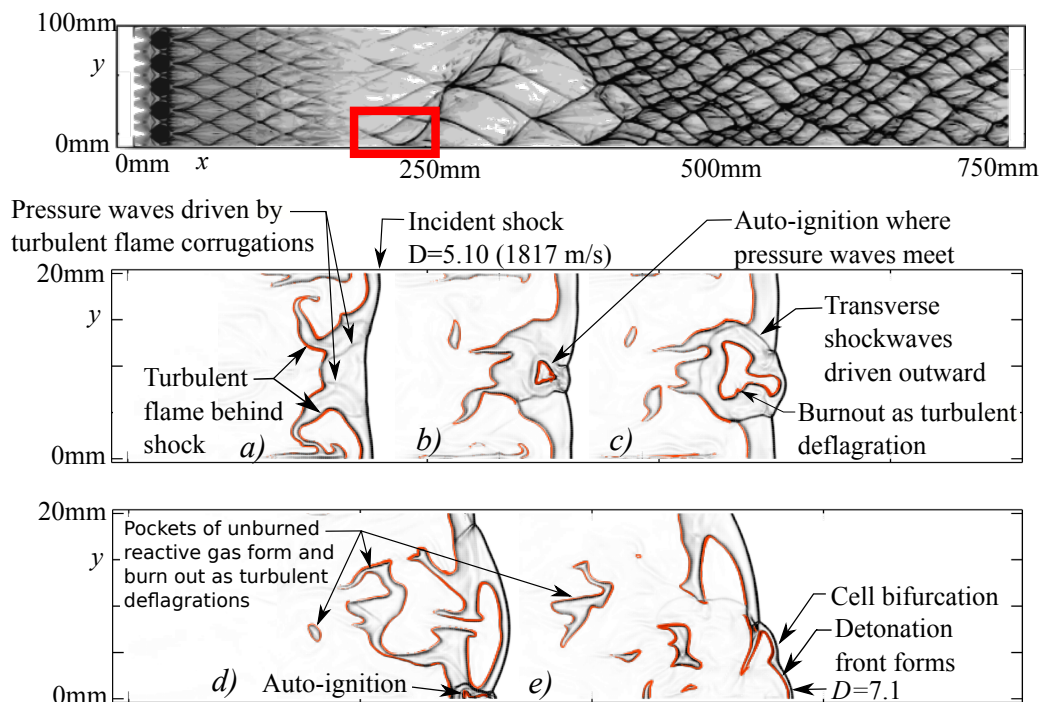


Figure 2.9: Two-dimensional transition from a shock–flame complex to detonation in using the CLEM-LES [134].

et al. [134] observed good agreement with experiments (shown in Fig. 2.9) for the transition of a shock–flame complex to detonation while highlighting that increased turbulent mixing rates had the potential to mitigate DDT. While CLEM-LES clearly possesses the capability to study FA and DDT using high-fidelity numerical simulations, it should be noted that it is a novel strategy that has been successfully applied in only a limited capacity [134–137, 142]. Successful applications of CLEM-LES thus far have also been limited in their chemical accuracy, and its application is still computationally expensive for studying the full DDT problem. Finally, from all the DNS and LES studies highlighted, only a small handful have been directly compared to experimental observations of FA [8, 28, 63, 236, 238, 240]. Even fewer have been compared to experimental DDT events [114, 115, 134].

While the significant role of turbulence in the initial FA process is well documented from experimental evidence and numerical studies, it is currently believed

that the main features of the eventual transition to detonation are governed by inviscid gas dynamics and chemical reactions [53]. The vast majority of numerical simulations where the quenching and re-initiation of detonations are investigated then solve the reactive Euler equations by ignoring turbulence. Instead of explicitly resolving molecular diffusion effects, deflagrative burning on reaction surfaces was instead accounted for and driven by numerical diffusion associated with the finite-volume scheme adopted. In the subsequent sections, an in-depth review of Euler simulations relevant to the cases investigated in the current study is carried out. By concentrating on Euler studies, the choice of the chemical kinetic model chosen was the primary distinction between the different studies. Chemical kinetic models in all combustion applications can be classified into two main categories: (1) elementary reaction mechanisms (ERMs), and (2) global reaction mechanisms (GRMs). Elementary reaction mechanisms provide the most precise description of reactive flows through single-transition-state reactions among real chemical species. At the same time, GRMs are formulated to cover only the dominant reaction paths through simplified global reaction steps.

2.5.1 Summary of detonation quenching and re-initiation investigations using global reaction mechanisms (GRMs)

To date, a vast majority of numerical DDT research has applied idealized GRMs, the most common being the standard one-step Arrhenius reaction model, which simplifies the chemistry of the kinetics to one reaction where reactants are converted to products according to Arrhenius law [2, 5, 15, 55, 66, 69, 78, 87, 88, 181, 204, 240]. In most cases, the reactive mixture is also assumed to be a calorically perfect gas (i.e., ideal gas behavior with constant heat capacities). However, this approach is well known to be inadequate for capturing the proper chemical ignition response of the gas, with Liberman et al. [114] having previously argued that it can lead to detonation re-initiation after quenching through incorrect mechanisms. This

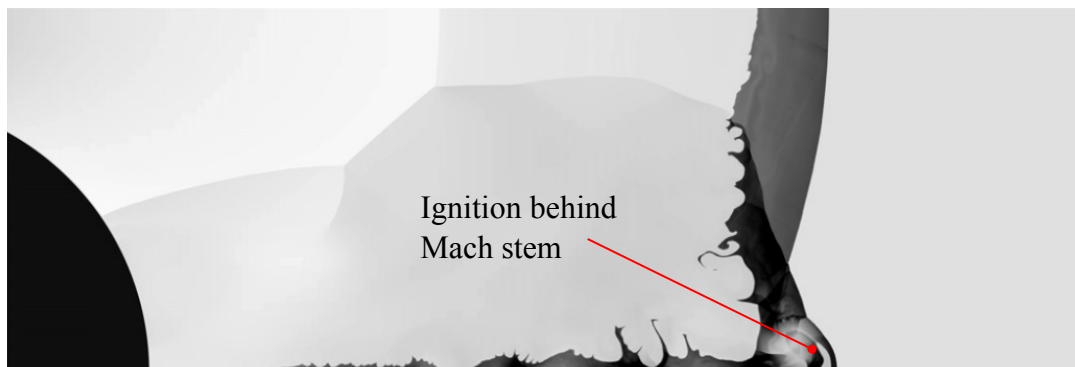


Figure 2.10: Numerical density field results from Bhattacharjee et al. [14] for CH_4+2O_2 and $p_0 = 10$ kPa using a 1-step model showing the critical ignition regime.

can, in part, be attributed to local instabilities in the reaction zone not accurately resolved using one-step chemistry [214]. Arienti and Shepherd [5] used a one-step reaction model characterized by different activation energies to study the critical diameter problem. While the results were in qualitative agreement with the experimental results of Schultz [195], the detonation cellular structure was suppressed in the numerical simulations, which limits the validity of the results for irregular mixtures. Khasainov et al. [88] observed better results for the detonation diffraction into diverging tubes with different divergence angles (α) in stoichiometric $\text{C}_2\text{H}_2 - \text{O}_2$ mixtures using a pressure-driven one-step model with heat capacities that vary linearly with temperature. In this case, the transverse detonations were successfully observed during re-initiation highlighting the limitations of the calorically perfect gas assumption. However, the simulations lacked adequate resolution, and the critical re-initiation was not investigated for detonation diffraction into free space.

Radulescu and Maxwell [181] used a one-step model and two-dimensional Euler simulations to replicate their experiments for detonation interaction with repeated columns of cylinders. This study demonstrated the abilities of the one-step model, including the ability to capture Mach reflections and the emergence of triple points that lead to detonation re-initiation. Bhattacharjee et al. [14] used the same

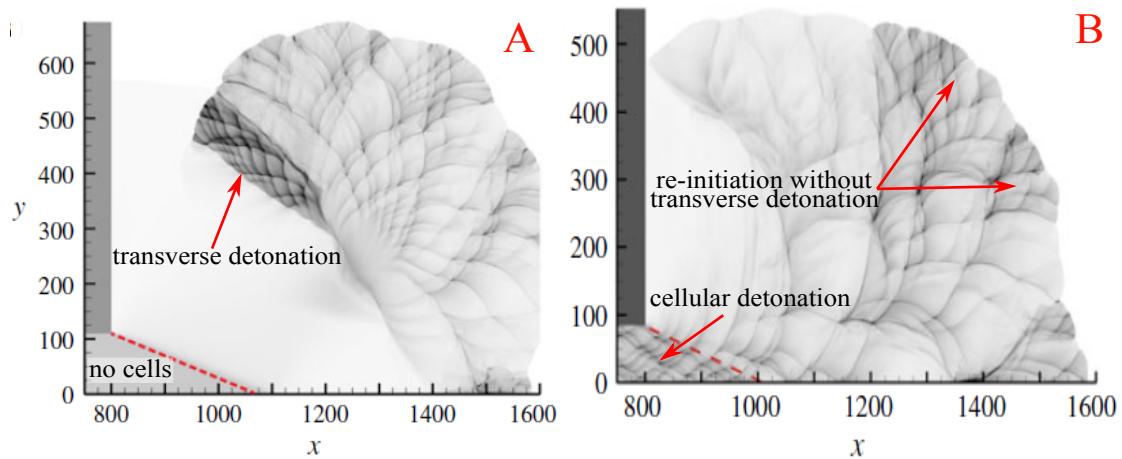


Figure 2.11: Numerical soot foils from the study by Shi et al. [204] showing detonation re-initiation following diffraction using a one-step model for (A) a planar detonation with no cells, and (B) a cellular detonation wave.

numerical modeling approach as that of Radulescu and Maxwell to simulate the flow field observed experimentally following detonation interaction with a single obstacle. At higher pressures, simulations elucidated that the shock reflection ignites behind the Mach stem, seen in Fig. 2.10, and it was concluded that the first ignition event is due to adiabatic compression. While some ignition events were observed in both of these studies, the simulations could not reproduce experimentally observed transverse detonations. The recent numerical study by Shi et al. [204] investigating detonation diffraction further highlights the deficiency of one-step models with calorically perfect gas assumptions. For re-initiation following detonation diffraction of cellular detonations, no transverse detonation was observed, and re-initiation was a result of local ignition events caused by random transverse triple point collisions only. An explosion bubble at the reaction front and re-initiation by a transverse detonation was only observed in the study for planar detonations without a cellular structure. These results are shown in Fig. 2.11.

Two-step models [40, 157], which consist of a strictly thermally neutral induction stage followed by a state-insensitive exothermic stage, have also been pre-

viously applied to study detonation quenching and re-initiation [73–76, 98, 109, 154, 163, 166, 242]. Jones et al. [73–76] and Oran et al. [163, 166] studied the detonation diffraction and re-initiation process for an abrupt 180° area expansion. Layered and uniform $\text{H}_2 - \text{O}_2(-\text{Ar})$ mixtures were modeled. While results from these studies resemble experimentally observed flow fields more closely than one-step chemistry with the induction delay correctly captured, two-step models are still typically limited in their chemical accuracy for hydrocarbon combustion. For example, the numerical study by Nagura et al. [154], used a two-step model tuned for stable hydrogen-oxygen combustion and suggested that two steps are insufficient for describing the combustion in stoichiometric ethylene-oxygen, which was used in the detonation diffraction experiments. A similar argument was made by Li et al. [109], who suggested that two-step chemistry cannot effectively describe combustion in irregular mixtures. The numerical study by Li et al. [109] also confirmed that the failure of a detonation wave following diffraction in highly regular mixtures follows the ‘*excessive curvature*’ mechanism proposed by Lee [100]. In the numerical study by Xu et al. [242], an obstacle was introduced near the tube exit following detonation diffraction in $\text{C}_2\text{H}_2 - \text{O}_2$ mixtures to promote instabilities and trigger the transverse detonation. In the absence of an obstacle, no transverse detonation was observed, as shown in Fig. 2.12. To further investigate the role of small obstacle-induced perturbations on the re-initiation following diffraction, Yuan et al. [245] recently attempted replicating the experiments of Xu et al. [242]. While re-initiation by the transverse detonation, triggered directly due to the enhanced cellular instabilities caused by the obstacle was successfully observed, the two-step model utilized was calibrated for $\text{H}_2 - \text{O}_2$ combustion instead of the $\text{C}_2\text{H}_2 - \text{O}_2$ mixture used in the experiment. Lau-Chapdelaine [98] used a two-step model in an Euler framework to replicate the experiments of Bhattacharjee [15] for detonation re-initiation behind a single obstacle. It was determined that detonation re-initiation was caused by adiabatic compression of the Mach stem shock wave in some cases

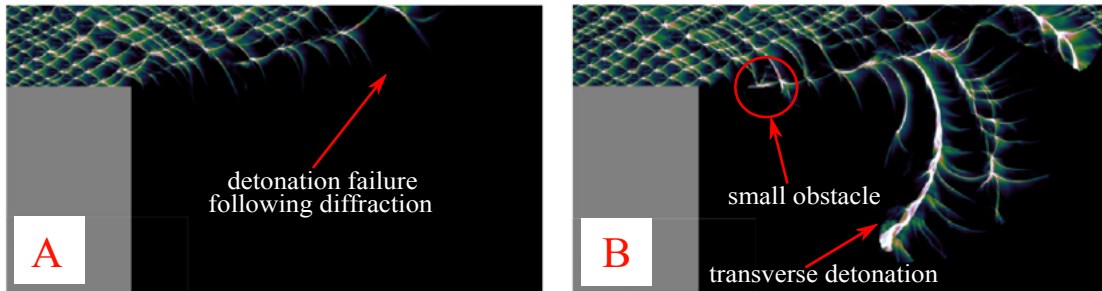


Figure 2.12: Numerical soot foils from the study by Xu et al. [242] showing (A) detonation failure following diffraction and (B) detonation re-initiation by a transverse detonation with an obstacle perturbation using a two-step chemistry model.

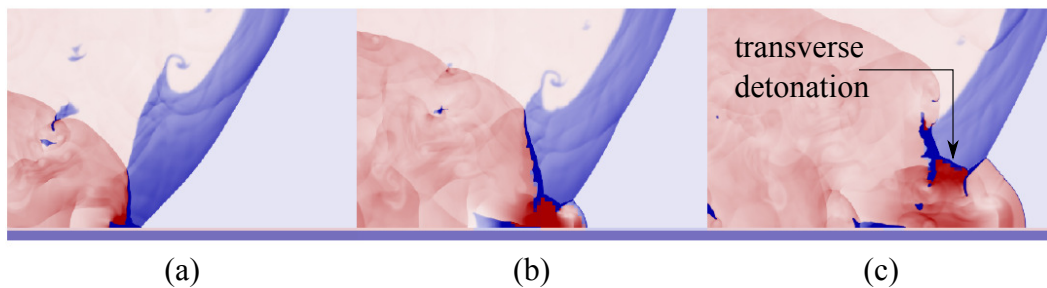


Figure 2.13: Numerical results from Lau-Chapdelaine [98] for CH₄+O₂ and $p_0 = 11.9$ kPa using a two-step chemistry model showing detonation quenching and re-initiation. The transverse detonation disappears shortly after Frame (c).

and by the wall-jetting in others. However, in this case, the transverse detonation was observed briefly in the numerical study before disappearing shortly after frame (c) in Fig. 2.13.

This brief review found that most numerical studies have been conducted using global (one- or two-step) kinetic schemes. Even though simple global chemical models enable the reproduction of many features of quenching and re-initiating detonations, the kinetics parameters are often adjusted to match some particular aspects of the experimental observations. Such an approach cannot provide reliable quantitative comparisons and is limited to a narrow range of conditions. For example, a fundamental drawback in DDT investigations is that the one-step ap-

proach can either be calibrated to capture the moment of DDT or the detonation behavior beyond DDT (such as cell size), and not both [191]. In a typical reaction, the temporal structure consists of a relatively long and nearly thermally neutral induction time followed by a comparatively short exothermic reaction time, in which the majority of the heat is released. However, the simple one-step model has no explicit thermally neutral induction phase. Heat is always released, and the induction/reaction zone scales have no independent control. As a result, the model cannot accurately reproduce the temporal reaction structures and stiffness associated with combustion. For detonation waves, the single global activation energy in the one-step model also controls both the spatial structures of the induction and reaction zones simultaneously and, therefore, cannot reproduce the correct steady Zel'dovich–von Neumann–Döring (ZND) structure in a detonation wave [108]. In fact, the ratio of the induction to reaction zone lengths is an important parameter that controls the multidimensional cellular stability of detonation waves [178]. While two-step models are a slight improvement to simple one-step chemistry, the model assumes that the chain branching explosion is instantaneous, with the fuel converted to radicals once the induction time is reached. This is inaccurate for reactive mixtures involving acetylene or hydrogen, where chain branching cross-over temperature effects influence the ignition delay time response to changes in temperature, and consequently, the detonation structure [138, 205]. Three-step models [16, 156, 205], which can handle chain branching cross-over effects, four-step models [77, 112] with an added chain-termination step, and five-step models [113], which account for radical competition, have also been proposed in the past. However, these GRMs are also largely limited to modeling hydrogen combustion.

2.5.2 *State of the art combustion models*

A large advantage of GRMs is that the resolution of the models can be increased significantly compared to detailed ERMs due to the reduction in required compu-

tational resources. Elementary reaction mechanisms (ERMs), while providing the most accurate mathematical description of the chemical kinetics during combustion, are typically limited in attainable resolution for their application to full-scale multi-dimensional numerical simulations. Typical numerical studies involving simple chemistry models can easily resolve laboratory scale phenomena to a grid size within 10 to 100 μm [58, 230], if not finer. Flame modeling studies with full chemistry, for example, typically either have a much coarser resolution or cannot be applied to model laboratory scale experiments [29, 231]. The lack of resolution in numerical studies adopting ERMs is largely due to the computational cost and memory requirements needed to process the reaction steps for several hundred reacting species. Through the elimination of redundant species (skeletal ERMs) [12, 121, 133, 224], followed by time-scale analysis and removal of quasi-steady-state (QSS) species [97, 124, 227], it is possible to create a moderate sized ERM that is still precise within a specific scope. However, the extent to which the mechanism can be reduced using these approaches is limited [120] and has only been successfully realized for a few reactive hydrocarbon mixtures such as those involving methane [133], acetylene [227], and ethylene [119]. It was also observed that for hydrocarbons, the minimum number of species for a reduced skeletal ERM reaches a value of around 10, after which further simplification is not feasible [246].

Mével et al. [147], and Gallier et al. [53] studied the detonation diffraction problem for a detonation initially propagating in a channel and tube, respectively, using an ERM (17 reactions and 9 species) for hydrogen combustion. In both cases, the numerical results were in excellent agreement with experimental observations, and strong transverse waves were observed in the critical regime during detonation re-initiation. Also clearly visible during re-initiation is the presence of a strong transverse detonation that propagated to the back wall in the band of shocked but unreacted gas formed by the abrupt area expansion. Fig. 2.14 shows the critical re-initiation of the diffracted detonation by the transverse detonation wave observed

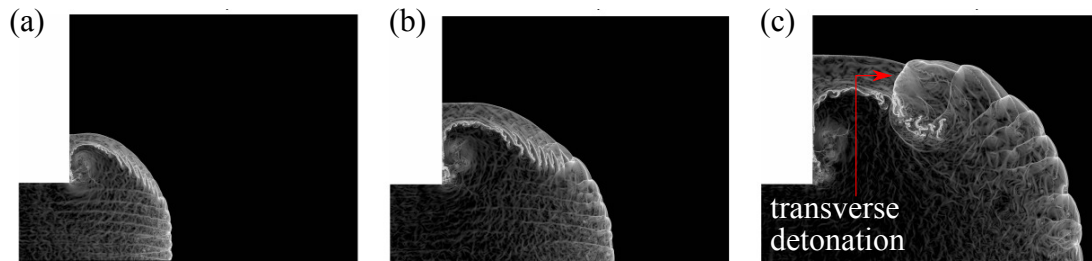


Figure 2.14: Numerical results from Mével et al. using a 9 species, 17 reaction model [146] for $2\text{H}_2 + \text{O}_2 + 2\text{Ar}$ and $p_0 = 13.8$ kPa for detonation diffraction [147].

by Mével et al. [147]. Gallier et al. [53] further speculated that the significant details of the detonation diffraction process are controlled by inviscid gas dynamics and chemical processes. Deiterding et al. [36] studied the failure and re-initiation of diffracting detonations in $\text{H}_2 - \text{O}_2 - \text{Ar}$ mixtures using an ERM consisting of 34 irreversible reactions and 9 species. The different regimes following detonation diffraction were observed and were found to be in very good agreement with the experiments conducted by Schultz [195]. Despite these successful applications of skeletal ERMs, there still remains much work to be done on accurately modeling these types of scenarios with much more complex fuel-air mixtures [182], such as hydrocarbons.

In this regard, Vijayakumar (2020) [228] implemented a skeletal ERM for highly irregular and critical detonation propagation in methane-oxygen to observe the failure and re-initiation modes. The reduced mechanism applied contained 13 species and 35 reactions. Transverse detonation waves were present with this multi-step chemistry, along with other features of re-initiation seen experimentally, such as the extended transverse wave, secondary triple point, hotspots, and reflected shock waves. Ziegler (2012) [255] also used a skeletal mechanism of 22 species and 53 reactions for the initiation of a propane detonation from a wedge, where transverse detonations were observed as well. These studies again imply the importance of including sufficient chemistry in a combustion model in order to capture the correct

features of re-initiation.

2.6 Numerical Modeling Approach in the Current Study

After analyzing the results from previous numerical investigations, the current section outlines the numerical modeling approach adopted in the current study. The overarching objective of the current study is to develop a better understanding of how detonations are re-initiated following failure using high-resolution numerical simulations. Specifically, the re-initiation of quenched detonations by transverse waves following detonation diffraction as observed by Schultz [195] and detonation interaction with a single obstacle observed by Bhattacharjee [15] are investigated in detail. Following the review of past studies presented in Section 2.5, it can be observed that the primary deficiency in past numerical studies is the lack of adequate chemical accuracy through the application of simple one- or two-step combustion models. Moreover, when more detailed descriptions of the chemistry have been adopted, they have largely been limited to simulating detonations in hydrogen mixtures or lacked adequate resolution due to the computational costs associated with using ERMs. Based on these observations, it has been determined that the combustion model for this thesis must be defined by the following features and improvements:

- A model that provides a more accurate description of the chemistry and thermodynamics of a detonation wave compared to simple GRMs without compromising computational efficiency.
- A model that does not require prohibitive computational resources and memory with the ability to resolve down to small-scale phenomena and to capture correct reaction sensitivity.

- This model should produce a better description of detonation re-initiation following quenching, namely the inclusion of transverse detonation waves as the dominating mode of re-initiation.

As a result, in the current study, a simple four-species, four-step reaction mechanism based on a thermochemical approach proposed by Zhu et al. [253] is developed further. The goal is to develop the model, which was initially applicable for only stoichiometric acetylene–oxygen combustion, to include several different premixed reactive hydrocarbon mixtures and provide the necessary chemical accuracy required to study detonation quenching and re-initiation. This combustion model is a GRM that utilizes discrete packs of chemical species as global species, which mimic the behavior of a detailed chemistry ERM. The process of using ignition data from ERMs to calibrate the reaction pathways sets this chemical kinetics model apart from traditional four- or five-step GRMs. By assuming the gas mixture to be thermally perfect, i.e., ideal gas behavior with temperature-dependent heat capacities, the model can respond appropriately to changes in the thermodynamic state. Through independent calibration of the reaction rate constants throughout the combustion regime, the model has been previously demonstrated to capture the detailed chemistry ignition temperature evolution for constant volume and constant pressure ignition problems for stoichiometric acetylene–oxygen combustion [253]. Since detonation waves involve the coupling of gas dynamics and chemical reactions and are influenced by changes in the thermodynamic properties of the medium, the model was also demonstrated to correctly predict the one-dimensional ZND reaction structure in stoichiometric acetylene–oxygen to a high level of accuracy. Finally, since the major details involved during re-initiation are controlled by inviscid gas dynamics and chemical processes [53], the four-step model is used to provide a description of the chemical details in an Euler framework.

Chapter 3

PROPOSED METHODOLOGY

3.1 Governing Equations

Compressible multi-component reactive flows are governed by the Navier-Stokes equations. A reacting gas involves a mixture of multiple species that must be tracked individually [175]. Continuity, or the conservation of mass, remains unchanged from non-reacting flows, where for a finite volume, the local rate of change of mass is balanced by the mass flux (or mass flow rate) through the volume surfaces. The conservation of momentum governs the local rate of change of linear momentum and is balanced by the momentum flux, pressure gradients, viscous shear stress, and the sum of body forces which act on each species. The rate of change of total energy is balanced by the flux of enthalpy, viscous dissipation, heat transfer, and external work from the body forces. The complete set of Navier-Stokes equations for a compressible and reactive flow, in differential form, can be written as

Conservation of mass:

$$\underbrace{\frac{\partial \rho}{\partial t}}_{\text{local rate of change of density}} + \underbrace{\nabla \cdot (\rho \underline{u})}_{\text{mass flux divergence}} = 0 \quad (3.1)$$

Conservation of momentum:

$$\underbrace{\frac{\partial (\rho \underline{u})}{\partial t}}_{\text{local change in linear momentum per unit volume}} + \underbrace{\nabla \cdot (\rho \underline{u} \otimes \underline{u})}_{\text{momentum flux divergence}} + \underbrace{\nabla p}_{\text{pressure gradient}} - \underbrace{\nabla \cdot \tau}_{\text{shear stress tensor divergence}} = \underbrace{\sum_{i=1}^N \rho Y_i \underline{f}_i}_{\text{sum of body forces acting on all species}} \quad (3.2)$$

Conservation of total energy:

$$\underbrace{\frac{\partial(\rho E)}{\partial t}}_{\text{local change in total energy per unit volume}} + \underbrace{\nabla \cdot ((\rho E + p)\underline{u})}_{\text{enthalpy flux divergence}} - \underbrace{\nabla \cdot (\underline{u} \cdot \underline{\tau})}_{\text{viscous dissipation}} + \underbrace{\nabla \cdot \underline{q}}_{\text{heat flux divergence}} = \underbrace{\sum_{i=1}^N (\rho \underline{u}_{d,i} Y_i) \cdot \underline{f}_i}_{\text{net rate of work done by body forces on all species}} \quad (3.3)$$

Conservation of mass of each i th out of N chemical species:

$$\underbrace{\frac{\partial(\rho Y_i)}{\partial t}}_{\text{local rate of change of density of the } i\text{th species}} + \underbrace{\nabla \cdot (\rho \underline{u} Y_i)}_{\text{mass flux divergence of the } i\text{th species}} + \underbrace{\nabla \cdot (\rho \underline{D}_i Y_i)}_{\text{diffusion of the } i\text{th species}} = \underbrace{\dot{\omega}_i}_{\text{rate of production of the } i\text{th species}} \quad (3.4)$$

where the variables are defined in the Nomenclature. For the purposes of this study, a number of assumptions are made to simplify the governing equations. In supersonic flow, i.e. detonation waves, diffusion terms are often neglected because the high Mach and Reynolds numbers involved cause the advective terms to dominate over the diffusive transport terms [99]. Gravity can be neglected because the effects are small compared to the overall momentum of the gas. Thermodynamic properties can be assumed to be functions of temperature only because changes in temperature dominate over changes in pressure [83]. The assumptions made can be summarized as:

- Thermally perfect gas with temperature dependent thermodynamic properties
- Neglect viscosity
- Neglect all heat transfer (i.e. neglect conduction, radiation, and Dufour effects)
- Neglect mass diffusivity, including Soret effects
- Neglect external body forces (i.e. gravity)

These assumptions lead to the inviscid reactive Euler equations typically solved to study flows involving detonations. Finally, to model the detonation diffraction from

a tube, the reactive Euler equations are further simplified by assuming that the flow is symmetric about the axial z direction in a cylindrical coordinate system. For the axisymmetric reactive Euler equations, the conservation laws for mass, momentum, total energy, and i th chemical species are approximated by a two-dimensional problem with an additional geometric source term in the r momentum equation [48]. Expanding the vector relations in (3.1)-(3.4), the axisymmetric governing equations can be summarized as:

$$\frac{\partial \mathbf{U}}{\partial t} + \frac{1}{r} \frac{\partial (r\mathbf{F})}{\partial r} + \frac{\partial \mathbf{G}}{\partial z} = \mathbf{S} \quad (3.5)$$

where:

$$\begin{cases} \mathbf{U} = [\rho, \rho u_r, \rho u_z, \rho E, \rho Y_i], \\ \mathbf{F} = [\rho u_r, \rho u_r^2 + p, \rho u_r u_z, u_r(\rho E + p), \rho u_r Y_i], \\ \mathbf{G} = [\rho u_z, \rho u_r u_z, \rho u_z^2 + p, u_z(\rho E + p), \rho u_z Y_i], \\ \mathbf{S} = [0, p/r, 0, 0, \dot{\omega}_i]. \end{cases} \quad (3.6)$$

Here \mathbf{S} represents the source terms with $\dot{\omega}_i$ representing the production rate of the i th chemical species. The pressure is determined through the ideal gas law,

$$p = \rho RT, \quad (3.7)$$

where the specific gas constant is calculated for every chemical species through

$$R = R^o \sum_{i=1}^N (Y_i/W_i). \quad (3.8)$$

The total specific energy for a thermally perfect gas is given by

$$\underbrace{E}_{\text{total specific energy}} = \underbrace{\sum_{i=1}^N (Y_i h_i)}_{\text{specific internal energy}} - \frac{p}{\rho} + \underbrace{\frac{1}{2} |\underline{u}|^2}_{\text{specific kinetic energy}}. \quad (3.9)$$

The speed of sound in the mixture is computed using the chemically frozen ratio of specific heat capacities through

$$c^2 = \gamma P / \rho, \quad (3.10)$$

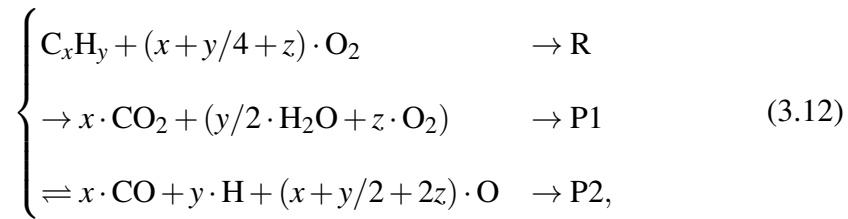
where $\gamma = c_p/c_v$. The specific heat capacities at constant pressure and volume, c_p and c_v , as well as the specific enthalpies for each species, h_i , are determined through the temperature-dependent NASA polynomial approximations for a multi-component gas [139], which have the form

$$\begin{cases} h_i = \frac{R^o}{W_i} \left(\sum_{n=1}^5 \frac{a_n T^n}{n} + a_6 \right) \\ c_{p,i} = \frac{R^o}{W_i} \sum_{n=1}^5 a_n T^{n-1}, \end{cases} \quad (3.11)$$

where a_n represent the NASA polynomials for a given i th species in the model, while W_i and R^o are the species molecular weight and universal gas constant. The total c_p and h are then computed by a weighted sum of all species based on the mass fraction.

3.2 The four-species, four-step combustion model

This combustion model is a GRM that utilizes discrete packs of chemical species as global species, which mimic the behavior of a detailed chemistry ERM. The global species in the four-step model are calibrated from the equilibrium results for a premixed combustion system using Cantera's [60] built-in minimum Helmholtz energy equilibrate function. The compact global species system for a generic fuel C_xH_y has been summarized by Zhu et al. [253] as



with $z \geq 0$ ($z = 0$: stoichiometric; $z > 0$: lean). The global species adequately predict the initial and terminal states of a combustion process but not the intermediate stages. The reaction paths are then built by fitting the reference data from a constant volume process for an ERM of choice using Cantera [60]. This is done by substituting the global species for a reactive mixture (R, P1, and P2) in the process

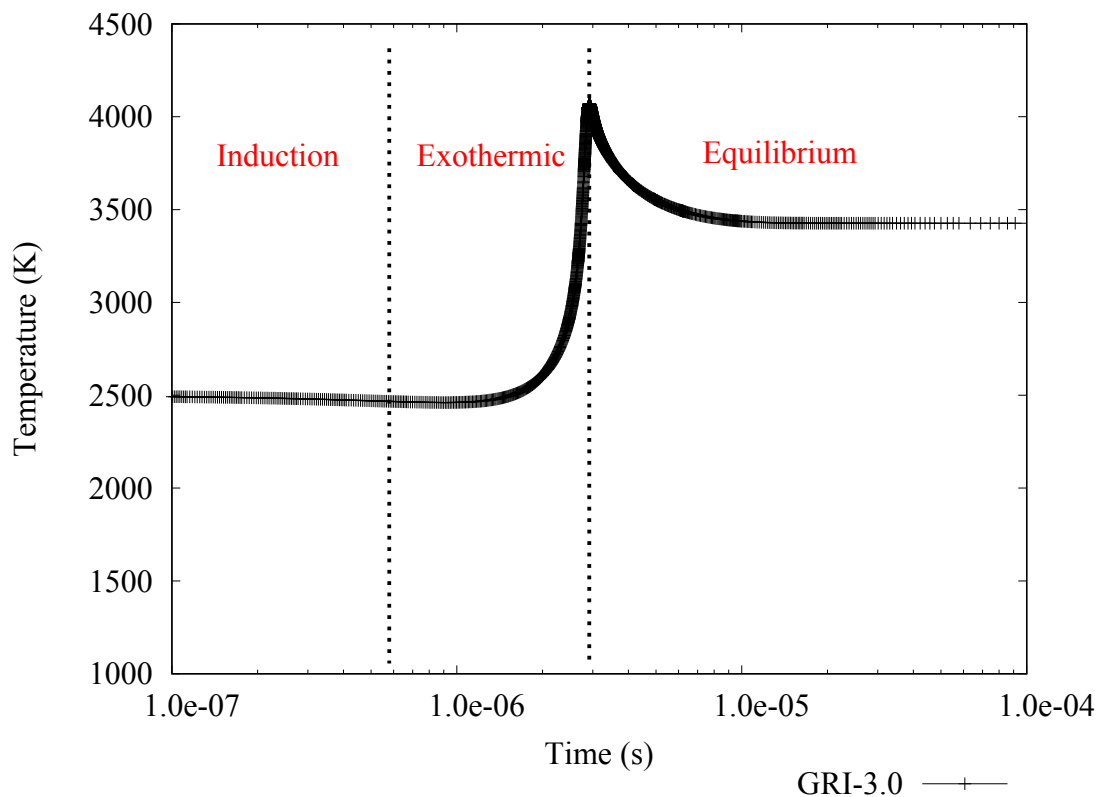
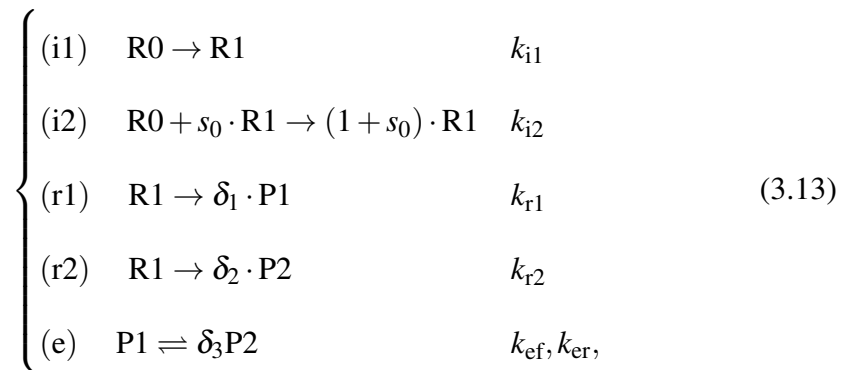


Figure 3.1: Constant volume reaction for a stoichiometric $\text{C}_2\text{H}_2 - \text{O}_2$ with $T_0 = 2500$ K and $p_0 = 1$ atm, showing the different zones where all of the fits are performed for calibrating the four-step model with data from detailed chemistry [34].

while conserving the overall thermodynamic properties. The reaction paths and corresponding reaction rates and orders are acquired by modeling the reaction as having two thermally neutral induction regime paths, two irreversible exothermic reaction paths that convert R to P1 and P2 separately, and an additional equilibrium step between P1 and P2. The three different regimes, induction, exothermic, and equilibrium, that require modeling are shown in Fig. 3.1 for a constant volume ignition process executed in Cantera [60].

The reaction scheme can be summarized as



where the absolute rate constants $k_i, k_{r1}, k_{r2}, k_{ef}$, and k_{er} rely only on the local thermal state of the mixture, while the stoichiometry coefficients are: $\delta_1 = W_R/W_{P1}$, $\delta_2 = W_R/W_{P2}$, $\delta_3 = W_{P1}/W_{P2}$. The species R1 in the model plays the role of an activated reactant meant to replace the numerous radicals and intermediate species formed during a typical combustion process from reactants to products. Since it is only possible to resolve the total amount of R from the detailed chemistry results in Cantera (since R0 and R1 are chemically identical), it is assumed that the chain initiation reaction (i1) and chain branching reaction (i2) are complete when a notable amount of product species P1 and P2 begin to form. While this value is not explicitly specified by Zhu [253], we assume the initiation reaction to be complete when the combined mole fractions of the forming products are greater than or equal to 0.1 since this is found to correspond well with the start of the main exothermic reaction. Similarly, in the equilibrium region, the amount of reactant R tends to zero since all the reactants are assumed to be consumed during the exothermic regime. Under these assumptions, the forward and backward rate constants k_{ef} and k_{er} , for the reaction (e), and the equilibrium constant, K_c , can be derived from the equilibrium regime, while the reaction rates k_{r1} and k_{r2} , for reactions (r1) and (r2), are calculated from the main exothermic regime of the ignition process. Finally, the reaction orders s_0, s_1, s_2 , and s_3 are evaluated through an iterative procedure meant to provide the best possible data set for the detailed chemistry that minimizes cumulative errors in the reaction rate parameters when fit to the predetermined functions for the reaction

rates in the model. The detailed procedure for deriving the functional dependence of the rate constants in the model can be found in the original manuscript by Zhu et al. [253] For detonation investigations, a single induction reaction existing as a packed formula with two paths, i1 and i2, was first explored by Fickett et al. [50] when studying induction zone kinetics. By assuming the ratio $k_{i1}/k_{i2} = \varepsilon$ is constant such that $\varepsilon \ll 1$, the production rates of the reactant species R0 and R1 can be modeled using only a single absolute rate constant, k_i . Through a high activation energy asymptotic expansion [33], it can then be shown that the absolute rate constant is inversely proportional to the ignition time for a given reactive mixture ($k_i \propto 1/\tau$). The rate constant k_i is then modeled using constant volume process ignition time measurements from detailed chemistry.

Finally, the production rates for the different global species is given by

$$\begin{cases} \dot{\omega}_{R0} = -\rho Y_{R0} \left[\varepsilon \left(\frac{Y_{R1} \cdot \rho}{W_{R1}} \right)^{s_0} \right] \cdot k_i \\ \dot{\omega}_{R1} = -\frac{W_{R1}}{W_{R0}} \dot{\omega}_{R0} - W_{R1} \left[\left(\frac{Y_{R1} \cdot \rho}{W_{R1}} \right)^{s_1} \cdot k_{r1} + \left(\frac{Y_{R1} \cdot \rho}{W_{R1}} \right)^{s_2} \cdot k_{r2} \right] \\ \dot{\omega}_{P1} = W_{P1} \left(\frac{Y_{R1} \cdot \rho}{W_{R1}} \right)^{s_1} \cdot k_{r1} \cdot \delta_1 - W_{P1} \left[\left(\frac{Y_{P1} \cdot \rho}{W_{P1}} \right)^{s_3} \cdot k_{ef} - \left(\frac{Y_{P2} \cdot \rho}{W_{P2}} \right)^{s_3 \delta_3} \cdot k_{er} \right]. \end{cases} \quad (3.14)$$

We note here that only three transport equations (for R0, R1, and P1) must be added to governing equations that conserve mass, momentum, and energy for fluid motion. Unlike Zhu's formulation, we do not include an explicit transport equation for product species P2 which is an improvement in memory requirements and efficiency. This simplification can be made since the sum of the mass fractions of the different species must be equal to unity ($\sum Y_i = 1.0$) for any gas mixture. Thus, the mass fraction of species P2 can be readily determined. Furthermore, under the constraint that $\sum (DY_i/Dt) = 0$, it is possible to obtain the production rate of P2 at any instant using equation set (3.14) if the mass fractions of the other species are known. Following the procedure above, four different stoichiometric hydrocarbon mixtures, acetylene-oxygen, methane-oxygen, propane-oxygen, and ethylene-oxygen, have

been calibrated, as well as three lean acetylene-oxygen mixtures with equivalence ratios (ϕ) 0.71, 0.5, and 0.33. To verify the performance of the model across different ERMs, the acetylene mixture is calibrated using the Konnov mechanism [34], the methane mixture using the GRI-3.0 mechanism [208], and the propane and ethylene mixtures using the USC II mechanism [232].

In Section 4, a series of zero- and one-dimensional ignition problems are simulated to validate the four-step model. In the Lagrangian description, following the procedure outlined by Kao et al. [82], the governing equations that follow a particle path can be written as

$$\begin{cases} \frac{D\rho}{Dt} = -\rho \frac{\dot{\sigma}}{\eta} \\ \frac{Dw}{Dt} = w \frac{\dot{\sigma}}{\eta} \\ \frac{DP}{Dt} = -\rho w^2 \frac{\dot{\sigma}}{\eta}, \end{cases} \quad (3.15)$$

where

$$\begin{cases} \dot{\sigma} = \sum_{i=1}^{N_y} \sigma_i \frac{DY_i}{Dt} \\ \sigma_i = \frac{W}{W_i} - \frac{h_i}{c_p T}. \end{cases} \quad (3.16)$$

Here, w is the particle path velocity, $\dot{\sigma}$ is the thermicity which measures the rate at which chemical energy is transformed into thermal energy and vice versa, and η is the sonic parameter defined as $\eta = 1 - M^2$. Three special cases exist for solving the governing equations (3.15). The steady-state solution corresponds to the 1-D ZND model, which describes the steady inviscid structure of a reaction zone behind a shock wave. The model presents the basic coupling of chemical reactions to steady-state gas dynamics in the frame of reference attached to the wave. The other two cases correspond to constant volume (CV) and constant pressure (CP) reactions. For the particular case of constant volume ignition, $(D\rho/Dt) = (Dw/Dt) = 0.0$ and $(DP/Dt) = -\rho c^2 \dot{\sigma}$, while for constant pressure ignition, $(DP/Dt) = (Dw/Dt) = 0.0$ and $(D\rho/Dt) = -\rho \dot{\sigma}$.

Chapter 4

COMBUSTION PROPERTIES OF A SIMPLE AND EFFICIENT FOUR-STEP MODEL

In this section, an in-depth analysis of the four-step model is carried out for several premixed reactive hydrocarbon mixtures with very different activation energies, ignition characteristics, and detonation stability. In particular, the author highlights the model's ability to predict important properties required for simulating realistic scenarios involving flame acceleration and detonations. The main properties of interest are the ignition delay, Chapman-Jouguet (CJ) velocity, expansion ratio, Zel'dovich number, activation energy, heat release, and detonation χ parameter for a wide range of conditions. In addition to stoichiometric fuel–oxygen mixtures, the four-step model performance has also been assessed for cases of heavy dilution and fuel lean ($\phi < 1.0$) mixtures. Finally, following the results and discussions presented in Sections 4.1 and 4.2, a summary of the limitations of the four-step model with regards to simulating the combustion of fuel-rich mixtures and reactive hydrogen mixtures is covered. In this sense, the aim is to determine the applicability and restrictions of the four-step, four-species model to be used as an effective reduced GRM for accurately modeling flame acceleration, supersonic combustion, and detonation waves in a variety of reactive hydrocarbon mixtures. The results presented in this Section are also available in the manuscript by Peswani et al. [171].

4.1 Preliminary Results for Stoichiometric, Lean, and Diluted Mixtures

This section aims to validate the four-step model for four hydrocarbon mixtures considered (acetylene–oxygen, methane–oxygen, propane–oxygen, and ethylene–oxygen) through comparison with detailed chemistry results from Cantera [60]. The preliminary results of the model performance in stoichiometric undiluted reactive

mixtures are first summarized through ignition time (τ) predictions and ZND detonation profiles. This is followed by validation of the four-step model for mixtures with varying equivalence ratios (ϕ) and dilution by an inert chemical species.

4.1.1 Stoichiometric Undiluted Reactive Mixtures

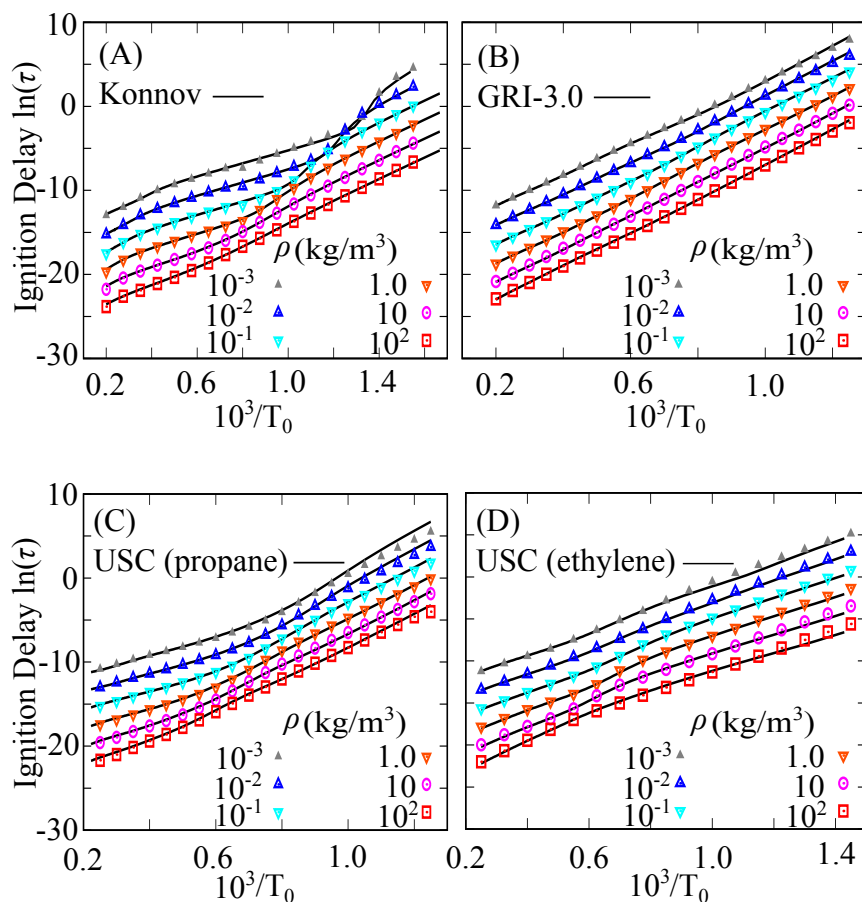


Figure 4.1: Constant volume ignition time predictions of the four-step model (points) compared to the detailed chemistry mechanisms (lines) of (A) Konnov [34] for the stoichiometric acetylene–oxygen mixture, (B) GRI-3.0 [208] for the stoichiometric methane–oxygen mixture, (C) USC for the stoichiometric propane–oxygen mixture [232], and (D) USC [232] for the stoichiometric ethylene–oxygen mixture.

Figure. 4.1 demonstrates the agreement of ignition times (τ) predicted using the four-step model and detailed chemistry, for each reactive mixture, over a wide range of initial temperatures and densities. The ignition time (τ) is calculated as the

maximum value of the derivative of temperature with respect to time, $(dT/dt)_{\max}$, during the complete ignition process. It is observed that the four-step model accurately recovers the detailed chemistry ignition delays for all four stoichiometric mixtures over the entire range of initial conditions tested. We first note that the linear behavior seen in the natural logarithm of ignition delay for methane is why the one-step model, with a single global activation energy, can capture the ignition delay times for this mixture reasonably but not for others [134]. However, it is well known that the correct temporal evolution of temperature (or reaction stiffness) for methane is not captured with the one-step model [137]. On the other hand, for fuels like acetylene and, to a lesser extent, propane and ethylene, which exhibit visible chain branching effects, independent control over the ignition time is necessary. In these cases, a single activation energy cannot correctly capture the ignition behavior over the entire temperature range.

Apart from the ignition time measurements, the four-step model replicates the reaction and equilibrium time scales and the thermodynamic state throughout the constant volume reaction process, as shown in Fig. 4.2. A comparable level of accuracy is also observed between the four-step model and detailed chemistry for a 1-D ZND detonation profile, as shown in Fig. 4.3 for a leading shock wave speed equal to the CJ detonation speed. The initial CJ speed for the four-step model and results for the detailed chemistry ERMs are obtained using the SD Toolbox libraries (for Cantera) [21] for an initial quiescent temperature of 300 K, and initial pressures of 1 kPa, 10 kPa, and 100 kPa. Apart from some deviation observed for the ethylene mixture and the low-pressure methane case, the four-step model is observed to recover almost precisely the correct temperature profiles and spatial scales of the reaction zone after a shock wave. These results present a big improvement over other simple GRMs, as shown in Fig. 4.4. Here, a comparison is drawn between the temperature profiles obtained behind a Mach 6.35 (2262.6 m/s) shock in stoichiometric methane–oxygen at $T_0 = 300$ K and $p_0 = 5.5$ kPa using the four-step model,

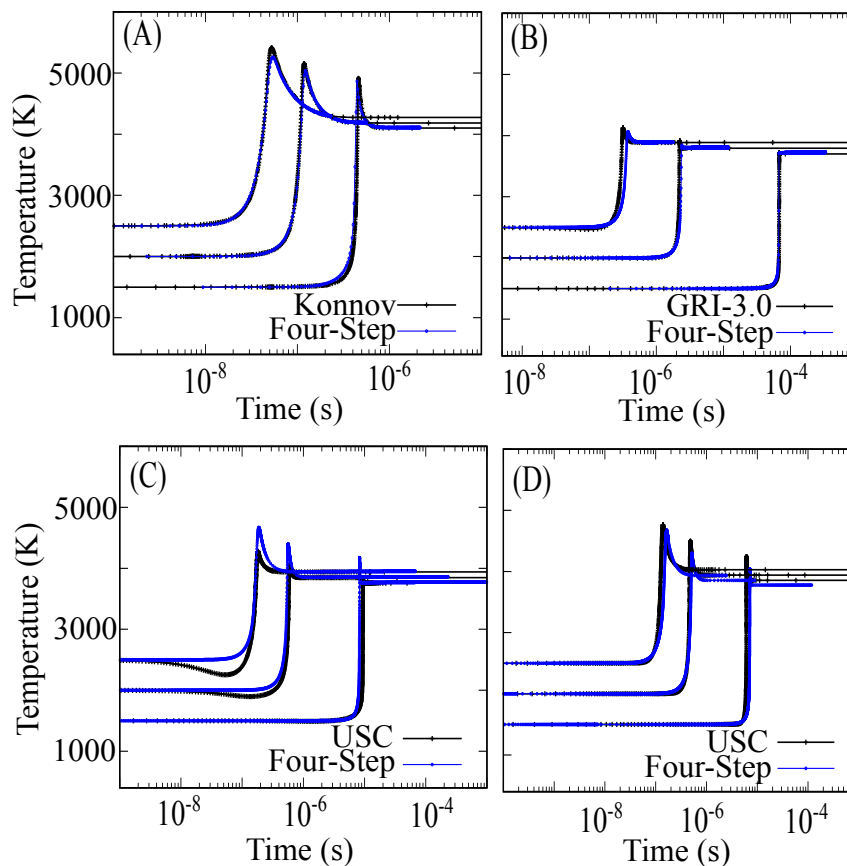


Figure 4.2: Constant volume ignition temperature profiles of the four-step model (points) compared to the detailed chemistry mechanisms (lines) for stoichiometric (A) acetylene–oxygen, (B) methane–oxygen, (C) propane–oxygen, and (D) ethylene–oxygen mixtures with $T_0 = 1500, 2000,$ and 2500 K and $\rho = 1.0$ kg/m³

conventional one- and two-step calorically perfect gas models [98], a one-step with temperature-dependent heat capacities, and the detailed GRI-3.0 mechanism [208]. We first note that the conventional one- and two-step perfect gas models [98] do not capture the correct post-shock or post-reaction state variables (i.e., temperature). Although the induction lengths have been tuned to the conditions behind the given incident shock strength, we point out that such tuning was actually performed at the wrong temperature (and pressure). During re-initiation of a quenched detonation wave by a transverse detonation, should a second shock form in the shocked mixture, and since the induction lengths were tuned only to the conditions behind the first shock, it is very likely that the ignition time would not be correct since the state

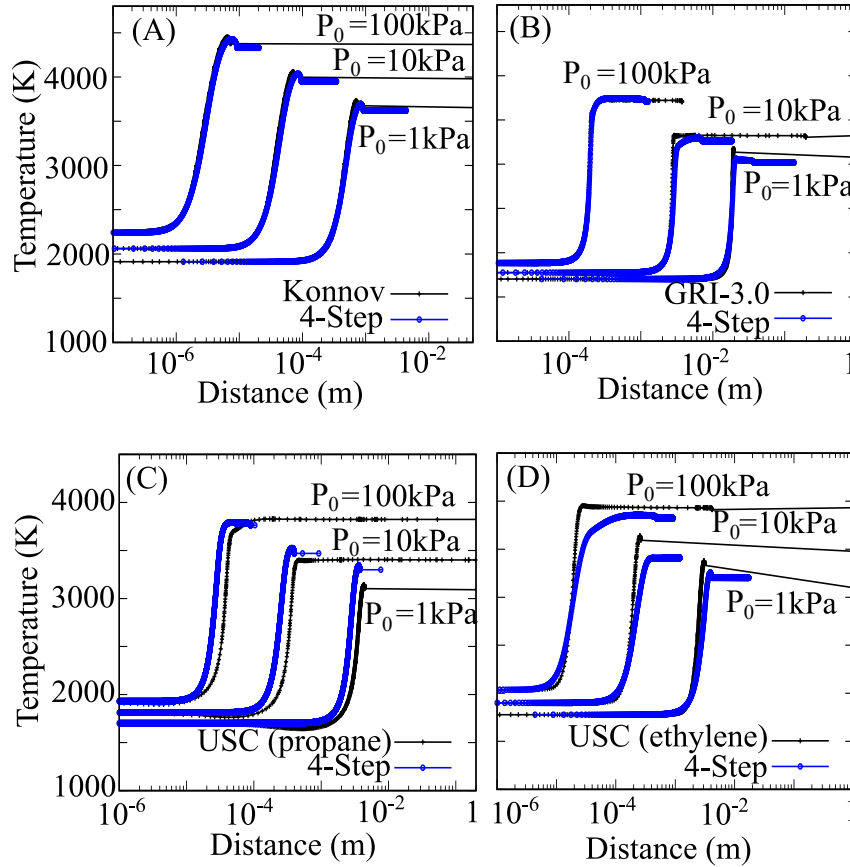


Figure 4.3: Temperature profiles for ZND detonation using the four-step model (points) and detailed chemistry mechanisms (lines) for stoichiometric (A) acetylene–oxygen, (B) methane–oxygen, (C) propane–oxygen, and (D) ethylene–oxygen mixtures with $T_0 = 300$ K.

variables would deviate further from the detailed chemistry. We also note that the one-step model performs poorly at minimizing heat release in the induction zone, which impacts the local ignition delay times and their gradients behind the shock. In fact, it was previously demonstrated that temperature gradients capable of allowing detonations to form calculated using detailed chemical models are much shallower compared to those predicted by simple chemical models [230]. This is likely due to the sensitivity of local ignition delay times and the coupling of shock and reaction zones to the temperature of the gas. Although a one-step combustion model with temperature-dependent heat capacities would perform better at capturing the post-shock states, as shown, and could be tuned to reproduce the ignition delays

in a wide range of temperatures and pressures, we note the incorrect product state. In this simple model, we considered only the reaction of $R0 \rightarrow P1$, governed by an Arrhenius reaction rate law in the form

$$\frac{DY_{R0}}{Dt} = A\rho^m T^n [R0]^s \exp\left(\frac{-(E_a/R)}{T}\right). \quad (4.1)$$

Here, $A = 2 \times 10^{12}$, $m = 0.2$, $n = -0.6$, and $(E_a/R) = 20,562$ K was used. In this model, equilibrium with products forming species P2 was not considered, yet the formation of such incomplete combustion products is known to be heavily dependent on the state variables and highly influential on the final enthalpy obtained [253]. This shortcoming would likely lead to incorrect detonation velocities since the enthalpy change (or heat release) thus differs significantly from the detailed chemistry. On the other hand, the four-step model is a minimal global combustion model with equilibrium effects that can reproduce the detailed detonation structure, with the exception of minor departures in the reaction zone stiffness, as shown in the figure.

4.1.2 Dilution by Inert Species

The influence of an inert diluent, such as argon or nitrogen, on premixed hydrocarbon detonations has been a long-standing problem. It was observed that the dilution of a stoichiometric acetylene-oxygen mixture by argon is capable of altering the detonation stability and structure of the mixture [183]. Past studies have concluded that this is due to a smaller amount of energy evolution per mole of the gas, with the reaction time (t_e) increasing with respect to the induction time (t_i) with increasing levels of dilution. It is then of some value to verify the performance of the four-step model for a dilute premixed reactive gas mixture without altering the four-step model parameters determined for undiluted cases. Assuming that there are no gradients in the amount of inert diluent, the presence of the inert diluent in the model equations Eq. (3.14) is accounted for simply by including the mass frac-

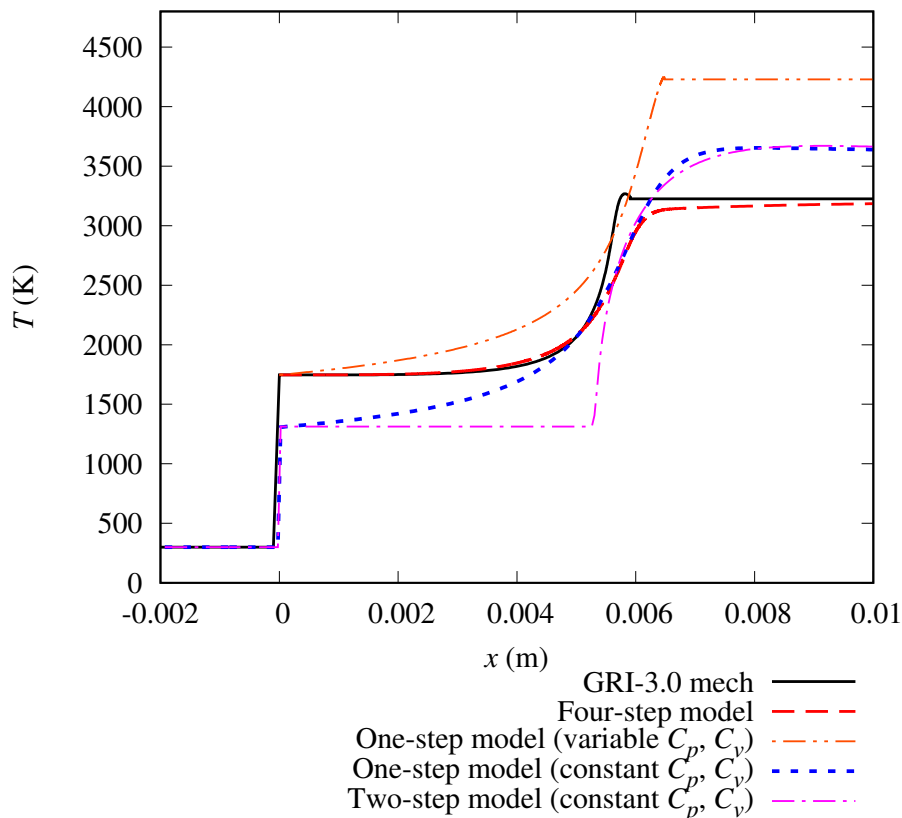


Figure 4.4: Temperature profiles behind a Mach 6.35 (2262.6 m/s) shock in stoichiometric methane–oxygen at $T_0 = 300$ K and $p_0 = 5.5$ kPa computed using conventional one- and two-step perfect gas models [98], a one-step model with temperature-dependent heat capacities, the four-step model [173], and the detailed GRI-3.0 mechanism [208].

tion contribution as a constant global variable. There is no need for an additional transport equation since the mass fraction of inert species in the mixture remains unchanged through the reaction. To investigate the performance of the four-step model on the addition of an inert diluent, we consider two different dilute gas mixtures: 40% by volume dilution of the methane-oxygen mixture with nitrogen, and 50% by volume dilution of the acetylene-oxygen mixture with argon.

The results for the two dilute mixtures are presented in Fig. 4.5, noting that noticeably longer ignition time scales result from mixture dilution when compared to undiluted cases. In fact, we note that the four-step model captures very well the diluted mixture ignition delays and final equilibrium temperature when compared to

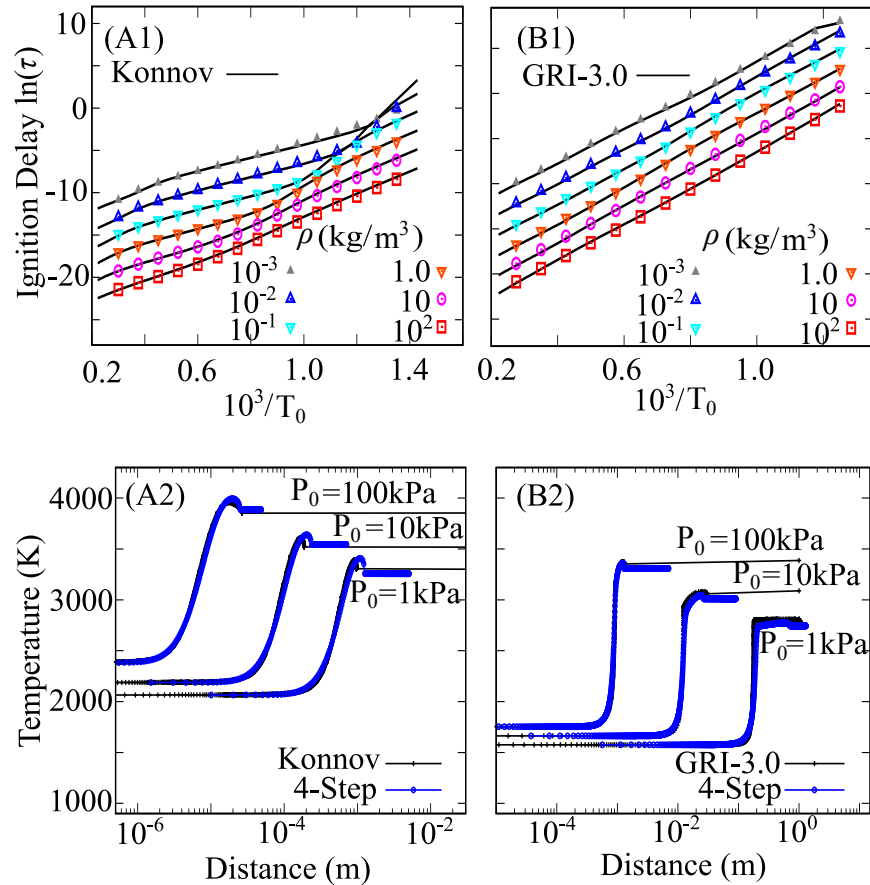


Figure 4.5: Constant volume ignition time predictions and ZND detonation temperature profiles with $T_0 = 300$ K using the four-step model (points) and detailed chemistry mechanisms (lines) for (A) dilute stoichiometric acetylene-oxygen [$2\text{C}_2\text{H}_2 + 5\text{O}_2 + 7\text{Ar}$] and (B) dilute stoichiometric methane-oxygen [$\text{CH}_4 + 2\text{O}_2 + 2\text{N}_2$] mixtures.

the detailed chemistry simulations, without the need to re-determine the combustion model parameters for the diluted cases. From the ZND profiles, we also note that the four-step model is able to capture the correct temperature profiles to a high level of accuracy for the situations shown. The time scales and thermal states are also captured for each case.

4.1.3 Fuel Lean Mixtures

Several past studies have highlighted the influence of varying equivalence ratios (ϕ) on the flame propagation and detonation dynamics of a combustible fuel/oxygen

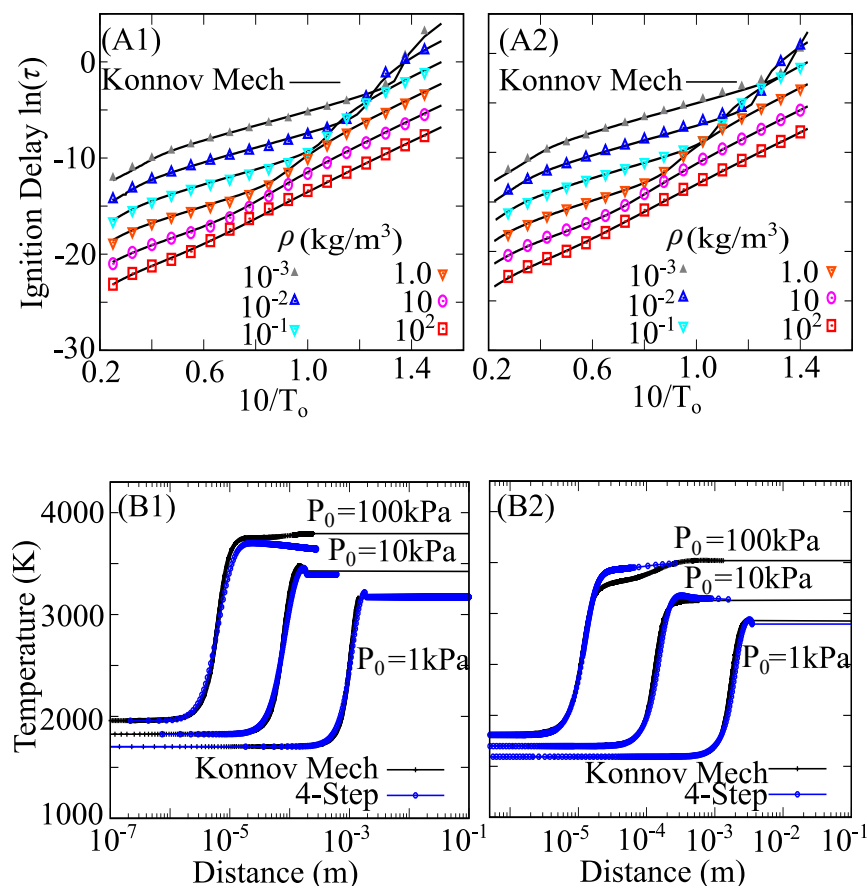


Figure 4.6: Constant volume ignition time predictions and ZND detonation temperature profiles with $T_0 = 300$ K using the four-step model (points) and detailed Konnov mechanism [34] (lines) for two lean acetylene–oxygen mixtures (A) $\phi = 0.5$ and (B) $\phi = 0.33$.

mixture. For flames, it was observed that the flame thickness and maximum flame speed are directly influenced by the equivalence ratio [35, 79], while the stable detonation velocity was found to increase as the equivalence ratio increases [67]. The variation in equivalence ratio is particularly important when studying deflagration to detonation transition (DDT) due to flame acceleration. Dorofeev et al. [41] concluded that any change in the mixture composition below stoichiometry results in a significant increase of run-up distance before the transition to detonation occurs for flame acceleration in a channel with obstacles. Similarly, an equivalence ratio of about 2.0 was found to result in the shortest run-up distance and time to DDT from experimental results for ethylene/oxygen mixtures [67]. It is then crucial to verify

the performance of the four-step model for equivalence ratios not equal to 1.0. We first note that limitations exist for applying the four-step model to fuel-rich mixtures [253], which we will discuss in detail in Section 4.4. Thus, we only consider three different fuel lean acetylene mixtures with equivalence ratios of 0.71, 0.5, and 0.33.

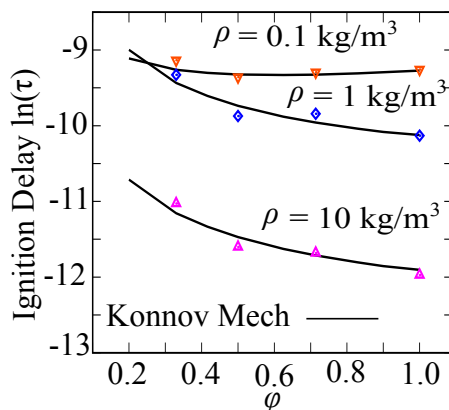


Figure 4.7: Constant volume ignition delay (τ) for acetylene–oxygen mixtures as a function of equivalence ratio (ϕ) using the four-step model (points) and the detailed Konnov mechanism [34] (lines).

The four-step model global species for fuel lean hydrocarbon mixtures ($\phi < 1.0$), are derived using Eq. (3.12), where the leftover oxygen in the mixture is accounted for in the product species P1 and P2. Since the four-step model parameters are derived by substituting the global species into detailed chemistry results for a constant volume ignition, there is a need to derive an entirely new parameter set for each unique equivalence ratio since the composition of product species P1 and P2 vary from the stoichiometric mixture. It is then not possible to include the excess oxygen in the mixture as a global variable that remains unchanged, similar to the approach adopted for the dilute mixtures in the study. The results for two lean mixtures are shown in Fig. 4.6, while the complete parameter set for the mixtures is available in the Appendix. From the figures, it can be observed that the four-step model is capable of predicting the detailed mechanism temporal evolution reasonably well, with the ignition time, thermodynamic state during the exothermic reaction, and stiffness predicted to a high level of accuracy. Apart from some mi-

nor deviations observed in the final mixture equilibrium temperature profile for the ZND results, the model is observed to provide an accurate prediction of the reaction zone structure behind the leading shock wave. Finally, Fig. 4.7 shows a comparison of the ignition delay (τ) predicted by the four-step model and detailed chemistry as a function of ϕ , for different initial densities, with an initial temperature of 1000 K.

4.2 Important Combustion Properties

This section aims to determine how well the four-step model captures fundamental properties of the reactive mixture that are relevant for modelling flame acceleration, DDT, and also detonation wave propagation, and reaction zone structures [215]. Here we compare the explosion limits, activation energies (E_a), heat release (Q), ignition time to reaction time ratios (t_i/t_e), Zel'dovich numbers (β), expansion ratios (σ), and detonation stability parameters (χ) to detailed chemistry results using Cantera. From this, we aim to determine the applicability of the four-step model to investigate compressible and reactive flows.

4.2.1 Explosion Limits

The explosion limits of fuel/oxidizer mixtures that separate the explosive and non-explosive regions for constant volume ignition are particularly important for demonstrating the essential role of chain branching during the ignition process. Perhaps the most well-known example of chain branching mechanisms in combustion is the “Z-shaped” non-monotonic explosion limits for hydrogen combustion, typically characterized in the pressure–temperature parameter space [234]. While small carbon chain hydrocarbon fuels, such as methane, typically demonstrate a relatively monotonic explosion curve [223], non-monotonic influences are more prominent for longer carbon chain hydrocarbons. For example, previous experiments have shown propane to demonstrate an “S-shaped” explosion curve [155]. Since the explosion curve measures the sensitivity of a reactive mixture to undergo a sponta-

K to 2500 K. Apart from deviations observed in the low pressure region, i.e., below 100 Pa, the four-step model reproduces the explosion curves for the different mixtures reasonably well on comparison with the detailed chemistry. The errors observed for low pressure ignition (less than 100 Pa) can, in part, be attributed to the methodology for deriving the four-step model parameters, where calibration was only performed for initial temperatures greater than 1000 K at low pressures [253]. This would explain why these deviations are not significant for the reactive methane mixture where the low pressure explosion limits occur at higher temperatures.

Another key observation here is the absence of the non-monotonic chain-branching for propane at higher pressures (greater than 1 atm) using the USC II mechanism [232], which is observed in both experiments [155] and numerically using alternate elementary reaction mechanisms, such as the Aramco 2.0 mechanism [111]. Instead, the applied detailed mechanism for propane (USC-II [232]) exhibits a relatively monotonic behavior similar to methane, and no “S-shaped” explosion limits are visible. This highlights the need for a better description of the USC-II mechanism’s low-temperature chain branching mechanisms for propane combustion [232]. To determine whether the four-step model can replicate this behavior for propane combustion, a second set of model parameters for stoichiometric–propane oxygen combustion was calibrated to the detailed Aramco 2.0 mechanism [111]. Based on the explosion curve results in Fig. 4.8, it appears that the four-step model is not capable of accurately replicating the non-monotonic chain branching observed at pressures greater than 1 atm. One possible reason for this is the model’s lack of a chain-termination reaction. This reaction is well known to have a controlling influence on the explosion limits. For example, the limits along the “S-shape” explosion curve, where the curve deviates from the monotonic chain branching, are controlled by competitive mechanisms of chain branching and chain termination [23]. In the absence of any chain termination mechanism, explosions predicted using the four-step model always proceed to consume the entire reactant. However,

based on the results using the Aramco mechanism [111], this is not perceived to be a significant drawback since only a maximum deviation of approximately 200 K was observed in the explosion limits where non-monotonic chain branching mechanisms are the most apparent (> 1.0 atm). More importantly, based on the explosion curves for all the hydrocarbon mixtures (including the results for propane using the Aramco 2.0 mechanism), during a constant volume explosion process resulting in an increase in temperature and pressure, there exists no scenario where the reaction terminates without consuming the entire reactant as a result of the thermodynamic state progressing into the non-explosive side of the explosion curve. This is contrary to the explosion curve observed for hydrogen and is the primary reason the four-step model is unsuitable for predicting hydrogen combustion. This is discussed in detail in Section 4.4. Based on these results, the four-step model can be expected to predict the onset of localized explosions in a numerical flow field reasonably well for the mixtures under consideration by providing the appropriate temperature and pressure-dependent ignition response.

4.2.2 Global Activation Energy (E_a) And Heat Release (Q)

The influence of the activation energy (E_a) on the regularity of a detonation cellular structure has been investigated heavily in the past [7]. In general, the activation energy plays the role of a control parameter in detonation systems that determines how the system responds to small disturbances, with premixed reactive mixtures with high activation energies exhibiting unstable detonation propagation with an irregular detonation structure. Similarly, the heat release directly measures the strength of pressure wave amplifications after the reaction in detonations. Predicting the correct activation energy and heat release are therefore crucial in numerical investigations of detonation waves in order to capture the correct wave speeds and overall detonation behavior.

Figure. 4.9 shows the results for the non-dimensional activation energy evalu-

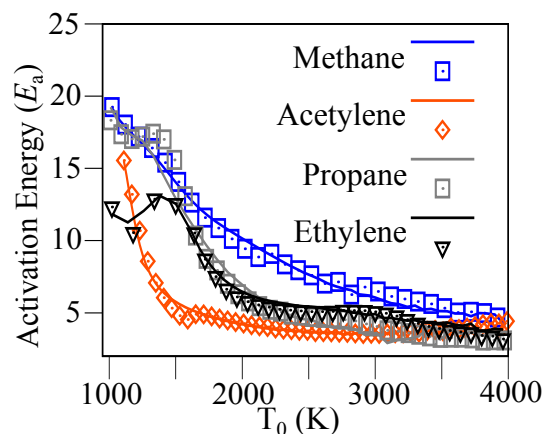


Figure 4.9: Non-dimensional activation energy (E_a) for stoichiometric hydrocarbon-oxygen mixtures, all at an initial density of $\rho = 1.0 \text{ kg/m}^3$ using the four-step model (points) and detailed chemistry mechanisms (lines).

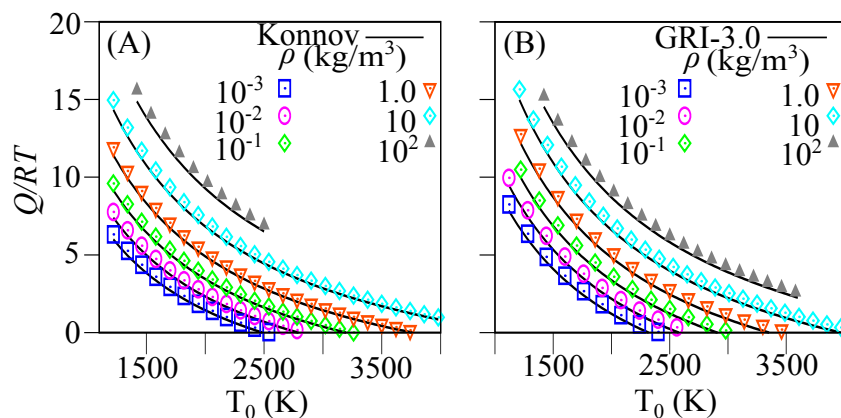


Figure 4.10: Dimensionless heat release (Q/RT) predictions for stoichiometric (A) acetylene oxygen and (B) methane oxygen mixtures using the four-step model (points) and detailed chemistry mechanisms (lines).

ated using the four-step model and Cantera for the different stoichiometric hydrocarbon mixtures, all with an initial density of $\rho = 1.0 \text{ kg/m}^3$. The non-dimensional activation energy (E_a/RT) for a constant volume ignition process is evaluated from

$$\frac{E_a}{RT_0} \approx \frac{1}{T_0} \frac{\ln(\tau_+) - \ln(\tau)}{1/T_{0+} - 1/T_0}, \quad (4.2)$$

where τ is the ignition delay time for the constant volume process with initial temperature T_0 . Similarly, τ_+ corresponds to the perturbed ignition delay time for the constant volume process at an initial temperature $T_{0+} = T_0 + \Delta T$, with $\Delta = 20 \text{ K}$.

This value for ΔT is chosen because it is small enough to account for any change in the slope of the ignition delay measurements. The four-step model here is shown to capture the non-dimensional energy very well over the entire spectrum of initial temperatures except for minor discrepancies observed in the high temperature ($T_0 > 3000$ K) results for the stoichiometric propane and ethylene reactive mixtures. Figure. 4.10 shows a comparison of the dimensionless heat release (Q/RT_0) evaluated from a constant volume ignition using Cantera and the four-step model for the acetylene and methane mixtures, where R represents the gas constant and T_0 is the initial temperature. For a constant volume process occurring at a constant density, the heat release (Q) is evaluated from the change in the internal energy between the initial reactants and final (or equilibrated) products. It can be observed that the model accurately predicts the heat release value for all the density cases considered over a wide range of initial temperatures in the post-shock range. The four-step model is a significant improvement over a simple one-step model, where the activation energy (E_a) and heat release (Q) must be prescribed as model parameters and tuned to recover the correct post-shock ignition delay and detonation induction length. The four-step model, on the other hand, is capable of recovering these properties automatically with a high level of accuracy.

4.2.3 Chapman-Jouguet (CJ) Detonation Velocity

The Chapman-Jouguet detonation velocity is the minimum wave speed for which a steady-state solution exists to the reaction path independent jump conditions in conserved mass, momentum, and energy from reactants to equilibrium products, such that the flow is sonic in the products relative to the wave speed itself. In this case, the equilibrium state is evaluated by finding the minimum Helmholtz energy in the products. Figure. 4.11 shows the CJ detonation velocity and temperature at the CJ state, which are calculated using the four-step model and detailed chemistry mechanisms. The detailed chemistry solutions are obtained using the Shock and

Detonation Toolbox libraries [201], while the same applied minimum-wave speed algorithm [21] is used to obtain the four-step model solutions, with the added assumption that only products P1 and P2 exist in equilibrium at the CJ state. The individual mole fractions of the product species in the final mixture are then calculated using the equilibrium function and coefficients derived as part of the four-step model parameter set for a given mixture.

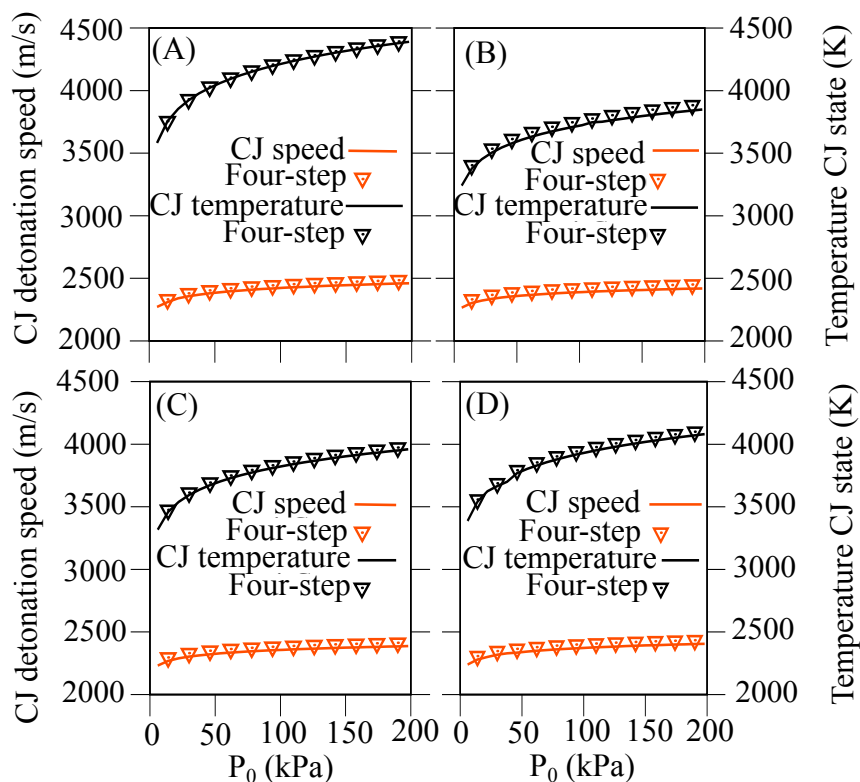


Figure 4.11: CJ detonation speed and temperature predictions using the four-step model (points) and detailed chemistry mechanisms (lines) for stoichiometric (A) acetylene–oxygen, (B) methane–oxygen, (C) propane–oxygen, and (D) ethylene–oxygen mixtures with varying initial pressures and $T_0 = 300$ K.

To further assess the four-step model performance, Fig. 4.12 shows a comparison of the CJ speeds and temperatures at the CJ state for the lean acetylene–oxygen mixtures, as well as a comparison of the CJ speeds for the four different hydrocarbon mixtures at $T_0 = 300$ K and $P_0 = 1$ atm with increasing amounts of inert dilution. A very good agreement is observed between the two sets of results for

all the hydrocarbon mixtures considered, with the four-step model recovering the correct CJ speed irrespective of the equivalence ratio (for $\phi \leq 1$) and concentration of inert diluent. The derived product species and equilibrium functions are clearly valid for predicting the equilibrium thermochemistry for the different reactive hydrocarbon mixtures investigated in this study for the stoichiometric, lean, and dilute cases.

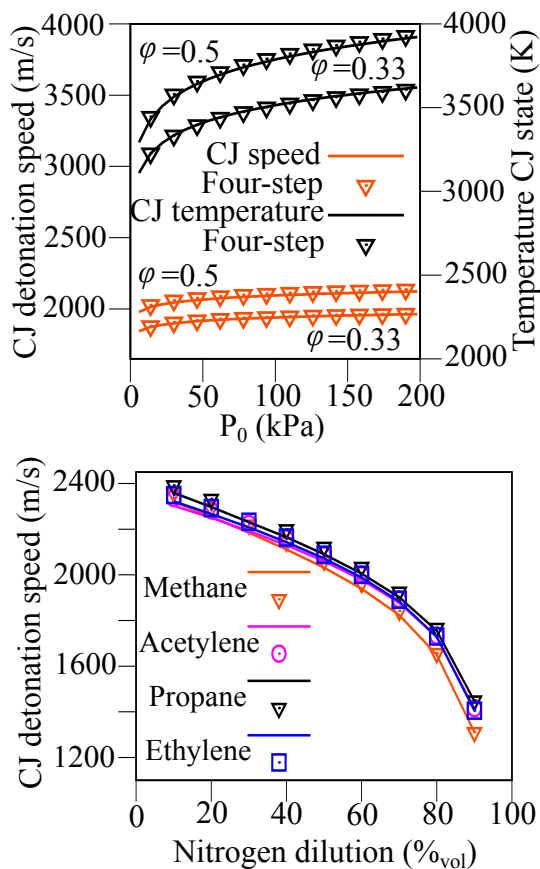


Figure 4.12: CJ detonation speed and temperature predictions using the four-step model (points) and detailed chemistry mechanisms (lines) for the lean acetylene mixtures (top) and dilute hydrocarbon mixtures (bottom).

4.2.4 Induction to Reaction Time Ratio (t_i/t_e)

A number of studies have shown that, in addition to activation energy and heat release, the detonation structure is also heavily influenced by the length of the induction zone (Δ_i) relative to the length of the reaction zone (Δ_e) [19]. This was first

demonstrated by Short and Sharpe [123], where the stability of a one-dimensional detonation was shown to be influenced both analytically and experimentally by the ratio Δ_i/Δ_e . It was found that a thin reaction zone compared to its induction zone, or a large value of Δ_i/Δ_e , has a destabilizing effect on the detonation structure due to enhanced pressure wave amplification. This is due to a large amount of energy deposited in the main reaction zone in a shorter duration, resulting in large local heat release rates [158]. This offers one reason why a simple one-step model with no ability to control the ignition and reaction lengths independently cannot accurately capture the ZND structure of real detonations [136]. Figure. 4.13 shows the ignition time ratio, t_i/t_e , evaluated for constant volume reactions using both the four-step model and detailed chemistry mechanisms with varying initial densities and temperatures. Here we define the induction time (t_i) as the time to the point of maximum energy release rate, while the reaction time (t_e) is evaluated at the induction time through

$$t_e = \left(\frac{d(\ln T)}{dt} \right)^{-1}. \quad (4.3)$$

Equation (4.3) effectively quantifies the exothermic pulse duration at the end of the induction period. Since t_i/t_e does not depend significantly on density, only three density cases are shown for clarity. For constant volume ignition processes over the entire spectrum of initial temperatures, the four-step model predicts the correct value of t_i/t_e for most cases and never deviates beyond the correct order of magnitude.

4.2.5 Detonation Stability and the χ Parameter

For detonation wave propagation, the non-dimensional χ -parameter, given by

$$\chi = \frac{t_i}{t_e} \left(\frac{E_a}{RT_{vn}} \right) \left(\frac{Q}{RT_{vn}} \right), \quad (4.4)$$

can be used to predict whether a reactive mixture is particularly prone to instabilities since it directly measures the propensity for disturbances to amplify from

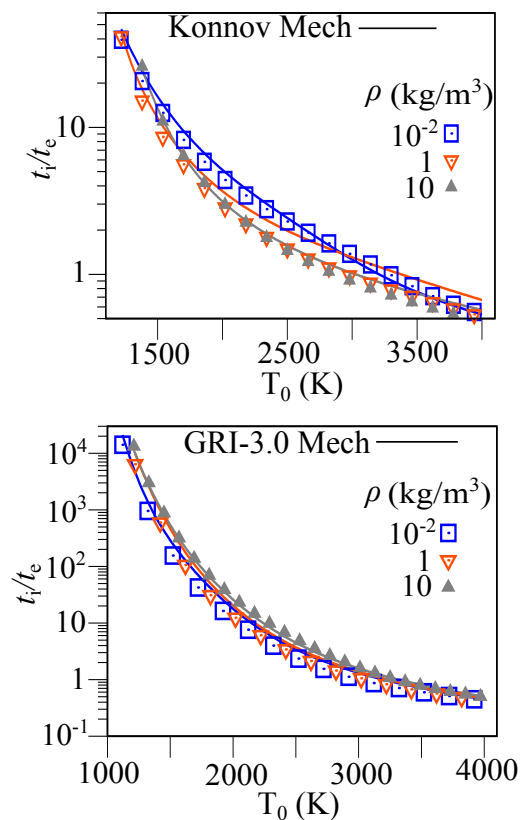


Figure 4.13: Ignition time to reaction time ratio (t_i/t_e) predictions using the four-step model (points) and detailed chemistry mechanisms (lines) for stoichiometric acetylene–oxygen (top) and methane–oxygen mixtures (bottom).

hot spot ignition. χ is simply the product of the ratios of characteristic induction and reaction times (t_i/t_e), the non-dimensional activation energy (E_a/RT_{vn}), and non-dimensional heat released during the reaction (Q/RT_{vn}) of the post-shocked reactive mixture. The precise role of the χ parameter has been investigated in past studies [19, 20, 178, 215], with a critical $\chi \approx 50 - 100$ correlating well with the onset of cellular instabilities. It was also found that mixtures with high χ values will develop highly unstable detonations due to the rapid amplification of gas dynamic disturbances in the reaction zone. More recently, for detonation propagation into reactive layers bounded by an inert gas [214], it was suggested that the χ parameter is important for determining the critical height of the reactive layer, after which detonation propagation is no longer possible. In this investigation, simula-

tions with detailed chemistry mechanisms were observed to have much larger χ parameter values than simulations with simpler combustion models. Consequently, the detonation wave simulated using detailed chemistry developed larger cellular instabilities for smaller reactive layer widths and was quenched at a much smaller critical height.

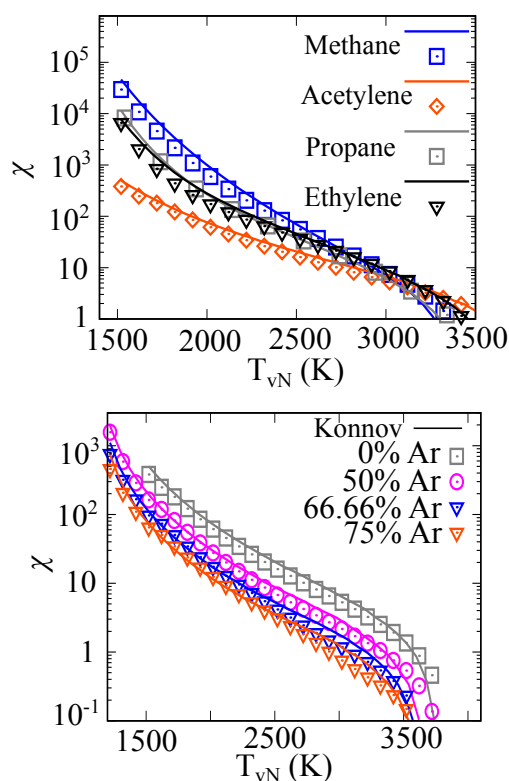


Figure 4.14: Dimensionless χ parameter predictions using the four-step model (points) and detailed chemistry mechanisms (lines) for the four different hydrocarbon mixtures (top) and dilute acetylene-oxygen mixtures (bottom).

Following the procedure outlined by Borzou et al. [20], the χ parameter values were evaluated from constant volume ignition problems for a wide range of initial post-shock (von Neumann) temperatures using both detailed chemistry and the four-step model. In Fig. 4.14, the χ values are shown first for the different stoichiometric mixtures and then for the acetylene oxygen mixtures for different levels of argon dilution, all for $\rho = 1.0 \text{ kg/m}^3$. As observed, the four-step model provides a reasonably accurate prediction of the χ value calculated using Cantera

over the entire range of post-shock temperatures. Additionally, the results for the stoichiometric mixtures are also in line with past experimental studies [178, 179], with the stoichiometric methane mixture exhibiting the most unstable, or irregular, cellular structure (the largest χ value) and the most stable detonation cellular structure is observed for acetylene. The addition of an inert diluent like argon has been shown to affect the stability and detonation structure due to an increase in the reaction length (Δ_e), with mixtures diluted by argon exhibiting more stable, or regular, cellular structures when compared to undiluted mixtures [7]. This behavior of the χ parameter decreasing with increasing amounts of a diluent is clearly visible in Fig. 4.14b. Based on these results, we expect that the four-step model is well-suited for simulating the multidimensional detonation propagation behavior and cellular structure, including local quenching and re-initiation behavior during propagation.

4.2.6 Expansion Ratio (σ) and the Zel'dovich Number (β)

Finally, since flame propagation is an important component feature of detonation waves, i.e., through its initiation via DDT, or even the burn up of unburned pockets in a detonations wake during propagation [137], it is also important to analyze corresponding key features associated with the chemical mechanism. Flames are often characterized using the laminar flame speed and thickness. In the limit of large activation energy, the problem of laminar flame propagation reduces to an eigenvalue problem with one solution for the laminar flame speed S_L [249]. As outlined by Zel'dovich et al. [247], the laminar flame speed is found to depend on three dimensionless parameters, the expansion ratio (σ), Zeldovich number (β), and Lewis number (Le) [31]. The expansion ratio is the ratio of unburned reactant density to the density of the burned products for a constant pressure process, i.e., $\sigma = \rho_u/\rho_b$, while the Lewis number is the ratio of thermal diffusivity to the mass diffusivity.

Finally, the Zel'dovich number is calculated from

$$\beta = \frac{E_a(T_b - T_u)}{RT_b^2}, \quad (4.5)$$

where T_u and T_b are the temperatures of the unburned reactants and burnt products, respectively, for a constant pressure ignition process, while E_a is evaluated at T_b , and R the mixture gas constant.

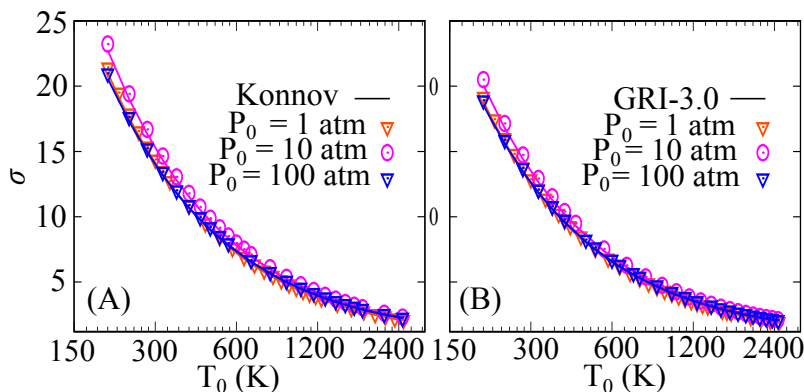


Figure 4.15: Expansion ratio (σ) predictions using the four-step model (points) and detailed chemistry mechanisms (lines) for the stoichiometric (A) acetylene–oxygen and (B) methane–oxygen mixtures for varying initial pressures.

Past research has highlighted the influence these dimensionless parameters have on the response of a combustion process to flow disturbances, particularly on the flame acceleration process and transition to detonation [43, 170, 196]. Since the expansion ratio (σ) physically represents how much a fluid particle will expand when it combusts, a more significant expansion ratio results in a stronger flame acceleration. Furthermore, Dorofeev et al. [43] noted that a large expansion ratio is a crucial parameter for the onset of significant flame acceleration in experiments with repeated obstacles inside a tube. Similarly, the Zel'dovich number (β) indicates the flame sensitivity to thermodynamic perturbations, with larger values corresponding to a greater reaction time variation for a given change in temperature. For flame acceleration of hydrocarbon mixtures in smooth channels and channels with obstructions [31], it has been observed that the critical expansion ratio (σ_c) that separates a slow flame from choked flames and detonations increases with an increase in

β . Lastly, Le is indicative of the characteristic heat transfer in a mixture relative to the diffusion of the rate-limiting species, with a smaller Lewis number favorable for flame propagation. It is then essential that the four-step model predict these parameters accurately to correctly calculate the flow kinetics and thermodynamics when investigating DDT in channels, flame acceleration processes, and transition to detonation after shock-flame interactions. To couple the four-step model equations to a Navier-Stokes framework CFD solver, the diffusion coefficients, and consequently Le , need to be carefully calibrated to capture the correct laminar burning velocity (S_L). However, this is beyond the scope of the current study, which focuses on accurately capturing the developing chemical details. We will then focus on evaluating the four-step model performance at recovering the expansion ratios and Zel'dovich numbers acquired directly from the combustion process when compared to the results from detailed chemistry mechanisms.

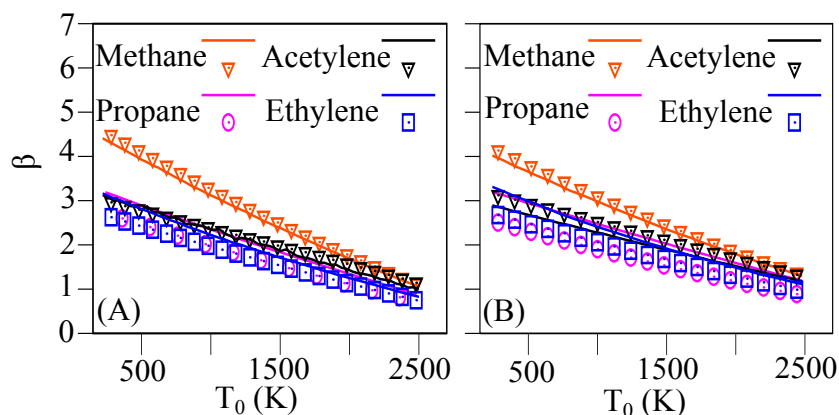


Figure 4.16: Zel'dovich number (β) predictions using the four-step model (points) and detailed chemistry mechanisms (lines) for the four different stoichiometric hydrocarbon mixtures with (A) $P_0 = 1$ atm and (B) $P_0 = 10$ atm.

Figures. 4.15 and 4.16 summarize the results for the expansion ratios and Zel'dovich numbers. To calculate σ , ρ_b is evaluated by equilibrating the reactive mixture at constant pressure and enthalpy, while the global activation energy for β was calculated using Eq. (4.2) from a constant volume process, with T_0 equal to the final temperature of the constant pressure ignition, T_b . This is consistent with previous

documented work of Bane et al. [9]. It was observed that for a given initial pressure, the values of σ overlapped closely for the different hydrocarbon mixtures over the entire range of initial temperatures. For the sake of clarity, the results in Fig. 4.15 show a comparison of the expansion ratio predicted by the four-step model for three different initial pressures for the stoichiometric acetylene and methane mixtures, with the model capturing the correct density values during the complete ignition process over the entire spectrum of initial temperatures for all constant pressure ignition processes. Similarly, the Zel'dovich numbers for initial pressures equal to 1 and 10 atm are shown in Fig. 4.16. Comparing the two sets of results, β is captured reasonably well over the entire range of initial temperatures for the four different stoichiometric hydrocarbon mixtures. Finally, since the four-step model has been shown in Section 4.1 to accurately predict the overall reaction stiffness (i.e., the temperature evolution), there should be no need to tune the diffusion coefficients. This addresses a significant limitation of the one-step model where there is a need to calibrate the diffusion coefficients to recover the correct laminar flame speed due to inaccurate temperature and species gradients modeling. The diffusion coefficients for the four-step model can likely be acquired directly from Cantera [60] using the appropriate chemistry mechanism and transport model. In this regard, the four-step model should also reproduce well the Lewis numbers at varying conditions. Based on this and the results above, the model can be expected to predict the laminar flame speed well compared to detailed chemistry, which is crucial for deflagration to detonation transition investigations.

4.3 Error Analysis

In order to fully evaluate the performance of the four-step model, a quantitative error analysis is carried out for the results presented. The agreement between the four-step model and detailed chemistry is investigated using an error function recently applied by Hu et al. [70], an improved error evaluation method over previously

applied methods [161]. The error function in the current study can be summarized as:

$$\left\{ \begin{array}{l} E_i = \frac{1}{N_i} \sum_{j=1}^{N_i} \left(\frac{Y_{ij}^{\text{model}} - Y_{ij}^{\text{ERM}}}{\overline{Y_{ij}^{\text{ERM}}}} \right) \\ E = \frac{1}{N} \sum_{i=1}^N E_i \\ \text{where:} \\ Y_{ij} = y_{ij} \end{array} \right. \quad (4.6)$$

Here E is the error value for N number of data sets analyzed, while E_i corresponds to the error value of the i th data set with N_i data points. Y_{ij}^{model} and Y_{ij}^{ERM} represent the results of interest for the four-step model and detailed chemistry, respectively, for the j th data point in the i th data set, while $\overline{Y_{ij}^{\text{ERM}}}$ is the average measurement of the i th data set. Normalizing the error with the number of data points (N_i) prevents bias towards data sets with a large number of points, and considering the average is necessary to prevent bias toward measured data points where the error is the largest. The model is considered to be correctly predicting the datum (i.e., the detailed chemistry result) when E has a value between 0 and 1 [4, 70].

Figure 4.17 summarizes the error function measurements for the four stoichiometric hydrocarbon mixtures under investigation for the different parameters that are compared throughout this chapter. The data sets selected for the error calculation of each measured parameter cover the entire spectrum of initial temperatures, densities, and pressures for detonations. As observed, the error value for all measurements is below 0.35. Moreover, the largest errors are observed for parameters that include multiple components, namely the induction to reaction time ratio (t_i/t_e), detonation χ parameter, and β . The results are particularly impressive for the natural logarithm of the induction time (τ), normalized E_a , CJ speeds, and expansion ratios, with error function values less than 0.1.

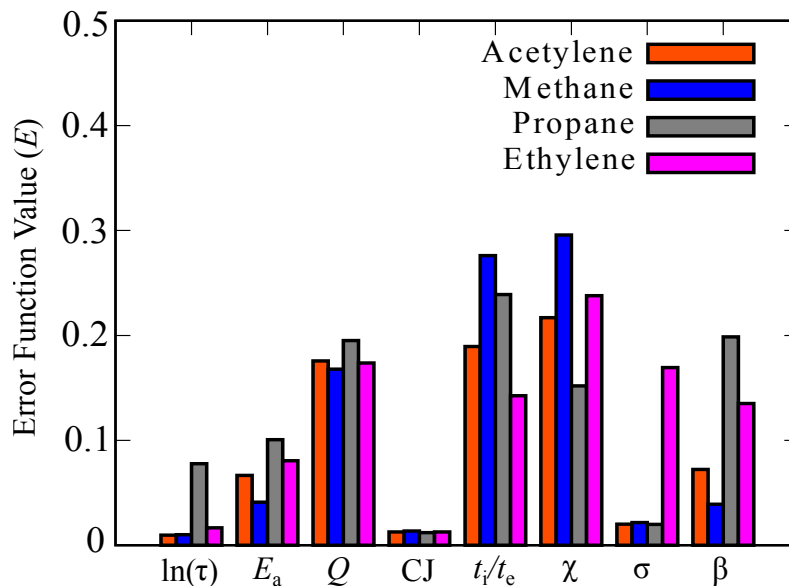


Figure 4.17: Error function (E) results for the four-step model for ignition time predictions (τ), non-dimensional activation energy (E_a), non-dimensional heat release (Q), CJ speed, induction time to reaction time ratio (t_i/t_e), detonation χ parameter, expansion ratio (σ), and Zel'dovich number (β) for the four different stoichiometric hydrocarbon mixtures under consideration.

4.4 Model Limitations

The primary limitation of the four-step model is its inability to account for situations where unreacted fuel is present in the final equilibrium mixture of a constant volume ignition process [253]. This makes the model unsuitable for investigating combustion in fuel rich hydrocarbon mixtures ($\phi > 1.0$) and also ignition processes where the chain-branching is highly non-monotonic, such as for hydrogen combustion. For example, stoichiometric hydrogen–oxygen mixtures were found to contain approximately 10-20% of hydrogen fuel by volume in cases where the combustion ends outside the explosion curve and the remaining reactant is not consumed. The current methodology requires no fuel present in the products after ignition to derive the functions that describe the concentration of the product species after ignition. The leftover fuel cannot simply be included in the product groups (P1 and P2) due to their unstable nature and their complicated dissociation and recombination pro-

cesses at elevated temperatures [253]. To account for situations where unreacted fuel is present in the equilibrium mixture would require a revision of the model to account for an additional product species (the leftover reactant) having independent equilibrium reactions with P1 and P2. This would increase the complexity and computational expense of the model. Excess oxygen, on the other hand, was found to be easier to incorporate into the product species for fuel lean mixtures. As highlighted in Section 3.2, the equilibrium rate constants (k_{ef} and k_{er}) are derived from a constant volume process under the assumption that the total amount of reactant R tends to zero after the exothermic reaction. Since the exothermic reaction rate constants (k_{r1} and k_{r2}) depend on the values of the equilibrium rate constants, the model is then incapable of characterizing the developing details during the main heat release reaction accurately for these cases. When modeling the stoichiometric hydrogen–oxygen ignition process was attempted, errors as large as 40% were observed in the final equilibrium temperature and pressure.

Finally, the four-step model assumption of a thermally neutral chain branching mechanism, and no dissociation reaction, cannot reproduce the endothermic behavior exhibited by some reactive hydrocarbon mixtures prior to ignition at higher temperatures. Since dissociation reactions are typically endothermic in nature, this temperature decrease is attributed to the formation of radicals in the induction regime that is not accounted for in the four-step model. Additional investigation is needed to properly understand the phenomenon, with the possible need to alter the chain initiation and branching equations in Eq. (3.13) to include additional radicals and thermodynamic states that could be produced in these cases. This, however, is not perceived to be a significant issue with the current methodology. The model recovers the fundamental parameters investigated in this section, even for cases exhibiting this endothermic behavior.

4.5 Conclusion

Thus far, a detailed investigation of a four-step combustion model [253] was carried out through comparison with detailed chemistry results in order to assess the validity of using the approach to model compressible and reactive flows (i.e., flame acceleration and flows involving detonations). Through the thermochemical approach of replicating the performance of a detailed chemistry mechanism, the four-step model is found to provide a very good approximation of the thermodynamic properties expected for a wide range of conditions for several reactive hydrocarbon mixtures. The independent tuning of the length and time scales in the reaction and induction zones leads to an accurate estimation of the overall reaction stiffness (i.e., temperature evolution) during the combustion process. This is particularly important for applications like modeling DDT, where the flame acceleration and transition to detonation occur over vastly different length and time scales and where the unreacted temperatures and pressures constantly change. Additionally, with the four-step model only requiring three supplementary transport equations to explain the developing chemistry details, it is a computationally inexpensive mechanism that can be efficiently coupled with CFD codes. Since the trade-off between accuracy and computational expense remains a dilemma when solving highly stiff detonation scenarios numerically, the four-step model results demonstrate a significant improvement in accuracy over other simpler idealized GRMs for reactive hydrocarbon mixtures. This advantage of requiring very little CPU overhead or memory requirements can permit higher resolutions to be attained compared to using detailed chemical models.

The four-step model is capable of reproducing important mixture properties associated with flame acceleration and detonation dynamics, namely the global activation energy, heat release, CJ velocity, induction to reaction time ratio, Zel'dovich number, χ parameter, and expansion ratio. With the model accurately recovering

these parameters and never deviating beyond the correct order of accuracy, we can expect good performance and accuracy when coupled to a Navier-Stokes solver. The four-step combustion model investigated here is well suited to investigate a variety of compressible and reactive flows in hydrocarbon mixtures. Such applicable flows would include flame acceleration and transition to detonation, detonation cellular dynamics, detonation quenching and re-initiation limits, and DDT via shock–flame interactions. Finally, it is also worth highlighting that the procedure for calibrating the four-step model is unchanged across different chemistry mechanisms and reactive mixtures. Since detailed chemistry mechanisms are continually developed to include more recent experiments, re-calibrating the model parameters to include these changes is trivial, and no loss in the model’s accuracy is anticipated.

Chapter 5

DETONATION WAVE DIFFRACTION IN STOICHIOMETRIC C₂H₄/O₂ MIXTURES

In the current Chapter, the four-step model is coupled to a CFD solver to investigate detonation diffraction in a mildly irregular hydrocarbon mixture. Specifically, the different regimes following detonation diffraction in irregular ethylene–oxygen mixtures as observed by Schultz [195] are studied using high-resolution numerical simulations. The numerical simulations are conducted using a two-dimensional axi-symmetric formulation of the reactive Euler equations. Results are first presented, summarizing the different regimes observed numerically. Particular interest is then given to investigating the critical regime and studying the mechanisms through which the transverse detonation is triggered, along with analyzing the transverse detonation propagation. The results presented in this section are also available in the manuscript by Peswani et al. [172].

5.1 Domain, initial and boundary conditions

The numerical domain in the current study is nearly identical to the experimental setup of Schultz [195], with a detonation initially propagating in an axi-symmetric tube with an internal diameter of 36 mm before undergoing a 90° expansion into a 144 mm wide channel, as shown in Fig. 5.1. An initially overdriven Zel'dovich–von Neumann–Döring (ZND) solution was imposed at $z = 0$ that was oriented to propagate to the right in the positive z -direction, while the left boundary is placed at $z = -50$ mm. In order to overcome startup errors associated with sharp discontinuities, the ZND solution was given an overdrive factor (f) of 1.2, where $f = (U_s/U_{CJ})^2$. Here, U_s is the overdriven shock speed, while U_{CJ} corresponds to the CJ-detonation speed. The right boundary condition is a zero-gradient type,

while the remaining boundaries are symmetric types. In the symmetry condition, only the normal velocity components are reversed, while slipping is permitted in the transverse direction. The tube length of 1.05 m was found to be sufficiently long to permit the detonation wave to settle to within 2% of the CJ-detonation speed by the time the wave reached the corner, for all initial pressures and resolutions considered. In order to observe the different regimes expected (sub-critical, critical, and super-critical), the initial pressure was varied anywhere from $p_0 = 10$ kPa to 20 kPa. The quiescent mixture composition is stoichiometric ethylene-oxygen ($C_2H_4 + 3O_2$), and initial temperature for all simulations was $T_0 = 300$ K.

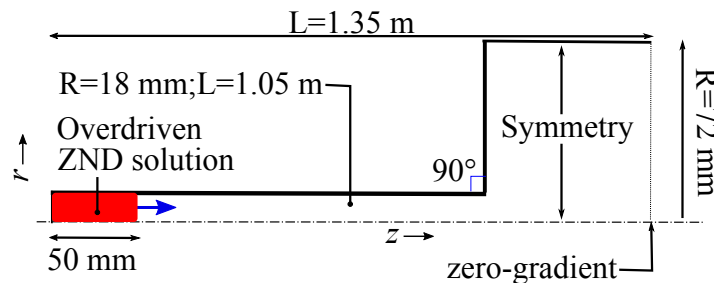


Figure 5.1: Numerical set-up, with a zero-gradient condition on the right boundary, and symmetric elsewhere.

To solve the governing equations, Eq. (3.6), the second order HLLC method [222] was applied using the van Albada slope limiter [3] using a numerical framework developed in C, that also makes use of Message Passing Interface (MPI) parallel programming for use on high-performance computing systems (HPCs). The usual operator splitting approach was applied, where the hydrodynamic evolution was solved first using a CFL (Courant–Friedrichs–Lewy) number of 0.4, followed by adding the first-order source term evaluation across the same time-step. The source terms ($\dot{\omega}_i$) from equation set Eq. (3.14) were evaluated using the implicit backward Euler method based on Newton iteration and implemented using the Sundials CVODE libraries [68]. Adaptive mesh refinement (AMR) [49] was also applied to compute detailed solutions only in regions of interest, such as the shocked and unburned gas. For this study, a computational cell was flagged as needing re-

finement if $Y_{R1} > 0.001$, or if $Y_{R0} > 0.99$ and $\rho > 1.1\rho_0$, where ρ_0 is the density of the quiescent fluid. Cells were also flagged as needing refinement when density changes of more than 10% occurred between grid levels. When a cell was flagged as ‘bad’ or needing refinement, the badness was also diffused by a few cells to ensure smooth solutions across fine-course cell boundaries. The base grid resolution for all cases was 5 mm, with anywhere between 6 to 9 additional levels of refinement applied, depending on the desired minimum grid resolution.

5.2 Results

5.2.1 Regimes observed following diffraction

This section presents an overview of the different outcomes observed by varying the initial pressure. The minimum grid resolution achieved and used in the current study was 20 μm , which was also found sufficient to capture the different regimes and flow features of interest. The effects of grid resolution were also investigated, presented later in Section 5.2.5. In general, the three main regimes, the sub-critical, critical, and super-critical, were successfully observed and were found to depend on the initial pressure of the quiescent mixture. Instead of using qualitative observations alone to classify the different regimes, Skews’ geometric reconstruction is applied here [206]. The reconstruction provides an approximation of the expansion front locus created by the abrupt expansion that propagates from the corner to the tube axis. The distance at which the disturbance reaches the tube axis (x_c) and the angle of the corner disturbance trajectory relative to the tube axis (α) for a diffracting detonation were obtained as

$$x_c = \frac{D}{2 \tan \alpha}, \quad (5.1)$$

where

$$\tan \alpha = \frac{\sqrt{c^2 - w^2}}{U_{\text{CJ}}}. \quad (5.2)$$

Here, $\sqrt{c^2 - w^2}$ is the disturbance speed propagating radially along the detonation front while D , c , w , and U_{CJ} are the tube diameter, local sound speed, post shock velocity in the shock-fixed frame, and detonation CJ speed respectively. w is evaluated using the shock-jump equations in the shock-fixed frame of reference, while the CJ speed is evaluated using the methodology described in Section 4.2.3. Despite the simplicity of Skews' model, x_c agrees reasonably well with the rapid decay of the decoupled shock and trailing reaction zone for the sub-critical regime [195, 242]. As a result, the outcome of a simulation in the current study is characterized as sub-critical if the shock and trailing reaction zone are sufficiently decoupled before x_c . On the other hand, if sufficient coupling of the shock and reaction zone exists beyond x_c before eventual quenching or re-initiation occurs, the outcome is characterized as the critical regime. The super-critical regime refers to cases where minimal shock and reaction zone separation are observed, and the detonation propagates relatively undisturbed following diffraction. In the current study, x_c is nearly constant at ~ 55 mm (± 1 mm) for the pressure range under consideration.

Based on Skews' reconstruction [206] and the qualitative observations, five total outcomes were observed numerically (the sub-critical and super-critical regimes, and three outcomes in the critical regime). Figures. 5.2 and 5.3 show example soot foil images obtained for each outcome, with the main distinctive features labeled. These numerical soot foil images were obtained by recording the maximum pressure ever experienced locally in each grid point throughout the course of the simulation. Since the pressures are highest at triple point locations, where the incident, Mach, and transverse shocks meet, this method effectively tracks the trajectories of triple points. Figure. 5.2a displays the *sub-critical regime* for $p_0 = 10$ kPa, where the detonation wave was completely quenched immediately after the area expansion, with the shock front and reaction zone sufficiently decoupled before x_c . This is evident from the disappearance of the detonation cellular pattern. In the critical regime, Fig. 5.2b displays *critical quenching* (CQ) for $p_0 = 13$ kPa where the det-

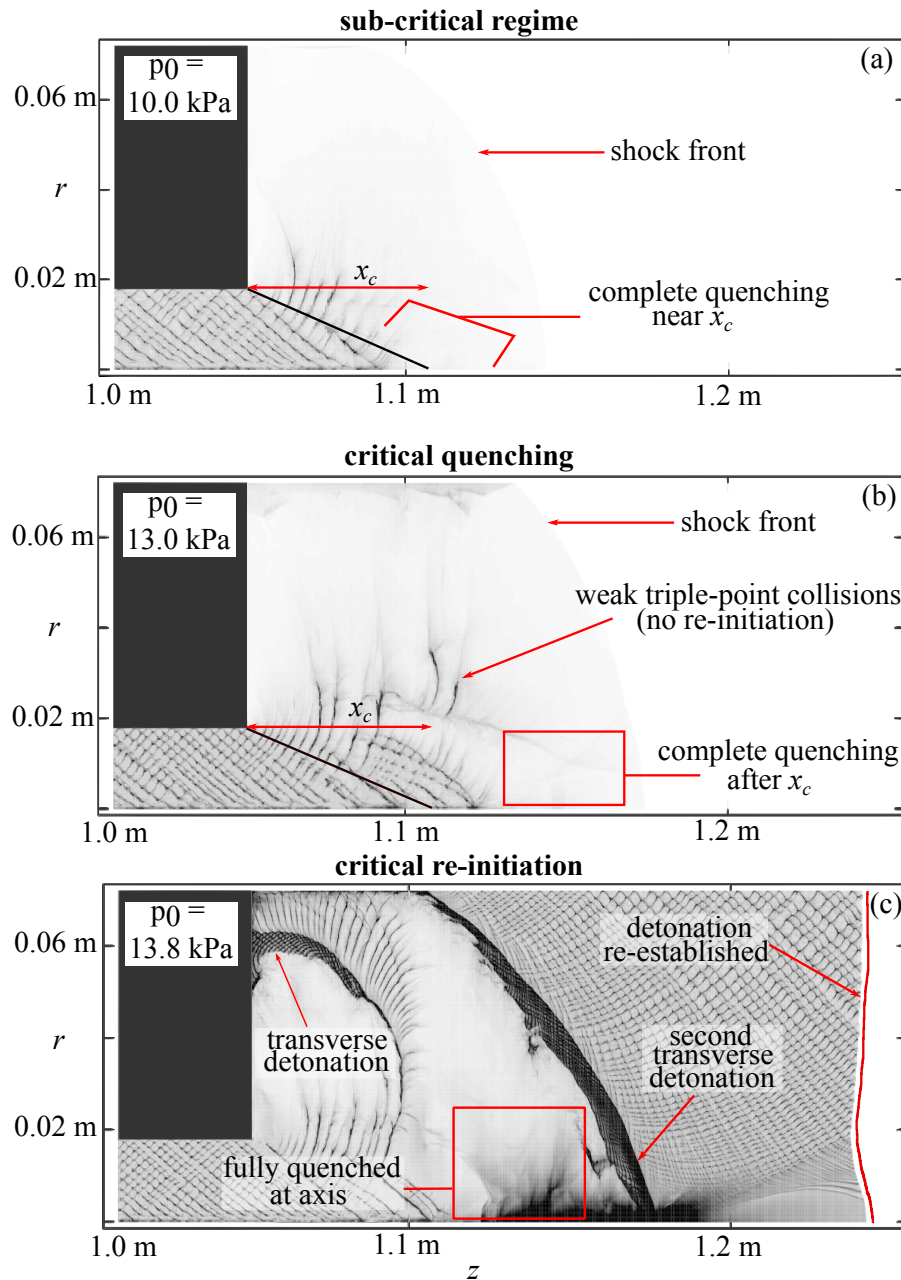


Figure 5.2: Numerical soot foils for the different regimes observed, all at $20\ \mu\text{m}$ resolution. (a) the sub-critical regime, (b) critical quenching, (c) critical re-initiation.

onation was once again completely quenched, but a degree of coupling of shock front and reaction zone persisted beyond x_c . As a result, the detonation cellular structure was sustained longer than the sub-critical regime. Next, Fig. 5.2c shows *critical detonation re-initiation* (CR) for $p_0 = 13.8$ kPa, which is an outcome of

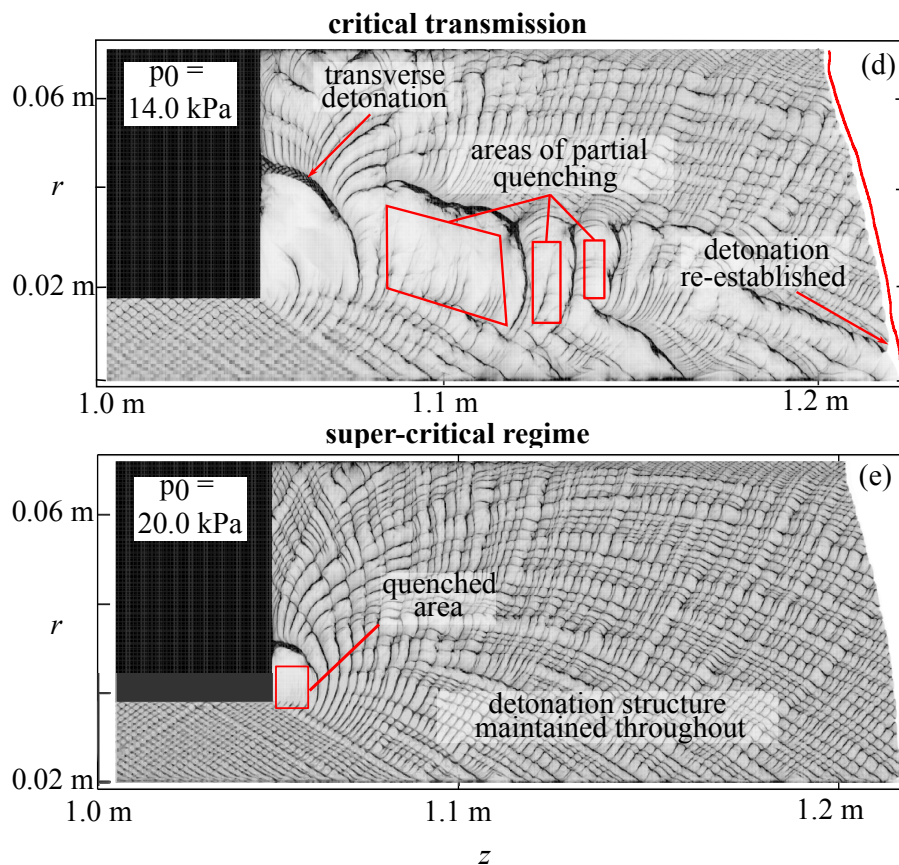


Figure 5.3: A continuation of the results shown in Fig. 5.2 showing the numerical soot foils for the (d) critical transmission and (e) super-critical regime outcomes observed.

particular interest in the current study. Like in the previous critical quenching case, the detonation was quenched near the tube axis. However, as shown in the figure, re-initiation occurred via a transverse detonation (characterized by the dark band) in the band of shocked gas mixture between the shock front and reaction zone that propagated towards the back wall. Following the reflection of the expanding wave front at the top boundary, a second transverse detonation swept across the diffracted shock front and re-initiated the detonation wave along the entire domain radius towards the center. Another outcome observed in the critical regime was *critical transmission* (CT) shown in Fig. 5.3d for $p_0 = 14.0$ kPa. Unlike the previous cases, the detonation wave was never completely quenched near the tube axis, and instead,

only partial quenching of the detonation was observed following diffraction. Partial quenching was characterized by the presence of localized areas without the cellular structure. Finally, Fig. 5.3e displays the *super-critical regime* for $p_0 = 20.0$ kPa where no significant areas of quenching were observed, and the detonation underwent diffraction with minimal separation of the shock front and reaction zone and continual cellular pattern.

Figure. 5.4 shows the speed of the leading shock wave (U_s) vs. z -position along the channel, obtained along the tube axis at $r = 0$ for each of the cases shown in Figs. 5.2 and 5.3. There are apparent differences observed between each outcome. Figure. 5.4a shows the sub-critical regime where the complete failure of the detonation wave occurred near x_c . This is clearly evident by the wave speed being substantially lower than the CJ speed at x_c , with the wave velocity continually decaying as the shock front and reaction zone decouple. The sub-critical regime outcome was observed for all simulations at low pressures with $p_0 \leq 11.5$ kPa. Failure of the detonation also occurred for critical quenching (CQ) observed at sufficiently low pressures in the range $11.75 \text{ kPa} \leq p_0 \leq 13.6 \text{ kPa}$. The key difference between the two failure outcomes (sub-critical regime and CQ) is that shock-reaction zone coupling near the tube axis was sustained beyond x_c for CQ before failure occurred. This behavior is clearly visible in Fig. 5.4b where the failure of the detonation wave was observed further along the channel indicated by the rapid decay of the wave front velocity. For both the sub-critical regime and CQ outcome, the final velocity dropped to $\sim 0.25 - 0.35U_{CJ}$ which is consistent with experimental observations [242]. Critical re-initiation (CR) was observed for $13.75 \text{ kPa} \leq p_0 \leq 13.9 \text{ kPa}$, where the detonation completely quenched near the tube axis and was subsequently re-initiated as shown in Fig. 5.4c. Here the wave front speed steadily decayed after x_c to a quasi-steady speed of $0.49U_{CJ}$ before the re-initiation event occurred. The re-initiation was indicated by the dramatic increase in the wave speed at $z \approx 1.155$ m. Interestingly, this sub-CJ speed of approximately $0.5U_{CJ}$ prior to re-initiation

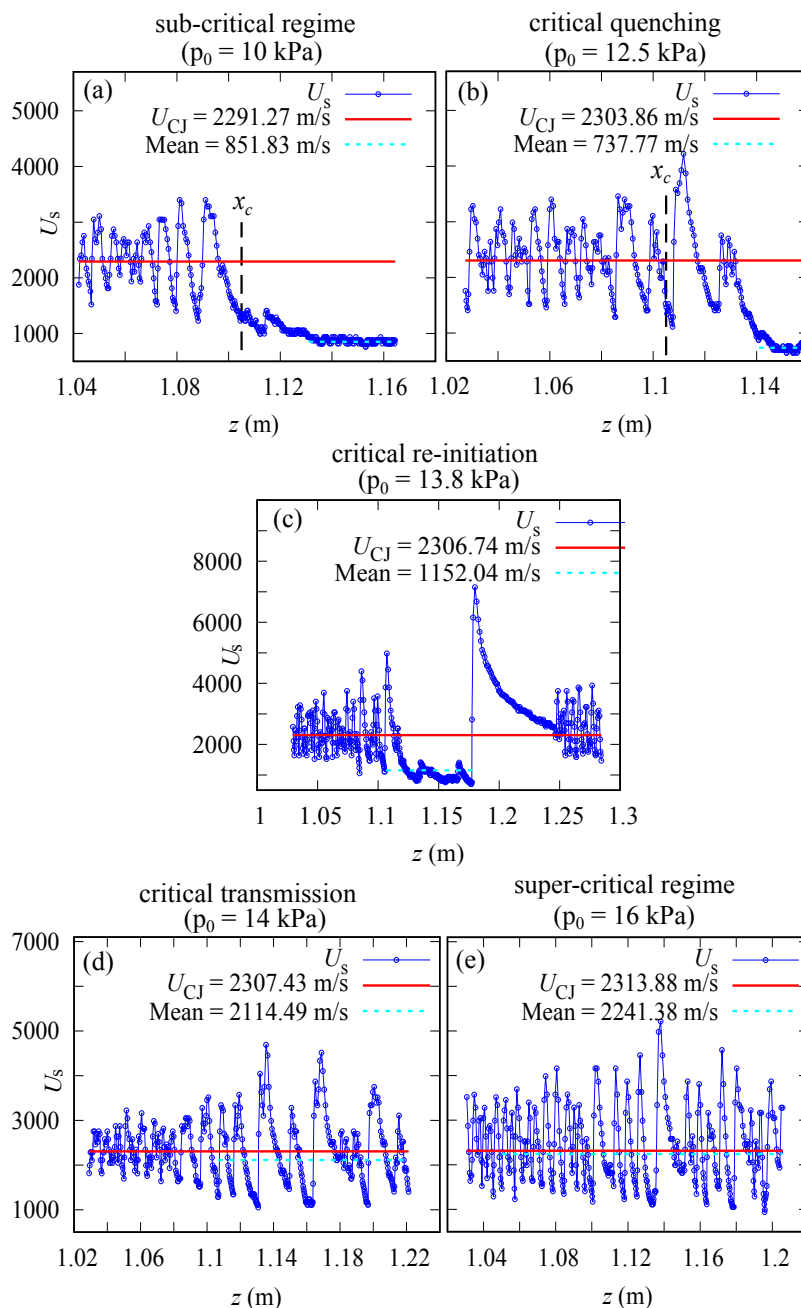


Figure 5.4: Speed of the wave front (U_s) as a function of z -distance for each outcome observed. (a) the sub-critical regime, (b) critical quenching, (c) critical re-initiation, (d) critical transmission, and (e) super-critical regime. Measurements are taken at the tube axis with $r = 0.0$ m.

agrees very well with previous detonation diffraction experiments conducted by Xu et al. [242] for stoichiometric C_2H_2/O_2 mixtures, where it was concluded that the critical wave velocity at which the detonation re-initiates following diffraction

is between 0.44 to 0.65 U_{CJ} . Similar conclusions were also drawn by Lee [101], where the wave front was found to propagate at $\sim 0.5U_{CJ}$ for critical conditions of detonation re-initiation. Following re-initiation, the detonation eventually settled and oscillated to within $\sim 0.06\%$ above the CJ speed. Finally, for critical transmission (CT) ($14 \text{ kPa} \leq p_0 \leq 15.75 \text{ kPa}$) and the super-critical regime ($16 \text{ kPa} \leq p_0 \leq 20 \text{ kPa}$), no significant quenched areas existed near the tube axis. The detonation speed was relatively undisturbed as shown in Figs. 5.4d and 5.4e. Here the speed history shows no quenching behavior and the detonation is observed to propagate at the CJ speed depending on the initial pressure chosen. Table 5.1 summarizes the results for the different initial pressures at the finest resolution of 20 μm .

The three outcomes; critical quenching, re-initiation, and transmission observed in the critical regime, are discussed in further detail. Critical outcomes were observed for simulations with initial pressures in the range $11.5 \leq p_0 \leq 15.75$, which corresponds to a tube diameter $D \sim 11.3\lambda - 19.2\lambda$. This range correlates very well with the limits for the critical regime in previous studies [149]. Moreover, in the critical regime, the first instance of successful detonation propagation via re-initiation of the diffracted detonation was observed at $p_0 = 13.75 \text{ kPa}$ with $D = 13.89\lambda$ which is also in agreement with the well known 13λ correlation [47, 91]. With manual measurements prone to significant errors, an autocorrelation procedure [197] was instead applied in the current study to measure the characteristic detonation cell size. We note here that the transition between the different regimes is observed at lower initial pressures numerically compared to the experimental results of Schultz. [195]. For instance, Schultz [195] observed detonation quenching following diffraction for $p_0 = 15 \text{ kPa}$ while in the current study, failure of the detonation was observed for simulations conducted with $p_0 \leq 13.6 \text{ kPa}$ at the 20 μm resolution. This was primarily due to the smaller cell sizes obtained numerically in the Euler simulations compared to experiments. This is partly due to the cell enlargement associated with losses and velocity deficits typically observed in

Table 5.1: Regimes observed at different initial pressures at the finest resolution of 20 μm resolution.

p_0 (kPa)	CJ Speed (m/s)	Outcome
10.0	2291.27	Sub-critical regime
10.25	2292.46	Sub-critical regime
10.5	2293.61	Sub-critical regime
10.75	2294.74	Sub-critical regime
11.0	2295.84	Sub-critical regime
11.25	2296.92	Sub-critical regime
11.5	2297.97	Critical quenching
11.75	2299.0	Critical quenching
12.0	2300.01	Critical quenching
12.25	2301.0	Critical quenching
12.5	2301.97	Critical quenching
12.75	2302.93	Critical quenching
13.0	2303.86	Critical quenching
13.25	2304.78	Critical quenching
13.5	2305.68	Critical quenching
13.6	2306.04	Critical quenching
13.75	2306.57	Critical re-initiation
13.8	2306.74	Critical re-initiation
13.9	2307.09	Critical re-initiation
14.0	2307.43	Critical transmission
14.25	2308.29	Critical transmission
14.5	2309.13	Critical transmission
15.0	2310.76	Critical transmission
15.5	2312.35	Critical transmission
16.0	2313.88	Super-critical regime
17.0	2316.81	Super-critical regime
18.0	2319.58	Super-critical regime
19.0	2322.2	Super-critical regime
20.0	2324.69	Super-critical regime

experiments [241]. For example, a 2x increase in numerical cell size for mildly irregular $\text{H}_2 - \text{N}_2\text{O} - \text{Ar}$ detonation was noted by Mevel et al. [145] when velocity deficits of 2.5% were introduced. The differences observed in the detonation cell sizes are also consistent with previous detonation diffraction studies using detailed chemistry [53, 147], with Gallier et al. [53] noting that detonation cell sizes using a detailed hydrogen mechanism were 1.5x - 4x smaller than available experimental data. In the current study, λ is approximately 1.5x - 2.5x smaller than experimentally reported values [91, 211]. Since D_c is directly influenced by λ , the transition

between different regimes can then be expected to occur at lower pressures.

5.2.2 Critical quenching (CQ)

Critical quenching (CQ), sometimes referred to as the ‘*the sub-critical outcome in the critical regime*’ [174] was observed in the experiment for $p_0 = 15$ kPa with $U/U_{CJ} = 1.0055$ (Figs. 5.5e and 5.5f). The current study observed CQ for sufficiently low initial pressures in the range $11.5 \text{ kPa} \leq p_0 \leq 13.5 \text{ kPa}$. The detailed sequence of events for a typical CQ case with $p_0 = 13.5$ kPa is shown in Fig. 5.5. The key difference between the two quenched outcomes (sub-critical regime and CQ) is that the shock–reaction zone coupling near the tube axis was sustained for a longer period of time for CQ in both the simulation and experiment. As the detonation underwent the area expansion, pockets of unreacted gas formed near the surviving detonation front. Despite the excessive curvature of the detonation, the detonation was not immediately quenched. Instead, a series of localized explosions occurred near the detonation front, which continued to sustain its propagation as shown in Fig. 5.5b. These localized explosions, discussed in more detail in Section 5.3.2, were triggered when transverse triple point collisions occurred near the pockets of unreacted gas. Moreover, as a detonation front expands, it is well known that the increased surface area leads to a weakened shock strength which lengthens the ignition delay times and increases the distance between the shock front and reaction zone [5]. This, in turn, leads to the formation of large unreacted gas pockets which when ignited temporarily overdrive the wave.

For CQ with $p_0 = 12.5$ kPa shown in Fig. 5.4.b, the wave front speed spiked to $\sim 1.77U_{CJ}$ at the location of an overdriven explosion at $z = 1.1125$ m. Based on the initial pressure chosen, the wave speeds were found to reach between $\sim 1.6 - 2.01U_{CJ}$ before failure occurred. Similar overdriven explosions were also noted in the numerical study by Shi et al. [204] for detonation diffraction near the critical limit. Based on Fig. 5.5, it also appears that these overdriven explosions

were crucial for triggering the transverse detonation observed during detonation re-initiation. For the highest initial pressures where CQ occurred ($p_0 = 13.5$ and 13.6 kPa), a re-initiation bubble was formed along the expanding detonation front away from the tube axis as shown in Fig. 5.5d. Similar re-initiation bubbles have been noted in previous studies prior to detonation re-initiation [195, 242]. For CQ, however, the explosion failed to trigger a transverse detonation, and in the absence of further triple point collisions, the detonation was progressively quenched.

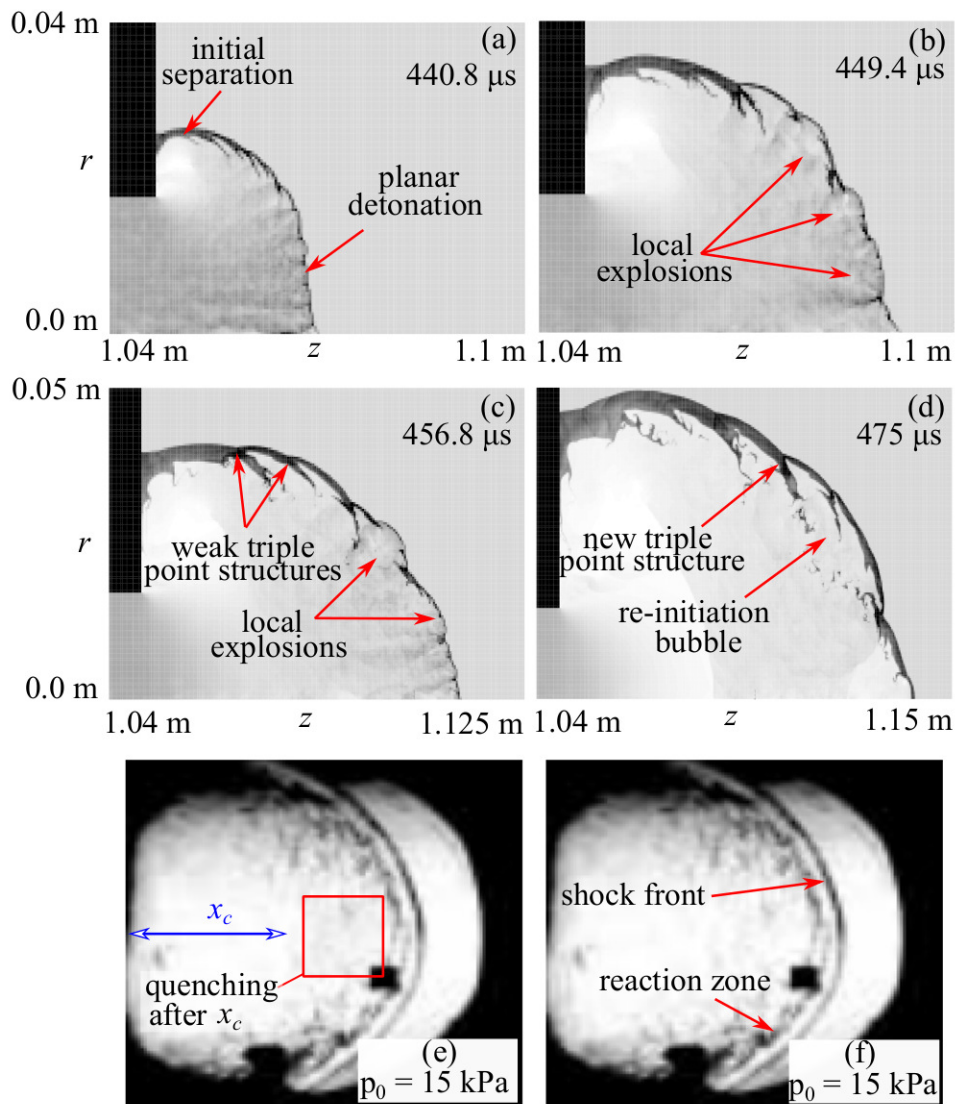


Figure 5.5: Density field evolution showing the failure of the detonation wave for critical quenching (CQ) with $p_0 = 13.5$ kPa (frames a-d). Experimental schlieren images for $p_0 = 15$ kPa with $U/U_{CJ} = 1.027$ (frames e and f) [195].

5.2.3 Critical re-initiation (CR)

Critical re-initiation was observed in the experiments [195] for $p_0 = 20$ kPa with a velocity deficit of 2% where weak coupling of the shock and reaction zone was observed near the tube axis following diffraction before re-initiation occurred as shown in Fig. 5.6e. It was later verified that the re-initiation resulted from a transverse detonation [5]. In the current study, critical detonation re-initiation was observed for $13.75 \leq p_0 \leq 13.9$ kPa. Figure. 5.6 shows a typical detonation re-initiation case for $p_0 = 13.8$ kPa. Unlike CQ, at these critical pressures, a transverse detonation wave was successfully initiated by a local explosion similar to the experiment as shown in Fig. 5.6a. The self-sustained transverse detonation was observed to propagate towards the back wall, continually consuming the shocked but unreacted gas mixture trapped behind the shock front caused due to the quenching of the detonation wave by the corner.

In the current study, we further expand on this result by investigating this transverse detonation's development. While the transverse detonation successfully re-coupled the wave front that was originally quenched by the corner, in the absence of sufficient transverse waves and hot spots triggered by triple point collisions, the detonation progressively quenched near the tube axis as shown in Fig. 5.6b. As the wave front continued to expand outwards, the detonation front established by the transverse detonation reflected off the top boundary. Following the reflection, a sustained detonation was re-initiated along the Mach shock and in the shocked mixture behind the incident shock front in the form of a new transverse detonation wave. The new transverse detonation was observed to propagate from the top boundary towards the tube axis, re-initiating the detonation in the channel as shown in Fig. 5.6d. The initiation, propagation, and characteristics of the transverse detonation waves during re-initiation are discussed in further detail in Sec. 5.3. We draw attention to this particular outcome since the critical re-initiation of the detonation wave by the transverse detonation has not been adequately captured in previous

numerical studies for irregular mixtures. We attribute this success to the adoption of the thermally perfect four-step combustion model, which was calibrated to reproduce the correct ignition delays at different temperatures and pressures when compared to the detailed USC II mechanism [232].

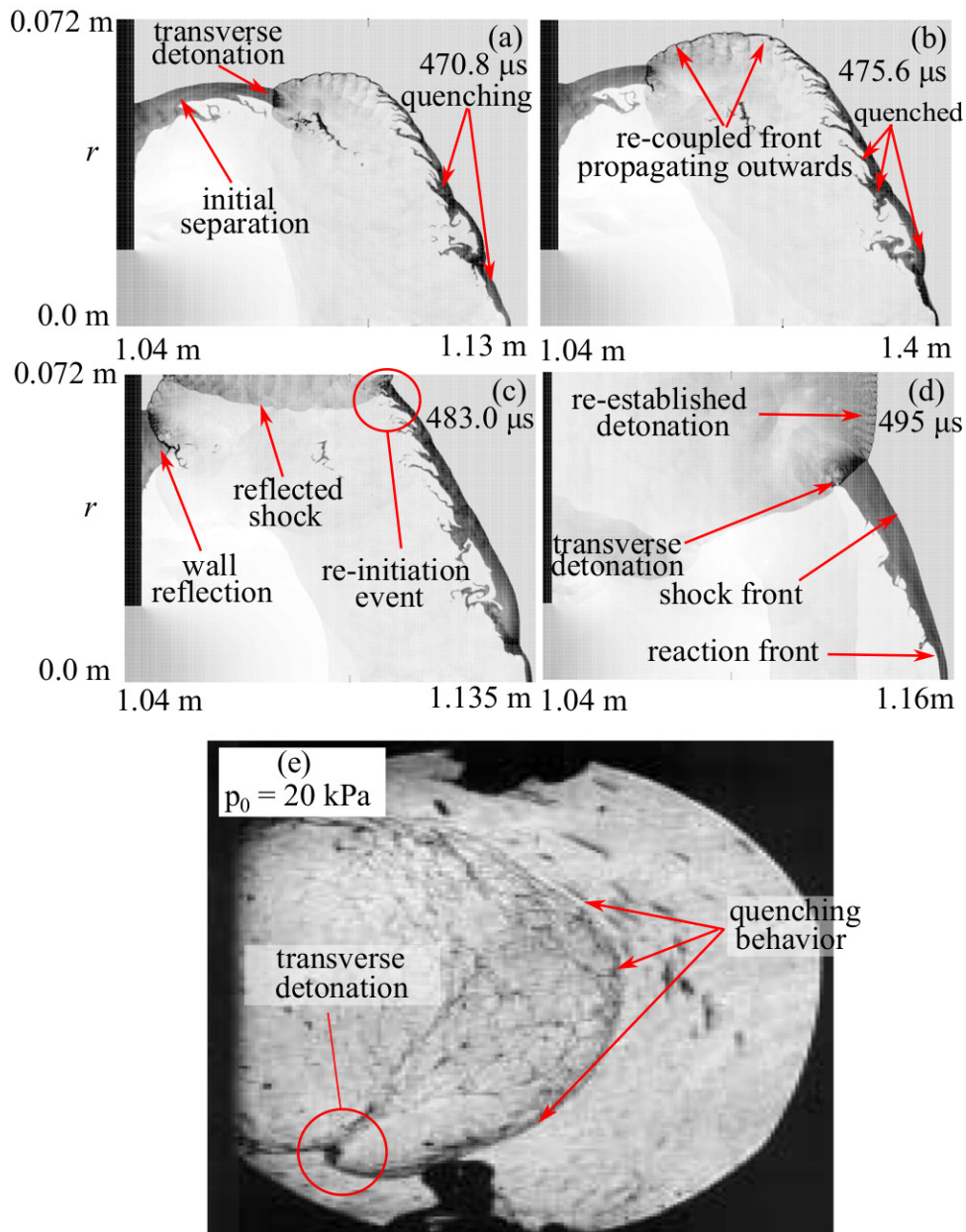


Figure 5.6: Density field evolution showing the failure and subsequent re-initiation of the detonation wave for critical re-initiation (CR) with $p_0 = 13.8$ kPa (a-d). Re-initiation observed in the experiment by Schultz for $p_0 = 20$ kPa with a velocity deficit of 2% reported prior to diffraction (e).

5.2.4 Critical transmission (CT)

Critical transmission (CT) is an outcome that has not been explicitly documented previously in detonation diffraction studies. For CT since the detonation never failed at the axis and was only partially quenched in locations along the diffracting detonation front, this can, in part be attributed to the somewhat subjective nature of quantifying the transition from the critical to super-critical regime. Another possible reason is the lack of soot foils further along the channel after the expansion. Since previous studies have typically prioritized determining the limiting conditions for detonation propagation and the shape of the detonation wave immediately following diffraction, the broader perspective was likely missed. However, based on the differences observed in the soot foils between CT (Fig. 5.3d) and the super-critical regime (Fig. 5.3e), the current outcome warrants further investigation. Therefore, the current study characterized critical transmission (CT) as a separate outcome.

In the current study, at the maximum resolution, CT was observed for all simulations with $14.0 \leq p_0 \leq 15.75$ kPa. This outcome was characterized by partial quenching where only a portion of the wave front displayed decoupling of the shock front and reaction zone. *Partial quenching* is defined here as the situation where the separation of the shock front and reaction zone never spanned across the complete curvature of the diffracting detonation and was instead limited to local segments along the wave front. As a result of this partial quenching, the wave front speed at the tube axis was found to propagate at about $0.9 - 0.94U_{CJ}$ following the area expansion. The detailed sequence for CT is shown in Fig. 5.7. Immediately visible from the figure is the significantly larger amount of reaction zone instability at the elevated initial pressures. Similar to CR, a transverse detonation was triggered at a location away from the tube axis and swept back towards the wall, but the detonation never completely failed near the tube axis. Multiple other re-initiation events and transverse detonations were observed to continually sweep across the

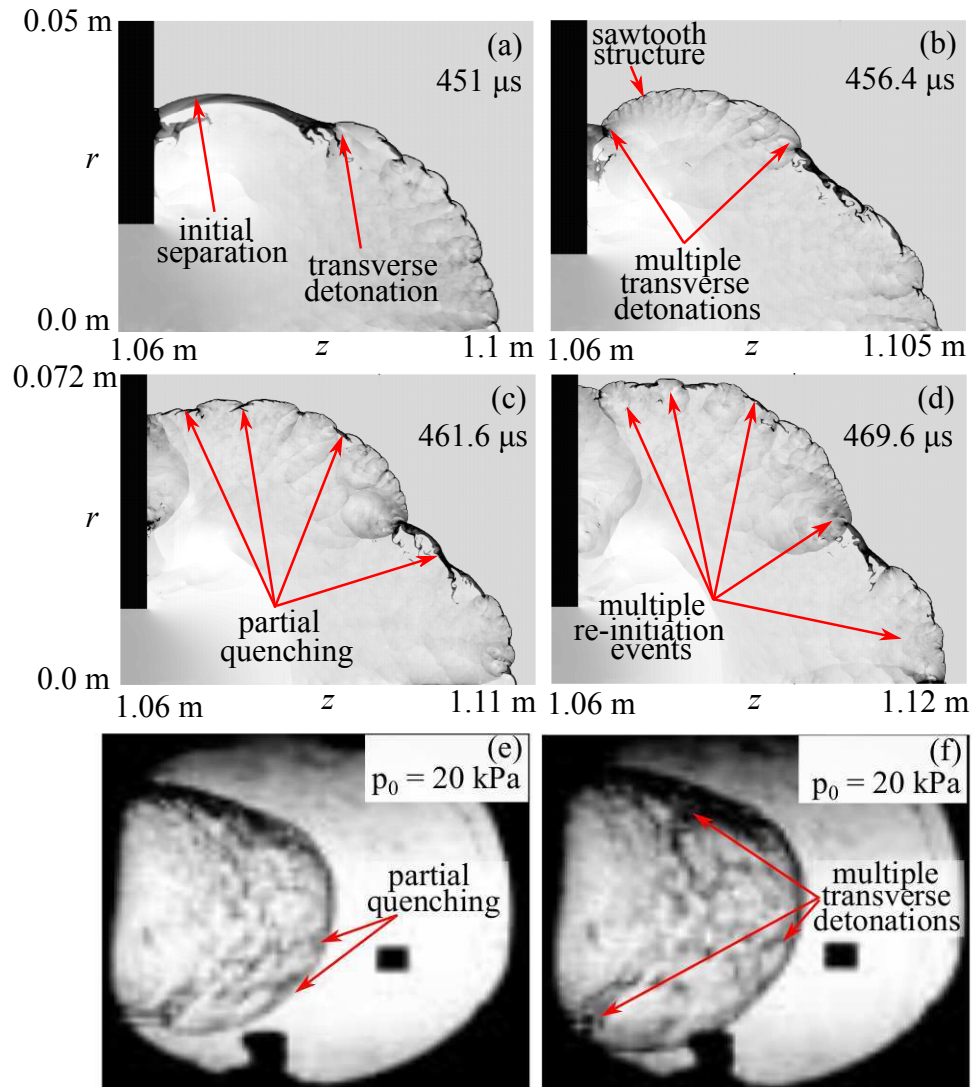


Figure 5.7: Density field evolution showing the critical transmission (CT) outcome with $p_0 = 14.5$ kPa (a-d). CT observed in the experiment by Schultz for $p_0 = 20$ kPa with an overdriven detonation (1% overdrive) reported prior to diffraction (e-f).

diffraction front, re-coupling the shock and reaction zone in the regions of partial quenching. In many cases, these additional transverse detonations collided with each other, as visible in the numerical soot foil for CT shown in Fig. 5.3d. The partial quenching and re-initiation by multiple transverse detonations was observed in the experiment for detonation diffraction of an overdriven detonation (1% overdrive) with $p_0 = 20$ kPa as shown in Figure. 5.7 (frames e and f).

5.2.5 Effects of grid resolution

In order to fully interpret the results obtained in this study, it was necessary to perform a grid resolution study in order to understand the influence of changes in the grid resolution. This was especially important since Euler simulations involving detonations are well known to give different solutions with changes in resolution [181, 198]. In Euler simulations, deflagrative burning at the interface of the burned and unburned gas can only occur through numerical diffusion. Since a finer resolution results in decreased numerical diffusion [184], the laminar burning rates also decrease. At the same time, turbulent motions are damped at coarser resolutions due to increased numerical diffusion.

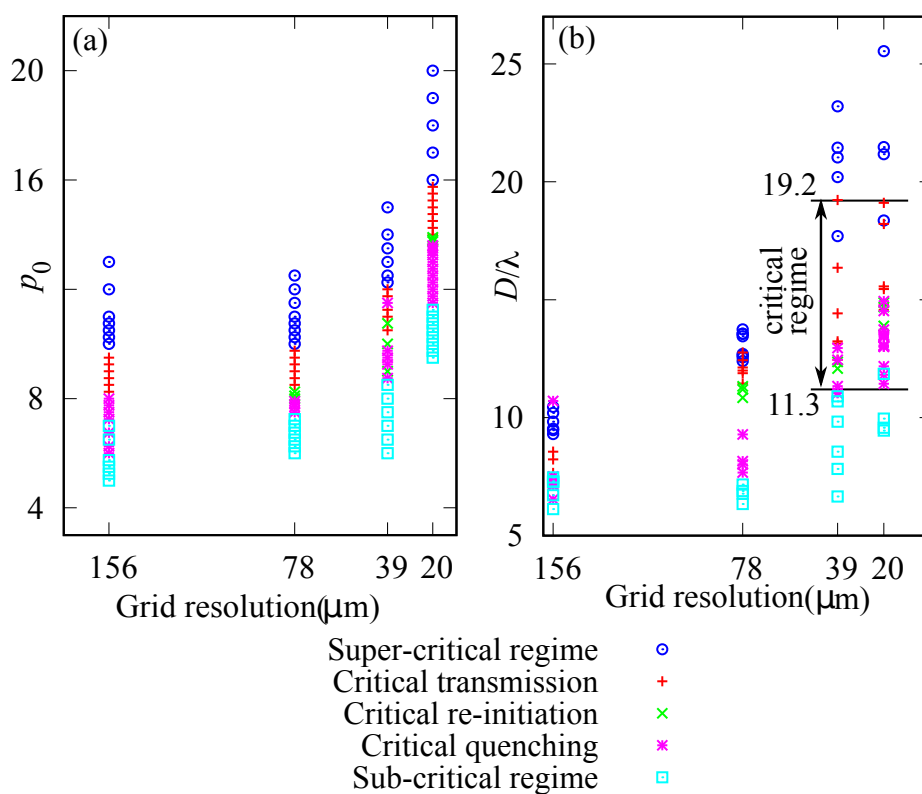


Figure 5.8: (a) The different outcomes observed at each minimum grid resolution and initial quiescent pressure (p_0). (b) D/λ for the different outcomes observed at each minimum grid resolution.

This study conducted simulations at resolutions as coarse as 156 μm and as fine

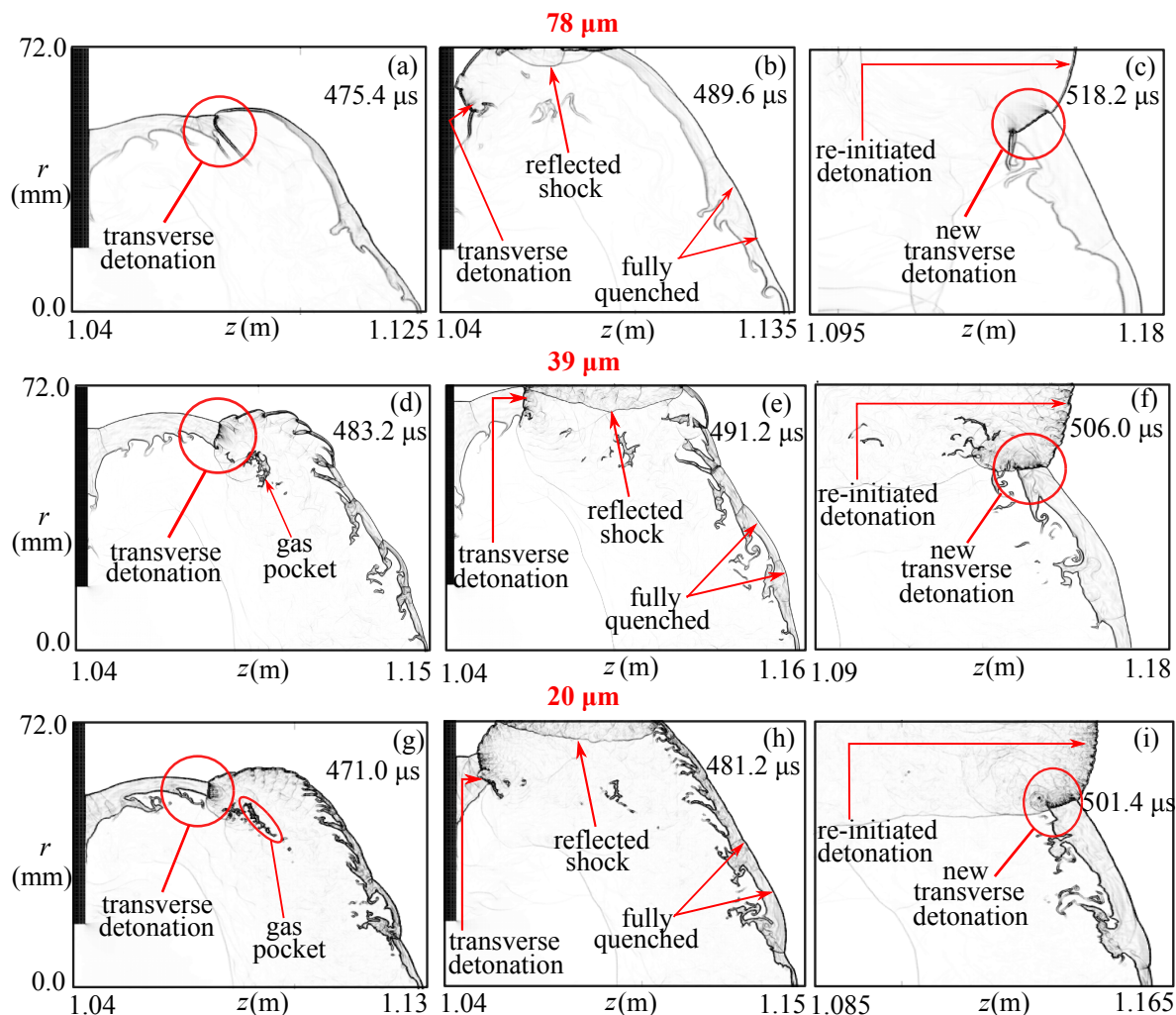


Figure 5.9: Density gradient evolution for the CR outcome as seen at a minimum grid resolution of $78 \mu\text{m}$ for $p_0 = 8 \text{ kPa}$ (a-c), $39 \mu\text{m}$ for $p_0 = 10.75 \text{ kPa}$ (d-f), and $20 \mu\text{m}$ for $p_0 = 13.8 \text{ kPa}$ (g-i).

as $20 \mu\text{m}$. A visual summary of the outcomes at each resolution and initial pressure is shown in Fig. 5.8a. In total, more than one hundred simulations were conducted. It was observed early on that as the resolution becomes finer, the range of pressures encompassing the critical regime shifts upward to higher pressures. For example, the range of pressures where critical outcomes were observed is $6 \leq p_0 \leq 7.5 \text{ kPa}$ for the coarsest resolution ($156 \mu\text{m}$), and $11.75 \leq p_0 \leq 15.75 \text{ kPa}$ for the finest resolution ($20 \mu\text{m}$). This behavior is not surprising since the detonation cell size in Euler simulations is known to scale with the resolution for fixed initial conditions

[181, 184]. This is true even when detailed chemistry mechanisms are adopted in an Euler framework for detonation studies [53]. We note here that due to the reaction zone not being sufficiently resolved, CR was not observed at the coarsest resolution of (156 μm). The principal result of the resolution study revealed that although the critical regime was observed at different pressures for the different resolutions, the critical regime predicted for the two finest resolutions (39 μm and 20 μm) remained unchanged when characterized by the detonation cell sizes (λ). As shown in Fig. 5.8b, the range of tube diameters where critical outcomes were observed ranged from $D = 11.3\lambda - 19.2\lambda$ for both of the finest resolutions which are in very good agreement with experimentally observed limits [149]. Based on these observations, a minimum resolution of 39 μm was deemed sufficient for the conclusions drawn in the current study. However, we chose to document results obtained at 20 μm since greater detail was available in the qualitative images obtained. Finally, with each simulation conducted at a minimum resolution of 20 μm taking approximately 2.5 weeks to complete on 192 CPUs (central processing units), adopting a finer resolution was not feasible to do a full complement of simulations at varying pressures due to time and computational constraints.

Despite the differences in regimes observed at different resolutions and the pressures at which they were observed, the occurrence of the CR outcome was found to be qualitatively similar across the resolutions, except at 156 μm where the outcome was not observed. Figure. 5.9 shows a comparison of the density gradient evolution for the CR outcome at the three different resolutions: $p_0 = 8.0$ kPa at the 78 μm resolution (frames a-c), $p_0 = 10.75$ kPa at the 39 μm resolution (frames d-f), and $p_0 = 13.8$ kPa at the 20 μm resolution (frames g-i). As the resolution became finer, more details of the various features present were visible. All the resolutions include the key features through which the detonation was re-initiated in the channel. These include the first transverse detonation that was initiated near the diffracting wave front and propagated to the wall, as well as the second transverse detonation,

which was triggered as a direct result of the wave reflection at the top boundary. For all resolutions, the triple point collisions near the vicinity of gas pockets created by the expansion were responsible for initiating the first transverse detonation. In most cases, pressure waves generated from the shock reflection initiated the detonation along the Mach stem first, followed by the second transverse detonation. However, in some other cases, as discussed in Section 5.3.2, the second transverse detonation was triggered directly along the detonation front prior to the reflection. The consistency of features observed across resolutions validates the strategy adopted to investigate detonation re-initiation when transverse detonations are present. The main differences between resolutions were the pressures at which the CR outcome occurred. Also, there was a prominent pocket of unburned gas present at the finer resolutions, seen in Fig. 5.9e and Fig. 5.9i, which was not present at the coarsest resolutions. This can likely be explained by the presence of higher numerical diffusion at coarser resolutions, which leads to quicker burning rates of shocked and unburned gas.

5.3 Discussion

5.3.1 *Transverse detonation re-initiation distance and wall reflection length*

A unique feature of outcomes following diffraction where the detonation is re-initiated or successfully propagates following the expansion is the presence of the main transverse detonation wave that propagates back to the wall. As a result, past studies have employed using the transverse detonation re-initiation distance (l_r) and wall reflection length (l_w) as unique length scales for quantifying the re-initiation of the diffracted detonation [53, 153, 154, 242]. The re-initiation distance and reflection length are measured as the horizontal distance from the corner of the tube to the local explosion that triggers the transverse detonation and distance from the corner to the point where the transverse detonation strikes the back wall respectively.

For unstable stoichiometric C_2H_4/O_2 mixtures Nagura et al. [153] noted that the re-initiation distance is relatively constant at $11.1\lambda \pm 3.0\lambda$ for detonation diffraction irrespective of the wall deviation angle in the experiment. In other words, it was concluded that the deviation angle affects the shape of the detonation diffraction but not the structures before re-initiation. A re-initiation distance of $12\lambda - 15\lambda$ was noted in the numerical study by Gallier et al. [53], which utilized a detailed chemistry mechanism for highly stable stoichiometric H_2/O_2 combustion. While the re-initiation distance was slightly higher than the previous measurements, it confirmed the hypothesis of Nagura et al. [154] that the re-initiation distance is relatively unchanged for different mixtures with varying levels of instabilities. A much higher re-initiation distance of $21.7\lambda \pm 1.67\lambda$ was noted by Xu et al. [242] for detonation diffraction experiments in stoichiometric C_2H_2/O_2 near the critical limit. The larger re-initiation distance observed was attributed to the difference in the geometry where the detonation propagates in a tube in the experiments by Xu et al. [242] instead of a channel prior to diffraction. Finally, Nagura et al. [153, 154] concluded that the wall reflection length varied slightly across different reactive mixtures but was relatively constant for detonation diffraction with different wall deviation angles. For detonation diffraction in stoichiometric C_2H_4/O_2 mixtures, the wall reflection length was found to $\sim 8.2\lambda - 15.5\lambda$.

Figure. 5.10 summarizes the results for the re-initiation distance measured in the current study for every outcome where the primary transverse detonation is observed. These include the outcomes for critical re-initiation (CR) and critical transmission (CT) in the critical regime as well as the super-critical regime. Also included in the figure are the re-initiation length limits from the experiments by Nagura et al. [154] and Xu et al. [242]. From the figure, it is observed that for the CT and super-critical regime outcomes, $l_r = 11.17\lambda \pm 2.09\lambda$, is in very good agreement with the experimental results of Nagura et al. [154]. On the other hand, for critical CR, $l_r = 20.57\lambda \pm 3.03\lambda$ agrees reasonably well with the experimental results of

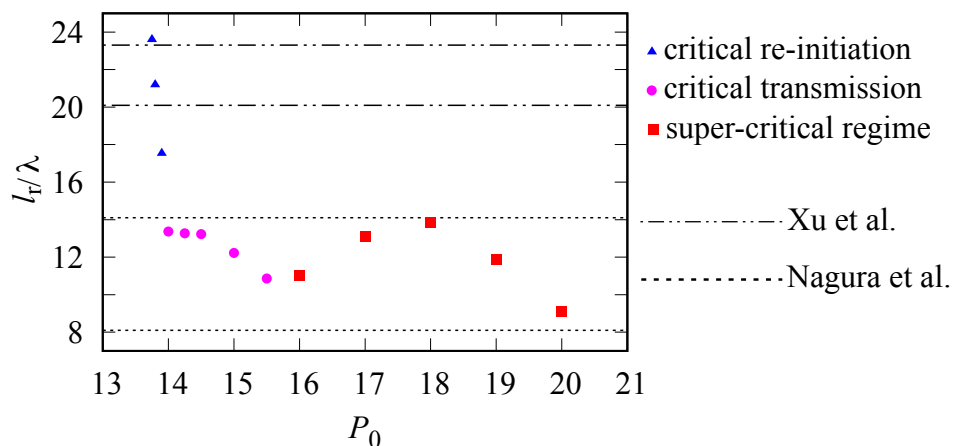


Figure 5.10: Ratio of transverse detonation initiation length to detonation cell size (l_r/λ) as a function of initial pressure (p_0). Dashed lines represent limits established in previous experiments by Xu et al. [242] and Nagura et al. [153].

Xu et al. [242]. The results then suggest that the differences observed between the limits for the two experiments are not caused by the differences in the geometry as previously concluded, but instead due to the regimes following diffraction that were investigated. Nagura et al. [153, 154], for example, investigated detonation diffraction in the super-critical regime with $p_0 \geq 20$ kPa which corresponded to $D \geq 11\lambda$ for the experimental setup used depending on the choice of cell sizes for stoichiometric C_2H_4/O_2 mixtures available in the literature [91, 211]. This is much higher than the critical $D_c \sim 3\lambda - 7\lambda$ criteria for detonation diffraction in channels with rectangular cross sections [10, 73]. On the other hand, the measurements taken by Xu et al. [242] for stoichiometric C_2H_2/O_2 at $6.5 \leq p_0 \leq 7.0$ kPa correspond to the critical $D_c \sim 13\lambda$ for the experimental setup used. Based on these observations it can be concluded that the re-initiation distance is heavily influenced by the initial pressure resulting in different outcomes following detonation diffraction.

Figure 5.11 summarizes the results for the wall reflection lengths in the current study for the cases where the transverse detonation propagates and reflects off the back wall. In the current study $l_w \sim 9.5\lambda - 17.2\lambda$ which agrees very well with the $8.2\lambda - 15.5\lambda$ measurements by Nagura et al. [153] for stoichiometric C_2H_4/O_2

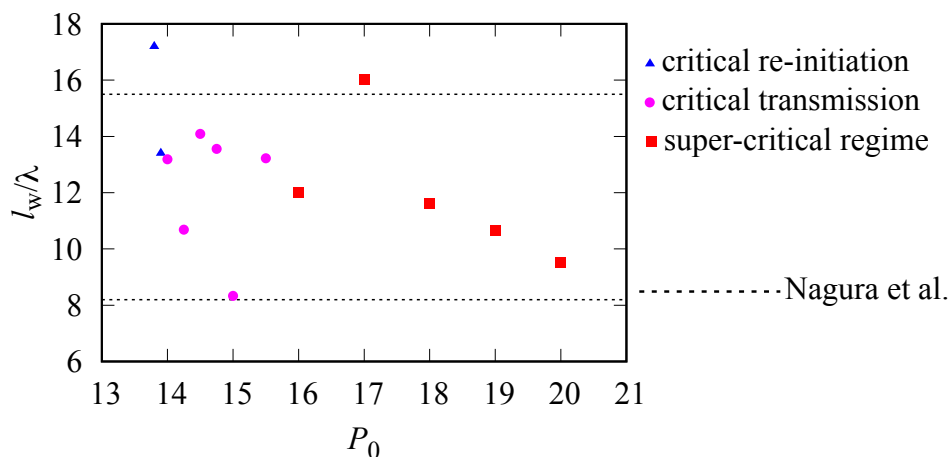


Figure 5.11: Ratio of transverse detonation reflection length to detonation cell size (l_w/λ) as a function of initial pressure (p_0). Dashed lines represent limits established in previous experiments by Nagura et al [153].

mixtures. The current result presents a significant improvement over the numerical study conducted by Nagura et al. [153] where the estimated wall reflection length was on the order of 20λ using a two-step combustion model. At the time, it was suggested that the difference between experimental results and simulations was due to the additional curvature of the diffracting wave in three dimensions which was lacking in the two-dimensional simulations. However, based on the results in Fig. 5.11, we conclude that the observed differences were likely due to the lack of chemical accuracy using a simple two-step combustion model and not due to the absence of three-dimensional effects in simulations. As a result, we attribute the improved predictions in wall reflection lengths to adopting the thermally perfect four-step combustion model. This conclusion is supported by the results observed in the two-dimensional numerical study by Gallier et al. [53] using a detailed chemistry mechanism for hydrogen combustion where the predicted wall reflection length compared very well with experimental measurements.

5.3.2 *Origin and role of transverse detonations during re-initiation*

Critical re-initiation where the detonation was quenched near the tube axis and subsequently re-initiated was observed for initial pressures ranging from $13.75 \leq p_0 \leq 13.9$ kPa at the 20 μm resolution. Although the exact location and timing of the explosion that triggered the first transverse detonation varied for each pressure, as shown in Section 5.3.1, the mechanism through which the transverse detonation was initiated remained unchanged. Figures 5.12 and 5.13 provide a closer look at a typical initiation explosion event for the transverse detonation with $p_0 = 13.8$ kPa triggered along the expanding detonation front. Figure 5.12a shows the onset of the localized explosion that eventually triggered the transverse detonation. Due to the weakening shock strength as the detonation expanded, a large pocket of unburned gas formed along the wave front in the vicinity of two triple points propagating in opposite directions. Also visible in the figure is a weak localized explosion formed by a triple point collision event as well as weak triple point structures that propagated towards the wall (to the left). These weak triple point structures were the result of transverse pressure waves from older localized explosions that failed to trigger a transverse detonation in the shocked mixture. As the triple points in Fig. 5.12a collided, the gas pocket was instantly ignited, and a strong explosion is observed in Fig. 5.12b. Two transverse detonations are then observed in Fig. 5.12c, one from each of the local explosions that propagated to the left. The ignited gas pocket, however, failed to trigger a transverse detonation in the gas mixture behind the incident shock, and the detonation was continually quenched near the tube axis. Due to its higher acoustic speed, the first transverse detonation quickly caught up with the weak triple point structure. An explosion event was then observed at the interface separating the burned and unburned gases as the transverse detonation passed over the weak triple point, as shown in Fig. 5.12d. Although this explosion at the interface was accompanied by an increase in the local pressure and temperatures, the first transverse detonation was observed to fail immediately following its

collision with the weak triple point as shown in Fig. 5.13e. Finally, the transverse detonation in the shocked mixture was fully established when the second transverse detonation interacted with the triple point structure formed by the failed first transverse detonation. An explosion event was again observed at the interface of the burned and unburned gases. In this case, however, the transverse detonation did not fail, and the fully established transverse detonation propagated to the back wall as shown in Fig. 5.13h.

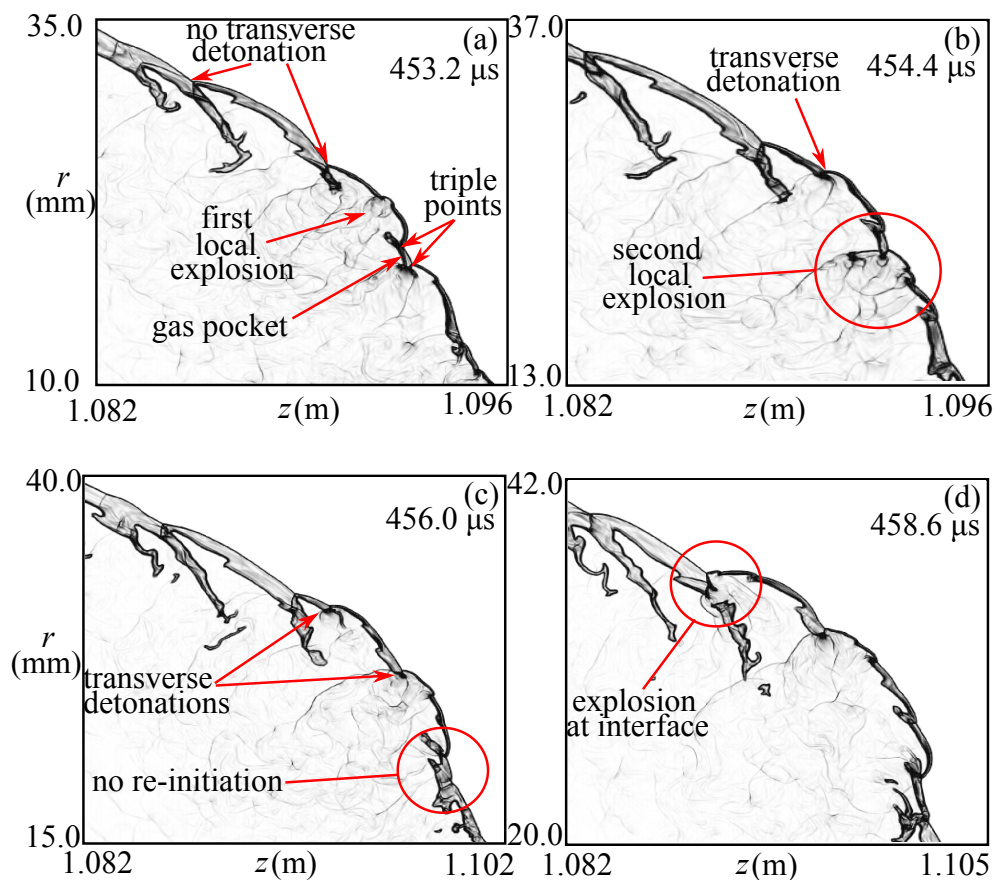


Figure 5.12: Density gradient evolution for $p_0 = 13.8$ kPa showing the mechanism by which the transverse detonation is triggered. Frames a-d show the localized explosion and onset of the transverse detonations.

Following the establishment of the self-sustained transverse detonation that propagated to the wall, Figs. 5.14 and 5.18 summarize the sequence leading to the full re-initiation of the detonation wave in the channel. In general, two distinct pathways

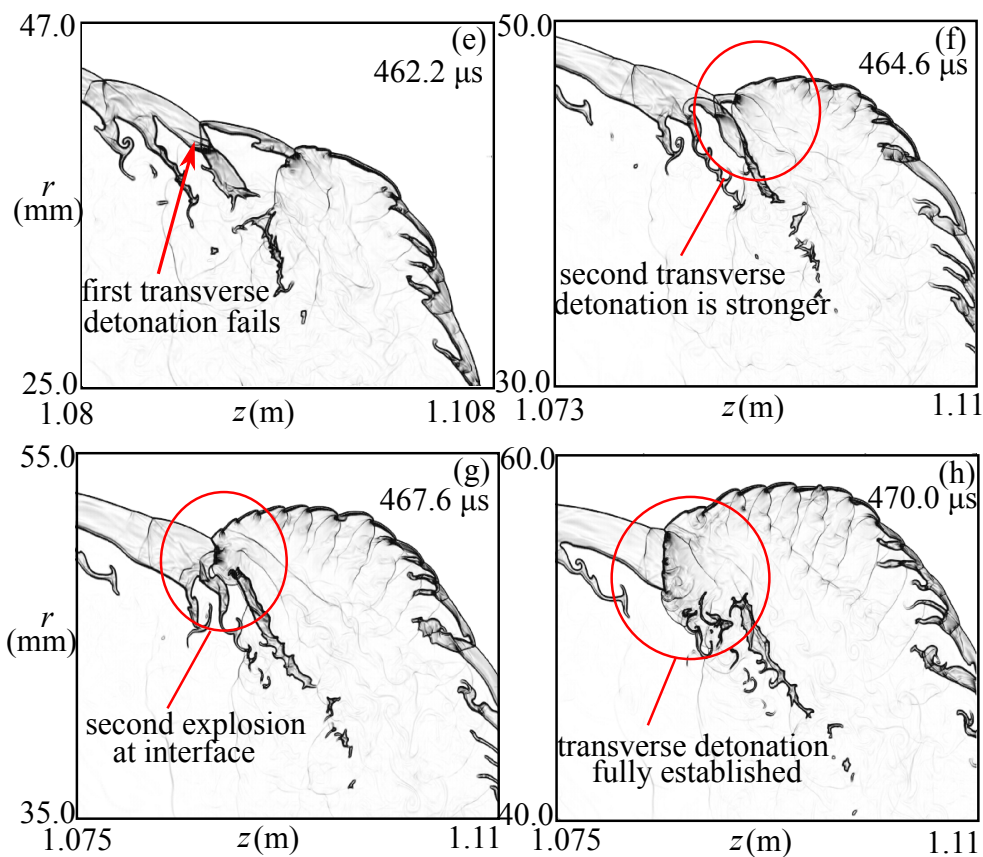


Figure 5.13: Continuation of Fig. 5.12. Frames e-h then show the failure of the first transverse detonation and sustained propagation of the second transverse detonation.

to re-initiation were observed depending on the initial pressure in the simulation. For $p_0 = 13.75$ and 13.8 kPa, the re-initiation was found to be a result of the direct reflection at the top boundary. The initiation of the detonation along the Mach wave and the transverse detonation that propagated to the tube axis for $p_0 = 13.8$ kPa is shown in the density gradient evolution in Fig. 5.14. As the first transverse detonation propagated through the band of shocked gas trapped between the decoupled shock and reaction front, it continually re-established a detonation wave in the region along the front which was originally quenched. This re-coupled portion of the detonation that propagated outwards is shown in Fig. 5.14a just prior to its reflection at the top boundary. Following the reflection, the detonation along the Mach wave

and the second transverse detonation were immediately triggered due to pressure waves caused by the shock reflection as shown in Figs. 5.14b and 5.14c. The self-sustained transverse detonation then propagated towards the tube axis, continually consuming the bulk of the pockets of unburned gas present near the incident shock. The remaining gas pockets burned up as deflagrations, which were most likely enhanced by Richtmyer-Meshkov (R-M) instabilities that arose from the passage of the reflected shock through the pocket surfaces. The established Mach detonation and transverse detonation successfully re-initiate the detonation in the full channel.

To gain more clarity on the formation of the detonation waves observed in Fig.5.14e, detailed density gradient, temperature, and local ignition delay profiles are shown in Figs.5.15 and 5.16 for time steps immediately following the reflection of the diffracted wave with the top boundary. In Fig.5.15, frame (a) at $t = 478.2 \mu\text{s}$ shows the reflected shock wave (sw1) from the top boundary just prior to its interaction with the burned–unburned gas interface (f1). In frame (b) at $t = 478.8 \mu\text{s}$, the interaction of the shock wave and interface led to enhanced burning rates with a localized explosion accompanied by an increase in temperature observed. These enhanced burning rates were likely due to Richtmyer-Meshkov instabilities that arose from the passage of the reflected shock wave through the flame surface. Following the explosion, sw1 is then observed to propagate into the gas which contained favorable ignition delay times behind the Mach shock as shown in frame (c) at $t = 481.0 \mu\text{s}$. In Fig.5.16, the detonation wave along the Mach wave (d1) shown in frame (d) then appears to be triggered directly by the local pressure amplification due to the explosion, which led to a rapid coupling of the shock and reaction zones. For both pressure cases ($p_0 = 13.75 \text{ kPa}$ and 13.8 kPa) where re-initiation was observed as a result of the reflection at the top boundary, the detonation along the Mach wave was established first. The transverse detonation (d2) is then found to be initiated directly by the passage of the reflected shock wave over multiple burned–unburned interfaces along the expanding detonation front. The established

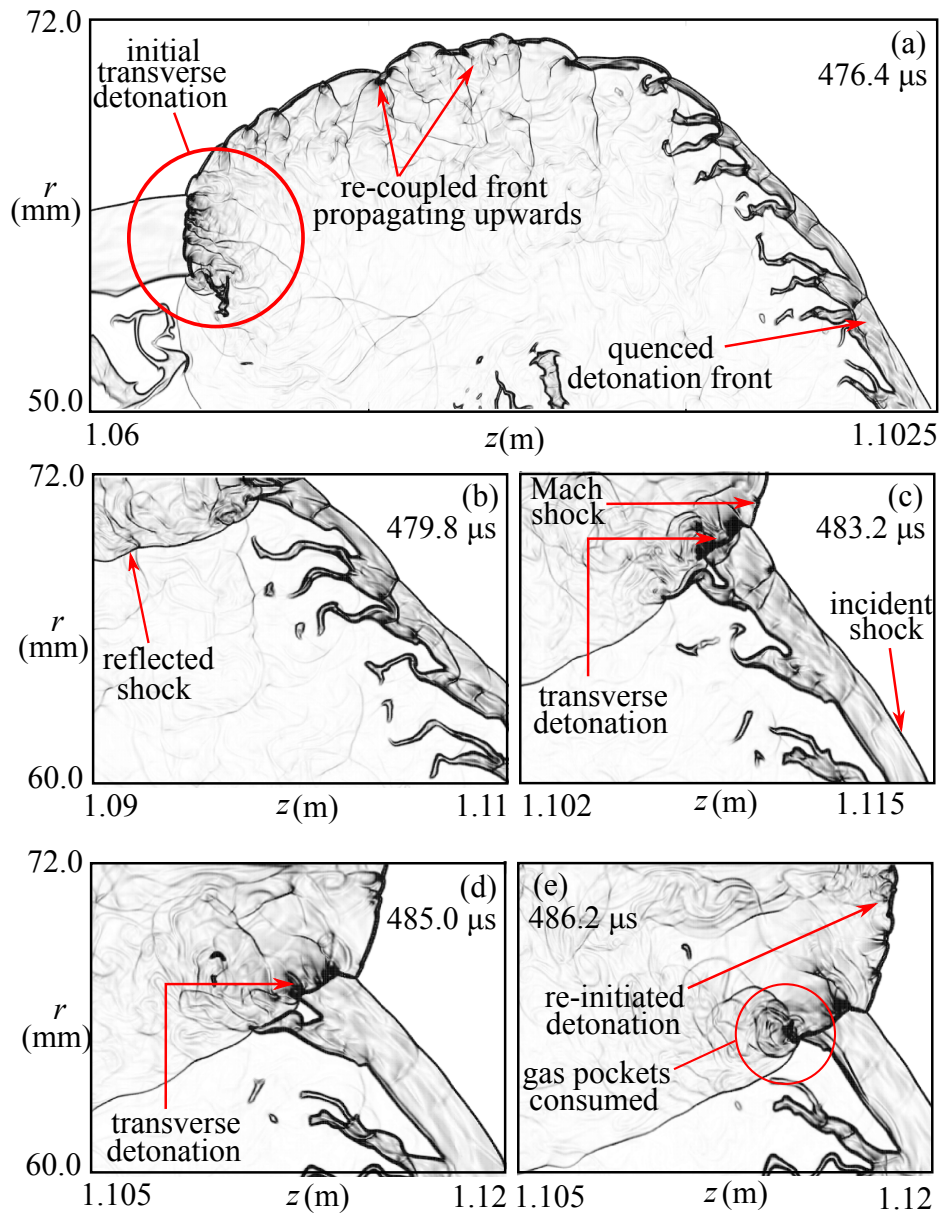


Figure 5.14: Density gradient evolution showing the establishment of the second transverse detonation (a-c) and subsequent detonation re-initiation in the channel (d and e) for $p_0 = 13.8$ kPa.

transverse detonation is shown in frame (e) at $t = 482.8$ μs .

Figure 5.17 shows the pressure and $\log(\text{ignition delay})$ profiles measured at different times along the top boundary at $r = 0.072$ m. According to the pressure profiles, sw1 clearly experiences a pressure amplification through time due to the enhanced burning rates and by propagating against the ignition time gradient shown

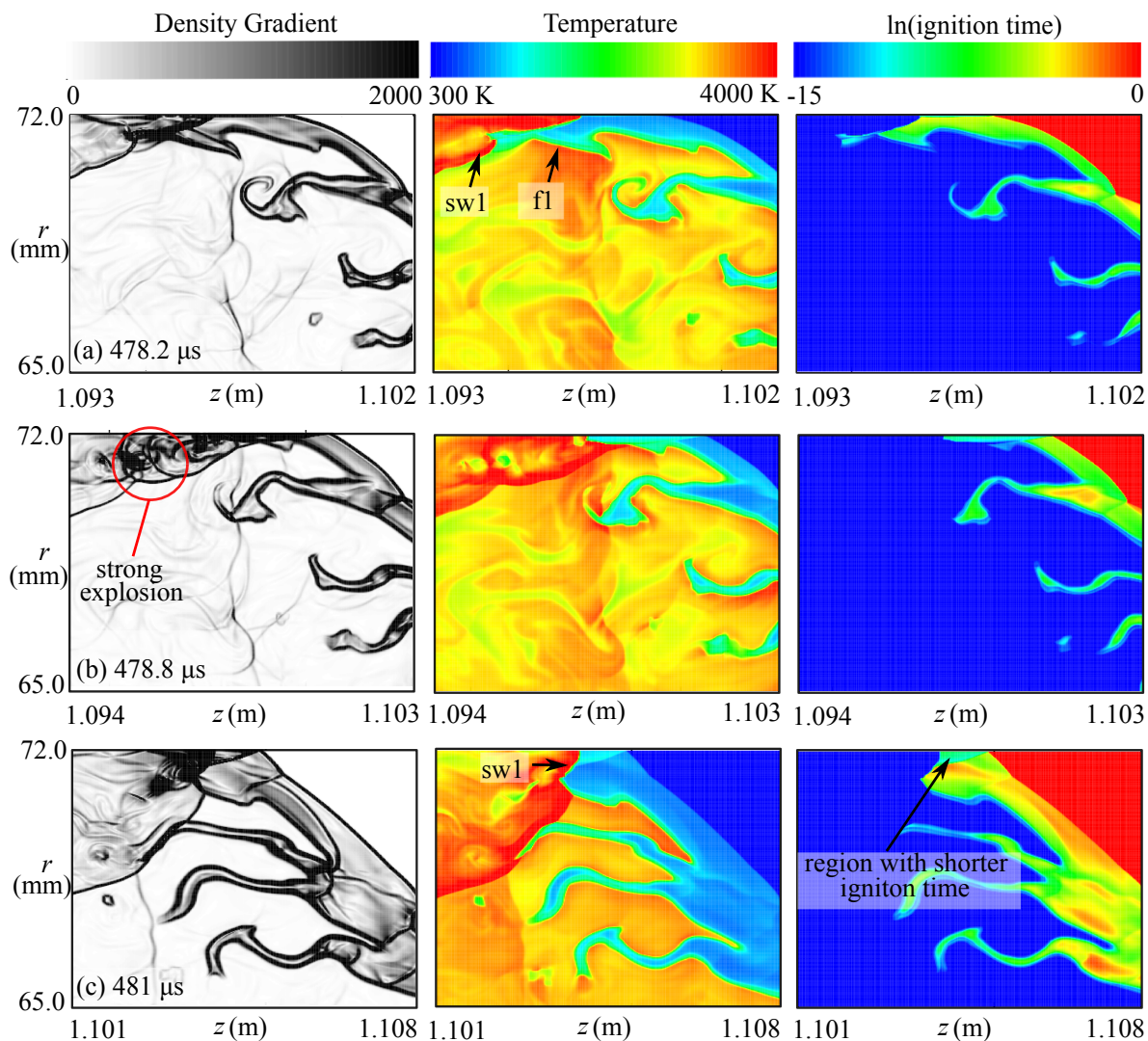


Figure 5.15: Details of the density gradient, temperature, and ignition delay times for CR observed with $p_0 = 13.8$ kPa.

in the delay time profiles. The mechanism of detonation initiation thus resembles the well known SWACER (Shock Wave Amplification by Coherent Energy Release) mechanism [107]. In this case, however, the initial explosion was driven and enhanced through Richtmyer-Meshkov instabilities by the passing of an external shock wave over an existing hot spot, and not started by the spontaneous ignition of the gas having minimum ignition delay. Upon measuring the ignition delay time gradient ahead of the reaction wave, it was found that the inverse of the ignition delay was $(\nabla \tau_{ig})^{-1} \sim 2250$ m/s only right before the wave front, at all times. Ahead

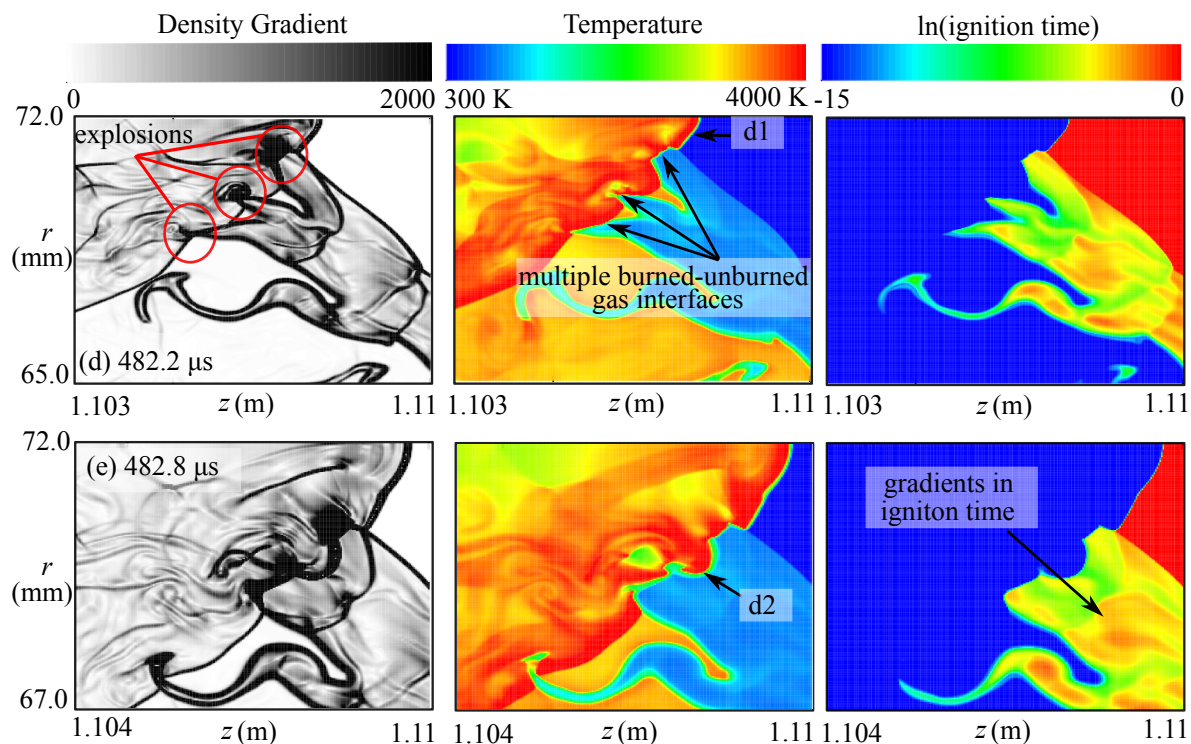


Figure 5.16: Continuation of Fig. 5.15.

of the wave, $(\nabla \tau_{ig})^{-1}$ was only $\mathcal{O}(1 \text{ to } 250)$ m/s. This observation is consistent with the past work of Kuznetsov et al. [95] where the $(\nabla \tau_{ig})^{-1}$ of the pre-heated mixture during DDT of ethylene–oxygen was also much less than the CJ-detonation speed. In fact, the recent work of Wang et al. [230] demonstrates that detailed mechanisms are able to permit detonation initiation in much shallower ignition delay gradients compared to simple combustion models (i.e., the one-step combustion model). Although gradients in τ_{ig} were shallow in this case, it is important to point out that non-uniformities did exist in the ignition delay time profiles of Figs. 5.16 and 5.17, and that such gradients may have promoted the propagation of the reaction wave until a sustained detonation has formed [165].

A markedly different pathway to detonation re-initiation in the channel was observed for CR at the highest pressure of $p_0 = 13.9$ kPa, with the second transverse detonation initiated before the detonation along the Mach wave. Figure. 5.18 summarizes the density gradient evolution for this case following the establishment of

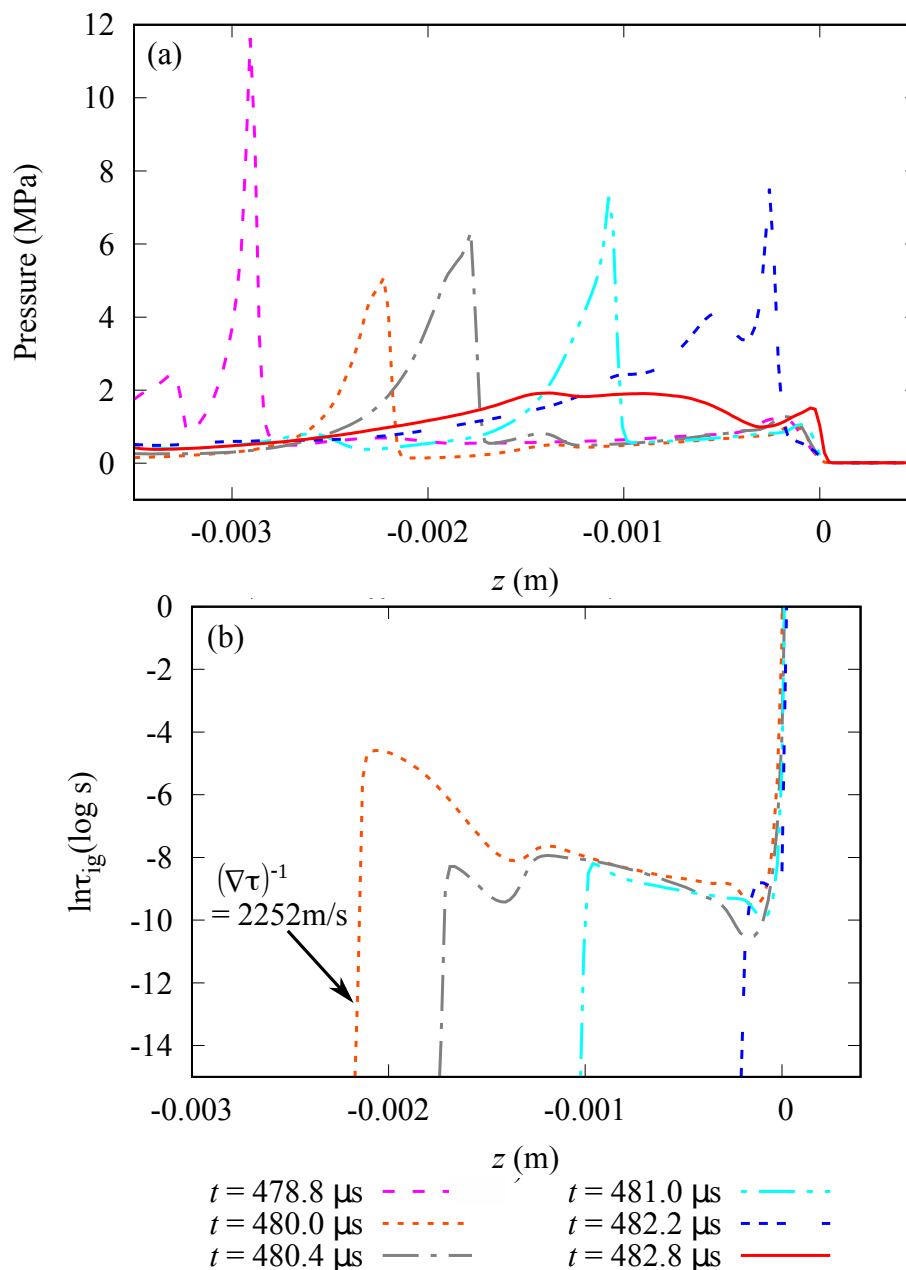


Figure 5.17: Pressure and ignition delay time profiles measured along $r = 0.072$ m for $p_0 = 13.8$ kPa. Distances are given in the frame of reference of the Mach shock.

the first transverse detonation. The slightly elevated pressure compared to the previous CR cases resulted in a smaller re-initiation distance (l_r) for the transverse detonation and consequently a shorter wall reflection length (l_w) as discussed in Section 5.3.1. The shorter wall reflection length then meant that the detonation continued to expand for a longer period of time before reflection occurred at the top bound-

ary. As a result of this prolonged expansion, the portion of the diffracted wave that was re-coupled by the first transverse detonation started to decouple as the shock strength weakened, as shown in Fig. 5.18a. Local explosions along the transverse detonation front that sustained its self-propagation then successfully triggered the second transverse detonation in this newly decoupled region as shown in Fig. 5.18b and 5.18c. Following the reflection of the first transverse detonation with the wall, a self-sustained detonation wave was observed to travel upwards along the wall to the top boundary. All this time, the second transverse detonation continued to propagate along the curved front of the original detonation as shown in Fig. 5.18e. Pressure waves generated from the reflection of the wall detonation with the top boundary were then observed to strengthen the second transverse detonation while supporting the Mach shock along the top boundary. This Mach shock which eventually transitioned to a self-sustained detonation, and the fully established second transverse detonation, which re-initiated the detonation in the channel, are then shown in Fig. 5.18g.

Interestingly, these results for CR share many similarities with a recent study by Xu et al. [242] as shown in Fig. 5.19 where re-initiation of the detonation wave following diffraction was investigated in stoichiometric C_2H_2/O_2 mixtures near the critical limit. In the experiments, re-initiation was observed for $p_0 = 6.5$ kPa and 7.5 kPa which corresponds to a critical diameter (D_c) $\sim 13\lambda$ based on the experimental setup. For $p_0 = 6.5$ kPa (Fig. 5.19b), re-initiation occurred due to a single transverse detonation that was triggered and observed to propagate to the top boundary. Following the reflection at the top boundary, the detonation is re-established in the channel with a second transverse detonation propagating to the tube axis. Although it is unclear from the experimental soot foil if the first transverse detonation reaches the back wall like the simulations due to the limiting size of the observation window, the numerical soot foils for $p_0 = 13.75$ kPa and 13.8 kPa were observed to agree with this result qualitatively. Unlike the experimental result for

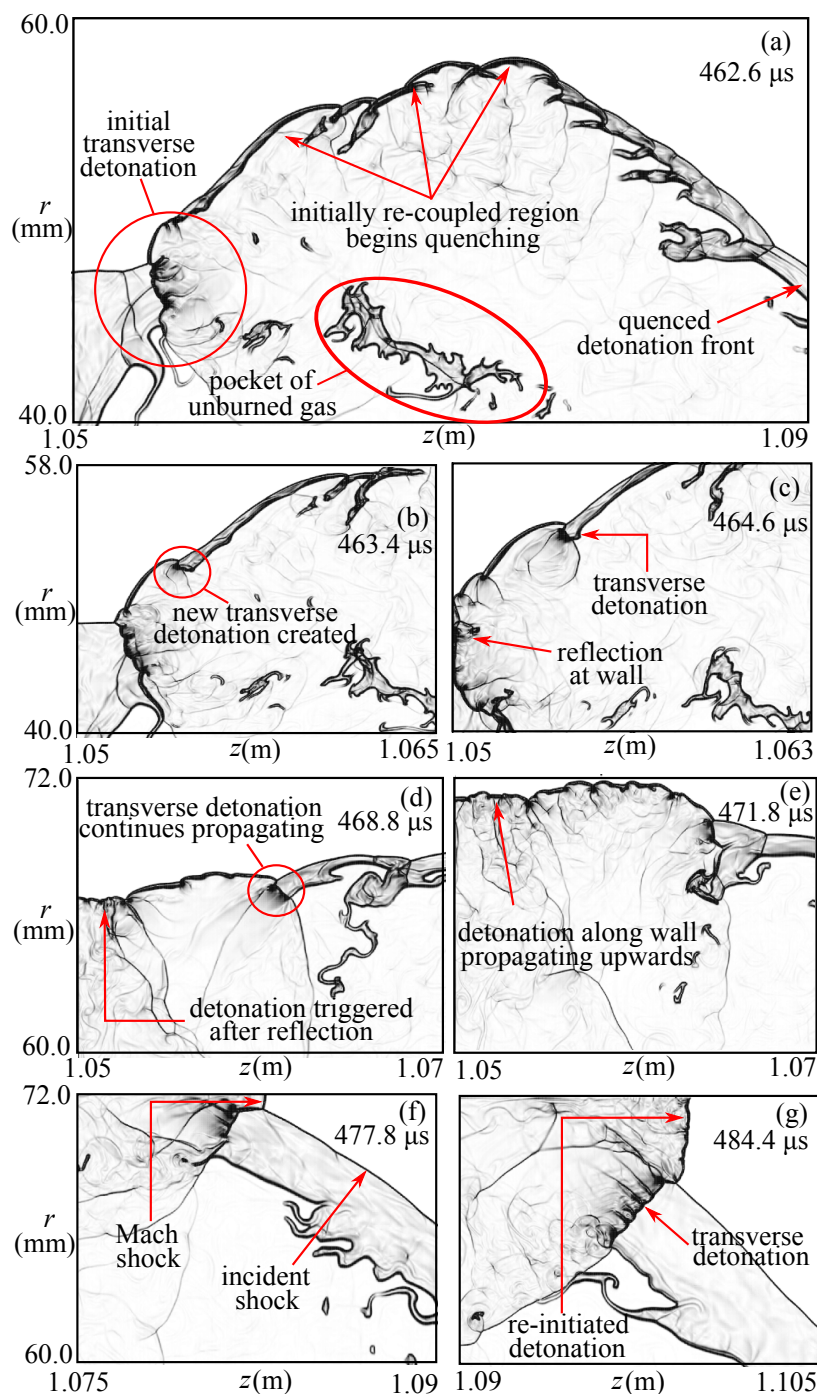


Figure 5.18: Density gradient evolution showing the establishment of the second transverse detonation (a-e) and subsequent detonation re-initiation in the channel (f and g) for $p_0 = 13.9$ kPa.

$p_0 = 6.5$ kPa, the experimental soot foil for $p_0 = 7$ kPa (Fig. 5.19d) clearly shows the second transverse detonation initiated from the first transverse detonation and

propagate to the tube axis, similar to the simulation result at $p_0 = 13.9$ kPa. As a result, very different pathways to re-initiation are possible based on the initial pressures in both experiments and simulations for irregular mixtures. This is not surprising as the evolution of shock reflections and triple point locations are likely influenced by the cellular structure of the detonation prior to quenching. Moreover, it is well known that the detonation cellular structure strongly depends on pressure. Finally, in all of the CR cases, transverse detonations appear to be the main feature through which the detonations survive complete quenching. While the sequence in which the transverse detonation forms can vary, it is always the avenue by which the re-established detonation front extends to the entire domain height, creating a fully established and self-sustained detonation wave.

5.3.3 Triple point and transverse detonation speeds

The triple point speeds and transverse detonation strengths were measured for a few cases in the current section. The triple points under consideration here are the locations where the incident shock, Mach shock, and transverse detonation meet. Figure 5.20 summarizes the results for the triple point speeds (U_{TP}) for the first transverse detonation observed for every outcome with $p_0 \geq 13.75$ kPa and the second transverse detonation which re-initiates the detonation in the channel for the CR cases. For simplicity, these are referred to as TP1 and TP2 in the results. Figure 5.20a shows the magnitude of the triple point speed normalized to the CJ speed of the quiescent mixture (U_{TP1}/U_{CJ}) from the time when the first transverse detonation is triggered up to its reflection at the wall. From Fig. 5.20a it is observed that the triple point attached to the first transverse detonation propagates at roughly the CJ speed (within +5%). This is consistent with the recent measurements by Yuan et al. [244], although much larger fluctuations in the triple point speeds ($\geq 10\%$) are observed for the unstable mixture in the current study. The normalized triple point speeds for the second transverse detonation observed for the CR outcome, which

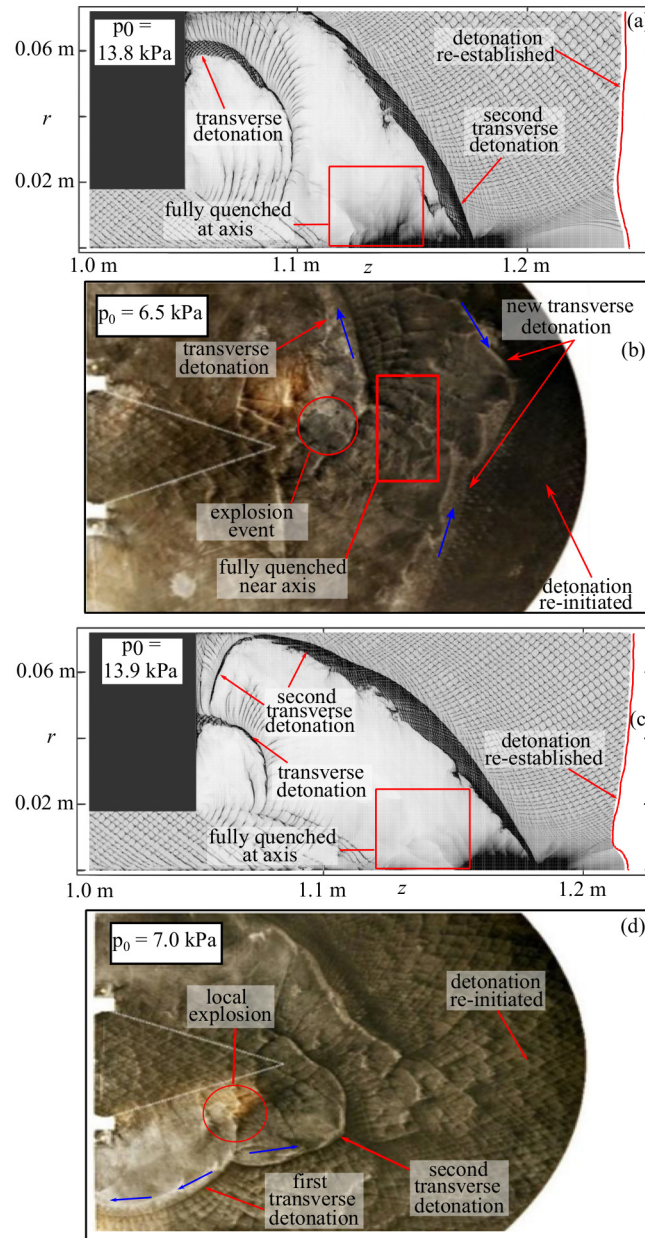


Figure 5.19: Comparison of numerical (frames a and c) and experimental [242] (frames b and d) soot foils showing the different pathways to detonation re-initiation for the CR outcome.

propagates from the top boundary to the tube axis, are shown in Fig. 5.20b. Unlike the previous results, the triple point speeds for the second transverse detonation are overdriven with a mean normalized speed of $U_{TP2}/U_{CJ} \sim 1.11 - 1.12$. A similarly overdriven triple point speed was noted in the experiments by Chin et al. [30] and

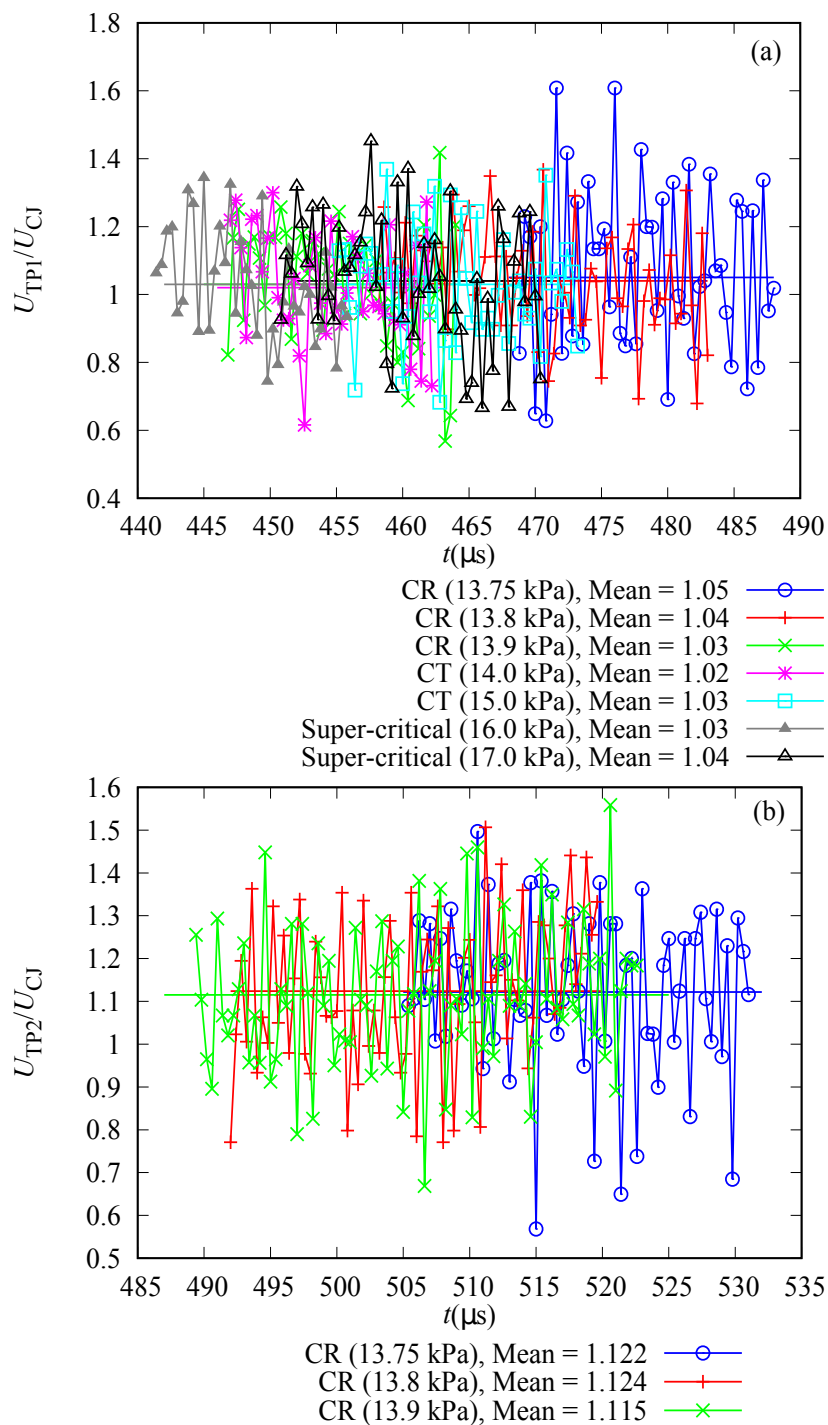


Figure 5.20: Triple point speed (U_{TP}) normalized to the CJ speed of the quiescent mixture as a function of time for (a) the first transverse detonation and (b) the second transverse detonation.

is discussed in more detail in the next Section.

Finally, to estimate the speed of the transverse detonation, we considered the

velocity vector of the triple point relative to the velocity vector of the shocked gas in front of the transverse detonation. Here, we chose to measure the triple point velocity as a reference point, as its absolute lab-frame velocity can be assumed to be close to that of the transverse detonation itself. This also removed uncertainty in finding a suitable reference point attached to the transverse wave. To determine the velocity of the shocked gas in front of the transverse wave, we considered a sample space with an approximate area of 12.25 mm^2 consisting of, on average, 25,000 points on the finest refinement level. From the data points in this range, mass-weighted averages were obtained for the shocked gas velocity components, denoted as $\tilde{u}_r(s)$ and $\tilde{u}_z(s)$. Here the mass-weighted average of a scalar was computed from $\tilde{\phi} = \frac{(\rho\phi)}{\bar{\rho}}$, where ϕ , represents the scalar of interest that was averaged, and the overline represents an ensemble average. The mass weighted velocity of the transverse detonation is then calculated as

$$\left\{ \begin{array}{l} U_{\text{TD1}} = \sqrt{(u_r(\text{TP1}) - \tilde{u}_r(s))^2 + (u_z(\text{TP1}) - \tilde{u}_z(s))^2} \\ \text{and} \\ U_{\text{TD2}} = \sqrt{(u_r(\text{TP2}) + \tilde{u}_r(s))^2 + (u_z(\text{TP2}) - \tilde{u}_z(s))^2}. \end{array} \right. \quad (5.3)$$

for the first and second transverse detonations, respectively. Then from the ensemble-averaged density and pressure, $\bar{\rho}$ and \bar{p} , the CJ speed associated with the shocked and unburned state was determined. Figure. 5.21 shows the transverse detonation speed normalized to the CJ speed of the shocked unburned gas. For all the CR and CT cases simulated, we found that the first transverse detonation was, in fact, a CJ detonation (within 5%), as shown in Fig. 5.21a. A similar result was also observed for the second transverse detonation observed during CR. Although the triple point attached to the transverse detonation is sufficiently overdriven for this case, the transverse detonation speed was found to be within 3% of the CJ solution, as shown in Fig. 5.21b.

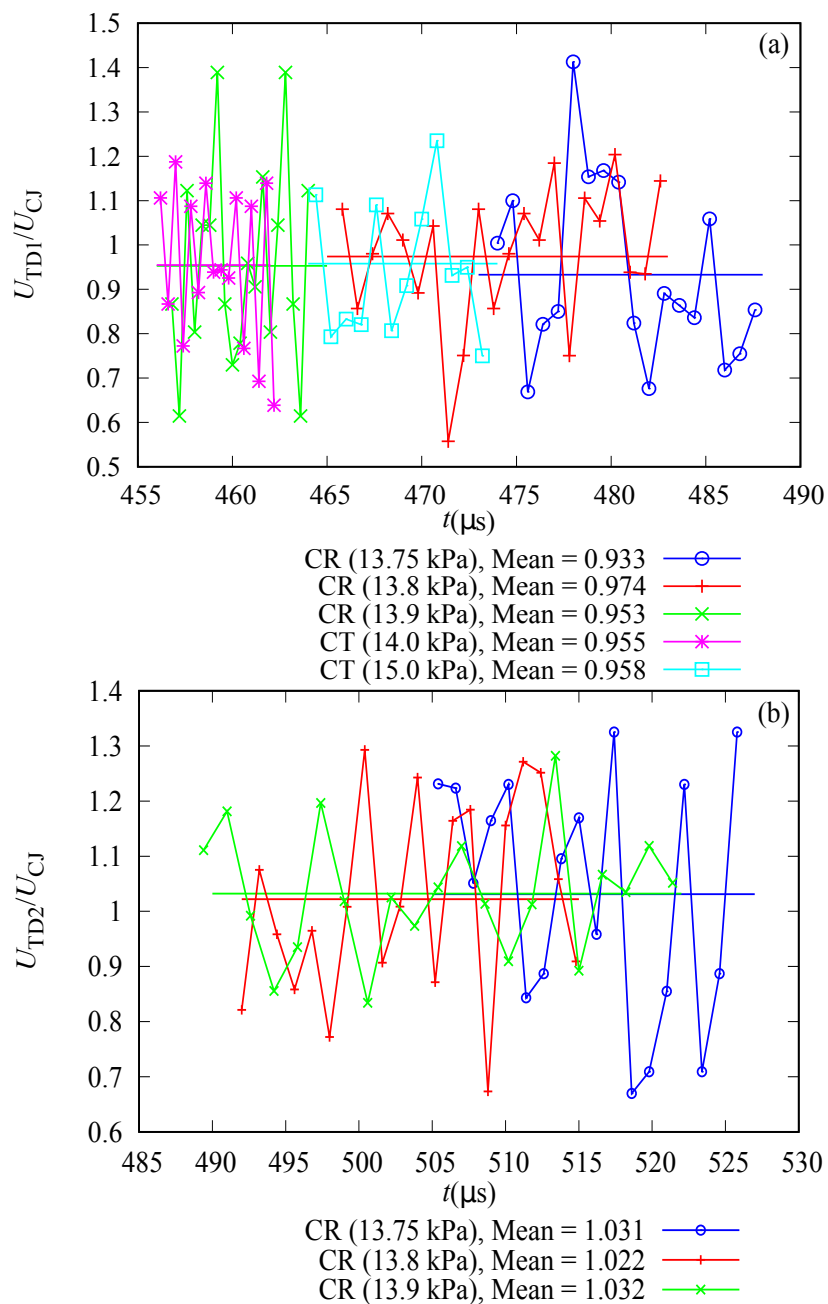


Figure 5.21: Transverse detonation speed (U_{TD}) normalized to the CJ speed of the shocked unburned mixture as a function of time for (a) the first transverse detonation and (b) the second transverse detonation.

5.3.4 The overdriven second triple point

To better understand why the second triple point (TP2) is overdriven, Fig. 5.22 shows the speed of the leading shock wave for the Mach detonation vs. z -position

along the top boundary at $r = 0.072$ m. From the figures, it is observed that the Mach detonation is only briefly overdriven when initiated and is subsequently found to propagate at the CJ speed of the quiescent mixture. On the other hand, TP2 remains overdriven throughout its propagation to the tube axis. With the second transverse detonation (TD2) and the Mach detonation, both CJ detonations with respect to the mixtures they propagate in, a better explanation is needed for the overdriven speed of TP2. In the previous section, the resultant velocity of the shocked gas in front of the transverse detonation was used in the triple point frame of reference to calculate the speed of the transverse detonation. Here, the vector relations are again considered to highlight how the direction and magnitude of the resultant velocity vector of the shocked gas influence the triple point speed.

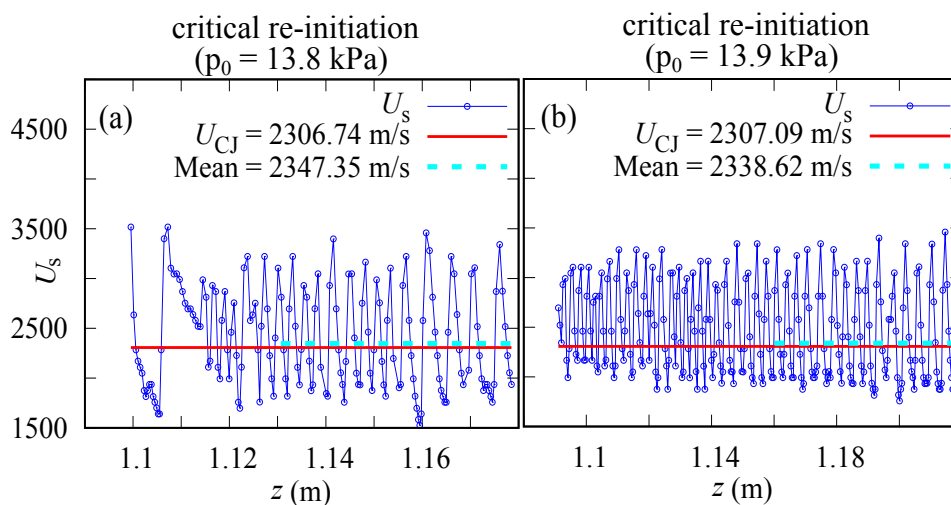


Figure 5.22: Speed of the wave front (U_s) as a function of z -distance for the Mach detonation measured along the top boundary at $r = 0.072$ m for (a) CR for $p_0 = 13.8$ kPa and (b) CR for $p_0 = 13.9$ kPa.

Frames (C1)-(C3) and (D1)-(D3) in Fig. 5.23 summarize our results for the triple point and transverse detonations speeds for the simulation with $p_0 = 13.8$ kPa through vector diagrams for the time steps where the shocked gas mixture velocity was measured. Here, \tilde{U} is the mass averaged resultant velocity of the shocked gas mixture that the transverse detonation propagates through, calculated as $\sqrt{\tilde{u}_r^2 + \tilde{u}_z^2}$.

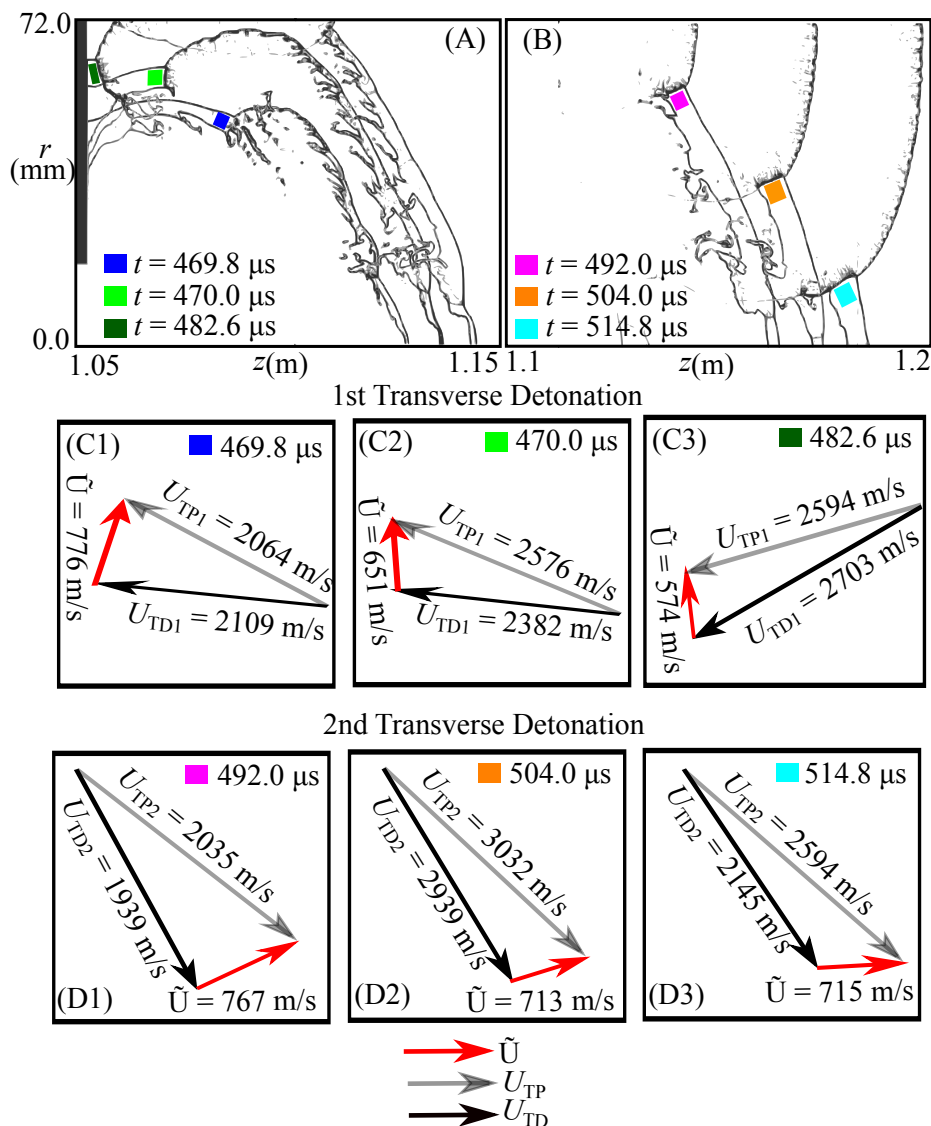


Figure 5.23: Density gradient composites showing the propagating transverse detonation waves for $p_0 = 13.8 \text{ kPa}$ along with the sample spaces where the shocked gas mixture velocity is extracted from (A and B). Frames (C) and (D) show the magnitude and the direction of the triple point speed (U_{TP}), transverse detonation speed (U_{TD}), and resultant velocity of the shocked mixture for the first and second transverse detonations respectively.

In frames (C1)-(C3), it is first observed that following the initiation of TD1, the resultant velocity of the shocked mixture not only decays in magnitude as the leading shock weakens but also changes direction as the transverse detonation propagates to the wall. This change in direction is caused by the unconstrained expansion of

the leading shock following the decoupling of the shock and reaction zone caused by the diffraction process. The unconstrained expansion then permits TP1 to propagate close to the CJ speed of the quiescent mixture while satisfying the respective vector relations. However, this is not the case for the second transverse detonation, where the expansion of the shocked gases behind the leading shock wave is constrained between TD2 and the tube axis. This is shown in frames (D1)-(D3), with the direction of \tilde{U} relatively fixed. Under the constraints that TP2 must be attached to the transverse detonation and the direction of \tilde{U} is fixed, satisfying the vector relations causes TP2 to be overdriven. In a separate study [51], the authors studied the re-initiation of a quenched detonation wave following its interaction with an obstacle where the triple point attached to the transverse detonation was also overdriven. After further investigation, it was found that the shocked mixture was once again constrained in this case. The results presented here then provide an explanation for the overdriven triple point in this study as well. Ultimately, from the figures, it can be concluded that the second triple point is overdriven simply because the shocked gas mixture is geometrically constrained for this case.

5.4 Conclusion

In this investigation, the four-step global combustion model was applied to investigate the critical regime following the detonation diffraction in a mildly irregular hydrocarbon mixture. Our simulations have demonstrated that the application of this minimal global combustion model is able to capture the sustained transverse detonation feature in this scenario, unlike past applications of simple one- and two-step combustion schemes [153, 204]. We attribute this to the fact that the relatively simple four-step model contains an adequate description to permit the correct ignition response when changes in temperature and pressure occur [171, 173], i.e. behind shocks and reflected shocks. This appears to be required not only to capture the transverse detonation but also to correctly predict the re-initiation distance and

wall reflection lengths for the sustained transverse detonation, which are crucial for developing a unified theory for detonation diffraction.

For detonation re-initiation, it was found that transverse detonations along the detonation front are triggered by strong triple point collisions in the vicinity of unreacted gas pockets formed due to the wave expansion. Local explosions triggered by the passing of the transverse detonation over the burned/unburned surfaces of weak triple points also appear to be crucial for establishing a self-sustained transverse detonation in the shocked mixture initially quenched by the corner. In addition, the results demonstrated that different pathways to re-initiating the detonation in the channel exist. Depending on the initial pressure, the second transverse detonation was either initiated following the reflection at the top boundary or via local explosions at the front of the first transverse detonation. For detonation re-initiation at the top boundary observed at lower pressures, it was found that the detonation behind the Mach shock was established before the transverse detonation. Further, the principal mechanism triggering both the detonation behind the Mach shock and the second transverse detonation was through pressure amplification of reaction zones at burned and unburned gas interfaces behind Mach shocks and in the presence of ignition delay time gradients. In this mechanism, the passing of the transverse shock wave over the burned and unburned gas interface leads to enhanced combustion rates through Richtmyer-Meshkov instabilities, which generates the pressure necessary to amplify into a coupled shock and reaction zone or detonation. An analysis of the transverse detonations and triple points revealed that both detonations are CJ detonations relative to the shocked and unburned gas mixture into which they propagate. However, unlike the triple point attached to the first transverse detonation, which propagates at the CJ speed of the quiescent mixture, the second triple point was found to be overdriven. For the second triple point, the overdriven speed was found to be due to the confinement of the shocked gas by the boundary, which forces the direction of the shocked wave and, therefore, the gas velocity vector.

Chapter 6

DETONATION WAVE INTERACTION WITH A SINGLE HALF-CYLINDER OBSTACLE

To further validate the four-step model, our research group previously investigated the re-initiation of a quenched detonation wave following its interaction with a half-cylinder obstacle [51]. The numerical study is based on the well-known experiments conducted by Bhattacharjee et al. [15] for detonations initiated in stoichiometric methane–oxygen mixtures. The study demonstrated the capabilities of the four-step model by replicating the different regimes of detonation behavior observed in the experiments. Six distinct regimes were observed numerically depending on the initial mixture quiescent pressure. These include (1) detonation quenching, (2) critical ignition without detonations, (3) critical detonation re-initiation (CDR), (4) critical detonation re-initiation without transverse detonation (CDR-NTD), (5) critical transmission, and (6) unattenuated detonation transmission. These results are summarized in Fig. 6.1, where a comparison between experimental results and numerically observed flow fields is drawn. The numerical study revealed that in the critical limit where the detonation was completely quenched and then re-initiated, the re-initiation was usually via a transverse detonation wave as shown in Fig. 6.1c. Although re-initiation without a transverse detonation is possible (i.e., CDR-NTD regime shown in Figure. 6.1d), this outcome was rarely observed in the experiments and numerical simulations. In the current Chapter, the author expands on these results to investigate the mechanisms by which the transverse detonation is triggered during CDR. The results presented, along with details about the remaining outcomes are available in the manuscript by Floring et al. [51].

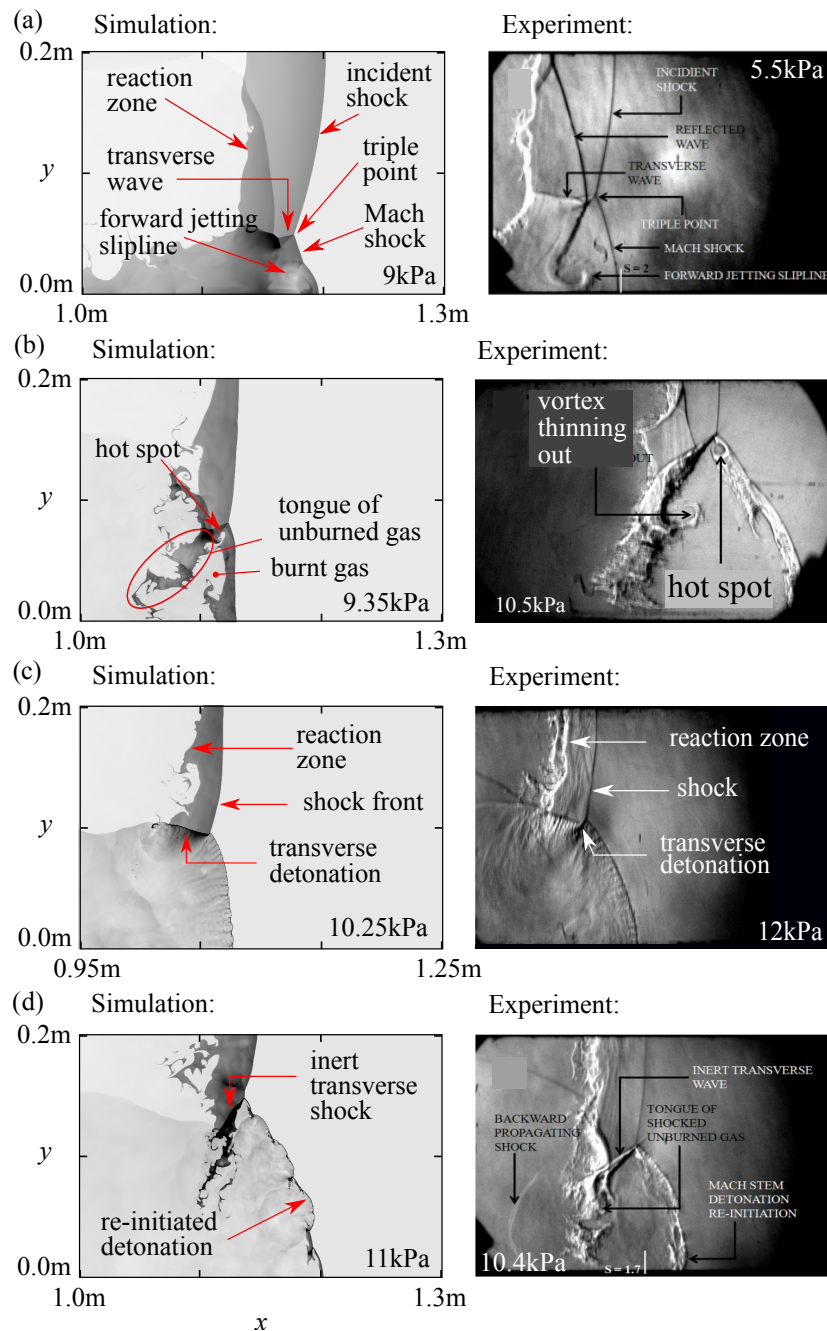


Figure 6.1: Different simulated density fields observed by Floring [52] and compared to experimental schlieren images, reproduced from Bhattacharjee [15]. (a) detonation quenching, (b) critical ignition without detonation, (c) critical detonation re-initiation, and (d) critical detonation re-initiation without transverse detonation.

6.1 Numerical Implementation

The numerical setup was chosen to mimic the experiments of Bhattacharjee [15]. As shown in Figure. 6.2, a detonation in stoichiometric methane–oxygen mixtures is simulated in a two-dimensional channel of 1.79 m length and 0.2 m height containing a half-cylinder obstacle with a radius of 150 mm. To initiate the detonation, an overdriven ZND solution ($f = 1.2$) is prescribed at $x = 0$ m. The detonation settled to within 3% of the CJ speed before interacting with the obstacle at $x = 0.5$ m. The initial temperature for all cases is $T_0 = 300$ K. Only the initial pressure was varied between cases, from $p_0 = 7$ kPa to 15 kPa. These choices of pressure were selected to observe the experiment’s different outcomes. The base grids chosen were 5 mm in size in both the x - and y - directions, with anywhere from 4 - 7 levels of refinement applied using AMR. Table 6.1 summarizes the results from the study by Floring [52], showing the pressures at which the different regimes were observed at the finest resolution of 78 μm corresponding to 7 levels of refinement.

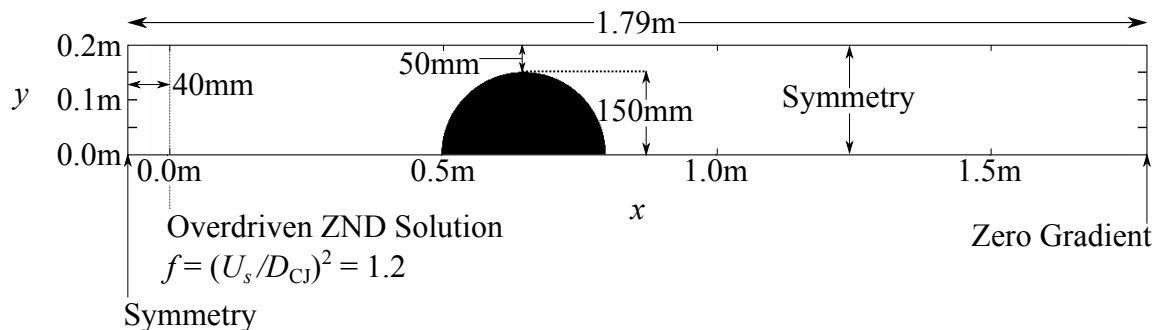


Figure 6.2: Numerical set-up used by Floring [52], with zero gradient boundary condition on the right, and symmetric elsewhere.

The numerical strategy adopted in the current study is nearly identical to the detonation diffraction study from Section. 5. The primary difference with the previous study is that, instead of the axi-symmetric formulation, the standard 2–D Euler equations in cartesian coordinates are solved to simulate the detonation propagation in a channel. Following the assumptions listed in Section. 3 to simplify the Navier-

Stokes equations, the 2–D governing equations solved for mass, momentum, total energy, and i th chemical species can be written as:

$$\frac{\partial \rho}{\partial t} + \nabla \cdot (\rho \underline{u}) = 0 \quad (6.1)$$

$$\frac{\partial (\rho \underline{u})}{\partial t} + \nabla \cdot (\rho \underline{u} \otimes \underline{u}) + \nabla p = 0 \quad (6.2)$$

$$\frac{\partial (\rho E)}{\partial t} + \nabla \cdot \left((\rho E + p) \underline{u} \right) = 0 \quad (6.3)$$

$$\frac{\partial (\rho Y_i)}{\partial t} + \nabla \cdot (\rho \underline{u} Y_i) = \dot{\omega}_i. \quad (6.4)$$

For complete details about the numerical strategy applied, including details about the grid refining criteria using AMR, and effects of grid resolution on the results, please refer to the manuscript by Floring et al. [51].

Table 6.1: Regimes observed by Floring [52] at different initial pressures at the finest resolution of 78 μm resolution.

p_0 (kPa)	CJ Speed (m/s)	Outcome
7	2301.83	Detonation quenching
8	2307.81	Detonation quenching
9	2313.1	Detonation quenching
9.15	2313.84	Detonation quenching
9.25	2314.33	Critical transmission
9.35	2314.81	Critical ignition
9.4	2315.05	Critical transmission
9.45	2315.29	Detonation quenching
9.5	2315.53	Critical detonation re-initiation
9.65	2316.23	Critical transmission
9.75	2316.7	Detonation quenching
9.85	2317.16	Unattenuated detonation transmission
10	2317.84	Critical detonation re-initiation without transverse detonation
10.25	2318.95	Critical detonation re-initiation
10.5	2320.03	Critical ignition
10.75	2321.09	Critical transmission
11	2322.13	Critical detonation re-initiation without transverse detonation
12	2326.05	Unattenuated detonation transmission
13	2329.67	Critical detonation re-initiation
14	2333.01	Unattenuated detonation transmission
15	2336.13	Unattenuated detonation transmission

6.2 Origin and Role of Transverse Detonations During Re-initiation

Critical detonation re-initiation cases involving a transverse detonation were observed for initial pressures ranging from $8.5 \leq p_0 \leq 13$ kPa at the $78 \mu\text{m}$ resolution. Although all other possible cases were observed with some random occurrence in this pressure range, this behavior is consistent with experimental observations of Bhattacharjee [15], who noted the stochastic nature of outcomes at critical pressures.

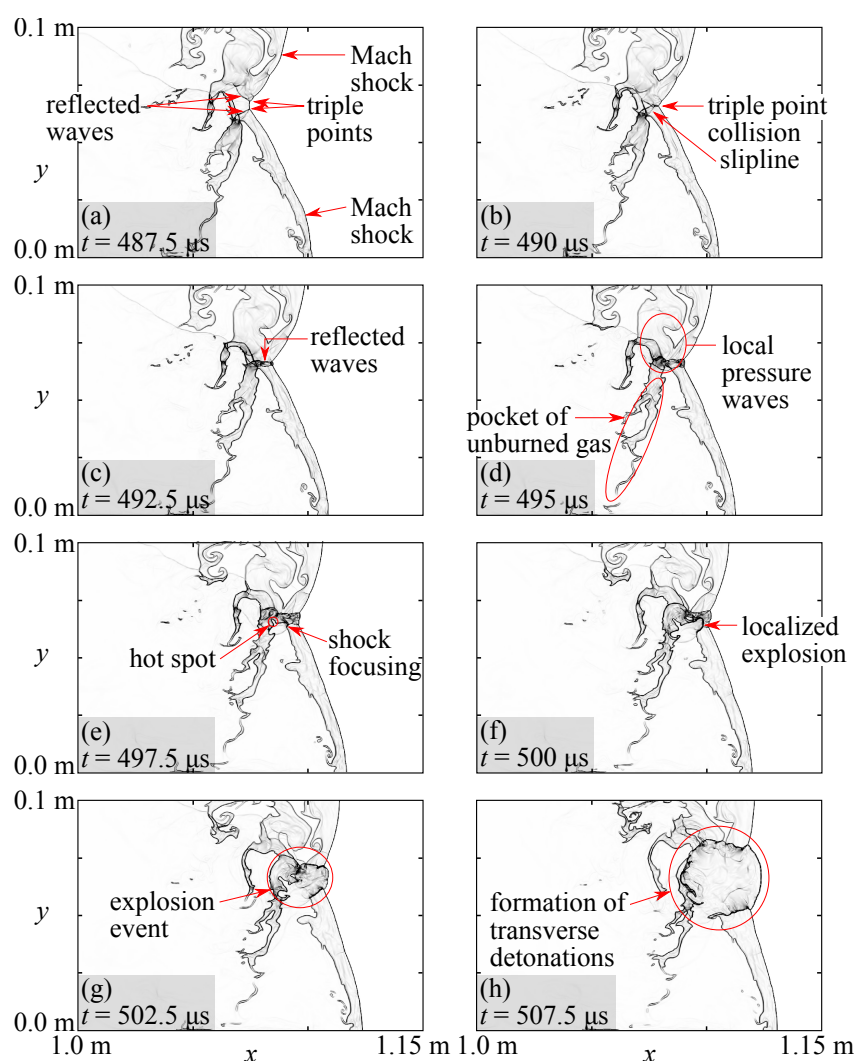


Figure 6.3: Density gradient evolution at the moment of detonation re-initiation for an initial pressure of $p_0 = 9.5$ kPa and a resolution of $78 \mu\text{m}$.

Although exact locations and timings of each detonation re-initiation event differed from simulation to simulation, it was found that in most cases detonation re-initiation occurred through a local explosion event that was triggered by the passing of a transverse pressure wave over the interface that separated burned from unburned gases. For example, a detailed sequence of events where detonation re-initiation occurred for $p_0 = 9.5$ kPa is shown in the density gradient evolution of Fig. 6.3. In Fig. 6.3a, two triple points have formed due to the propagation of reflected waves from both the top and bottom boundaries of the simulation. These triple points traveled toward each other and eventually collided, as shown in Fig. 6.3b. This caused the formation of new reflected waves with increased temperature and pressure behind them (Fig. 6.3c). At the same time, a pocket of unburned gas formed behind the various shock dynamics (Fig. 6.3d). The reflected waves propagated through areas of both shocked and unburned gas as well as the burned gas, and passed through the latter more quickly due to its lower acoustic impedance (Fig. 6.3e). The downward reflected shock wave triggered a hot spot near the reaction zone. At the same time, this shock wave, which was traveling in both the burned and unburned gases, triggered a localized explosion on the surface of the interface, as shown in Fig. 6.3f. The subsequent and nearly simultaneous detonation re-initiations along both the Mach and transverse waves are shown in Figs. 6.3g and h. These transverse detonation waves were self-sustained and continued to propagate to the upper and lower boundaries of the channel until the detonation front was completely re-established. The bulk of the pockets of unburned gas were consumed by the expanding explosion event itself and the newly formed transverse detonations. The remaining gas pockets burned up as deflagrations, which were most likely enhanced by Richtmyer-Meshkov instabilities that arose from the passage of the reflected transverse shock through the pocket surfaces. This sequence of events is in contrast to Bhattacharjee's observations, who speculated that the transverse detonations were formed as a consequence of turbulent burning of the pocket of

unburned gas [13]. Instead, the simulations show that the formation of an explosion event arising from the passing of reflected transverse waves over a burned/unburned gas surface near the Mach shock and after a triple point collision plays a key role in transverse detonation formation. In the sequence of events observed here, the burn up of the pockets of unburned gas were instead influenced by the passing of the transverse waves after the transverse detonations have formed.

To gain more clarity on the formation of the detonation waves observed in Fig. 6.3, detailed temperature, pressure, and local ignition delay time profiles are shown in Fig. 6.4 for the moments where detonation initiation occurred. In frame (a), at $t = 495 \mu\text{s}$, the downward propagating transverse shock wave (sw) passed over the burned and unburned gas interface. This led to the rapid growth of the existing flame surface, or hot spot (hs1). At $t = 497.5 \mu\text{s}$, the rapid energy release in this region led to the localized formation of increased pressure, as seen in the pressure plot of frame (b). The growth of hot spot (hs1) spread faster in the region of lower ignition delay times, but the increased pressure also directly coupled the rapid chemical reactions to the downward propagating transverse shock wave. The transverse detonation (d1) thus appears to have been initiated directly by the passing of the transverse shock over the burned/unburned gas interface, which led to a local pressure amplification and rapid coupling of the shock and reaction zone. The detonation (d2), on the other hand, appears to have formed through amplification of pressure through the spread of the hot spot (hs1) into the gas which contained favorable ignition delay times behind the Mach shock. In fact, the ignition delay times behind the Mach shock were so short, that auto-ignition of new hot spots, such as hot spot (hs2), was possible. Figure 6.5 shows the temperature, pressure, and $\log(\text{ignition delay})$ profiles at different times along the horizontal dashed line shown in Fig. 6.4a, at $y = 0.064 \text{ m}$. According to the pressure profiles, the explosion hot spot (hs1) clearly experienced a pressure amplification through time. As the wave propagated against the ignition delay time gradient, shown in the ignition

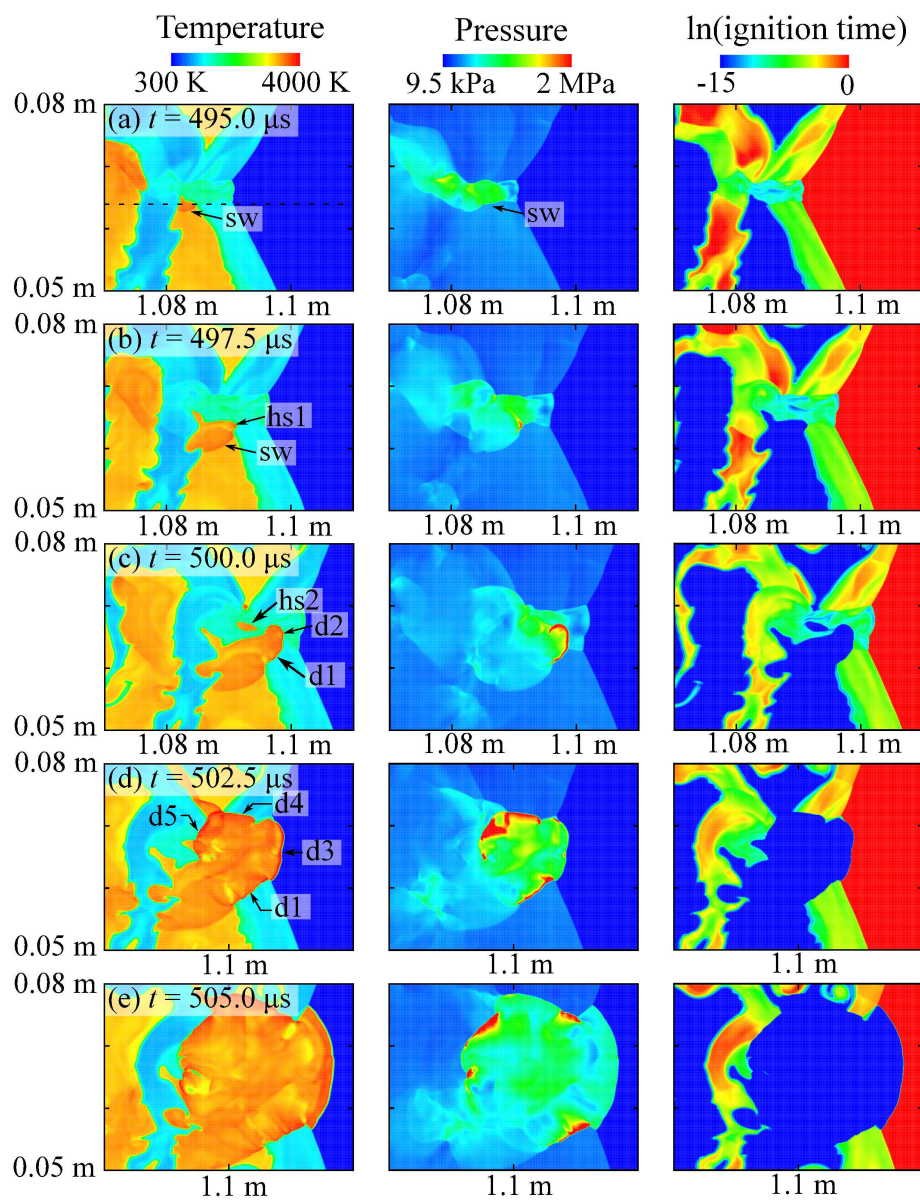


Figure 6.4: Details of temperature, pressure, and ignition delay times for detonation re-initiation of $p_0 = 9.5 \text{ kPa}$ and a resolution of $78 \mu\text{m}$.

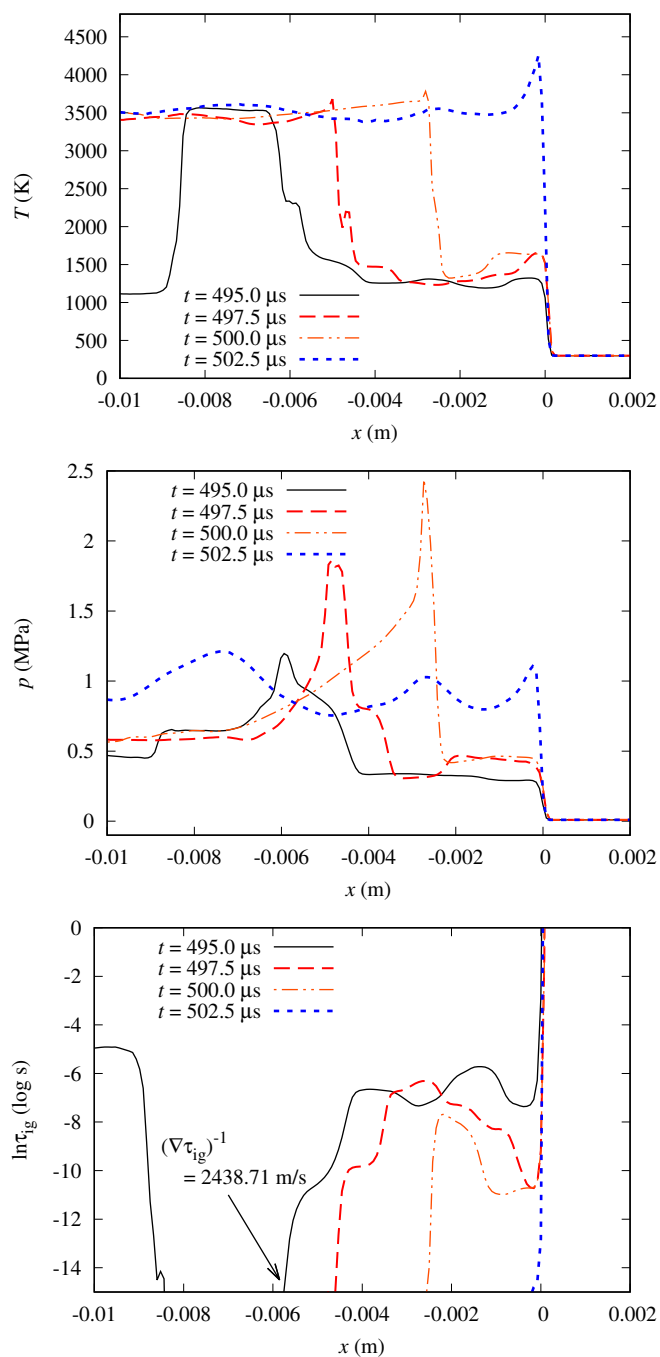


Figure 6.5: Temperature, pressure, and ignition delay time profiles measured along $y = 0.064 \text{ m}$ (the dashed line indicated in Fig. 6.4a) for $p_0 = 9.5 \text{ kPa}$. Distances are given in the frame of reference of the Mach shock.

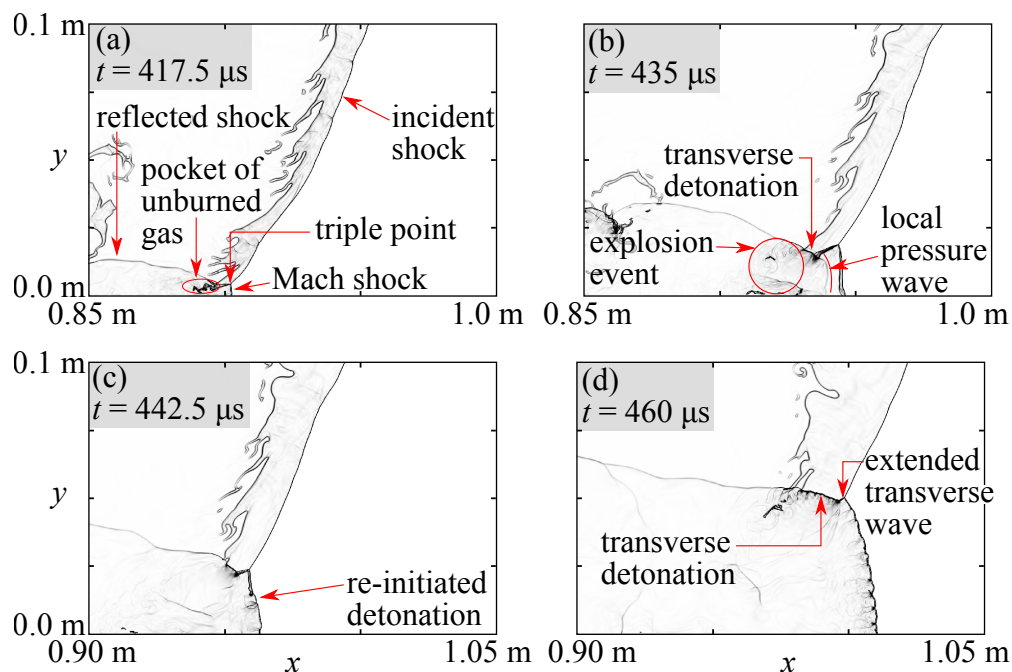


Figure 6.6: Density gradient evolution at the moment of detonation re-initiation for an initial pressure of $p_0 = 10.25$ kPa and a resolution of $78 \mu\text{m}$.

delay time profiles, further amplification of the pressure wave occurred. The mechanism of detonation initiation then resembles the SWACER mechanism [107], with the initial explosion driven and enhanced through Richtmyer-Meshkov instabilities by the passing of an external shock wave over an existing hot spot. Upon measuring the ignition delay time gradient ahead of the reaction wave, it was found that the inverse of the ignition delay was $(\nabla\tau_{\text{ig}})^{-1} \sim 2400$ m/s only right before the wave front, at all times. Ahead of the wave, $(\nabla\tau_{\text{ig}})^{-1}$ was only $\mathcal{O}(1 \text{ to } 100)$ m/s, consistent with the past work of Kuznetsov et al. [95]. Non-uniformities were noted in the ignition delay time profiles of Figs. 6.4 and 6.5, and that such gradients may have promoted the propagation of the reaction wave until a sustained detonation has formed [165]. In this case, the detonation front (d2) eventually propagated outward in every direction and reached the Mach shock and upper transverse shock, where the problem became one of detonation transmission from one fluid to another.

The case of $p_0 = 10.25$ kPa had a slightly different sequence of events, as shown

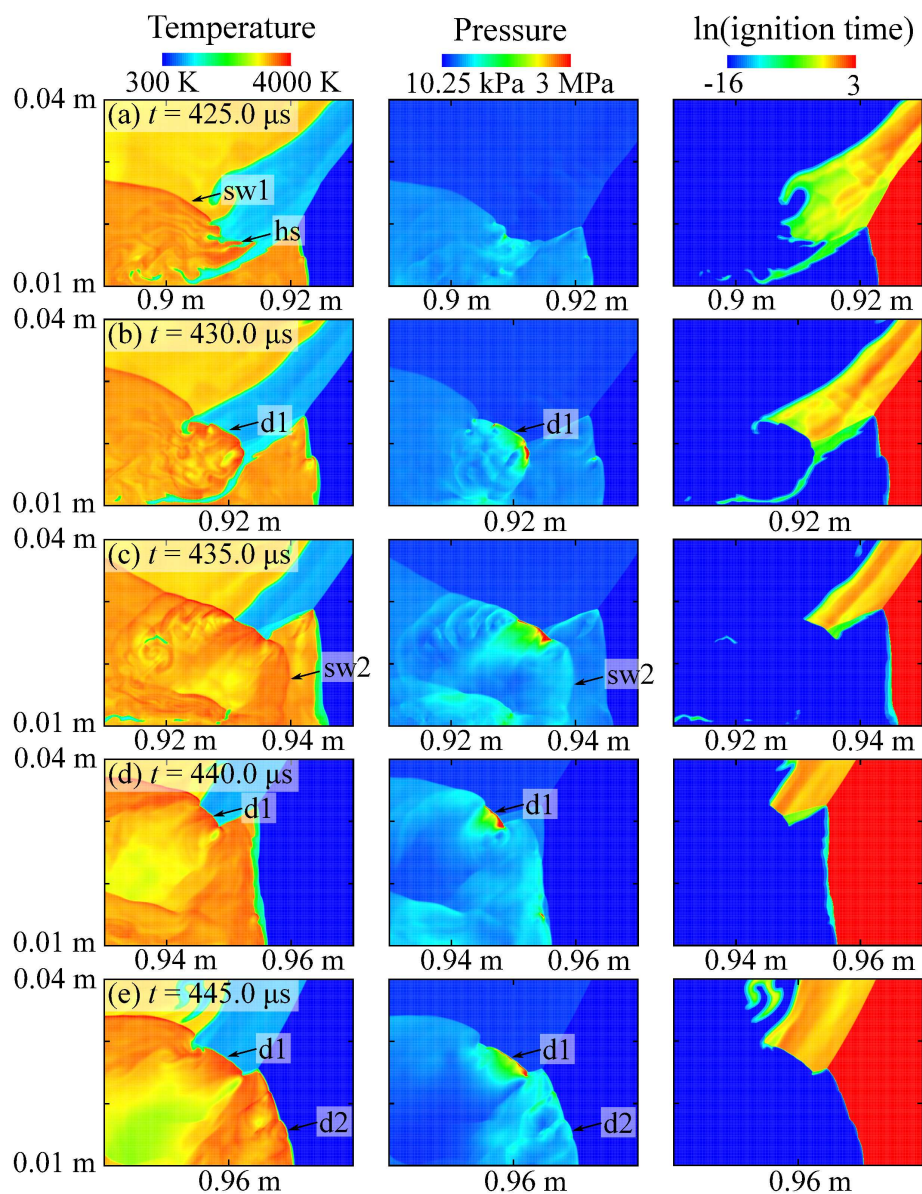


Figure 6.7: Details of temperature, pressure, and ignition delay times for detonation re-initiation of $p_0 = 10.25$ kPa and a resolution of $78 \mu\text{m}$.

in Figs. 6.6 and 6.4. Instead of detonation re-initiation forming behind the collision of two reflected waves propagating toward each other, the detonation re-initiated behind the transverse shock reflection on the bottom boundary. The different outcomes of reflected wave patterns at different pressures is not surprising, as the evolution of shock reflections and triple point locations are likely influenced by the cellular structure of the detonation prior to quenching. Moreover, it is well known that the detonation cellular structure has a strong dependence on pressure [81]. Figure 6.6a shows the initial formation of the reflected transverse shock, Mach shock, and triple point. An explosion event occurred on the surface of the pocket of unburned reactive gas as a result of the passing of the reflected shock wave. This explosion event triggered a transverse detonation wave and also generated local pressure waves that propagated outward toward the Mach shock (Fig. 6.6b). The explosion event also directly consumed the pocket of unburned gas. The supported Mach shock transitioned into a self-sustaining detonation wave as shown in Fig. 6.6c. At the same time, the transverse detonation wave continued to consume shocked but unburned gas behind the incident shock wave (Fig. 6.6d). The details of the detonation initiation, in this case, are revealed in Fig. 6.7. In this case, and much like the 9.5 kPa case discussed previously, the reflected transverse shock (sw1) passed over the burned/unburned gas interface. As a result, the reaction rate of hot spot (hs) was enhanced by Richtmyer-Meshkov instabilities, which generated a local pressure rise as observed in the pressure plot of Fig. 6.7b. This led to the direct rapid coupling of transverse shock and reaction zone, which thus initiated the transverse detonation (d1). In Fig. 6.7c, a shock wave (sw2), generated from the local explosion of the hot spot (hs), propagated towards the Mach shock. At first this shock travelled in the burned gas, but then initiated the detonation along the Mach shock (d2) through pressure amplification in a short region of shocked and unburned gas that contained gradients in ignition delay times. This can be seen in Figs. 6.7d and e.

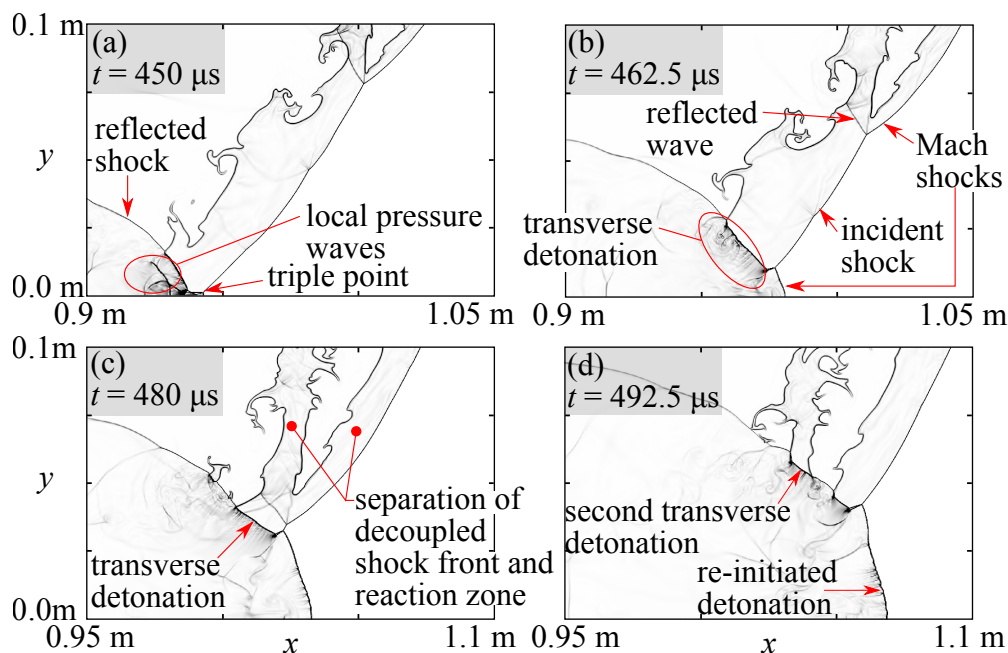


Figure 6.8: Density gradient evolution at the moment of detonation re-initiation for an initial pressure of $p_0 = 13$ kPa and a resolution of $78 \mu\text{m}$.

At elevated pressures, the transverse detonation was observed to form shortly after from the initial shock reflection on the bottom wall. This is shown for $p_0 = 13$ kPa in the density gradient evolution of Fig. 6.8. This rapid initiation of the transverse detonation wave appears to be similar to the formation previously shown by Lau-Chapdelaine [98], who observed a transverse detonation initiation directly from the shock reflection using a two-step model at $p_0 = 13.9$ kPa. However, in this past work, the transverse detonation was not self-sustained as it was in this current study. A main difference in this case compared to the other two cases discussed above is the split in the decoupled shock front and the reaction zone, or a pocket that formed from the shock reflection from the top wall. This created two zones of shocked yet unreacted gas (Fig. 6.8c). Because of this, two transverse detonations formed that originated from the bottom of the channel (Fig. 6.8d). The second transverse detonation served to consume the second decoupled reaction zone (the pocket), and disappeared after that. The details of the detonation initiation, in this

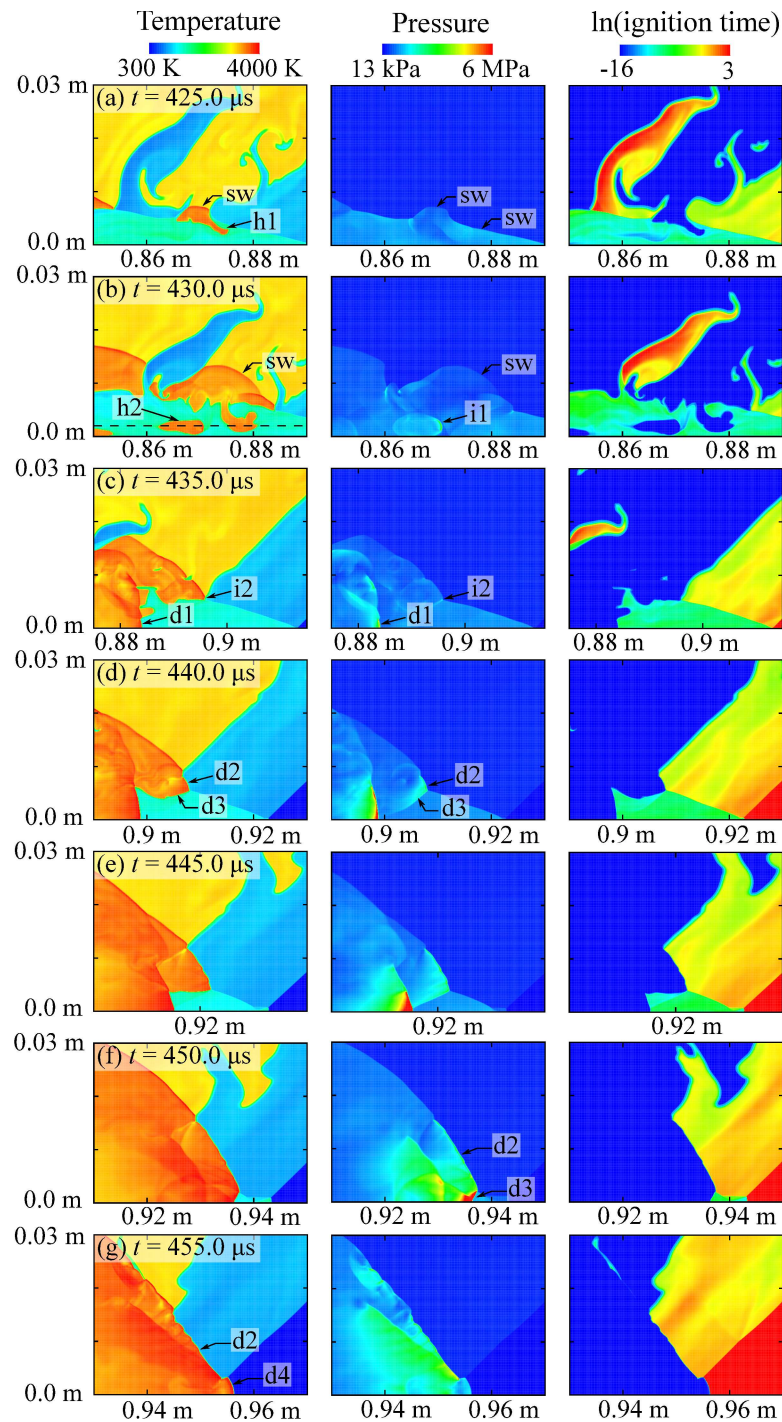


Figure 6.9: Details of temperature, pressure, and ignition delay times for detonation re-initiation of $p_0 = 13 \text{ kPa}$ and a resolution of $78 \mu\text{m}$.

case, are shown in Fig. 6.9. Much like the previous two cases, the reflected transverse shock (sw) passed over a burned/unburned gas interface, enhancing its combustion and increased reaction rate through Richtmyer-Meshkov instabilities. This led to the rapid growth of the shocked hot spot (h1) into the gas with a favourable ignition delay time, as shown in Fig. 6.9a. Much like the 9.5 kPa case, a hot spot (h2) was formed spontaneously in the region of lowest ignition delay, as shown in Fig. 6.9b. In this case, however, the rapid ignition of the newly formed hot spot (h2) was sufficient to trigger a pressure increase locally where shown (i1). In fact, this hot spot was found to transition to detonation (d1) through the same pressure amplification mechanism previously shown for the 9.5 kPa case. This is shown in Fig. 6.10, which shows the temperature, pressure, and $\log(\text{ignition delay})$ profiles at different times along the horizontal dashed line shown in Fig. 6.9b, at $y = 0.002$ m. In fact, early on at $t = 427.5 \mu\text{s}$, $(\nabla \tau_{\text{ig}})^{-1} = 3746.15$ m/s at the ignition spot (i1). Since $(\nabla \tau_{\text{ig}})^{-1} > U_{\text{CJ}}$, a spontaneous wave was able to form, which eventually developed into the detonation (d1). In Fig. 6.9c another region of increased pressure was generated where the transverse shown (sw) met with an unburned/burned gas interface. This ignition spot (i2) led to the direct coupling of shock and reaction zone, which thus initiated detonations (d2) and (d3) shown in Fig. 6.9d. In fact, while (d2) was initiated directly from the rapid compression and energy deposition, (d3) was found to also develop through the pressure amplification mechanism into the gas containing mild gradients of ignition delay times. Eventually it was detonation (d3) that was able to first reach the Mach shock to initiate the self-sustained detonation (d4). Although detonation on the Mach shock, in all of the cases presented above, originated by the passing of a transverse shock on a burned/unburned gas interface, we do note that it is possible for a detonation to be initiated by the spontaneous formation of a hot spot through the Zeldovich gradient mechanism [165, 250], such as the formation of detonation (d1) discussed here. In all situations, however, pressure amplification of reactive waves was found to be a common

feature in the re-establishment of the detonation wave in the CDR regime.

6.3 Conclusion

In this section, the four-step model was used to investigate critical detonation attenuation, and the role of transverse detonations during its re-establishment following its interaction with obstacles [15]. The results demonstrated that the application of this minimal global combustion model is able to capture the sustained transverse detonation feature in this scenario, unlike past applications of simple one- and two-step combustion schemes [14, 98]. This is due to the relatively simple four-step model containing an adequate description to permit the correct ignition and thermodynamic state response when changes in temperature and pressure occur [171], i.e. behind shocks and reflected shocks. This appears to be required not only to capture the transverse detonation but also to capture the less frequent situations where detonation re-initiation occurs without a transverse detonation. In both of these cases, accurate treatment of ignition delay time behind shock compression is important, which is unlikely to have been predicted accurately using one- and two-step combustion models.

For the critical detonation re-initiation outcome, it was found that one principal mechanism through which transverse detonations and detonations along the Mach shock can form is through pressure amplification of reaction zones at burned and unburned gas interfaces behind Mach shocks and in the presence of ignition delay time gradients. In this mechanism, the passing of the transverse shock wave over the burned and unburned gas interface leads to enhanced combustion rates through Richtmyer-Meshkov instabilities, which generates the pressure necessary to amplify into a coupled shock and reaction zone, or detonation. These detonations are also possible to form through spontaneous ignition of the gas, i.e. from a hot spot formed by the passing of transverse shocks in regions of lowest ignition delay times, which can ultimately form through the Zeldovich gradient mechanism [250].

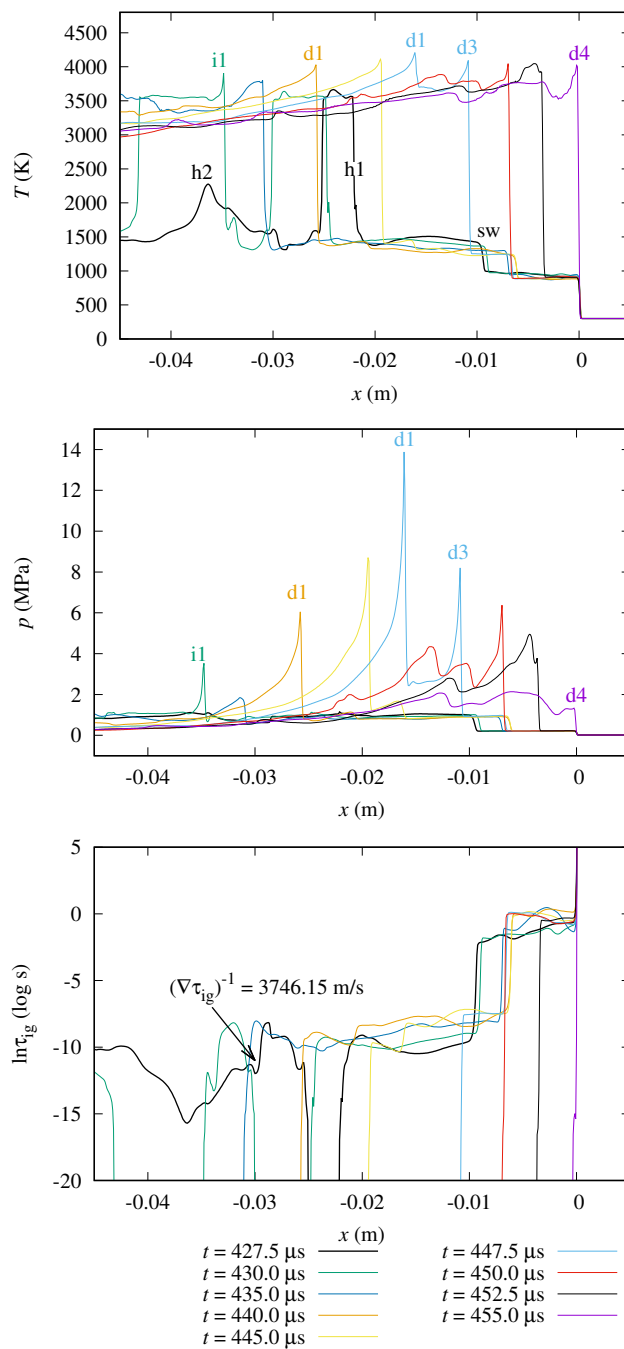


Figure 6.10: Temperature, pressure, and ignition delay time profiles measured along $y = 0.002$ m (the dashed line indicated in Fig. 6.9b) for $p_0 = 13$ kPa. Distances are given in the frame of reference of the Mach shock.

Finally, the simulations have revealed that while pockets of unburned gas may exist when transverse detonations occur, it is not the direct burn-up of these pockets that give rise to transverse detonations as previously suspected. Instead, the pockets of unburned gas are consumed by their own deflagrative burning or by the passing of such transverse detonation waves.

Chapter 7

CONCLUSIONS AND RECOMMENDATIONS FOR FUTURE WORK

As highlighted in the literature review presented in Chapter 2, a fundamental drawback in numerical studies investigating FA and DDT is a lack of chemical accuracy through the adoption of simple one- and two-step global reaction mechanisms (GRMs). Since adopting elementary reaction mechanisms (ERMs) is still unfeasible for most laboratory-scale studies, in the current work, a four-step combustion model for premixed hydrocarbon mixtures has been developed for investigating detonation propagation and the late stages of DDT. The model development is an extension of the work by Zhu et al. [253], whose capabilities were previously only verified for detonations initiated in stoichiometric premixed acetylene–oxygen mixtures. In this work, a large focus has been on highlighting the model’s capability as an effective and economical chemical modeling approach for detonation studies. In Chapter 4, a series of 0–D and 1–D combustion problems were conducted using the model, and the results were validated against predictions using elementary reaction mechanisms (ERMs). As part of further validating the model, in Chapters 5 and 6, the combustion model was coupled to a CFD solver to numerically study the re-initiation of quenched detonations following diffraction and detonation interaction with a single cylindrical obstacle. A key feature investigated in both studies is the re-initiation of the quenched detonation wave by transverse detonations, which has not been adequately investigated in previous numerical studies.

7.1 Conclusions

The current section outlines the major conclusions from the current work. Since simple GRMs have previously proven insufficient for providing the appropriate

chemical accuracy to model highly compressible and reactive flows, the four-step model was found to be an affordable yet accurate alternative to ERM, particularly for hydrocarbon combustion. By utilizing the thermochemical approach, the model was found to provide the correct thermodynamic response throughout a constant volume ignition process. This results in the model correctly predicting the reaction zone structure behind a shock wave, and as a result, the correct detonation CJ speed. Moreover, compared with the results from detailed chemistry ERMs, the model was also found to correctly predict key combustion properties crucial for numerical simulations of detonation waves. For all the different properties considered, the maximum error between the four-step model and the results from ERMs was found to be within 35%. However, the maximum errors were observed for properties that included multiple individual parameters.

In both studies where the four-step model was used, it was found that the detonation re-initiation invariably occurred due to transverse detonation waves. Unlike previous studies involving simple one- or two-step models, sustained transverse detonations were successfully observed. It was also found that the re-establishment of a sustained detonation wave in both studies was triggered by gradients observed in the ignition delay time in front of the shock wave. Perhaps the past applications of one- and two-step combustion models to this scenario did not contain sufficiently steep gradients in ignition delay times to trigger or sustain transverse detonations. Since the four-step model applied gives rise to ignition delay times that effectively respond appropriately to changes in the thermodynamic state, when compared to detailed chemistry, detonations can likely form in shallower ignition delay time gradients compared to the past one- and two-step modeling approaches. It is then concluded that in order to observe these features, a combustion model should, at the minimum, contain an adequate thermodynamic response when changes in pressure and temperature occur. Apart from the transverse detonation, an adequate chemistry description also appears to be necessary to predict the correct re-initiation

length and wall reflection distance for the detonation diffraction study as well as to capture the less frequent situation where detonation re-initiation occurs without a transverse detonation following its interaction with an obstacle.

7.2 Recommendations

The recommendations proposed here are to further advance the application of the four-step combustion model and suggest improvements to the numerical strategy in future studies investigating detonation re-initiation. First, the primary deficiency of the four-step model is its inability to model combustion in fuel rich reactive mixtures where the reactant is not completely consumed during the ignition process. One way to address this would be by modeling the fuel and oxidizer as separate species during the reaction instead of a single global reactant. It would then be possible to model the equilibrium regime of the reaction while accounting for the dissociation of the reacting fuel in the final mixture. It remains to be seen if the equilibrium composition of fuel rich mixtures can be correlated to the local thermal state, which is the strategy currently utilized in the model to predict the equilibrium mole fraction of the products [253]. While adding an additional species to the model would increase its cost and complexity, if successfully executed, it would significantly advance the applicability of the combustion model. The model could then predict combustion not only in fuel rich mixtures but also be used to model hydrogen combustion and combustion in mixtures that exhibit non-monotonic chain branching behavior where the reaction invariably ends up outside of the explosion limit curve. Alternate applications of the four-step model include modeling combustion for long-chain hydrocarbons such as jet-fuel surrogates and oxygenated fuels (alcohols and ethers). Although a thorough analysis of the applicability of the model for these reactive mixtures is out of the scope of the current study and left for future investigation, preliminary results indicate that the equilibrium mixtures of these fuels after combustion do indeed exhibit a degree of regularity in compo-

sition which is needed to formulate the species in the four-step model. As a result, the four-step model is expected to predict the initial and terminal states of the combustion in these fuels reasonably well.

While a good qualitative agreement with experiments was observed in both numerical studies, it is important to acknowledge that the results using the current numerical strategy cannot be used in a purely predictive manner for detonation reinitiation. In both studies, the different regimes were observed at lower pressures numerically compared to the experiments, in part, due to the cell size enlargement associated with losses and velocity deficits observed in experiments. It must also be acknowledged that closure of turbulent mixing is likely important during the reinitiation of the detonation wave, as previously highlighted by Maxwell et al. [137]. In fact, it has been demonstrated that for hydrocarbon mixtures that exhibit an irregular detonation structure, closure of subgrid-scale turbulent mixing is required to resolve the correct cell size. Since the outcome in both numerical studies is driven by the detonation cell size, it is recommended that molecular diffusion, boundary layer effects, and turbulence be accounted for in future studies investigating the problems. Since DNS is not amenable to most practical problems, it is recommended that in future studies, the four-step model is coupled to the compressible linear eddy model for large eddy simulation (CLEM-LES) approach. Finally, DNS and large-scale LES studies of FA and DDT have highlighted the need for three-dimensional geometries in numerical studies [59, 69, 86, 125]. In fact, different FA rates and mechanisms by which detonations occur were noted compared to two-dimensional simulations [59, 69]. It is likely that the additional degree of freedom alters the flame and shock dynamics through transverse waves in the third dimension leading to enhanced turbulence generation. It is then recommended that future numerical investigations using the four-step model account for the multidimensional structure of propagating detonations.

Appendix A

IMPORTANT FOUR-STEP MODEL EQUATIONS

Equilibrium mole fraction

$$\left\{ \begin{array}{l} \lambda_{eP1} = \left(1 + \exp[-\eta \cdot (\beta_0 + \beta_1 \cdot \eta + \beta_2 \cdot \eta^2)] \right)^{-1} \\ \lambda_{eP2} = 1.0 - \lambda_{eP1} \\ \text{where:} \\ \eta = \frac{10^2 \cdot \xi - (\alpha_1 + \alpha_2 \cdot \theta)}{\delta_0 + \delta_1 \cdot \theta + \delta_2 \cdot \theta^2} \\ \theta = \ln \rho \\ \xi = 10^3 / T(K) \end{array} \right. \quad (\text{A.1})$$

α, β, δ are the equilibrium relation coefficients.

Equilibrium constant (K_c)

$$\left\{ \begin{array}{l} K_c = \left(\frac{[P2]_e^{\delta_3}}{[P1]_e} \right)^{1/s_3} \\ \text{where : } [X]_e = \lambda_{eX} \cdot \frac{\rho_{P1} + \rho_{P2}}{W_{P1} + W_{P2}} \end{array} \right. \quad (\text{A.2})$$

Rate constants for the equilibrium reaction (e)

$$\left\{ \begin{array}{l} k_{ef} = A \cdot \rho^m \cdot T^n \cdot \exp\left(\frac{E_a \cdot T_0}{T}\right) \\ k_{er} = k_{ef} / K_c \\ \text{where : } T_0 = 298.0 \text{ K} \\ \text{and } A, m, n, E_a : \text{ Constants from the curve fitting procedure.} \end{array} \right. \quad (\text{A.3})$$

A, m, n, E_a are the constants from the curve fitting procedure.

Rate constants for reactions (r1) and (r2)

$$\left\{ \begin{array}{l} k_{r1} = \phi_{r1} \cdot k_{r1H} + (1 - \phi_{r1}) \cdot k_{r1L} \\ k_{r2} = \phi_{r2} \cdot k_{r2H} + (1 - \phi_{r2}) \cdot k_{r2L} \\ k_{rH} = A \cdot \rho^m \cdot T^n \cdot \exp\left(\frac{E_a \cdot T_0}{T}\right) \\ k_{rL} = A \cdot \rho^m \cdot T^n \cdot \exp\left(\frac{E_a \cdot T_0}{T}\right) \\ \text{where : } \phi = \left(1 + \exp(\mu \cdot (\xi - \xi_c))\right)^{-1} \end{array} \right. \quad (\text{A.4})$$

ϕ : Transit function ; μ : Transit function slope ; ξ_c : Value of ξ where $\phi = 0.5$.

Rate constant for reactions (i1) and (i2)

$$\left\{ \begin{array}{l} k_i = \phi_i \cdot k_{iH} + (1 - \phi_i) \cdot k_{iL} \\ k_{iH} = A \cdot \rho^m \cdot T^n \cdot \exp\left(\frac{E_a \cdot T_0}{T}\right) \\ k_{iL} = A \cdot \rho^m \cdot T^n \cdot \exp\left(\frac{E_a \cdot T_0}{T}\right) \\ \text{where : } \phi = \left(1 + \exp(\mu \cdot (\xi - \xi_c))\right)^{-1} \end{array} \right. \quad (\text{A.5})$$

Appendix B

FOUR-STEP MODEL PARAMETERS FOR THE DIFFERENT MIXTURES CONSIDERED IN SECTION 4

Following the nomenclature adopted by Zhu [253], the model parameters for the different hydrocarbons are summarized in this section.

B.1 Stoichiometric acetylene-oxygen mixture

Reactants : $2\text{C}_2\text{H}_2 + 5\text{O}_2$

Mechanism : Konnov [34]

Equilibrium relation coefficients:

$$\left\{ \begin{array}{ll} \alpha_1 = 26.966 & \alpha_2 = -1.7044 \\ \beta_0 = 3.7136 & \beta_1 = -1.4730 \\ \beta_2 = 1.0328 & \delta_0 = 15.7345 \\ \delta_1 = 0.2625 & \delta_2 = 0.0048 \end{array} \right.$$

Reaction orders:

$$\left\{ \begin{array}{ll} s_0 = 0.339 & s_1 = 0.867 \\ s_2 = 0.867 & s_3 = 1.09 \end{array} \right.$$

$$k_{\text{ef}} = 2.88 \times 10^{30} \rho^{0.925} T^{-4.826} \cdot \exp\left(\frac{-235.76T_0}{T}\right)$$

$$k_{r1} \begin{cases} k_{r1H} = 1.31 \times 10^9 \rho^{1.081} \cdot \exp\left(\frac{-26.91T_0}{T}\right) \\ k_{r1L} = 1.339 \times 10^9 \rho^{1.084} \cdot \exp\left(\frac{-43.56T_0}{T}\right) \\ \mu_{r1} = 50.0; \quad \xi_{c1} = 0.115 + \frac{0.088}{\rho^{0.1}} \end{cases}$$

$$k_{r2} \begin{cases} k_{r2H} = 1.394 \times 10^9 \rho^{1.087} \cdot \exp\left(\frac{-32.2T_0}{T}\right) \\ k_{r2L} = 8.298 \times 10^8 \rho^{1.071} \cdot \exp\left(\frac{-47.67T_0}{T}\right) \\ \mu_{r2} = 45.0; \quad \xi_{c2} = 0.1296 + \frac{0.096}{\rho^{0.1}} \end{cases}$$

$$k_i \begin{cases} k_{iH} = 1.127 \times 10^{-2} \rho^{0.658} T^{2.94} \cdot \exp\left(\frac{-11.24T_0}{T}\right) \\ k_{iL} = 8.298 \times 10^8 \rho^{1.071} \cdot \exp\left(\frac{-47.67T_0}{T}\right) \\ \mu_i = 0.0028\rho^5 + 0.01038\rho^4 - 0.054619\rho^3 + 0.4165\rho^2 - 3.0473\rho + 20.00 \\ \xi_{ci} = 0.0002654588\rho^3 + 0.0010179\rho^2 - 0.0753064\rho + 0.80079 \end{cases}$$

B.1.1 Stoichiometric methane-oxygen mixture

Reactants : $\text{CH}_4 + 2\text{O}_2$

Mechanism : GRI-3.0 [208]

Equilibrium relation coefficients:

$$\begin{cases} \alpha_1 = 25.4105 & \alpha_2 = -1.7502 \\ \beta_0 = 3.7696 & \beta_1 = -0.9962 \\ \beta_2 = 0.4663 & \delta_0 = 14.457 \\ \delta_1 = 0.28865 & \delta_2 = 0.00686 \end{cases}$$

Reaction orders:

$$\begin{cases} s_0 = 0.3727 & s_1 = 0.724 \\ s_2 = 0.724 & s_3 = 1.026 \end{cases}$$

$$k_{\text{ef}} = 2.645 \times 10^{33} \rho^{0.9726} T^{-5.471} \cdot \exp\left(\frac{-244.5T_0}{T}\right)$$

$$k_{\text{r1}} \begin{cases} k_{\text{r1H}} = 1.414 \times 10^{10} \rho^{1.267} \cdot \exp\left(\frac{-58.48T_0}{T}\right) \\ k_{\text{r1L}} = 2.394 \times 10^9 \rho^{1.304} \cdot \exp\left(\frac{-55.65T_0}{T}\right) \\ \mu_{\text{r1}} = 26.632; \quad \xi_{\text{c1}} = 0.279 + \frac{0.048}{\rho^{0.1}} \end{cases}$$

$$k_{\text{r2}} \begin{cases} k_{\text{r2H}} = 5.056 \times 10^9 \rho^{1.266} \cdot \exp\left(\frac{-59.98T_0}{T}\right) \\ k_{\text{r2L}} = 1.124 \times 10^9 \rho^{1.308} \cdot \exp\left(\frac{-61.49T_0}{T}\right) \\ \mu_{\text{r2}} = 25.74; \quad \xi_{\text{c2}} = 0.3107 + \frac{0.0282}{\rho^{0.1}} \end{cases}$$

$$k_{\text{i}} \begin{cases} k_{\text{iH}} = 8.555 \times 10^{11} \rho^{0.621} T^{-0.6011} \cdot \exp\left(\frac{-68.967T_0}{T}\right) \\ k_{\text{iL}} = 9.908 \times 10^8 \rho^{0.4269} \cdot \exp\left(\frac{-68.9189T_0}{T}\right) \\ \mu_{\text{i}} = -0.000451\rho^5 + 0.00222\rho^4 + 0.06997\rho^3 - 0.2004\rho^2 - 1.878\rho + 11.00 \\ \xi_{\text{ci}} = 0.00035647\rho^3 - 0.003383\rho^2 - 0.0513858\rho + 0.52555 \end{cases}$$

B.1.2 Stoichiometric propane-oxygen mixture

Reactants : $\text{C}_3\text{H}_8 + 5\text{O}_2$

Mechanism : USC II [232]

Equilibrium relation coefficients:

$$\left\{ \begin{array}{ll} \alpha_1 = 25.87966 & \alpha_2 = -1.735998 \\ \beta_0 = 2.2067 & \beta_1 = -0.47167 \\ \beta_2 = 0.1751 & \delta_0 = 9.11008 \\ \delta_1 = 0.18916 & \delta_2 = 0.003929 \end{array} \right.$$

Reaction orders:

$$\left\{ \begin{array}{ll} s_0 = 0.339 & s_1 = 0.85 \\ s_2 = 0.85 & s_3 = 1.01 \end{array} \right.$$

$$k_{\text{ef}} = 2.284 \times 10^{27} \rho^{0.986} T^{-4.051} \cdot \exp\left(\frac{-221.1T_0}{T}\right)$$

$$k_{r1} \left\{ \begin{array}{l} k_{r1H} = 2.925 \times 10^9 \rho^{1.065} \cdot \exp\left(\frac{-47.53T_0}{T}\right) \\ k_{r1L} = 3.122 \times 10^9 \rho^{0.9339} \cdot \exp\left(\frac{-53.09T_0}{T}\right) \\ \mu_{r1} = 61.895; \quad \xi_{c1} = 0.234 + \frac{0.0777}{\rho^{0.1}} \end{array} \right.$$

$$k_{r2} \left\{ \begin{array}{l} k_{r2H} = 2.126 \times 10^9 \rho^{1.116} \cdot \exp\left(\frac{-58.63T_0}{T}\right) \\ k_{r2L} = 8.351 \times 10^8 \rho^{0.928} \cdot \exp\left(\frac{-52.58T_0}{T}\right) \\ \mu_{r2} = 17.029; \quad \xi_{c2} = 0.2286 + \frac{0.0648}{\rho^{0.1}} \end{array} \right.$$

$$k_i \left\{ \begin{array}{l} k_{iH} = 2997445.79311 \times 10^9 \rho^{.625} T^{0.522} \cdot \exp\left(\frac{-31.508T_0}{T}\right) \\ k_{iL} = 45563 \times 10^8 \rho^{0.43307} \cdot \exp\left(\frac{-67.1979T_0}{T}\right) \\ \mu_i = 0.00183\rho^5 + 0.0099\rho^4 - 0.0758\rho^3 - 0.4527\rho^2 + 0.3503\rho + 26.12 \\ \xi_{ci} = -0.00016686\rho^3 - 0.00219299\rho^2 - 0.024983\rho + 0.578888 \end{array} \right.$$

B.1.3 Stoichiometric ethylene-oxygen mixture

Reactants : $C_2H_4 + 3O_2$

Mechanism : USC II [232]

Equilibrium relation coefficients:

$$\begin{cases} \alpha_1 = 26.19335 & \alpha_2 = -1.72655 \\ \beta_0 = 3.391898 & \beta_1 = -1.13166 \\ \beta_2 = 0.694805 & \delta_0 = 14.2155 \\ \delta_1 = 0.25896 & \delta_2 = 0.0045767 \end{cases}$$

Reaction orders:

$$\begin{cases} s_0 = 0.339 & s_1 = 0.724 \\ s_2 = 0.724 & s_3 = 1.02 \end{cases}$$

$$k_{\text{ef}} = 2.323 \times 10^{38} \rho^{0.9957} T^{-6.805} \cdot \exp\left(\frac{-254.1T_0}{T}\right)$$

$$k_{r1} \begin{cases} k_{r1H} = 3.706 \times 10^9 \rho^{1.238} \cdot \exp\left(\frac{-45.43T_0}{T}\right) \\ k_{r1L} = 5.521 \times 10^9 \rho^{1.164} \cdot \exp\left(\frac{-54.99T_0}{T}\right) \\ \mu_{r1} = 63.7757; \quad \xi_{c1} = 0.1959 + \frac{0.1302}{\rho^{0.10998}} \end{cases}$$

$$k_{r2} \begin{cases} k_{r2H} = 1.536 \times 10^9 \rho^{1.234} \cdot \exp\left(\frac{-47.42T_0}{T}\right) \\ k_{r2L} = 4.42 \times 10^9 \rho^{1.158} \cdot \exp\left(\frac{-60.09T_0}{T}\right) \\ \mu_{r2} = 19.3347; \quad \xi_{c2} = 0.2156 + \frac{0.03279}{\rho^{0.30459}} \end{cases}$$

$$k_i \begin{cases} k_{iH} = 9.0615 \times 10^3 \rho^{0.595} T^{1.3167} \cdot \exp\left(\frac{-32.152T_0}{T}\right) \\ k_{iL} = 3.34 \times 10^7 \rho^{0.615} \cdot \exp\left(\frac{-38.99T_0}{T}\right) \\ \mu_i = 0.00322\rho^5 + 0.01779\rho^4 - 0.2355\rho^3 - 1.226\rho^2 + 4.1982\rho + 33.0 \\ \xi_{ci} = -0.000584\rho^3 - 0.00589\rho^2 - 0.01446499\rho + 0.606825 \end{cases}$$

B.1.4 Lean acetylene-oxygen mixture ($\phi = 0.714$)

Reactants : $2C_2H_2 + 7O_2$

Mechanism : Konnov [34]

Equilibrium relation coefficients:

$$\begin{cases} \alpha_1 = 25.93548 & \alpha_2 = -1.7119 \\ \beta_0 = 3.2895 & \beta_1 = -0.71475 \\ \beta_2 = 0.727578 & \delta_0 = 12.785428 \\ \delta_1 = 0.23094 & \delta_2 = 0.0053167 \end{cases}$$

Reaction orders:

$$\begin{cases} s_0 = 0.334 & s_1 = 0.867 \\ s_2 = 0.867 & s_3 = 1.09 \end{cases}$$

$$k_{ef} = 3.507 \times 10^{31} \rho^{0.9292} T^{-5.098} \cdot \exp\left(\frac{-239.8T_0}{T}\right)$$

$$k_{r1} \begin{cases} k_{r1H} = 9.907 \times 10^9 \rho^{0.99} \cdot \exp\left(\frac{-60.36T_0}{T}\right) \\ k_{r1L} = 1.114 \times 10^9 \rho^{1.098} \cdot \exp\left(\frac{-39.5T_0}{T}\right) \\ \mu_{r1} = 40.1457; \quad \xi_{c1} = 0.2481 + \frac{0.0793}{\rho^{0.1}} \end{cases}$$

$$k_{r2} \begin{cases} k_{r2H} = 5.847 \times 10^9 \rho^{0.982} \cdot \exp\left(\frac{-61.00T_0}{T}\right) \\ k_{r2L} = 1.057 \times 10^9 \rho^{1.054} \cdot \exp\left(\frac{-48.99T_0}{T}\right) \\ \mu_{r2} = 75.4195; \quad \xi_{c2} = 0.2463 + \frac{0.0333}{\rho^{0.1}} \end{cases}$$

$$k_i \begin{cases} k_{iH} = 5.163 \rho^{0.707} T^{2.245} \cdot \exp\left(\frac{-18.83T_0}{T}\right) \\ k_{iL} = 1.6325 \times 10^9 \rho^{0.55} \cdot \exp\left(\frac{-44.78T_0}{T}\right) \\ \mu_i = 0.008626 \rho^5 + 0.063737 \rho^4 - 0.2628 \rho^3 - 1.18668 \rho^2 - 2.9749 \rho + 30.0 \\ \xi_{ci} = 0.00018 \rho^3 + 0.000359 \rho^2 - 0.081826 \rho + 0.828095 \end{cases}$$

B.1.5 Lean acetylene-oxygen mixture ($\phi = 0.5$)

Reactants : $2C_2H_2 + 10O_2$

Mechanism : Konnov [34]

Equilibrium relation coefficients:

$$\begin{cases} \alpha_1 = 25.2274 & \alpha_2 = -1.718726 \\ \beta_0 = 3.335907 & \beta_1 = -0.711998 \\ \beta_2 = 0.5399 & \delta_0 = 12.19536 \\ \delta_1 = 0.20035 & \delta_2 = 0.0053149 \end{cases}$$

Reaction orders:

$$\begin{cases} s_0 = 0.339 & s_1 = 0.85 \\ s_2 = 0.85 & s_3 = 1.02 \end{cases}$$

$$k_{ef} = 5.66 \times 10^{29} \rho^{1.022} T^{-4.655} \cdot \exp\left(\frac{-231.1T_0}{T}\right)$$

$$k_{r1} \begin{cases} k_{r1H} = 5.787 \times 10^9 \rho^{1.038} \cdot \exp\left(\frac{-47.51T_0}{T}\right) \\ k_{r1L} = 1.307 \times 10^9 \rho^{1.109} \cdot \exp\left(\frac{-38.46T_0}{T}\right) \\ \mu_{r1} = 42.8557; \quad \xi_{c1} = 0.19826 + \frac{0.06223}{\rho^{0.1}} \end{cases}$$

$$k_{r2} \begin{cases} k_{r2H} = 3.091 \times 10^9 \rho^{1.027} \cdot \exp\left(\frac{-54.55T_0}{T}\right) \\ k_{r2L} = 5.843 \times 10^8 \rho^{1.115} \cdot \exp\left(\frac{-43.82T_0}{T}\right) \\ \mu_{r2} = 48.46338; \quad \xi_{c2} = 0.1989 + \frac{0.071355}{\rho^{0.1}} \end{cases}$$

$$k_i \begin{cases} k_{iH} = 4.05 \times 10^{-3} \rho^{0.70441} T^{3.05118} \cdot \exp\left(\frac{-11.4966T_0}{T}\right) \\ k_{iL} = 9.91749 \times 10^8 \rho^{0.63} \cdot \exp\left(\frac{-45.77T_0}{T}\right) \\ \mu_i = 0.002832\rho^5 + 0.01038\rho^4 - 0.0546\rho^3 + 0.4165\rho^2 - 3.0473\rho + 20.0 \\ \xi_{ci} = 0.0002655\rho^3 + 0.0010179\rho^2 - 0.0753064\rho + 0.80079 \end{cases}$$

B.1.6 Lean acetylene-oxygen mixture ($\phi = 0.33$)

Reactants : $2C_2H_2 + 15O_2$

Mechanism : Konnov [34]

Equilibrium relation coefficients:

$$\begin{cases} \alpha_1 = 24.650396 & \alpha_2 = -1.721397 \\ \beta_0 = 3.357345 & \beta_1 = -0.771712 \\ \beta_2 = 0.47847 & \delta_0 = 11.789399 \\ \delta_1 = 0.167798 & \delta_2 = 0.0049935 \end{cases}$$

Reaction orders:

$$\begin{cases} s_0 = 0.339 & s_1 = 0.867 \\ s_2 = 0.867 & s_3 = 1.09 \end{cases}$$

$$k_{\text{ef}} = 1.276 \times 10^{24} \rho^{0.9248} T^{-3.304} \cdot \exp\left(\frac{-213.9T_0}{T}\right)$$

$$k_{\text{r1}} \begin{cases} k_{\text{r1H}} = 6.575 \times 10^9 \rho^{1.002} \cdot \exp\left(\frac{-49.35T_0}{T}\right) \\ k_{\text{r1L}} = 1.709 \times 10^9 \rho^{1.097} \cdot \exp\left(\frac{-38.72T_0}{T}\right) \\ \mu_{\text{r1}} = 15.692; \quad \xi_{\text{c1}} = 0.271 + \frac{0.0009}{\rho^{0.8415}} \end{cases}$$

$$k_{\text{r2}} \begin{cases} k_{\text{r2H}} = 3.587 \times 10^9 \rho^{0.9857} \cdot \exp\left(\frac{-63.19T_0}{T}\right) \\ k_{\text{r2L}} = 4.885 \times 10^8 \rho^{1.092} \cdot \exp\left(\frac{-43.85T_0}{T}\right) \\ \mu_{\text{r2}} = 24.9728; \quad \xi_{\text{c2}} = 0.25947 + \frac{0.099}{\rho^{0.1}} \end{cases}$$

$$k_{\text{i}} \begin{cases} k_{\text{iH}} = 2.122 \times 10^{-2} \rho^{0.628} T^{2.865} \cdot \exp\left(\frac{-16.817T_0}{T}\right) \\ k_{\text{iL}} = 7.13138 \times 10^8 \rho^{0.61077} \cdot \exp\left(\frac{-45.973T_0}{T}\right) \\ \mu_{\text{i}} = 0.00515\rho^5 + 0.023716\rho^4 - 0.15017\rho^3 - 0.031435\rho^2 - 3.4744\rho + 25.0 \\ \xi_{\text{ci}} = 0.0005\rho^3 + 0.00226\rho^2 - 0.08338\rho + 0.83397 \end{cases}$$

BIBLIOGRAPHY

- [1] A. Adebisi, O. Abidakun, and V. Akkerman. “Acceleration of Premixed Flames in Obstructed Pipes with Both Extremes Open”. In: *Energies* 13.16 (2020). DOI: 10.3390/en13164094.
- [2] V. Akkerman, C. K. Law, V. Bychkov, and L.-E. Eriksson. “Analysis of flame acceleration induced by wall friction in open tubes”. In: *Physics of Fluids* 22.5 (2010), p. 053606. DOI: 10.1063/1.3425646.
- [3] G. D. van Albada, B. van Leer, and W. W. Roberts. “A Comparative Study of Computational Methods in Cosmic Gas Dynamics”. In: *Upwind and High-Resolution Schemes*. Springer, 1997, pp. 95–103. DOI: 10.1007/978-3-642-60543-7_6.
- [4] S.A. Alturaifi, C.R. Mulvihill, O. Mathieu, and E.L. Petersen. “Speciation measurements in shock tubes for validation of complex chemical kinetics mechanisms: Application to 2-Methyl-2-Butene oxidation”. In: *Combustion and Flame* 225 (2021), pp. 196–213. DOI: <https://doi.org/10.1016/j.combustflame.2020.10.041>.
- [5] M. Arienti and J. E. Shepherd. “A numerical study of detonation diffraction”. In: *Journal of Fluid Mechanics* 529 (2005), pp. 117–146. DOI: 10.1017/S0022112005003319.
- [6] A. Aspden, N. Nikiforakis, S. Dalziel, and J. Bell. “Analysis of implicit LES methods”. In: *Communications in Applied Mathematics and Computational Science* 3.1 (2009), pp. 103–126. DOI: 10.2140/camcos.2008.3.103.
- [7] J. M. Austin. “The role of instability in gaseous detonation”. PhD thesis. California Institute of Technology Pasadena, 2003. URL: <https://thesis.library.caltech.edu/2234/>.

- [8] M. Baigmohammadi, O. Roussel, and C. M. Dion. “A Numerical Study of Lean Propane-Air Flame Acceleration at the Early Stages of Burning in Cold and Hot Isothermal Walled Small-Size Tubes”. In: *Flow, Turbulence and Combustion* 104 (2020), pp. 179–207. DOI: 10.1007/s10494-019-00057-5.
- [9] S. P. M. Bane, J. L. Ziegler, and J. E. Shepherd. “Development of one-step chemistry models for flame and ignition simulation”. In: *GALCIT Report GALTCITFM 2010* (2010). URL: https://shepherd.caltech.edu/EDL/publications/reprints/galcit_fm2010-002.pdf.
- [10] W. B. Benedick, R. Knystautas, and J. H. S. Lee. “Large-scale experiments on the transmission of fuel-air detonations from two-dimensional channels”. In: *Dynamics of Shock Waves, Explosions, and Detonations*. American Institute of Aeronautics and Astronautics, 1985, pp. 546–555. DOI: <https://doi.org/10.2514/5.9781600865695.0546.0555>.
- [11] M. Berthelot and P. Vieille. “On the velocity of propagation of explosive processes in gases”. In: *CR Hebd. Seances Acad. Sci* 93.2 (1881), pp. 18–21.
- [12] B. Bhattacharjee, D. A. Schwer, P. I. Barton, and W. H. Green. “Optimally-reduced kinetic models: Reaction elimination in large-scale kinetic mechanisms”. In: *Combustion and Flame* 135.3 (2003), pp. 191–208. DOI: [https://doi.org/10.1016/S0010-2180\(03\)00159-7](https://doi.org/10.1016/S0010-2180(03)00159-7).
- [13] R. R. Bhattacharjee. “Experimental Investigation of Detonation Re-initiation Mechanisms Following a Mach Reflection of a Quenched Detonation”. MA thesis. Ottawa, Canada: University of Ottawa, 2013.
- [14] R. R. Bhattacharjee, S. S. M. Lau-Chapdelaine, G. Maines, L. Maley, and M. I. Radulescu. “Detonation re-initiation mechanism following the Mach reflection of a quenched detonation”. In: *Proceedings of the Combustion*

- Institute* 34.2 (2013), pp. 1893–1901. DOI: <https://doi.org/10.1016/j.proci.2012.07.063>.
- [15] R.R. Bhattacharjee. “Experimental investigation of detonation re-initiation mechanisms following a Mach reflection of a quenched detonation”. MA thesis. University of Ottawa (Canada), 2013. DOI: <https://doi.org/10.48550/arXiv.1202.2318>. URL: <https://ruor.uottawa.ca/handle/10393/24933>.
- [16] P. Blythe, A. K. Kapila, and M. Short. “Homogeneous ignition for a three-step chain-branching reaction model”. In: *Journal of Engineering Mathematics* 60 (2006), pp. 125–126. DOI: <https://doi.org/10.1007/s10665-006-9055-0>.
- [17] W.A. Bone, R.P. Fraser, and W.H. Wheeler. “A photographic investigation of flame movements in gaseous explosions VII—The phenomenon of spin in detonation”. In: *Philosophical Transactions of the Royal Society of London. Series A, Mathematical and Physical Sciences* 235.746 (1935), pp. 29–68. DOI: 10.1098/rsta.1935.0015.
- [18] A. A. Borisov, S. V. Khomik, V. N. Mikhalkin, and E. V. Saneev. “Critical energy of direct detonation initiation in gaseous mixtures”. In: *Dynamics of detonations and explosions: Detonations* (1991), pp. 142–155. DOI: <https://doi.org/10.2514/5.9781600866067.0142.0155>.
- [19] B. Borzou, B. Maxwell, and M. I. Radulescu. “Influence of the reaction-to-induction length ratio on the stability of cellular detonations”. In: *23rd International Colloquium on the Dynamics of Explosions and Reactive Systems. Irvine, USA*. 2011.
- [20] B. Borzou and M. I. Radulescu. “Evaluation of hydrogen, propane and methane-air detonations instability and detonability”. In: *Brussels, Belgium: International Conference on Hydrogen Safety, ICHS*. 2013.

- [21] S. Browne, J. Ziegler, and J. E. Shepherd. “Numerical solution methods for shock and detonation jump conditions”. In: *GALCIT Report FM2006 6* (2008). URL: <https://shepherd.caltech.edu/EDL/PublicResources/sdt/>.
- [22] Buncefield Major Incident Investigation Board. *The Buncefield Incident 11 December 2005*. Final Report Volumes 1 and 2. <http://www.hse.gov.uk/comah/buncefield/miib-final-volume1.pdf>. Buncefield Major Incident Investigation Board, 2008.
- [23] D. Burgess. “Combustion, flames, and explosions of gases”. In: *Journal of Chemical Education* 39.4 (1962), A312. DOI: 10.1021/ed039pA312.2.
- [24] V. Bychkov, V. Akkerman, G. Fru, A. Petchenko, and L.E. Eriksson. “Flame acceleration in the early stages of burning in tubes”. In: *Combustion and Flame* 150.4 (2007), pp. 263–276. DOI: <https://doi.org/10.1016/j.combustflame.2007.01.004>.
- [25] J. Chao, T. Otsuka, and J.H.S. Lee. “An experimental investigation of the onset of detonation”. In: *Proceedings of the Combustion Institute* 30.2 (2005), pp. 1889–1897. DOI: <https://doi.org/10.1016/j.proci.2004.08.193>.
- [26] J.C. Chao. “Critical deflagration waves that lead to the onset of detonation”. PhD thesis. McGill University, 2006. URL: <https://escholarship.mcgill.ca/concern/theses/zg64tr13v>.
- [27] W. R. Chapman and R. V. Wheeler. “The propagation of flame in mixtures of methane and air. Part IV. The effect of restrictions in the path of the flame”. In: *J. Chem. Soc.* 129 (0 1926), pp. 2139–2147. DOI: 10.1039/JR9262902139.
- [28] P. Chen, S. Guo, Y. Li, and Y. Zhang. “Experimental and LES investigation of premixed methane/air flame propagating in a tube with a thin obstacle”. In: *Combustion Theory and Modelling* 21.2 (2017), pp. 274–292. DOI: 10.1080/13647830.2016.1218054.

- [29] C. Chi, G. Janiga, K. Zähringer, and D. Thévenin. “DNS study of the optimal heat release rate marker in premixed methane flames”. In: *Proceedings of the Combustion Institute* 37.2 (2019), pp. 2363–2371. DOI: 10.1016/j.proci.2018.07.095.
- [30] H. M. Chin, D. R. Cuppoletti, T. Ombrello, K. D. Rein, and K. A. Ahmed. “Time-resolved Measurements of Detonation Decoupling and Amplification”. In: *AIAA Scitech Forum and Exposition*. 2020.
- [31] G. Ciccarelli and S. Dorofeev. “Flame acceleration and transition to detonation in ducts”. In: *Progress in Energy and Combustion Science* 34.4 (2008), pp. 499–550. ISSN: 0360-1285. DOI: <https://doi.org/10.1016/j.pecs.2007.11.002>.
- [32] C. Clanet and G. Searby. “On the “tulip flame” phenomenon”. In: *Combustion and Flame* 105.1 (1996), pp. 225–238. ISSN: 0010-2180. DOI: 10.1016/0010-2180(95)00195-6.
- [33] J. F. Clarke. “The pre-mixed flame with large activation energy and variable mixture strength: elementary asymptotic analysis”. In: *Combustion Science and Technology* 10.5-6 (1975), pp. 189–194. DOI: <https://doi.org/10.1080/00102207508946670>.
- [34] F.H.V. Coppens, J. De Ruyck, and A.A. Konnov. “The effects of composition on burning velocity and nitric oxide formation in laminar premixed flames of CH₄ + H₂ + O₂ + N₂”. In: *Combustion and Flame* 149 (June 2007), pp. 409–417. DOI: 10.1016/j.combustflame.2007.02.004.
- [35] G. Dayma, F. Halter, and P. Dagaut. “New insights into the peculiar behavior of laminar burning velocities of hydrogen–air flames according to pressure and equivalence ratio”. In: *Combustion and Flame* 161.9 (2014), pp. 2235–2241. DOI: <https://doi.org/10.1016/j.combustflame.2014.02.009>.

- [36] R. Deiterding. “High-resolution numerical simulation and analysis of Mach reflection structures in detonation waves in low-pressure $\text{H}_2 - \text{O}_2 - \text{Ar}$ mixtures: a summary of results obtained with the adaptive mesh refinement framework AMROC”. In: *Journal of combustion* 2011 (2011). DOI: <https://doi.org/10.1155/2011/738969>.
- [37] D. Desbordes, C. Gueraud, L. Hamada, and H. N. Presles. “Failure of the classical dynamic parameters relationships in highly regular cellular detonation systems”. In: *Progress in Astronautics and Aeronautics* 153 (1993), pp. 347–347. DOI: <https://doi.org/10.2514/5.9781600866265.0347.0359>.
- [38] F. Diegelmann, V. Tritschler, S. Hickel, and N. Adams. “On the pressure dependence of ignition and mixing in two-dimensional reactive shock-bubble interaction”. In: *Combustion and Flame* 163 (2016), pp. 414–426. DOI: <https://doi.org/10.1016/j.combustflame.2015.10.016>.
- [39] Felix Diegelmann, Stefan Hickel, and Nikolaus A. Adams. “Shock Mach number influence on reaction wave types and mixing in reactive shock–bubble interaction”. In: *Combustion and Flame* 174 (2016), pp. 85–99. DOI: <https://doi.org/10.1016/j.combustflame.2016.09.014>.
- [40] J.W. Dold and A.K. Kapila. “Comparison between shock initiations of detonation using thermally-sensitive and chain-branching chemical models”. In: *Combustion and Flame* 85.1 (1991), pp. 185–194. ISSN: 0010-2180. DOI: [https://doi.org/10.1016/0010-2180\(91\)90186-F](https://doi.org/10.1016/0010-2180(91)90186-F).
- [41] S.B. Dorofeev. “Hydrogen flames in tubes: Critical run-up distances”. In: *International Journal of Hydrogen Energy* 34.14 (2009), pp. 5832–5837. DOI: <https://doi.org/10.1016/j.ijhydene.2009.01.008>.
- [42] S.B. Dorofeev. “Run-up distances to supersonic flames in smooth tubes”. In: *CD-ROM. Proceedings of the 21st international colloquium on the dynamics of explosions and reactive systems, Poitiers, France. 2007*.

- [43] S.B. Dorofeev, M.S. Kuznetsov, V.I. Alekseev, A.A. Efimenko, and W. Breitung. “Evaluation of limits for effective flame acceleration in hydrogen mixtures”. In: *Journal of Loss Prevention in the Process Industries* 14.6 (2001), pp. 583–589. DOI: [https://doi.org/10.1016/S0950-4230\(01\)00050-X](https://doi.org/10.1016/S0950-4230(01)00050-X).
- [44] E. Dziemińska and A. K. Hayashi. “Auto-ignition and DDT driven by shock wave – Boundary layer interaction in oxyhydrogen mixture”. In: *International Journal of Hydrogen Energy* 38.10 (2013), pp. 4185–4193. DOI: <https://doi.org/10.1016/j.ijhydene.2013.01.111>.
- [45] C. A. Eckett, J. J. Quirk, and J. E. Shepherd. “The role of unsteadiness in direct initiation of gaseous detonations”. In: *Journal of Fluid Mechanics* 421 (2000), pp. 147–183. DOI: 10.1017/S0022112000001555.
- [46] D. H. Edwards and J. M. Morgan. “Instabilities in detonation waves near the limits of propagation”. In: *Journal of Physics D: Applied Physics* 10.17 (Dec. 1977), p. 2377. DOI: 10.1088/0022-3727/10/17/009.
- [47] D. H. Edwards, G. O. Thomas, and M. A. Nettleton. “The diffraction of a planar detonation wave at an abrupt area change”. In: *J. Fluid Mech.* 95.1 (1979), pp. 79–96. DOI: 10.1017/S002211207900135X.
- [48] S. A. E. G. Falle. “Self-similar jets”. In: *Mon. Not. R. Astron. Soc.* 250.3 (June 1991), pp. 581–596. DOI: 10.1093/mnras/250.3.581.
- [49] S. A. E. G. Falle and J. R. Giddings. “Body capturing using adaptive cartesian grids”. In: *Numerical Methods for Fluid Dynamics IV*. Oxford University Press, 1993, pp. 337–343.
- [50] W. Fickett, J. D. Jacobson, and G. L. Schott. “Calculated Pulsating One-Dimensional Detonations with Induction-Zone Kinetics”. In: *AIAA Journal* 10.4 (1972), pp. 514–516. DOI: 10.2514/3.50130.

- [51] G. Floring, M. Peswani, and B. Maxwell. “On the role of transverse detonation waves in the re-establishment of attenuated detonations in methane–oxygen”. In: *Combustion and Flame* 247 (2023), p. 112497. DOI: <https://doi.org/10.1016/j.combustflame.2022.11249>.
- [52] G. N. Floring. “Detonation Quenching and Re-initiation Behind an Obstacle Using a Global 4-Step Combustion Model”. MA thesis. Case Western Reserve University, 2022. URL: https://etd.ohiolink.edu/apexprod/rws_ohiolink/r/1501/10?clear=10&p10_accession_num=case1649245505265699.
- [53] S. Gallier, F. Le Palud, F. Pintgen, R. Mével, and J.E. Shepherd. “Detonation wave diffraction in H₂–O₂–Ar mixtures”. In: *Proceedings of the Combustion Institute* 36.2 (2017), pp. 2781–2789. DOI: <https://doi.org/10.1016/j.proci.2016.06.090>.
- [54] V. Gamezo and E. Oran. “Flame Acceleration in Narrow Tubes: Applications for Micropropulsion in Low-Gravity Environments”. In: *43rd AIAA Aerospace Sciences Meeting and Exhibit*. 2005. DOI: 10.2514/6.2005-540.
- [55] V. N. Gamezo, C. L. Bachman, and E. S. Oran. “Flame acceleration and DDT in large-scale obstructed channels filled with methane-air mixtures”. In: *Proceedings of the Combustion Institute* 38.3 (2021), pp. 3521–3528. DOI: <https://doi.org/10.1016/j.proci.2020.09.018>.
- [56] V. N. Gamezo, A. M. Khokhlov, and E. S. Oran. “The Influence of Shock Bifurcations on Shock-Flame Interactions and DDT”. In: *Combustion and Flame* 126.4 (2001), pp. 1810–1826. DOI: [https://doi.org/10.1016/S0010-2180\(01\)00291-7](https://doi.org/10.1016/S0010-2180(01)00291-7).
- [57] V. N. Gamezo, T. Ogawa, and E. S. Oran. “Flame acceleration and DDT in channels with obstacles: Effect of obstacle spacing”. In: *Combustion and Flame* 155 (2008), pp. 302–315.

- [58] V.N. Gamezo, D. Desbordes, and E.S. Oran. “Formation and evolution of two-dimensional cellular detonations”. In: *Combustion and Flame* 116.1 (1999), pp. 154–165. DOI: 10.1016/S0010-2180(98)00031-5.
- [59] V.N. Gamezo, E.S. Oran, and A.M. Khokhlov. “Three-dimensional reactive shock bifurcations”. In: *Proceedings of the Combustion Institute* 30.2 (2005), pp. 1841–1847. DOI: <https://doi.org/10.1016/j.proci.2004.08.259>.
- [60] D. G. Goodwin, R. L. Speth, H. K. Moffat, and B. W. Weber. *Cantera: An Object-oriented Software Toolkit for Chemical Kinetics, Thermodynamics, and Transport Processes*. <https://www.cantera.org>. Version 2.4.0. 2018. DOI: 10.5281/zenodo.1174508.
- [61] K. Gottiparthi, F. Genin, S. Srinivasan, and S. Menon. “Simulation of Cellular Detonation Structures in Ethylene-Oxygen Mixtures”. In: *47th AIAA Aerospace Sciences Meeting including The New Horizons Forum and Aerospace Exposition*. 2009. DOI: 10.2514/6.2009-437.
- [62] J. S. Grondin and J. H. S. Lee. “Experimental observation of the onset of detonation downstream of a perforated plate”. In: *Shock Waves* 20.5 (2010), pp. 381–386. DOI: <https://doi.org/10.1007/s00193-010-0267-x>.
- [63] S. R. Gubba, S. S. Ibrahim, W. Malalasekera, and A. R. Masri. “Measurements and LES calculations of turbulent premixed flame propagation past repeated obstacles”. In: *Combustion and Flame* 158.12 (2011), pp. 2465–2481. DOI: <https://doi.org/10.1016/j.combustflame.2011.05.008>.
- [64] S. A. Gubin, S. M. Kogarko, and V. N. Mikhalkin. “Experimental studies into gaseous detonations in conical tubes”. In: *Fizika gorenia i vzryva* 18.5 (1982), pp. 111–117.
- [65] C. M. Guirao, R. Knystautas, and J. H. S. Lee. “A summary of hydrogen-air detonation experiments”. In: *Sandia National Laboratories/McGill University, Report NUREG/CR-4961* (May 1989). DOI: 10.2172/6066054.

- [66] W. Han, Y. Gao, and C. K. Law. “Flame acceleration and deflagration-to-detonation transition in micro- and macro-channels: An integrated mechanistic study”. In: *Combustion and Flame* 176 (2017), pp. 285–298. DOI: <https://doi.org/10.1016/j.combustflame.2016.10.010>.
- [67] A. Hasson, M. Avinor, and A. Burcat. “Transition from deflagration to detonation, spark ignition, and detonation characteristics of ethylene-oxygen mixtures in a tube”. In: *Combustion and Flame* 49.1 (1983), pp. 13–26. DOI: [https://doi.org/10.1016/0010-2180\(83\)90147-5](https://doi.org/10.1016/0010-2180(83)90147-5).
- [68] A. C. Hindmarsh, P. N. Brown, K. E. Grant, S. L. Lee, R. Serban, D. E. Shumaker, and C. S. Woodward. “SUNDIALS: Suite of nonlinear and differential/algebraic equation solvers”. In: *ACM Transactions on Mathematical Software (TOMS)* 31.3 (2005), pp. 363–396. DOI: 10.1145/1089014.1089020.
- [69] R. W. Houim, A. Ozgen, and E. S. Oran. “The role of spontaneous waves in the deflagration-to-detonation transition in submillimetre channels”. In: *Combustion Theory and Modelling* 20.6 (2016), pp. 1068–1087. DOI: 10.1080/13647830.2016.1249523.
- [70] F. Hu, P. Li, K. Wang, W. Li, J. Guo, L. Liu, and Z. Liu. “Evaluation, development, and application of a new skeletal mechanism for fuel-NO formation under air and oxy-fuel combustion”. In: *Fuel Processing Technology* 199 (2020), p. 106256. DOI: <https://doi.org/10.1016/j.fuproc.2019.106256>.
- [71] C. Johansen and G. Ciccarelli. “Modeling the initial flame acceleration in an obstructed channel using large eddy simulation”. In: *J. Loss Prevent. Proc. Ind.* 26.4 (2013), pp. 571–585. DOI: <https://doi.org/10.1016/j.jlp.2012.12.005>.

- [72] M. Johnson. “The potential for vapour cloud explosions - lessons from the Buncefield accident”. In: *J. Loss Prevent. Proc. Ind.* 23.6 (2010), pp. 921–927. DOI: <https://doi.org/10.1016/j.jlp.2010.06.011>.
- [73] D. A. Jones, G. Kemister, E. S. Oran, and M. Sichel. “The influence of cellular structure on detonation transmission”. In: *Shock Waves* 6.3 (1996), pp. 119–129. DOI: <https://doi.org/10.1007/BF02510992>.
- [74] D. A. Jones, M. Sichel, and E. S. Oran. “Reignition of detonations by reflected shocks”. In: *Shock Waves* 5.1 (1995), pp. 47–57. DOI: <https://doi.org/10.1007/BF02425035>.
- [75] D.A. Jones, M. Sichel, E.S. Oran, and R. Guirguis. “Detonation transmission in layered explosives”. In: *Symposium (International) on Combustion* 23.1 (1991), pp. 1805–1811. DOI: [https://doi.org/10.1016/S0082-0784\(06\)80460-1](https://doi.org/10.1016/S0082-0784(06)80460-1).
- [76] DA Jones, G Kemister, NA Tonello, ES Oran, and M Sichel. “Numerical simulation of detonation reignition in $H_2 - O_2$ mixtures in area expansions”. In: *Shock Waves* 10.1 (2000), pp. 33–41. DOI: [10.1007/s001930050177](https://doi.org/10.1007/s001930050177).
- [77] W. P. Jones and R. P. Lindstedt. “Global reaction schemes for hydrocarbon combustion”. In: *Combustion and flame* 73.3 (1988), pp. 233–249. DOI: [https://doi.org/10.1016/0010-2180\(88\)90021-1](https://doi.org/10.1016/0010-2180(88)90021-1).
- [78] L. Kagan and G. Sivashinsky. “On the Transition from Deflagration to Detonation in Narrow Tubes”. In: *Flow, Turbulence and Combustion* 84 (2010), pp. 423–437. DOI: <https://doi.org/10.1007/s10494-010-9252-9>.
- [79] M. M. Kamal, R. S. Barlow, and S. Hochgreb. “Conditional analysis of turbulent premixed and stratified flames on local equivalence ratio and progress of reaction”. In: *Combustion and Flame* 162.10 (2015), pp. 3896–3913. DOI: <https://doi.org/10.1016/j.combustflame.2015.07.026>.

- [80] M. Kamel. “An investigation of the diffraction of detonation waves around single cylinders”. PhD thesis. McGill University, 1993. URL: <https://escholarship.mcgill.ca/concern/theses/kd17ct86x?locale=en>.
- [81] M. Kaneshige and J.E Shepherd. *Detonation database*. Tech. rep. FM97-8. California Institute of Technology, 1997.
- [82] S. Kao and J. E. Shepherd. “Numerical solution methods for control volume explosions and ZND detonation structure”. In: *GALCIT report FM2006 7* (2008), pp. 1–46.
- [83] R. J. Kee, F. M. Rupley, E. Meeks, and J. A. Miller. *CHEMKIN-III: A FORTRAN chemical kinetics package for the analysis of gas-phase chemical and plasma kinetics*. Tech. rep. Sandia National Labs., Livermore, CA (United States), 1996.
- [84] M. Kellenberger and G. Ciccarelli. “Advancements on the propagation mechanism of a detonation wave in an obstructed channel”. In: *Combustion and Flame* 191 (2018), pp. 195–209. DOI: <https://doi.org/10.1016/j.combustflame.2017.12.023>.
- [85] M. Kellenberger and G. Ciccarelli. “Three-dimensional behaviour of quasi-detonations”. In: *Combustion and Flame* 215 (2020), pp. 145–156. DOI: <https://doi.org/10.1016/j.combustflame.2020.01.027>.
- [86] D. A. Kessler, V. N. Gamezo, and E. S. Oran. “Numerical Simulations of Deflagration-to-Detonation Transition in Methane-Air Mixtures on Large Scales”. In: *Proceedings of the Seventh Intational Seminar on Fire and Explosion Hazards*. Ed. by D Bradley, G Makhviladze, V Molkov, P Sunderland, and F Tamanini. Research Publishing, 2013. DOI: 10.3850/978-981-07-5936-0_12-04.

- [87] D. A. Kessler, V. N. Gamezo, and E. S. Oran. “Simulations of flame acceleration and deflagration-to-detonation transitions in methane-air systems”. In: *Combustion and Flame* 157 (2010), pp. 2063–2077. DOI: <https://doi.org/10.1016/j.combustflame.2010.04.011>.
- [88] B. Khasainov, H. N. Presles, D. Desbordes, P. Demontis, and P. Vidal. “Detonation diffraction from circular tubes to cones”. In: *Shock Waves* 14.3 (2005), pp. 187–192. DOI: 10.1007/s00193-005-0262-9.
- [89] B. Khasainov, C. Priault, H. N. Presles, and D. Desbordes. “Influence d’un obstacle central sur la transmission d’une détonation d’un tube dans un grand volume”. In: *Comptes Rendus de l’Académie des Sciences - Series IIB - Mechanics* 329.9 (2001), pp. 679–685. DOI: [https://doi.org/10.1016/S1620-7742\(01\)01386-1](https://doi.org/10.1016/S1620-7742(01)01386-1).
- [90] A. M. Khokhlov, E. S. Oran, and G. O. Thomas. “Numerical Simulations of Deflagration-to-Detonation Transition: The Role of Shock-Flame Interactions in Turbulent Flames”. In: *Combustion and Flame* 117.1 (1999), pp. 323–339. DOI: [https://doi.org/10.1016/S0010-2180\(98\)00076-5](https://doi.org/10.1016/S0010-2180(98)00076-5).
- [91] R. Knystautas, J.H. Lee, and C.M. Guirao. “The critical tube diameter for detonation failure in hydrocarbon-air mixtures”. In: *Combustion and Flame* 48 (1982), pp. 63–83. DOI: [https://doi.org/10.1016/0010-2180\(82\)90116-X](https://doi.org/10.1016/0010-2180(82)90116-X).
- [92] S. M. Kogarko. “Possibility of the detonation of gas mixtures in conical tubes”. In: *Bulletin of the Academy of Sciences of the USSR, Division of chemical science* 5.4 (1956), pp. 409–416.
- [93] SM Kogarko and Ya B Zeldovich. “On detonation of gaseous mixtures”. In: *Dokl. Akad. Nauk SSSR*. Vol. 63. 1948, pp. 553–556.

- [94] M. Kuznetsov, V. Alekseev, I. Matsukov, and S. Dorofeev. “DDT in a smooth tube filled with a hydrogen–oxygen mixture”. In: *Shock Waves* 14 (3 2005), pp. 205–215. DOI: 10.1007/s00193-005-0265-6.
- [95] M. Kuznetsov, M. Liberman, and I. Matsukov. “Experimental Study of the Preheat Zone Formation and Deflagration to Detonation Transition”. In: *Combustion Science and Technology* 182.11-12 (2010), pp. 1628–1644. DOI: 10.1080/00102202.2010.497327.
- [96] P. Laffitte. “Experimental research on the explosive wave and the shock wave”. In: *Annals of Physics*. Vol. 10. EDP Sciences. 1925, pp. 587–694.
- [97] S. H. Lam and D. A. Goussis. “The CSP method for simplifying kinetics”. In: *International journal of chemical kinetics* 26.4 (1994), pp. 461–486. DOI: <https://doi.org/10.1002/kin.550260408>.
- [98] S.S.M. Lau-Chapdelaine. “Numerical Simulations of Detonation Re-Initiation Behind an Obstacle”. English. MA thesis. University of Ottawa (Canada), 2013, p. 124. ISBN: 978-0-494-86060-1. URL: <http://hdl.handle.net/10393/23814>.
- [99] C.K. Law. *Combustion physics*. Cambridge university press, 2010.
- [100] J. H. Lee. “On the critical diameter problem”. In: *Dynamics of exothermicity* (1996), pp. 321–336.
- [101] J. H. S. Lee. *The Detonation Phenomenon*. Cambridge University Press, 2008. DOI: 10.1017/CBO9780511754708.
- [102] J. H. S. Lee and A. J. Higgins. “Comments on criteria for direct initiation of detonation”. In: *Philosophical Transactions of the Royal Society of London. Series A: Mathematical, Physical and Engineering Sciences* 357.1764 (1999), pp. 3503–3521. DOI: 10.1098/rsta.1999.0506.

- [103] J. J. Lee, G. Dupré, R. Knystautas, and J. H. Lee. “Doppler interferometry study of unstable detonations”. In: *Shock Waves* 5.3 (1995), pp. 175–181. DOI: <https://doi.org/10.1007/BF01435525>.
- [104] J.H. Lee, R. Knystautas, and C.K. Chan. “Turbulent flame propagation in obstacle-filled tubes”. In: *Symposium (International) on Combustion* 20.1 (1985), pp. 1663–1672. DOI: [https://doi.org/10.1016/S0082-0784\(85\)80662-7](https://doi.org/10.1016/S0082-0784(85)80662-7).
- [105] J.H. Lee, R. Knystautas, and N. Yoshikawa. “Photochemical initiation of gaseous detonations”. In: *Acta Astronautica* 5.11 (1978), pp. 971–982. DOI: [https://doi.org/10.1016/0094-5765\(78\)90003-6](https://doi.org/10.1016/0094-5765(78)90003-6).
- [106] J.H.S. Lee and I.O. Moen. “The mechanism of transition from deflagration to detonation in vapor cloud explosions”. In: *Progress in Energy and Combustion Science* 6.4 (1980), pp. 359–389. DOI: [https://doi.org/10.1016/0360-1285\(80\)90011-8](https://doi.org/10.1016/0360-1285(80)90011-8).
- [107] J.H.S. Lee and I.O. Moen. “The mechanism of transition from deflagration to detonation in vapor cloud explosions”. In: *Progress in Energy and Combustion Science* 6.4 (1980), pp. 359–389. ISSN: 0360-1285. DOI: [https://doi.org/10.1016/0360-1285\(80\)90011-8](https://doi.org/10.1016/0360-1285(80)90011-8).
- [108] C. Leung, M. Radulescu, and G. Sharpe. “Characteristics analysis of the one-dimensional pulsating dynamics of chain-branching detonations”. In: *Physics of Fluids* 22 (Dec. 2010). DOI: 10.1063/1.3520188.
- [109] J. Li, J. Ning, C. B. Kiyanda, and H. D. Ng. “Numerical simulations of cellular detonation diffraction in a stable gaseous mixture”. In: *Propulsion and Power Research* 5.3 (2016), pp. 177–183. DOI: <https://doi.org/10.1016/j.jprr.2016.07.004>.

- [110] X. Li, J. Dong, K. Jin, Q. Duan, J. Sun, M. Li, and H. Xiao. “Flame acceleration and deflagration-to-detonation transition in a channel with continuous triangular obstacles: Effect of equivalence ratio”. In: *Process Safety and Environmental Protection* 167 (2022), pp. 576–591. DOI: <https://doi.org/10.1016/j.psep.2022.09.033>.
- [111] Y. Li, C. W. Zhou, K. P. Somers, K. Zhang, and H. J. Curran. “The oxidation of 2-butene: A high pressure ignition delay, kinetic modeling study and reactivity comparison with isobutene and 1-butene”. In: *Proceedings of the Combustion Institute* 36.1 (2017), pp. 403–411. DOI: <https://doi.org/10.1016/j.proci.2016.05.052>.
- [112] Z. Liang and L. Bauwens. “Cell structure and stability of detonations with a pressure-dependent chain-branching reaction rate model”. In: *Combustion Theory and Modelling* 9.1 (2005), pp. 93–112. DOI: <https://doi.org/10.1080/13647830500051885>.
- [113] Z. Liang, S. Browne, R. Deiterding, and J. E. Shepherd. “Detonation front structure and the competition for radicals”. In: *Proceedings of the Combustion Institute* 31.2 (2007), pp. 2445–2453. DOI: <https://doi.org/10.1016/j.proci.2006.07.244>.
- [114] M. A. Liberman, M. F. Ivanov, A. D. Kiverin, M. S. Kuznetsov, A. A. Chukalovsky, and T. V. Rakhimova. “Deflagration-to-detonation transition in highly reactive combustible mixtures”. In: *Acta Astronautica* 67.7 (2010), pp. 688–701. DOI: <https://doi.org/10.1016/j.actaastro.2010.05.024>.
- [115] M. A. Liberman, M. Kuznetsov, A. Ivanov, and I. Matsukov. “Formation of the preheated zone ahead of a propagating flame and the mechanism underlying the deflagration-to-detonation transition”. In: *Physics Letters A* 373.5 (2009), pp. 501–510. DOI: <https://doi.org/10.1016/j.physleta.2008.12.008>.

- [116] R.P. Lindstedt and H.J. Michels. “Deflagration to detonation transitions and strong deflagrations in alkane and alkene air mixtures”. In: *Combustion and Flame* 76.2 (1989), pp. 169–181. DOI: [https://doi.org/10.1016/0010-2180\(89\)90065-5](https://doi.org/10.1016/0010-2180(89)90065-5).
- [117] J. Liu, R. Yu, B. Ma, and C. Tang. “On the Second Explosion Limits of Hydrogen, Methane, Ethane, and Propane”. In: *ACS Omega* 5.30 (2020), pp. 19268–19276. DOI: 10.1021/acsomega.0c02825.
- [118] Y.K. Liu, J.H. Lee, and R. Knystautas. “Effect of geometry on the transmission of detonation through an orifice”. In: *Combustion and Flame* 56.2 (1984), pp. 215–225. DOI: [https://doi.org/10.1016/0010-2180\(84\)90038-5](https://doi.org/10.1016/0010-2180(84)90038-5).
- [119] T. Lu and C. K. Law. “A directed relation graph method for mechanism reduction”. In: *Proceedings of the Combustion Institute* 30.1 (2005), pp. 1333–1341. DOI: <https://doi.org/10.1016/j.proci.2004.08.145>.
- [120] T. Lu and C. K. Law. “Toward accommodating realistic fuel chemistry in large-scale computations”. In: *Progress in Energy and Combustion Science* 35.2 (2009), pp. 192–215. ISSN: 0360-1285. DOI: <https://doi.org/10.1016/j.pecs.2008.10.002>.
- [121] Tianfeng Lu, Yiguang Ju, and Chung K Law. “Complex CSP for chemistry reduction and analysis”. In: *Combustion and Flame* 126.1-2 (2001), pp. 1445–1455. DOI: [https://doi.org/10.1016/S0010-2180\(01\)00252-8](https://doi.org/10.1016/S0010-2180(01)00252-8).
- [122] G.A. Lyamin, V.V. Mitrofanov, A.V. Pinaev, and V.A. Subbotin. “Propagation of Gas Explosion in Channels with Uneven Walls and in Porous Media”. In: *Dynamic Structure of Detonation in Gaseous and Dispersed Media*. Dordrecht: Springer Netherlands, 1991, pp. 51–75. DOI: 10.1007/978-94-011-3548-1_3.

- [123] M.Short and G. J. Sharpe. “Pulsating instability of detonations with a two-step chain-branching reaction model: theory and numerics”. In: *Combustion Theory and Modelling* 7.2 (2003), pp. 401–416. DOI: 10.1088/1364-7830/7/2/311. eprint: <https://www.tandfonline.com/doi/pdf/10.1088/1364-7830/7/2/311>.
- [124] U. Maas and S. B. Pope. “Simplifying chemical kinetics: Intrinsic low-dimensional manifolds in composition space”. In: *Combustion and flame* 88.3-4 (1992), pp. 239–264. DOI: [https://doi.org/10.1016/0010-2180\(92\)90034-M](https://doi.org/10.1016/0010-2180(92)90034-M).
- [125] T. Machida, M. Asahara, A. K. Hayashi, and N. Tsuboi. “Three-Dimensional Simulation of Deflagration-to-Detonation Transition with a Detailed Chemical Reaction Model”. In: *Combustion Science and Technology* 186.10-11 (2014), pp. 1758–1773. DOI: 10.1080/00102202.2014.935647.
- [126] Y. Mahmoudi, N. Karimi, R. Deiterding, and S. Emami. “Hydrodynamic instabilities in gaseous detonations: Comparison of Euler, Navier-Stokes, and large-eddy simulation”. In: *J. Propul. Power* 30.2 (2014), pp. 384–396. DOI: 10.2514/1.B34986.
- [127] A Makris, H Shafique, J H S Lee, and R Knystautas. “Influence of mixture sensitivity and pore-size on detonation velocities in porous-media”. In: *Shock Waves* 5.1 (1995), pp. 89–95. DOI: 10.1007/BF02425039.
- [128] A. Makris. “The propagation of gaseous detonations in porous media”. PhD thesis. Montreal, Canada: McGill University, 1993. URL: http://digitool.Library.McGill.CA:80/R/-?func=dbin-jump-full&object_id=41700&silolibrary=GEN01.
- [129] A. Makris. “The propagation of gaseous detonations in porous media”. PhD thesis. Montreal, Canada: McGill University, 1993. URL: <https://escholarship.mcgill.ca/concern/theses/zp38wf29w>.

- [130] L. Maley. “On Shock Reflections in Fast Flames”. MA thesis. Ottawa, Canada: University of Ottawa, 2015.
- [131] E. Mallard and H.L. Le Chatelier. “Recherches expérimentales et théoriques sur la combustion des mélanges gazeux explosifs”. In: *Ann. Mines* (1883). URL: <https://hal.science/jpa-00238602/document>.
- [132] G. H. Markstein. *Nonsteady Flame Propagation*. Pergamon Press, 1964.
- [133] A. Massias, D. Diamantis, E. Mastorakos, and D. A. Goussis. “An algorithm for the construction of global reduced mechanisms with CSP data”. In: *Combustion and Flame* 117.4 (1999), pp. 685–708. DOI: [https://doi.org/10.1016/S0010-2180\(98\)00132-1](https://doi.org/10.1016/S0010-2180(98)00132-1).
- [134] B. Maxwell, A. Pekalski, and M. Radulescu. “Modelling of the transition of a turbulent shock-flame complex to detonation using the linear eddy model”. In: *Combustion and Flame* 192 (2018), pp. 340–357. DOI: <https://doi.org/10.1016/j.combustflame.2018.02.013>.
- [135] B. M. Maxwell, R. R. Bhattacharjee, S. S. M. Lau-Chapdelaine, S. A. E. G. Falle, G. J. Sharpe, and M. I. Radulescu. “Influence of Turbulent Fluctuations on Detonation Propagation”. In: *J. Fluid Mech.* 818 (2017), pp. 646–696. DOI: <https://doi.org/10.1017/jfm.2017.145>.
- [136] B. McN. Maxwell. “Turbulent combustion modelling of fast-flames and detonations using compressible LEM-LES”. PhD thesis. Université d’Ottawa/University of Ottawa, 2016. URL: <https://ruor.uottawa.ca/handle/10393/34122>.
- [137] B. McN. Maxwell, R. R. Bhattacharjee, S. S. M. Lau-Chapdelaine, S. A. E. G. Falle, G. J. Sharpe, and M. I. Radulescu. “Influence of turbulent fluctuations on detonation propagation”. In: *Journal of Fluid Mechanics* 818 (2017), pp. 646–696. DOI: [10.1017/jfm.2017.145](https://doi.org/10.1017/jfm.2017.145).

- [138] K. Mazaheri and S. A. Hashemi. “THE EFFECT OF CHAIN INITIATION REACTION ON THE STABILITY OF GASEOUS DETONATIONS”. In: *Combustion Science and Technology* 179.8 (2007), pp. 1701–1736. DOI: 10.1080/00102200701259916. eprint: <https://doi.org/10.1080/00102200701259916>.
- [139] B. J. McBride. *Coefficients for calculating thermodynamic and transport properties of individual species*. 1993.
- [140] N. Mehrjoo, Y. Gao, C. B. Kiyanda, H. D. Ng, and J. H. S. Lee. “Effects of porous walled tubes on detonation transmission into unconfined space”. In: *Proceedings of the Combustion Institute* 35.2 (2015), pp. 1981–1987. DOI: <https://doi.org/10.1016/j.proci.2014.06.031>.
- [141] N. Mehrjoo, B. Zhang, R. Portaro, H. D. Ng, and J. H. S. Lee. “Response of critical tube diameter phenomenon to small perturbations for gaseous detonations”. In: *Shock Waves* 24.2 (2014), pp. 219–229. DOI: <https://doi.org/10.1007/s00193-013-0491-2>.
- [142] J. Melguizo-Gavilanes, M. Peswani, and B.M. Maxwell. “Detonation-diffuse interface interactions: failure, re-initiation and propagation limits”. In: *Proceedings of the Combustion Institute* 38.3 (2021), pp. 3717–3724. DOI: <https://doi.org/10.1016/j.proci.2020.07.143>.
- [143] J. Meredith, H. D. Ng, and J. H. S. Lee. “Detonation diffraction from an annular channel”. In: *Shock Waves* 20.6 (2010), pp. 449–455. DOI: <https://doi.org/10.1007/s00193-010-0256-0>.
- [144] E. E. Meshkov. “Instability of the interface of two gases accelerated by a shock wave”. In: *Fluid Dynamics* 4.5 (Jan. 1972), pp. 101–104. DOI: 10.1007/BF01015969.
- [145] R. Mével, D. Davidenko, F. Lafosse, N. Chaumeix, G. Dupré, C. É. Paillard, and J. E. Shepherd. “Detonation in hydrogen–nitrous oxide–diluent mixtures: An experimental and numerical study”. In: *Combustion and Flame*

- 162.5 (2015), pp. 1638–1649. DOI: <https://doi.org/10.1016/j.combustflame.2014.11.026>.
- [146] R. Mével, S. Javoy, F. Lafosse, N. Chaumeix, G. Dupré, and C.É. Pailard. “Hydrogen–nitrous oxide delay times: Shock tube experimental study and kinetic modelling”. In: *Proceedings of the Combustion Institute* 32.1 (2009), pp. 359–366. ISSN: 1540-7489. DOI: 10.1016/j.proci.2008.06.171.
- [147] R. Mével, Q. Xiao, and M. Radulescu. “Hydrogen-oxygen-argon detonation diffraction in a narrow channel”. In: *26th International Colloquium on Dynamics of Explosions and Reactive Systems, Boston, USA*. 2017. URL: <http://www.icders.org/ICDERS2017/abstracts/ICDERS2017-0922.pdf>.
- [148] S. Miller, P. King, F. Schauer, and J. Hoke. “Ignition Design For a Rotating Detonation Engine”. In: *51st AIAA Aerospace Sciences Meeting*. 2013. DOI: 10.2514/6.2013-1174.
- [149] I. O. Moen. “Detonation length scales for fuel-air explosives”. In: *Prog. Astro. Aero.* 94 (1984), pp. 55–79. DOI: 10.2514/5.9781600865695.0055.0079.
- [150] I. O. Moen, A. Sulmistras, G. O. Thomas, D. Bjerketvedt, and PA Thibault. “Influence of cellular regularity on the behavior of gaseous detonations”. In: *Dynamics of explosions* (1986), pp. 220–243. DOI: <https://doi.org/10.2514/5.9781600865800.0220.0243>.
- [151] I.O. Moen, M. Donato, R. Knystautas, and J.H. Lee. “Flame acceleration due to turbulence produced by obstacles”. In: *Combustion and Flame* 39.1 (1980), pp. 21–32. DOI: [https://doi.org/10.1016/0010-2180\(80\)90003-6](https://doi.org/10.1016/0010-2180(80)90003-6).
- [152] S.B. Murray and J.H. Lee. “On the transformation of planar detonation to cylindrical detonation”. In: *Combustion and Flame* 52 (1983), pp. 269–289. DOI: [https://doi.org/10.1016/0010-2180\(83\)90138-4](https://doi.org/10.1016/0010-2180(83)90138-4).

- [153] Y. Nagura, J. Kasahara, and A. Matsuo. “Multi-frame visualization for detonation wave diffraction”. In: *Shock waves* 26.5 (2016), pp. 645–656. DOI: <https://doi.org/10.1007/s00193-016-0663-y>.
- [154] Y. Nagura, J. Kasahara, Y. Sugiyama, and A. Matsuo. “Comprehensive visualization of detonation-diffraction structures and sizes in unstable and stable mixtures”. In: *Proceedings of the Combustion Institute* 34.2 (2013), pp. 1949–1956. DOI: <https://doi.org/10.1016/j.proci.2012.07.078>.
- [155] D. M. Newitt and L. S. Thornes. “348. The oxidation of propane. Part I. The products of the slow oxidation at atmospheric and at reduced pressures”. In: *J. Chem. Soc.* (0 1937), pp. 1656–1665. DOI: 10.1039/JR9370001656.
- [156] H. D. Ng and J. H. S. Lee. “Direct initiation of detonation with a multi-step reaction scheme”. In: *Journal of Fluid Mechanics* 476 (2003), pp. 179–211. DOI: 10.1017/S0022112002002872.
- [157] H. D. Ng, M. I. Radulescu, A. J. Higgins, N. Nikiforakis, and J. H. S. Lee. “Numerical investigation of the instability for one-dimensional Chapman–Jouguet detonations with chain-branching kinetics”. In: *Combustion Theory and Modelling* 9.3 (2005), pp. 385–401. DOI: <https://doi.org/10.1080/13647830500307758>.
- [158] H. D. Ng, M. I. Radulescu, A. J. Higgins, N. Nikiforakis, and J. H. S. Lee. “Numerical investigation of the instability for one-dimensional Chapman–Jouguet detonations with chain-branching kinetics”. In: *Combustion Theory and Modelling* 9.3 (2005), pp. 385–401. DOI: 10.1080/13647830500307758. eprint: <https://doi.org/10.1080/13647830500307758>.
- [159] T. Obara, J. Sentanuhady, Y. Tsukada, and S. Ohyagi. “Reinitiation process of detonation wave behind a slit-plate”. In: *Shock Waves* 18.2 (2008), pp. 117–127. DOI: 10.1007/s00193-008-0147-9.

- [160] S. Ohyagi, T. Obara, S. Hoshi, P. Cai, and T. Yoshihashi. “Diffraction and re-initiation of detonations behind a backward-facing step”. In: *Shock Waves* 12.3 (2002), pp. 221–226. DOI: 10.1007/s00193-002-0156-z.
- [161] C. Olm, I. G. Zsély, R. Pálvölgyi, T. Varga, T. Nagy, H. J. Curran, and T. Turányi. “Comparison of the performance of several recent hydrogen combustion mechanisms”. In: *Combustion and Flame* 161.9 (2014), pp. 2219–2234. DOI: <https://doi.org/10.1016/j.combustflame.2014.03.006>.
- [162] A. K. Oppenheim and R. I. Soloukhin. “Experiments in Gasdynamics of Explosions”. In: *Annual Review of Fluid Mechanics* 5.1 (1973), pp. 31–58. DOI: 10.1146/annurev.fl.05.010173.000335.
- [163] E. S. Oran, J. P. Boris, D. A. Jones, and M. Sichel. “Ignition in a complex Mach structure”. In: *Progress in Astronautics and Aeronautics* 153 (1993), pp. 241–241.
- [164] E. S. Oran and V. N. Gamezo. “Flame Acceleration and Detonation Transition in Narrow Tubes”. In: *20th International Colloquium on the Dynamics of Explosions and Reactive Systems*. Montreal, Canada, 2005. URL: <http://www.icders.org/ICDERS2005/PapersICDERS2005/ICDERS2005-240.pdf>.
- [165] E. S. Oran and V. N. Gamezo. “Origins of the deflagration-to-detonation transition in gas-phase combustion”. In: *Combustion and Flame* 148.1 (2007), pp. 4–47. ISSN: 0010-2180. DOI: <https://doi.org/10.1016/j.combustflame.2006.07.010>.
- [166] E. S. Oran, D. A. Jones, and M. Sichel. “Numerical simulations of detonation transmission”. In: *Proceedings of the Royal Society of London. Series A: Mathematical and Physical Sciences* 436.1897 (1992), pp. 267–297. DOI: <https://doi.org/10.1098/rspa.1992.0018>.

- [167] J. D. Ott, E. S. Oran, and J. D. Anderson. “A Mechanism for Flame Acceleration in Narrow Tubes”. In: *AIAA Journal* 41.7 (2003), pp. 1391–1396. DOI: 10.2514/2.2088.
- [168] P. Pal, C. Xu, G. Kumar, S. A. Drennan, B. A. Rankin, and S. Som. “Large-Eddy Simulations and Mode Analysis of Ethylene/Air Combustion in a Non-Premixed Rotating Detonation Engine”. In: *AIAA Propulsion and Energy 2020 Forum*. 2020. DOI: 10.2514/6.2020-3876.
- [169] E. G. Pantow, M. Fischer, and T. Kratzel. “Decoupling and recoupling of detonation waves associated with sudden expansion”. In: *Shock waves* 6.3 (1996), pp. 131–137. DOI: <https://doi.org/10.1007/BF02510993>.
- [170] O. Peraldi, R. Knystautas, and J.H. Lee. “Criteria for transition to detonation in tubes”. In: *Symposium (International) on Combustion* 21.1 (1988), pp. 1629–1637. ISSN: 0082-0784. DOI: [https://doi.org/10.1016/S0082-0784\(88\)80396-5](https://doi.org/10.1016/S0082-0784(88)80396-5).
- [171] M. Peswani, C. Gerace, and B. Maxwell. “Combustion properties of a simple and efficient four-step model”. In: *Shock Waves* 32.6 (2022), pp. 517–537. DOI: <https://doi.org/10.1007/s00193-022-01090-6>.
- [172] M. Peswani and B. Maxwell. “Detonation wave diffraction in stoichiometric C_2H_4/O_2 mixtures using a global four-step combustion model”. In: *Physics of Fluids* 34.10 (2022), p. 106104. DOI: 10.1063/5.0116804.
- [173] M. Peswani and B. McN. Maxwell. “Performance of a Generic 4-Step Global Reaction Mechanism With Equilibrium Effects for Detonation Applications”. In: *ASME IMECE*. Vol. Volume 11: Heat Transfer and Thermal Engineering. Nov. 2020. DOI: 10.1115/IMECE2020-23786.
- [174] F. Pintgen and J.E. Shepherd. “Detonation diffraction in gases”. In: *Combustion and Flame* 156.3 (2009), pp. 665–677. ISSN: 0010-2180. DOI: <https://doi.org/10.1016/j.combustflame.2008.09.008>.

- [175] T. Poinso and D. Veynante. *Theoretical and Numerical Combustion*. 2nd. Edwards, 2005.
- [176] S. Pope. *Turbulent Flows*. Cambridge University Press, 2000.
- [177] C. Priault. “Diamètre critique de transmission d’une détonation : influence de la géométrie de diffraction”. PhD thesis. Université de Poitiers, 2003, [11]-124–[12] p. URL: <http://www.theses.fr/2003POIT2268>.
- [178] M. Radulescu, G. Sharpe, and D. Bradley. “A universal parameter quantifying explosion hazards, detonability and hot spot formation: The χ number”. In: *ISFEH7 Proceedings of the Seventh International Seminar*. Jan. 2013, pp. 617–626. DOI: 10.3850/978-981-07-5936-0_10-01.
- [179] M. I. Radulescu. “The propagation and failure mechanism of gaseous detonations: experiments in porous-walled tubes”. PhD thesis. McGill University Libraries, 2003.
- [180] M. I. Radulescu and J. H. S. Lee. “The failure mechanism of gaseous detonations: experiments in porous wall tubes”. In: *Combustion and Flame* 131.1 (2002), pp. 29–46. ISSN: 0010-2180. DOI: [https://doi.org/10.1016/S0010-2180\(02\)00390-5](https://doi.org/10.1016/S0010-2180(02)00390-5).
- [181] M. I. Radulescu and B. M. Maxwell. “The mechanism of detonation attenuation by a porous medium and its subsequent re-initiation”. In: *J. Fluid Mech.* 667 (2011), pp. 96–134. DOI: 10.1017/S0022112010004386.
- [182] M. I. Radulescu, R. Mével, Q. Xiao, and S. Gallier. “On the self-similarity of diffracting gaseous detonations and the critical channel width problem”. In: *Physics of Fluids* 33.6 (2021), p. 066106. DOI: 10.1063/5.0054219.
- [183] M. I. Radulescu, H. D. Ng, J. H. S. Lee, and B. Varatharajan. “The effect of argon dilution on the stability of acetylene/oxygen detonations”. In: *Proceedings of the Combustion Institute* 29.2 (2002), pp. 2825–2831. DOI: [https://doi.org/10.1016/S1540-7489\(02\)80345-5](https://doi.org/10.1016/S1540-7489(02)80345-5).

- [184] M. I. Radulescu, G. J. Sharpe, C. K. Law, and J. H. S. Lee. “The hydrodynamic structure of unstable cellular detonations”. In: *Journal of Fluid Mechanics* 580 (2007), pp. 31–81. DOI: 10.1017/S0022112007005046.
- [185] M. I. Radulescu, W. Wang, M. Saif, M. Levin, and A. Pekalski. “On Chapman Jouguet deflagrations”. In: *25th International Colloquium on the Dynamics of Explosions and Reactive Systems*. Leeds, UK, 2015. URL: <http://www.icders.org/ICDERS2015/abstracts/ICDERS2015-266.pdf>.
- [186] G. Rainsford, D. J. S. Aulakh, and G. Ciccarelli. “Visualization of detonation propagation in a round tube equipped with repeating orifice plates”. In: *Combustion and Flame* 198 (2018), pp. 205–221. DOI: <https://doi.org/10.1016/j.combustflame.2018.09.015>.
- [187] W. Rakotoarison, B. Maxwell, A. Pekalski, and M. I. Radulescu. “Mechanism of flame acceleration and detonation transition from the interaction of a supersonic turbulent flame with an obstruction: Experiments in low pressure propane–oxygen mixtures”. In: *Proceedings of the Combustion Institute* 37 (3 2019), pp. 3713–3721. DOI: 10.1016/j.proci.2018.08.050.
- [188] W. Rakotoarison, A. Pekalski, and M.I. Radulescu. “Detonation transition criteria from the interaction of supersonic shock-flame complexes with different shaped obstacles”. In: *Journal of Loss Prevention in the Process Industries* 64 (2020), p. 103963. DOI: <https://doi.org/10.1016/j.jlp.2019.103963>.
- [189] R. D. Richtmyer. “Taylor instability in shock acceleration of compressible fluids”. In: *Communications on Pure and Applied Mathematics* 13.2 (1960), pp. 297–319. DOI: <https://doi.org/10.1002/cpa.3160130207>.
- [190] G.D. Roy, S.M. Frolov, A.A. Borisov, and D.W. Netzer. “Pulse detonation propulsion: challenges, current status, and future perspective”. In: *Progress*

- in Energy and Combustion Science* 30.6 (2004), pp. 545–672. DOI: <https://doi.org/10.1016/j.pecs.2004.05.001>.
- [191] M. Saif, W. Wang, A. Pekalski, M. Levin, and M.I. Radulescu. “Chapman–Jouguet deflagrations and their transition to detonation”. In: *Proceedings of the Combustion Institute* 36.2 (2017), pp. 2771–2779. DOI: <https://doi.org/10.1016/j.proci.2016.07.122>.
- [192] M. Saif, W. Wang, A. Pekalski, M. Levin, and M.I. Radulescu. “Chapman–Jouguet deflagrations and their transition to detonation”. In: *Proceedings of the Combustion Institute* 36.2 (2017), pp. 2771–2779. DOI: <https://doi.org/10.1016/j.proci.2016.07.122>.
- [193] G.D. Salamandra, T.V. Bazhenova, and I.M. Naboko. “Formation of detonation wave during combustion of gas in combustion tube”. In: *Symposium (International) on Combustion* 7.1 (1958), pp. 851–855. DOI: [https://doi.org/10.1016/S0082-0784\(58\)80128-9](https://doi.org/10.1016/S0082-0784(58)80128-9).
- [194] T. Scarinci, J. H. Lee, G. O. Thomas, R.J. Bambrey, and D. H. Edwards. “Amplification of a pressure wave by its passage through a flame front”. In: *Dynamics of Heterogeneous Combustion and Reacting Systems*. Ed. by A. L. Kuhl, J. C. Leyer, and A. A. Borisov. Vol. 152. Progress in Astronautics and Aeronautics. American Institute of Aeronautics and Astronautics, 1993, pp. 3–24. DOI: 10.2514/5.9781600866258.0003.0024.
- [195] E. Schultz. “Detonation diffraction through an abrupt area expansion”. PhD thesis. California Institute of Technology, 2000. URL: <https://resolver.caltech.edu/CaltechETD:etd-11122003-180459>.
- [196] E. Schultz, E. Wintenberger, and J. Shepherd. “Investigation of deflagration to detonation transition for application to pulse detonation engine ignition systems”. In: *36th JANNAF Combustion and Airbreathing Propulsion Subcommittees Meeting. Cocoa Beach*. 1999.

- [197] G. J. Sharpe and M. I. Radulescu. “Statistical analysis of cellular detonation dynamics from numerical simulations: one-step chemistry”. In: *Combustion Theory and Modelling* 15.5 (2011), pp. 691–723. DOI: 10.1080/13647830.2011.558594.
- [198] G.J. Sharpe. “Transverse waves in numerical simulations of cellular detonations”. In: *J. Fluid Mech.* 447 (2001), pp. 31–51. DOI: 10.1017/S0022112001005535.
- [199] K. I. Shchelkin. “Influence of the wall roughness on initiation and propagation of detonation in gases”. In: *Zh. Eksp. Teor. Fiz.* 10 (1940), pp. 823–827.
- [200] K. I. Shchelkin. “Occurance of detonation in gases in rough-walled tubes”. In: *Sov J Tech Phys* 17 (1947), p. 613.
- [201] J. E. Shepherd. “Shock & Detonation Toolbox—Cantera 2.1”. In: *Explosion Dynamics Laboratory, California Institute of Technology*, accessed Oct 11 (2018), p. 2019. URL: <https://shepherd.caltech.edu/EDL/PublicResources/sdt/>.
- [202] J. E. Shepherd and J. H. S. Lee. “On The Transition from Deflagration to Detonation”. In: *Major Research Topics in Combustion*. New York, NY: Springer, 1992, pp. 439–487. ISBN: 978-1-4612-2884-4. DOI: 10.1007/978-1-4612-2884-4_22.
- [203] J.E. Shepherd, I.O. Moen, S.B. Murray, and P.A. Thibault. “Analyses of the cellular structure of detonations”. In: *Symposium (International) on Combustion* 21.1 (1988), pp. 1649–1658. DOI: [https://doi.org/10.1016/S0082-0784\(88\)80398-9](https://doi.org/10.1016/S0082-0784(88)80398-9).
- [204] L. Shi, K.C.K Uy, and C.Y Wen. “The re-initiation mechanism of detonation diffraction in a weakly unstable gaseous mixture”. In: *J. Fluid Mech.* 895 (2020). DOI: 10.1017/jfm.2020.311.

- [205] M. Short and J. J. Quirk. “On the nonlinear stability and detonability limit of a detonation wave for a model three-step chain-branching reaction”. In: *Journal of Fluid Mechanics* 339 (1997), pp. 89–119. DOI: 10.1017/S002211209700503X.
- [206] B.W. Skews. “The shape of a diffracting shock wave”. In: *J. Fluid Mech.* 29.2 (1967), pp. 297–304. DOI: 10.1017/S0022112067000825.
- [207] T. Slungaard, T. Engebretsen, and O. K. Sonju. “The influence of detonation cell size and regularity on the propagation of gaseous detonations in granular materials”. In: *Shock Waves* 12.4 (2003), pp. 301–308. DOI: 10.1007/s00193-002-0166-x.
- [208] G. P. Smith, D. M. Golden, M. Frenklach, N. W. Moriarty, B. Eiteneer, M. Goldenberg, C. T. Bowman, R. K. Hanson, S. Song, W. C. Gardiner Jr, V. V. Lissianski, and Z. Qin. *GRI 3.0 Mechanism*. 1999. URL: http://www.me.berkeley.edu/gri_mech/.
- [209] R.I. Soloukhin. “Deflagration to detonation transition in gases”. In: *Soviet Prikladn Mech i Techn Phys (Appl Mech Tech Phys)* 4 (1961), p. 128.
- [210] R. Sorin, R. Zitoun, B. Khasainov, and D. Desbordes. “Detonation diffraction through different geometries”. In: *Shock Waves* 19.1 (2009), pp. 11–23. DOI: <https://doi.org/10.1007/s00193-008-0179-1>.
- [211] R. A. Strehlow and C. D. Engel. “Transverse waves in detonations. II - structure and spacing in H₂-O₂, C₂H₄-O₂, and CH₄-O₂ systems.” In: *AIAA Journal* 7.3 (1969), pp. 492–496. DOI: 10.2514/3.5134.
- [212] R.A. Strehlow and A.J. Crooker. “The structure of marginal detonation waves”. In: *Acta Astronautica* 1.3-4 (1974), pp. 303–315. DOI: 10.1016/0094-5765(74)90100-3.

- [213] X. Sun, C. Yan, Y. Yan, X. Mi, J. H.S. Lee, and H. D. Ng. “Critical tube diameter for quasi-detonations”. In: *Combustion and Flame* 244 (2022), p. 112280. ISSN: 0010-2180. DOI: <https://doi.org/10.1016/j.combustflame.2022.112280>.
- [214] S. Taileb, J. Melguizo-Gavilanes, and A. Chinnayya. “Influence of the chemical modeling on the quenching limits of gaseous detonation waves confined by an inert layer”. In: *Combustion and Flame* 218 (2020), pp. 247–259. ISSN: 0010-2180. DOI: <https://doi.org/10.1016/j.combustflame.2020.04.018>.
- [215] J. Tang and M.I. Radulescu. “Dynamics of shock induced ignition in Fickett’s model: Influence of χ ”. In: *Proceedings of the Combustion Institute* 34.2 (2013), pp. 2035–2041. DOI: <https://doi.org/10.1016/j.proci.2012.05.079>.
- [216] A. Teodorczyk, J. H. S. Lee, and K. Knystautas. “Propagation mechanism of quasi-detonations”. In: *Symposium (International) on Combustion* 22.1 (1989), pp. 1723–1731. DOI: [https://doi.org/10.1016/S0082-0784\(89\)80185-7](https://doi.org/10.1016/S0082-0784(89)80185-7).
- [217] A. Teodorczyk and J.H.S. Lee. “Detonation attenuation by foams and wire meshes lining the walls”. In: *Shock Waves* 4.4 (1995), pp. 225–236. DOI: <https://doi.org/10.1007/BF01414988>.
- [218] A. Teodorczyk, J.H.S. Lee, and R. Knystautas. “Propagation mechanism of quasi-detonations”. In: *Symposium (International) on Combustion* 22.1 (1989), pp. 1723–1731. ISSN: 0082-0784. DOI: 10.1016/S0082-0784(89)80185-7.
- [219] G. Thomas, R. Bambrey, and C. Brown. “Experimental observations of flame acceleration and transition to detonation following shock-flame interaction”. In: *Combustion Theory and Modelling* 5.4 (2001), pp. 573–594.

DOI: 10.1088/1364-7830/5/4/304. eprint: <https://doi.org/10.1088/1364-7830/5/4/304>.

- [220] G. O. Thomas, D. H. Edwards, J. H. Lee, R. Knystautas, I. O. Moen, and Y. M. Wei. “Detonation diffraction by divergent channels”. In: *Dynamics of Explosions, Prog Astro Aero* 106 (1986), pp. 144–154. DOI: <https://doi.org/10.2514/5.9781600865800.0144.0154>.
- [221] G. O. Thomas and R. L. Williams. “Detonation interaction with wedges and bends”. In: *Shock waves* 11.6 (2002), pp. 481–492. DOI: <https://doi.org/10.1007/s001930200133>.
- [222] E. F. Toro. *Riemann Solvers and Numerical Methods for Fluid Dynamics*. 3rd. Springer, 2009. DOI: 10.1007/b79761.
- [223] D. T. A. Townend and E. A. C. Chamberlain. “The influence of pressure on the spontaneous ignition and limits of inflammability of ether-air mixtures”. In: *Proceedings of the Royal Society of London. Series A-Mathematical and Physical Sciences* 158.894 (1937), pp. 415–429. DOI: <https://doi.org/10.1098/rspa.1937.0030>.
- [224] T. Turányi. “Applications of sensitivity analysis to combustion chemistry”. In: *Reliability Engineering & System Safety* 57.1 (1997), pp. 41–48. DOI: [https://doi.org/10.1016/S0951-8320\(97\)00016-1](https://doi.org/10.1016/S0951-8320(97)00016-1).
- [225] A. Ungut, P. J. Shuff, and J. A. Eyre. “Initiation of unconfined gaseous detonation by diffraction of a detonation front emerging from a pipe”. In: *Prog. Astronaut. Aeronaut* 94 (1984), pp. 523–545. DOI: <https://doi.org/10.2514/5.9781600865695.0523.0545>.
- [226] P. A. Urtiew, A. K. Oppenheim, and Sir Owen Saunders. “Experimental observations of the transition to detonation in an explosive gas”. In: *Proceedings of the Royal Society of London. Series A. Mathematical and Physical Sciences* 295.1440 (1966), pp. 13–28. DOI: 10.1098/rspa.1966.0223.

- [227] B Varatharajan and FA Williams. “Chemical-kinetic descriptions of high-temperature ignition and detonation of acetylene-oxygen-diluent systems”. In: *Combustion and Flame* 124.4 (2001), pp. 624–645. DOI: [https://doi.org/10.1016/S0010-2180\(00\)00235-2](https://doi.org/10.1016/S0010-2180(00)00235-2).
- [228] N. Vijayakumar. “Reinitiation Mode Study of Highly Irregular Detonation”. PhD thesis. The University of Texas at Arlington, 2020. URL: <https://rc.library.uta.edu/uta-ir/handle/10106/29143>.
- [229] B.V. Voitsekhovskii, V.V. Mitrofanov, and M.E. Topchian. “Investigation of the structure of detonation waves in gases”. In: *Symposium International on Combustion* 12 (1969), pp. 829–837. DOI: 10.1016/S0082-0784(69)80464-9.
- [230] C. Wang, C. Qian, J. Liu, and M.A. Liberman. “Influence of chemical kinetics on detonation initiating by temperature gradients in methane/air”. In: *Combustion and Flame* 197 (2018), pp. 400–415. DOI: 10.1016/j.combustflame.2018.08.017.
- [231] H. Wang, E.R. Hawkes, B. Zhou, J.H. Chen, Z. Li, and M. Aldén. “A comparison between direct numerical simulation and experiment of the turbulent burning velocity-related statistics in a turbulent methane-air premixed jet flame at high Karlovitz number”. In: *Proceedings of the Combustion Institute* 36.2 (2017), pp. 2045–2053. DOI: 10.1016/j.proci.2016.07.104.
- [232] H. Wang, X. You, A. V. Joshi, S. G. Davis, A. Laskin, F. Egolfopoulos, and CK Law. *USC Mech Version II. High-temperature combustion reaction model of H₂/CO/C1-C4 compounds*. http://ignis.usc.edu/USC_Mech_II.htm. Combustion Kinetics Laboratory, University of Southern California, Los Angeles, CA, 2007.

- [233] L. Q. Wang, H. H. Ma, Z. W. Shen, and J. Pan. “Bidirectional diffraction and re-initiation of irregular structure detonation”. In: *Shock Waves* 31.5 (2021), pp. 469–480. DOI: <https://doi.org/10.1007/s00193-021-01030-w>.
- [234] X. Wang and C. K. Law. “An analysis of the explosion limits of hydrogen-oxygen mixtures”. In: *The Journal of Chemical Physics* 138.13 (2013), p. 134305. DOI: 10.1063/1.4798459.
- [235] X. Wang and C. K. Law. “An analysis of the explosion limits of hydrogen-oxygen mixtures”. In: *The Journal of Chemical Physics* 138.13 (2013), p. 134305. DOI: 10.1063/1.4798459.
- [236] X. Wen, T. Su, Z. Liu, M. Xie, F. Wang, and Z. Liu. “Numerical Investigation on Porous Media Quenching Behaviors of Premixed Deflagrating Flame using RANS/LES Model”. In: *Journal of Thermal Science* 28 (4 2019), pp. 780–788. DOI: 10.1007/s11630-019-1131-7.
- [237] D. R. White. “Turbulent Structure of Gaseous Detonation”. In: *The Physics of Fluids* 4.4 (1961), pp. 465–480. DOI: 10.1063/1.1706350.
- [238] H. Xiao, D. Makarov, J. Sun, and V. Molkov. “Experimental and numerical investigation of premixed flame propagation with distorted tulip shape in a closed duct”. In: *Combustion and Flame* 159.4 (2012), pp. 1523–1538. DOI: <https://doi.org/10.1016/j.combustflame.2011.12.003>.
- [239] H. Xiao and E. S. Oran. “Flame acceleration and deflagration-to-detonation transition in hydrogen-air mixture in a channel with an array of obstacles of different shapes”. In: *Combustion and Flame* 220 (2020), pp. 378–393. DOI: <https://doi.org/10.1016/j.combustflame.2020.07.013>.
- [240] H. Xiao and E. S. Oran. “Shock focusing and detonation initiation at a flame front”. In: *Combustion and Flame* 203 (2019), pp. 397–406. DOI: <https://doi.org/10.1016/j.combustflame.2019.02.012>.

- [241] Q. Xiao, A. Sow, B. M. Maxwell, and M. I. Radulescu. “Effect of boundary layer losses on 2D detonation cellular structures”. In: *Proceedings of the Combustion Institute* 38.3 (2021), pp. 3641–3649. DOI: <https://doi.org/10.1016/j.proci.2020.07.068>.
- [242] H. Xu, X. Mi, C. B. Kiyanda, H. D. Ng, J. H. S. Lee, and C. Yao. “The role of cellular instability on the critical tube diameter problem for unstable gaseous detonations”. In: *Proceedings of the Combustion Institute* 37.3 (2019), pp. 3545–3553. DOI: <https://doi.org/10.1016/j.proci.2018.05.133>.
- [243] N. Yoshikawa. “Coherent shock wave amplification in photochemical initiation of gaseous detonations”. PhD thesis. Department of Mechanical Engineering, McGill University, 1980. URL: <https://escholarship.mcgill.ca/concern/theses/xk81jm32t>.
- [244] X. Q. Yuan, X. C. Mi, H. D. Ng, and J. Zhou. “A model for the trajectory of the transverse detonation resulting from re-initiation of a diffracted detonation”. In: *Shock Waves* 30.1 (2020), pp. 13–27. DOI: 10.1007/s00193-019-00904-4.
- [245] X. Q. Yuan, C. Yan, J. Zhou, and H. D. Ng. “Computational study of gaseous cellular detonation diffraction and re-initiation by small obstacle induced perturbations”. In: *Physics of Fluids* 33.4 (2021), p. 047115. DOI: 10.1063/5.0044164.
- [246] A.C. Zambon and H.K. Chelliah. “Explicit reduced reaction models for ignition, flame propagation, and extinction of C₂H₄/CH₄/H₂ and air systems”. In: *Combustion and Flame* 150 (2007), pp. 71–91. ISSN: 0010-2180. DOI: <https://doi.org/10.1016/j.combustflame.2007.03.003>.
- [247] I. A. Zeldovich, G. I. Barenblatt, V. B. Librovich, and G. M. Makhviladze. *Mathematical theory of combustion and explosions*. Consultants Bureau, New York, NY, 1985.

- [248] I. B. Zeldovich. “An experimental investigation of spherical detonation of gases”. In: *Soviet Phys. Tech. Phys.* 1 (1956), pp. 1689–1713.
- [249] J.B. Zeldovich and D.A. Frank-Kamenetzki. “A Theory of Thermal Propagation of Flame”. In: *Dynamics of Curved Fronts*. San Diego: Academic Press, 1988, pp. 131–140. DOI: <https://doi.org/10.1016/B978-0-08-092523-3.50015-0>.
- [250] Ya. B. Zeldovich, V. B. Librovich, G. M. Makhviladze, and G. I. Sivashinsky. “On the development of detonation in a nonuniformly heated gas”. In: *Astronaut. Acta* 15 (1970), pp. 313–321.
- [251] B. Zhang, N. Mehrjoo, H. D. Ng, J. H. S. Lee, and C. Bai. “On the dynamic detonation parameters in acetylene–oxygen mixtures with varying amount of argon dilution”. In: *Combustion and Flame* 161.5 (2014), pp. 1390–1397. DOI: <https://doi.org/10.1016/j.combustflame.2013.11.016>.
- [252] K. Zheng, M. Yu, Y. Liang, L. Zheng, and X. Wen. “Large eddy simulation of premixed hydrogen/methane/air flame propagation in a closed duct”. In: *International Journal of Hydrogen Energy* 43.7 (2018), pp. 3871–3884. DOI: <https://doi.org/10.1016/j.ijhydene.2018.01.045>.
- [253] Y. Zhu, J. Yang, and M. Sun. “A thermochemically derived global reaction mechanism for detonation application”. In: *Shock Waves* 22 (July 2012), pp. 363–379. DOI: 10.1007/s00193-012-0375-x.
- [254] Y. J. Zhu, J. Chao, and J. H. S. Lee. “An experimental investigation of the propagation mechanism of critical deflagration waves that lead to the onset of detonation”. In: *Proceedings of the Combustion Institute* 31.2 (2007), pp. 2455–2462. DOI: <https://doi.org/10.1016/j.proci.2006.07.209>.
- [255] J.L. Ziegler. “Simulations of compressible, diffusive, reactive flows with detailed chemistry using a high-order hybrid WENO-CD scheme”. PhD the-

sis. California Institute of Technology, 2012. URL: <https://thesis.library.caltech.edu/6759/>.